UNIVERSITY OF BUCHAREST
Faculty of Physics
Doctoral School of Physics

Alexandru Cătălin ENE

OBSERVATION OF THE PRODUCTION AND DECAY OF PARTICLES IN THE FORWARD REGION AT THE LHCb EXPERIMENT

PhD. THESIS

Coordinator:
Prof.univ.dr. Alexandru JIPA

Bucharest, 2020

Abstract

This thesis is structured around two main studies, namely a study of Monte Carlo hadronic collisions generators and an LHCb data analysis. In the first study, the predictions of PYTHIA [1], EPOS [2], QGSJET [3], and SIBYLL [4], all with tunes based on "central" rapidity measurements from the LHC general purpose detector experiments, i.e. ATLAS [5], ALICE [6] and CMS [7], are compared to "forward" rapidity measurements of observables in pp collisions at $\sqrt{s} = 7$ TeV from LHCb [8] and TOTEM [9]. These measurements fall into four categories, namely energy flow [10], charged hadron multiplicities and densities [11–13], charged hadron production ratios [14] and V^0 hadron production ratios [15]. The results of the study are published in [16]. The overarching conclusion of the study is that the tuning in the "central" region improves the predictions in the "forward" region, too, but tuning with measurements from the latter is necessary for better descriptions therein [16]. The measurements of prompt V^0 (K^0_S and Λ^0) production cross-sections and ratios in pp collisions at $\sqrt{s} = 13$ TeV are the subject of the LHCb data analysis. The measurements are carried out in a two-dimensional phase space of rapidity and transverse momentum, divided into a 6×6 array of symmetric bins in $2 \leq y < 5$ and $1 \leq \log(p_T[\mathrm{MeV/c}]) < 4$. The full analysis phase space values of the cross-sections are $\sigma_{K^0_S} = 64\,501.5 \pm 4\,787.3$ µb, $\sigma_{\Lambda^0} = 22\,106.3 \pm 1\,656.3$ µb and $\sigma_{\overline{\Lambda^0}} = 21\,013.7 \pm 1\,654.3$ µb. For the $\overline{\Lambda^0}/\Lambda^0$ and $\overline{\Lambda^0}/K^0_S$ ratios, values of 0.960 ± 0.052 and 0.329 ± 0.023, respectively, have been obtained. The quoted uncertainties are the quadratic sum of the statistical and systematic uncertainties, with the former being comparatively negligible. This latter work represents the stem of a future LHCb analysis note.

Thanks

I would like to thank Prof.Dr. Alexandru JIPA for his guidance from my undergraduate studies and up to the present PhD. thesis, Dr. Florin MACIUC, team leader of the Romanian LHCb group, my supervisor within the LHCb Collaboration and at IFIN-HH, the members of the LHCb collaboration for the opportunity to do an LHCb data analysis, and my colleagues from the Department of Elementary Particle Physics (DFPE). I would also like to thank my family and friends for their support during the arduous years leading to the completion of this thesis.

This work, as well as participations to international conferences and schools, have been financially supported by the PN II IDEI (56/07.10.2011), IFA România-CERN (7/16.03.2016) (LHCb-Ro) and IFA România-CERN (9/10.03.2020) (LHCb-Ro) projects.

Contents

Introduction

Experimental high energy physics has arguably been the foremost source of discoveries regarding fundamental properties of matter in the last decades, culminating with the construction of the Large Hadron Collider (LHC) at CERN and the subsequent finding of the Higgs boson, which completed the Standard Model (SM) of particle physics. Searches for a plethora of novel phenomena and tests of various SM predictions are ongoing at the LHC experiments, like CP violation phases indicative of New Physics beyond the Standard Model, lepton flavour violation and exotic hadrons at the LHCb experiment, just to name a few [8, 17]. Although processes taking place in the perturbative region of quantum chromodynamics (QCD) are rather well understood, the same can not be said about phenomena like multiparton interactions and hadronization, which are described using phenomenological models with free parameters to be determined using experimental data (see Chapter 2). Various Monte Carlo hadronic collisions generators which implement different models and effective theories with elements from QCD, the parton model and/or the Gribov-Regge Theory have been developed, like PYTHIA [1], EPOS [2], QGSJET [3], and SIBYLL [4], with the first focused on collider physics and the next three on high energy cosmic ray studies. All of the aforementioned generators have been tuned to various measurements from the LHC experiments, as detailed in Section 2.8. For the bulk of the tuning procedures, minimum bias and underlying event observables from the LHC experiments probing the "central" pseudorapidity region, $|\eta| \leq 2.5$, namely ATLAS [5], ALICE [6] and CMS [7], have been used, while measurements from the "forward" rapidity region ($\eta > 2.5$) experiments like LHCb ($2 \leq \eta \leq 5$) [8] and TOTEM ($3.1 \leq \eta \leq 6.5$) [9] are used to a far lesser extent [16]. Particles produced in partonic scatterings taking place in the perturbative region of QCD, dubbed "hard" QCD processes, are characterized by high transverse momenta and such, small rapidities, while those produced in "soft" processes like diffraction, multiparton interactions (MPI) and beam remnant fragmentation typically have larger rapidities. Thus, measurements from the "central" region are expected to constrain parameters related to hard partonic processes, rather than soft ones, and vice versa in the case of measurements in the "forward" region [16]. In order to study the effect that tuning with "central" region measurements has in the "forward" region, the generator predictions for several observables like energy flow, charged hadron multiplicities and densities, charged hadron and V^0 production ratios in pp collisions at $\sqrt{s} = 7$ TeV have been compared to the measurements from LHCb and TOTEM. The results of this study have been published in [16] and are given in Chapter 4. Measurements of V^0 hadron production (K_S^0 meson and Λ^0 baryon) provide a prospect for constraining the strange quark and diquark suppression parameters of hadronization models [15, 18] (see Section 2.7), as detailed in Section 5.1. The preliminary results for measurements of prompt V^0 production cross-sections and ratios at LHCb in pp collisions at $\sqrt{s} = 13$ TeV, with comprehensive descriptions of the analysis methods and determination of the experimental uncertainties, are given in Chapter 5. This work has been presented during an LHCb QEE (QCD, Electroweak, and Exotica) working group meeting and is the basis for an upcoming LHCb analysis note.

The cross-sections for K_S^0 production have been previously measured at LHCb in pp collisions at $\sqrt{s} = 0.9$ TeV [19] and the $\overline{\Lambda^0}/K_S^0$, $\overline{\Lambda^0}/\Lambda^0$ ratios at $\sqrt{s} = 7$ TeV [15]. Strange hadron production has also been studied in the central rapidity region at different collision energies at the LHC experiments with general purpose detectors [20–23].

The thesis is structured as follows: a short overview of the theory and phenomenology involved in high energy hadronic collisions is given in Chapter 2, a detailed description of the LHCb experiment in Chapter 3, the study of Monte Carlo event generators and the results of V^0 production measurements introduced above are given in Chapters 4 and 5, respectively, and the overall conclusions of the thesis in Chapter 6. The references are given in the Bibliography section and my activity during the PhD. school, including, but not limited to, publications and conferences, is detailed in the Author's activity section.

This work represents a natural continuation of my master's [A] and bachelor's [B] studies. The topic of the latter is different to the one of the former and the present thesis, but is nonetheless in the same broader domain of experimental particle physics.

As mentioned above, the study presented in Chapter 4 has been published in [16], in which a description of the generators from Section 2.8 can also be found. Consequently, some degree of similarity between the texts therein is unavoidable. Proper references have been given where high similarities are found and also in the captions of the figures that have been published.

As per the LHCb Constitution, the results of the LHCb data analysis from Chapter 5 are the intellectual property of the LHCb Collaboration. According to the LHCb Publication Procedure, independent publication of physics results that are not previously published by LHCb is exceptionally permitted for PhD. theses when most of the work to obtain the results is done by the author of the thesis. The LHCb data analysis results from Chapter 5 have not yet been officially peer reviewed within the LHCb Collaboration.

The figures from the present thesis that are not the result of my own work are included for the sole purpose of helping the reader better understand the text. The sources of these figures are referenced at the end of the captions and to the best of my knowledge are publically available for reproduction under fair use with proper attribution, no copyright infringement being intended.

Theory and phenomenology of particle physics

2.1 The Standard Model

The fundamental particles and interactions, with the exception of gravity, are described by the Standard Model (SM). There are three generations of fermions, in increasing order of their mass, which participate in electromagnetic, weak and strong interactions via the exchange of gauge bosons. The masses of the fermions and of the weak interaction bosons are generated via interactions with the Higgs field. The elementary particles, their classification and several properties, namely mass, electric charge and spin, are shown in Figure 2.1. The fermions are further divided into the quark and lepton families. The electric charges of the quarks are fractions of the elementary charge, namely $(2/3)e$ and $-(1/3)e$ for u, c, t, and d, s, b, respectively. For each charged lepton, namely electron, muon and tau, there is one associated neutrino, which has null electric charge [24–26].

The quarks participate in all of the aforementioned interactions. Leptons lack colour charge and so, do not participate in the strong interaction. Neutrinos, having null electric charge, participate only in the weak interaction. The bosons of the electromagnetic and strong interactions are the massless and electrically neutral photon and gluon, respectively. The weak interaction proceeds via the exchange of charged, $W^{\pm}$, or neutral, Z^0, bosons [24–26].

The Standard Model is based on the $\mathrm{SU}(3) \times \mathrm{SU}(2) \times \mathrm{U}(1)$ symmetry group, where the $\mathrm{SU}(3)$ corresponds to the colour symmetry group from quantum chromodynamics, and the last two terms represent the electro-weak component [24–26].

2.2 Quantum chromodynamics

The interactions involving colour are described by a quantum field theory suggestively named quantum chromodynamics, or QCD for short [24]. The (anti) quarks carry single (anti) colour charges, while gluons carry one colour and one anticolour charges at the same time [27, 28]. There are three colour charges corresponding to the column vectors:

$$\mathrm{R} = \begin{pmatrix} 1 \\ 0 \\ 0 \end{pmatrix}; \quad \mathrm{G} = \begin{pmatrix} 0 \\ 1 \\ 0 \end{pmatrix}; \quad \mathrm{B} = \begin{pmatrix} 0 \\ 0 \\ 1 \end{pmatrix}. \tag{2.1}$$

which form the fundamental representation of the colour $\mathrm{SU}(3)$ group [28, 29].

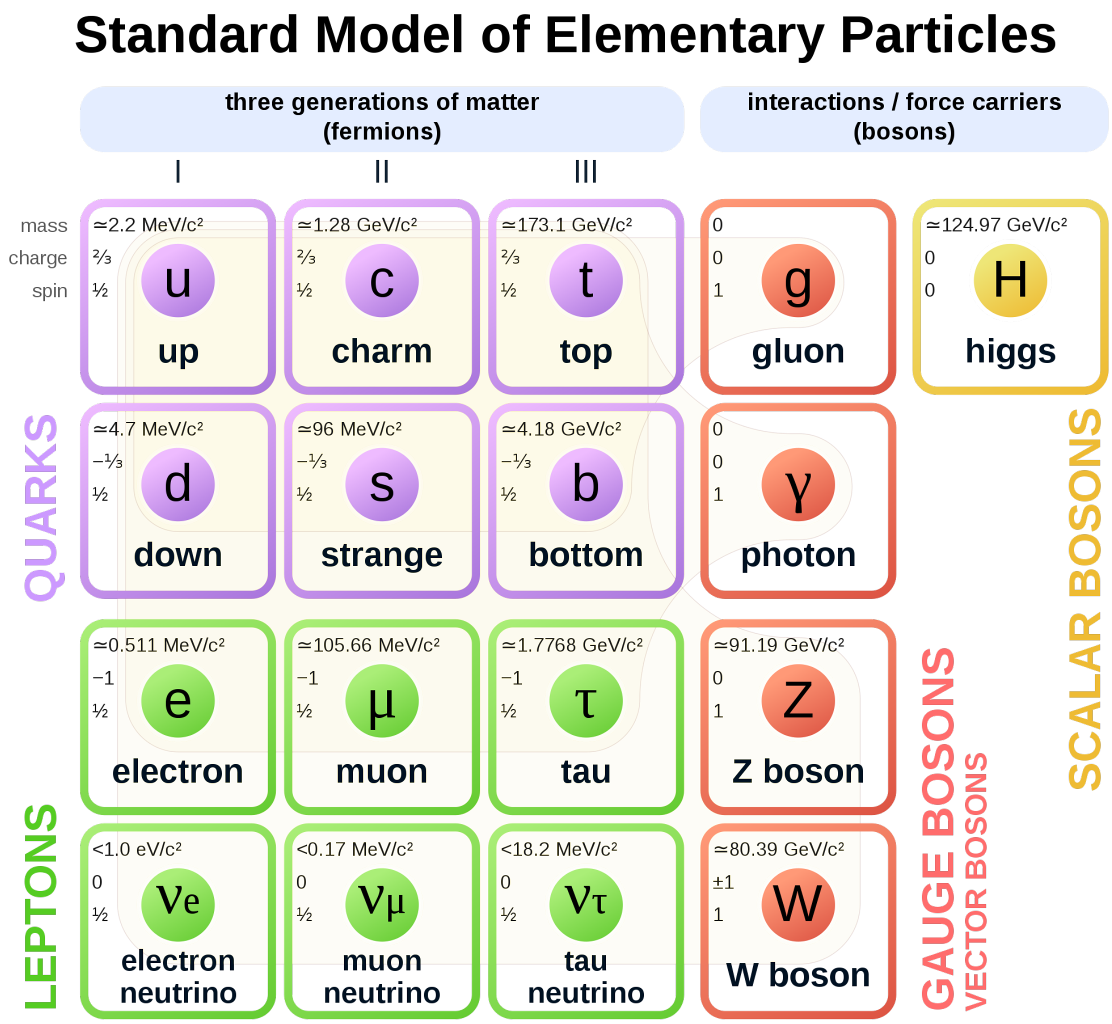

Figure 2.1: Schematic representation of the Standard Model [25].

Combining this representation with the one corresponding to the anticolours yields an octet and a singlet [24]:

$$3 \otimes \overline{3} = 8 \oplus 1. \tag{2.2}$$

The octet states are:

$$\begin{gathered}
\mathrm{R\overline{G}}, \mathrm{R\overline{B}}, \mathrm{G\overline{R}}, \mathrm{G\overline{B}}, \mathrm{B\overline{R}}, \mathrm{B\overline{G}}, \frac{1}{\sqrt{2}}\left(\mathrm{R\overline{R}} - \mathrm{G\overline{G}}\right), \frac{1}{\sqrt{6}}\left(\mathrm{R\overline{R}} + \mathrm{G\overline{G}} - 2\mathrm{B\overline{B}}\right) \\
\text{and the singlet is } \frac{1}{\sqrt{3}}\left(\mathrm{R\overline{R}} + \mathrm{G\overline{G}} + \mathrm{B\overline{B}}\right),
\end{gathered} \tag{2.3}$$

so there are 8 gluons corresponding to the octet, as the singlet state carries no net colour charge [29].

The generators of the SU(3) symmetry group are the Gell-Mann matrices [29, 31, 32]:

$$\begin{gathered}\lambda_1 = \begin{pmatrix} 0 & 1 & 0 \\ 1 & 0 & 0 \\ 0 & 0 & 0 \end{pmatrix}; \quad \lambda_2 = \begin{pmatrix} 0 & -i & 0 \\ i & 0 & 0 \\ 0 & 0 & 0 \end{pmatrix}; \qquad \lambda_3 = \begin{pmatrix} 0 & 1 & 0 \\ -1 & 0 & 0 \\ 0 & 0 & 0 \end{pmatrix}; \\ \lambda_4 = \begin{pmatrix} 0 & 0 & 1 \\ 0 & 0 & 0 \\ 1 & 0 & 0 \end{pmatrix}; \quad \lambda_5 = \begin{pmatrix} 0 & 0 & -i \\ 0 & 0 & 0 \\ i & 0 & 0 \end{pmatrix}; \qquad \lambda_6 = \begin{pmatrix} 0 & 0 & 0 \\ 0 & 0 & 1 \\ 0 & 1 & 0 \end{pmatrix}; \\ \lambda_7 = \begin{pmatrix} 0 & 0 & 0 \\ 0 & 0 & -i \\ 0 & i & 0 \end{pmatrix}; \quad \lambda_8 = \frac{1}{\sqrt{3}} \begin{pmatrix} 1 & 0 & 0 \\ 0 & 1 & 0 \\ 0 & 0 & -2 \end{pmatrix}. \end{gathered} \tag{2.4}$$

In high energy scatterings, the strength of the lowest order colour interactions relative to the electromagnetic ones is given by:

$$\frac{f\alpha_s}{e_1 e_2 \alpha}, \tag{2.5}$$

where $e_{1,2}$ are the electric charges given as a function of the elementary charge, α is the fine structure constant, α_s is the strong coupling constant and f is a so-called colour factor [27, 29, 33]. For quark-quark scatterings:

$$f(lj \to ki) = \frac{1}{4} \sum_{a=1}^{8} \lambda^a_{ji} \lambda^a_{lk} = \frac{1}{2}\delta_{il}\delta_{jk} - \frac{1}{6}\delta_{ij}\delta_{kl} \tag{2.6}$$

where $i, j, k, l = 1, 3$ are indices corresponding to the colour states (R,G,B $\to 1, 2, 3$), the λ terms are the elements of the Gell-Mann matrices and δ is the Kronecker delta. To obtain the factors for quark-antiquark interactions, the indices for the initial and final states are swapped for one of the quarks in the right-hand side of the above equation. Due to colour conservation, the possible interactions for $qq \to qq$ are the ones in which the colours do not change, e.g. RR $\to$ RR ($f = 1/3$) and RG $\to$ RG ($f = -1/6$), or the colours are swapped between the quarks, e.g. RG $\to$ GR ($f = 1/2$). For $q\overline{q} \to q\overline{q}$, the colour swapping interactions are obviously not permitted, but the ones in which colour neutral final states differ from the initial ones like R$\overline{\text{R}}$ $\to$ G$\overline{\text{G}}$ ($f = 1/2$) are. The colour factors for the other interaction types are the same as for the qq case [27, 33].

The colour interaction has a Coulomb type potential for high energy scatterings (corresponding to short distance interactions):

$$V(r) \sim \pm f \frac{\alpha_s}{r}, \tag{2.7}$$

with negative sign for $q\overline{q}$ and positive for qq ($\overline{qq}$), in analogy with the electromagnetic interaction which is attractive for opposite sign charges and repulsive for same sign ones [27, 33]. Summing over all contributions to $q\overline{q}$ in a colour singlet state yields a colour factor of:

$$f = \frac{4}{3}, \tag{2.8}$$

so the colour interaction is attractive, while in the case of an octet state it is repulsive, as $f = -1/6$ [27, 29, 33].

As quarks carry colour which forms a symmetric triplet, the combination of two quarks will form a symmetric sextet and an antisymmetric triplet [29]:

$$3 \otimes 3 = 6 \oplus \overline{3}. \tag{2.9}$$

A baryon is a three quark system and must be in a colour singlet state, so a quark, which is in a symmetric colour state, must couple with a pair of quarks in an antisymmetric state, as [28, 29, 33]:

$$\begin{gathered} 3 \otimes 3 \otimes 3 = (6 \oplus \overline{3}) \otimes 3 = (6 \otimes 3) \oplus (\overline{3} \otimes 3) = (10_S \oplus 8_{M_S}) \oplus (8_{M_A} \oplus 1_A), \\ \text{with } 1_A = \frac{1}{\sqrt{6}} \left(\mathrm{RGB} - \mathrm{RBG} + \mathrm{GBR} - \mathrm{GRB} + \mathrm{BRG} - \mathrm{BGR}\right), \end{gathered} \tag{2.10}$$

where the S, A and $M_{S,A}$ subscripts are assigned to symmetric, antisymmetric and mixed-symmetry multiplets, respectively. Under the interchange of the first two quarks, M_S states are symmetric, while M_A states are antisymmetric [24, 29, 34].

The $\overline{3}$ is formed by [33]:

$$\frac{1}{\sqrt{2}} \left(\mathrm{RG} - \mathrm{GR}\right), \frac{1}{\sqrt{2}} \left(\mathrm{BR} - \mathrm{RB}\right), \frac{1}{\sqrt{2}} \left(\mathrm{GB} - \mathrm{BG}\right). \tag{2.11}$$

For interactions between quarks from pairs in which the final and initial states are the same and part of $\overline{3}$, the colour factor is $-2/3$, which translates into an attractive colour force between any two valence quarks of a baryon [29, 33].

The coupling strengths of [26]:

$$g \to q\overline{q}, \quad q \to qg, \quad g \to gg, \tag{2.12}$$

are given by the SU(3) values of the SU(N) invariants:

$$T_F = \frac{1}{2}, \quad C_F = \frac{4}{3}, \quad C_A = 3. \tag{2.13}$$

the determination of which is detailed in [26, 33].

Charged particles can emit virtual photons via quantum fluctuations, which can subsequently produce virtual electron-positron pairs. The electrons and positrons will be repelled by and attracted towards negative charges, respectively, and vice versa in the case of positive charges, a phenomenon known as vacuum polarization which causes the charge to be "screened". This effect is equivalent to replacing the charge with an effective charge which decreases with distance. Thus, the coupling constant of the electromagnetic interaction increases as the distance to the charge decreases. There is also a similar "screening" effect in the case of colour charges caused by virtual gluons splitting into $q\overline{q}$ pairs. The gluons, however, may also split into two other gluons and as these are colour charged, an "antiscreening" effect is produced. This effect is greater than the former and so, the strong coupling constant increases with distance, leading to the phenomena of asymptotic freedom and confinement [29, 31, 35].

The strong coupling constant satisfies:

$$\mu_R^2 = \frac{d\alpha_s}{d\mu_R^2} = \beta(\alpha_s) = -\left(b_0\alpha_s^2 + b_1\alpha_s^3 + b_2\alpha_s^4 + \ldots\right) \tag{2.14}$$

called the renormalization group equation, where μ_R is called the renormalization scale and $\beta(\alpha_s)$ is called the beta function which is negative valued, as opposed to its quantum electrodynamics (QED) counter-part. The b_i terms from the perturbative expansion correspond to the $(i+1)$ Feynman diagram loops and:

$$b_0 = \frac{33 - 2n_f}{12\pi}, \tag{2.15}$$

where n_f is the number of quark flavours with $m_q \ll \mu_R$ [24, 26, 35].

Neglecting the $b_{i>0}$ terms, the leading log approximation (LLA) is obtained:

$$\alpha_s\left(Q^2\right) = \frac{\alpha_s\left(\mu_R^2\right)}{1 + \alpha_s\left(\mu_R^2\right) b_0 \ln\left(Q^2/\mu_R^2\right)} = \frac{1}{b_0 \ln\left(Q^2/\Lambda^2\right)}, \tag{2.16}$$

where $\Lambda \sim 300$ MeV is the QCD scale parameter through which the perturbative region $Q^2 \gg \Lambda^2$ is defined [24, 26, 31, 32, 35]. The strong coupling constant is usually given at the scale of the Z^0 boson mass, $\alpha_s\left(M_Z^2\right) \sim 0.12$ [24, 26, 35].

2.3 Hadrons in the quark model

Hadrons are bound colour singlet states of quarks and antiquarks, namely mesons are $q\overline{q}$ states and (anti) baryons are $(\overline{qqq})$ qqq states. Quarks have many associated intrinsic quantum numbers, besides the familiar spin and charge, and are detailed in the following [24].

As the masses of the u and d quarks are similar, the colour interaction may be considered to be invariant under the interchange of these flavours [28, 31]. Thus, they form the fundamental representation of an SU(2) symmetry group called isospin [28, 29]. This symmetry, however, is only approximate due to the fact that the masses are not the same [28, 31]. The u and d states are represented by the column vectors [28]:

$$u = \begin{pmatrix} 1 \\ 0 \end{pmatrix} ; d = \begin{pmatrix} 0 \\ 1 \end{pmatrix} ; \tag{2.17}$$

and the generators of the isospin group are, in analogy to spin [28, 29]:

$$\begin{gathered} I_i = \frac{1}{2}\tau_i, \\ \text{with } \tau_1 = \begin{pmatrix} 0 & 1 \\ 1 & 0 \end{pmatrix} ; \tau_2 = \begin{pmatrix} 0 & -i \\ i & 0 \end{pmatrix} ; \tau_3 = \begin{pmatrix} 1 & 0 \\ 0 & -1 \end{pmatrix} . \end{gathered} \tag{2.18}$$

Thus, u and d form an isospin doublet with $I = 1/2$ and $I_3 = \pm 1/2$, where [28, 31]:

$$I_3 = (N_u - N_d). \tag{2.19}$$

The baryon number is defined as $\mathcal{B} = 1, -1$ and 0 for baryons, antibaryons and mesons, respectively [31]. Consequently, a baryon number of $\mathcal{B} = 1/3$ is assigned to quarks and $\mathcal{B} = -1/3$ to antiquarks [24, 29].

The flavours of the lightest quarks are encoded in their I_3 values and, by extension to the heavier quarks, the strangeness (S), charmness (C), bottomness (B) and topness (T) quantum numbers are assigned, with values of ± 1. By convention, the sign is dictated by the sign of the charge, Q, of the respective quark, namely they must be the same [24].

The generalized Gell-Mann-Nishijima formula gives the relationship between the quantum numbers defined above [24]:

$$Q = I_3 + \frac{\mathcal{B} + S + C + B + T}{2}. \tag{2.20}$$

Another quantum number can be constructed from the previously defined numbers, with the exception of isospin, called the hypercharge:

$$Y = \mathcal{B} + S - \frac{C - B + T}{3}, \tag{2.21}$$

with values of 1/3 for u and d, $-2/3$ for s, and 0 for the heavier flavours [24].

All of these quantum numbers are additive, but there are also multiplicative ones like parity, P, and C-parity, C, given by the eigenvalues of the parity and charge conjugation operators, respectively. The intrinsic parities of quarks and antiquarks are set, by convention, to 1 and -1, respectively [24, 31].

As mentioned, the mesons are $q\overline{q}$ states, with $P = (-1)^{L+1}$ and $C = (-1)^{L+S}$, where L is the angular momentum and S the spin. The total spin of the meson is given by $J = L + S$ [24, 29]. The allowed values of these numbers are detailed in [24].

The lightest three quarks, u, d, and s form the fundamental representation of the approximate flavour SU(3) symmetry group. Combining a quark with an antiquark, an octet and a singlet are obtained, collectively known as a meson nonet [24, 29]:

$$3 \otimes \overline{3} = 8 \oplus 1. \tag{2.22}$$

The meson nonets are classified according to their J^{PC} and a detailed description can be found in [24]. The $L = 0$ nonets are the pseudoscalar, 0^{-+}, and vector, 1^{--}, ones [24] and are schematically shown in Figure 2.2.

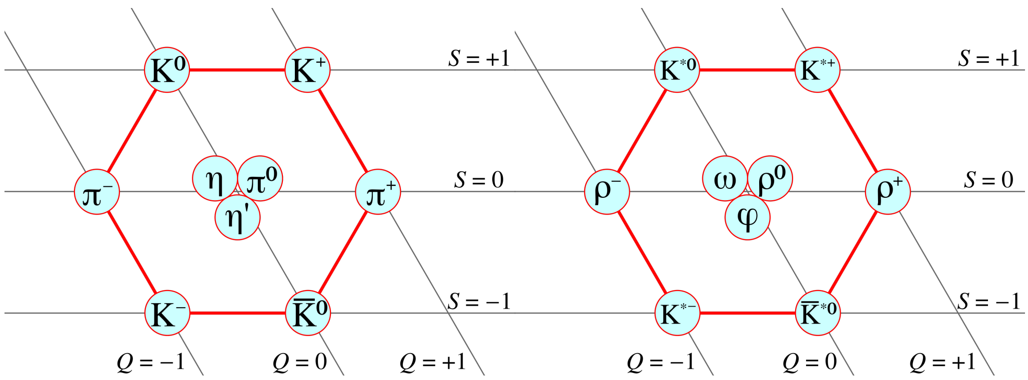

Figure 2.2: The pseudoscalar (left) [36] and vector (right) [37], $L = 0$, meson nonets.

Baryons are qqq states and their wave functions may be expressed as [24, 28, 38]:

$$\psi = \psi_{\text{colour}} \times \psi_{\text{flavour}} \times \psi_{\text{spin}} \times \psi_{\text{space}}. \tag{2.23}$$

The combination of the quark spins yields [28, 29, 34]:

$$2 \otimes 2 \otimes 2 = 4_S \oplus 2_{M_S} \oplus 2_{M_A}, \tag{2.24}$$

where 4_S is a symmetric $S = 3/2$ quadruplet, 2_{M_S} and 2_{M_A} are $S = 1/2$ doublets, symmetric and antisymmetric under the interchange of the first two quarks, respectively [28, 29]. It is clear that baryons are fermions, so their wave functions must be antisymmetric. As they are in a singlet colour state which is antisymmetric, the $\psi_{\text{flavour}} \times \psi_{\text{spin}} \times \psi_{\text{space}}$ component of the wave function must be symmetric [28, 29, 38].

Three quark combinations in flavour SU(3) yield the same multiplet configuration as for colour SU(3) (see Equation (2.10)) [24, 28, 29, 34, 38]:

$$10_S \oplus 8_{M_S} \oplus 8_{M_A} \oplus 1_A. \tag{2.25}$$

For $L = 0$ baryons, $P = 1$ and, consequently, the spatial component of the wave function is symmetric. Thus, the $\psi_{\text{flavour}} \times \psi_{\text{spin}}$ component must also be symmetric [24, 28, 29].

Combining the spin and flavour multiplets yields the following symmetric multiplet:

$$\begin{gathered} 56_S = {}^4 10 \oplus {}^2 8, \\ \text{with } {}^4 10 = (10_S, 4_S)\,; {}^2 8 = \frac{1}{\sqrt{2}} \left[\left(8_{M_S}, 2_{M_S} \right), \left(8_{M_A}, 2_{M_A} \right) \right]; \end{gathered} \tag{2.26}$$

where ${}^4 10$ and ${}^2 8$ indicate baryons in the symmetric flavour decuplet that are also in the symmetric spin quadruplet and baryons in the mixed symmetry octets are also in the matching mixed symmetry spin doublets [24, 29].

This reasoning can be extended to obtain $L > 0$ hadrons or to include heavier quarks by considering SU(N > 3) flavour symmetries (details in [24, 29]). The SU(3) ground-state baryon decuplet and octet are schematically shown in Figure 2.3.

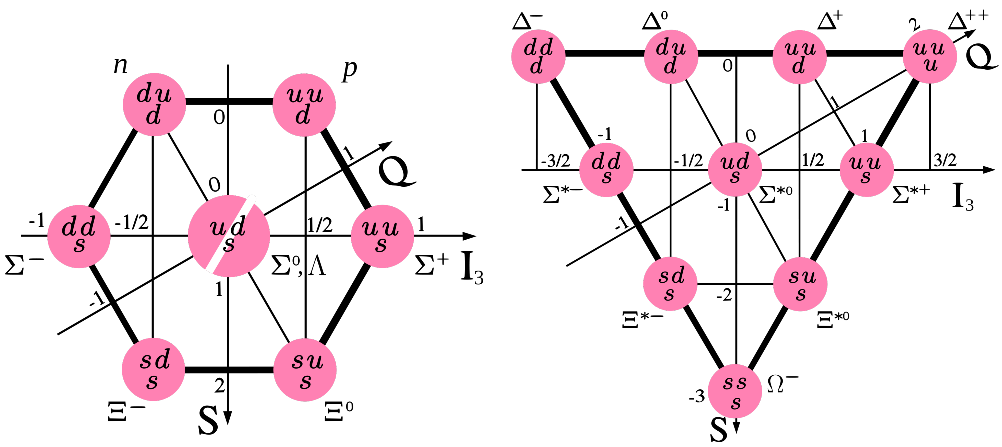

Figure 2.3: The $L = 0$ baryon octet (left) [39] and decuplet (right) [40].

2.4 CP violation in neutral kaon decays

The strangeness quantum number, S, is not conserved by the weak interaction and so, the K^0 ($d\bar{s}$, $S = +1$) and $\overline{K^0}$ ($s\bar{d}$, $S = -1$) neutral kaon states can mix. There are two observed neutral kaon states, which decay via the weak interaction, namely the short-lived, K_S^0, and long-lived, K_L^0, states that are linear combinations of K^0 and $\overline{K^0}$ [25, 29, 31].

The lifetimes, main decay modes and the corresponding branching fractions of the observed states are [24]:

$$\begin{array}{ll}
\mathcal{B}\left(K_S^0 \to \pi^+\pi^-\right) = 30.69 \pm 0.05\%; & \mathcal{B}\left(K_S^0 \to \pi^+\pi^-\right) = 69.20 \pm 0.05\%; \\
\mathcal{B}\left(K_L^0 \to \pi^\pm e^\mp \nu_e\right) = 40.55 \pm 0.11\%; & \mathcal{B}\left(K_L^0 \to \pi^\pm \mu^\mp \nu_e\right) = 27.04 \pm 0.07\%; \\
\mathcal{B}\left(K_L^0 \to 3\pi^0\right) = 19.52 \pm 0.12\%; & \mathcal{B}\left(K_L^0 \to \pi^+\pi^-\pi^0\right) = 12.54 \pm 0.05\%; \\
\tau_{K_S^0} = (0.8954 \pm 0.0004) \times 10^{-10}\ s; & \tau_{K_L^0} = (5.116 \pm 0.021) \times 10^{-8}\ s.
\end{array} \tag{2.27}$$

The 2π and 3π final states can be easily shown to have $CP = 1$ and $CP = -1$, respectively [25, 31]. The intrinsic parity of the neutral kaons is $P = -1$ and, by convention [25, 29, 31, 41]:

$$C|K^0\rangle = -|\overline{K^0}\rangle; \quad C|\overline{K^0}\rangle = -|K^0\rangle; \tag{2.28}$$

leading to [25, 29, 31, 41]:

$$CP|K^0\rangle = |\overline{K^0}\rangle; \quad CP|\overline{K^0}\rangle = |K^0\rangle. \tag{2.29}$$

Thus, the K^0 and $\overline{K^0}$ states are not CP eigenstates, but the following linear combinations are [31, 41]:

$$\begin{array}{ll}
K_1^0 = \frac{1}{\sqrt{2}}\left(|K^0\rangle + |\overline{K^0}\rangle\right); & CP|K_1^0\rangle = |K_1^0\rangle; \\
K_2^0 = \frac{1}{\sqrt{2}}\left(|K^0\rangle - |\overline{K^0}\rangle\right); & CP|K_2^0\rangle = -|K_2^0\rangle.
\end{array} \tag{2.30}$$

If CPT is conserved by the weak interaction, K_S^0 and K_L^0 can be defined as:

$$|K_S^0\rangle = \frac{1}{\sqrt{1+|\epsilon|^2}}\left(|K_1^0\rangle + \epsilon|K_2^0\rangle\right); \quad |K_L^0\rangle = \frac{1}{\sqrt{1+|\epsilon|^2}}\left(|K_2^0\rangle + \epsilon|K_1^0\rangle\right); \tag{2.31}$$

where $\epsilon = 0$ if CP is conserved [25, 31]. This is not the case, however, as $K_S^0 \to 3\pi$ and $K_L^0 \to 2\pi$ decays have been observed with [24]:

$$\begin{array}{l}
\mathcal{B}\left(K_S^0 \to \pi^+\pi^-\pi^0\right) = \left(3.5\ {}^{+1.1}_{-0.9}\right) \times 10^{-7}; \\
\mathcal{B}\left(K_L^0 \to \pi^+\pi^-\right) = (1.967 \pm 0.010) \times 10^{-3}; \\
\mathcal{B}\left(K_L^0 \to \pi^0\pi^0\right) = (8.64 \pm 0.06) \times 10^{-4}.
\end{array} \tag{2.32}$$

The CP violation may either be indirect, generated by decays of the $\epsilon|K^0_{1,2}\rangle$ components of $|K^0_{L,S}\rangle$, or direct, namely the main $|K^0_{1,2}\rangle$ components decay into the corresponding CP forbidden states. The magnitude of CP violation can be determined from the amplitude ratios of CP forbidden and allowed decays:

$$\eta_{+-} = \frac{A\left(K^0_L \to \pi^+\pi^-\right)}{A\left(K^0_S \to \pi^+\pi^-\right)} = \epsilon + \epsilon'; \quad \eta_{00} = \frac{A\left(K^0_L \to \pi^0\pi^0\right)}{A\left(K^0_S \to \pi^0\pi^0\right)} = \epsilon - 2\epsilon'; \tag{2.33}$$

where ϵ and ϵ' are the indirect and direct CP violation parameters, respectively [24–26, 31].

Given the $\Delta S = \Delta Q$ selection rule (at the quark level, the change in strangeness must be equal to the change in electric charge) the real part of the indirect CP violation parameter can also be determined from the charge assymetry in K^0_L semi-leptonic decays [24–26, 31]:

$$A_L = \frac{\Gamma\left(K^0_L \to \pi^- l^+ \overline{\nu}_l\right) - \Gamma\left(K^0_L \to \pi^+ l^- \nu_l\right)}{\Gamma\left(K^0_L \to \pi^- l^+ \overline{\nu}_l\right) + \Gamma\left(K^0_L \to \pi^+ l^- \nu_l\right)} \approx 2\mathrm{Re}(\epsilon). \tag{2.34}$$

The following values are obtained experimentally [24]:

$$\begin{aligned} |\epsilon| &= (2.228 \pm 0.011) \times 10^{-3}, \\ \mathrm{Re}\left(\epsilon'/\epsilon\right) \approx \epsilon'/\epsilon &= (1.66 \pm 0.23) \times 10^{-3}, \\ A_L &= (3.32 \pm 0.06) \times 10^{-3}, \end{aligned} \tag{2.35}$$

so CP violation is dominated by the indirect component [31].

2.5 The parton model

The results from deep inelastic lepton-nucleon scattering experiments prompted the development of the parton model. In the so-called infinite momentum frame, in which a nucleon has very large momentum, it can be considered as being composed of point-like particles called partons, which travel in the same direction as the nucleon and carry a fraction of its momentum given by the so-called Björken x variable:

$$\begin{gathered} x = \frac{Q^2}{2p \cdot q} \to x = \frac{Q^2}{2M\nu} \text{ (lab frame)}, \\ \text{with } Q^2 = -q^2 = -(k - k')^2 \text{ and } \nu = \frac{p \cdot q}{M} \to \nu = E - E' \text{ (lab frame)}, \end{gathered} \tag{2.36}$$

where p is the four-momentum of the nucleon, M its mass, k and k' are the four-momenta of the lepton before and after the scattering, respectively, E and E' are the initial and final lepton energies, respectively, in the laboratory frame of reference, and q, ν are the momentum and energy transfers, respectively, between the lepton and the nucleon. The partons were subsequently identified with quarks and gluons. As gluons have no electrical charge, the leptons scatter off the quarks. Due to time dilation, the quark may be considered to be a free particle during the interaction with the lepton and thus, the inelastic lepton-nucleon cross-section may be obtained from summing the individual lepton-quark cross-sections [29, 31, 32, 42].

At low enough momentum transfers as to neglect contributions from weak boson exchanges, the double differential cross-section as a function of x and Q^2 is:

$$\frac{d^2\sigma}{dxdQ^2} = \frac{4\pi\alpha^2}{xQ^4}\left[(1-y)\,F_2\left(x,Q^2\right) + xy^2F_1\left(x,Q^2\right)\right], \quad \text{with } y = \frac{p\cdot q}{p\cdot k} \rightarrow y = \frac{\nu}{E} \text{ (lab frame)}, \tag{2.37}$$

where α is the fine structure constant, y is the fractional energy transfer and $F_{1,2}\left(x,Q^2\right)$ are so-called structure functions [24, 32, 42, 43].

The F_2 structure function obeys the approximate Björken scaling:

$$Q^2, \nu \rightarrow \infty \text{ with } x \text{ fixed} \Rightarrow F_2\left(x,Q^2\right) \rightarrow F_2(x) \tag{2.38}$$

and is defined as:

$$F_2(x) = \sum_i e_i^2 x f_i(x), \tag{2.39}$$

where the i subscript refers to the quark flavour, i.e. u, d, s etc., e_i is the electrical charge and $xf_i(x)$ is referred to as the parton distribution function (PDF) of quark i, with $f_i(x)$ being the probability of the quark to have a momentum fraction between x and $x+dx$ [24, 29, 32, 42, 43]. The scaling is broken due to gluon radiation, the magnitude of which increases with Q^2. Gluon emission decreases the momenta of the quarks and increases the gluon densities, as well as the sea quark ones through subsequent $g \rightarrow q\overline{q}$ splittings. This effect becomes more prominent with decreasing x [24, 31, 32]. The following equality:

$$F_2(x) = 2xF_1(x), \tag{2.40}$$

is called the Callan-Gross relation and is a consequence of the fact that quarks in the infinite momentum frame can not absorb longitudinally polarized photons [24, 29, 31, 32, 42].

The parton distribution functions of the different constituents of the nucleons can be expressed as:

$$
\begin{aligned}
xu_v = xu - x\overline{u}; \quad xd_v = xu - x\overline{u}; \quad 0 = xs - x\overline{s}; \quad \cdots \\
xu_s = 2x\overline{u}; \quad xd_s = 2x\overline{d}; \quad xs_s = 2x\overline{s}; \quad \cdots \\
xU = xu + xc + xt; \quad x\overline{U} = x\overline{u} + x\overline{c} + x\overline{t}; \\
xD = xd + xs + xb; \quad x\overline{D} = x\overline{d} + x\overline{s} + x\overline{b}; \\
\text{so } xu_v = xU - x\overline{U}; \quad xd_v = xD - x\overline{D}; \quad xS = 2x\left(\overline{U} + \overline{D}\right);
\end{aligned}
\tag{2.41}
$$

where the v and s subscripts indicate valence and sea quarks, respectively, xU ($x\overline{U}$) and xD ($x\overline{D}$) are the sum of the u-type and d-type quark (antiquark) PDFs, respectively, and xS is the sum of all sea quark PDFs. The gluon PDF is simply written as xg [42, 43]. The presence of flavour i quarks in the sea contribution is dictated by $Q^2 > 2m_i^2$, where m_i is the mass of the respective quark [43]. An example of a PDF set is shown in Figure 2.4.

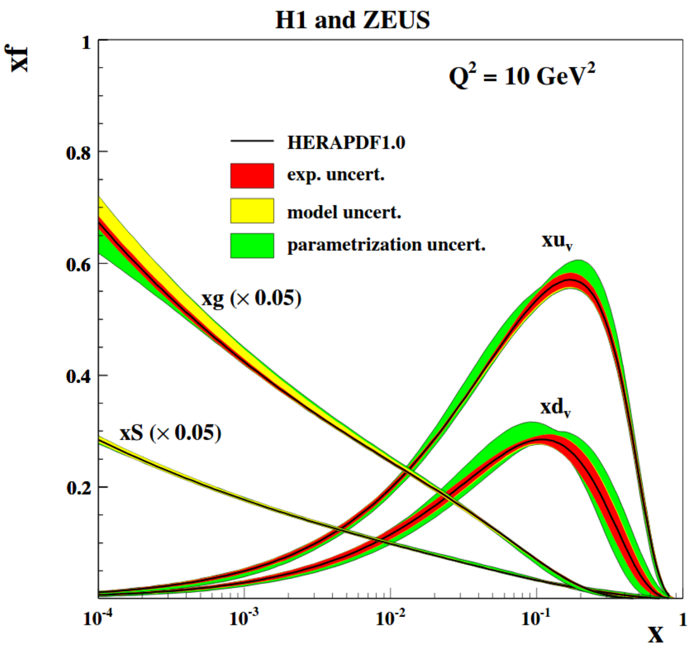

Figure 2.4: Parton distribution functions at $Q^2 = 10$ GeV^2 measured using the H1 and ZEUS detectors in $e^{\pm}p$ scatterings at HERA [43].

Given that protons have two u quarks and one d quark as valence quarks:

$$
\int_0^1 u_v(x)dx = 2; \quad \int_0^1 d_v(x)dx = 1; \tag{2.42}
$$

and vice versa for neutrons [29, 32, 42]. As gluons can not be probed directly in lepton-nucleon scatterings, their PDF is inferred from:

$$
\int_0^1 x\left[u_v(x) + d_v(x) + S(x)\right]dx + \int_0^1 xg(x)dx = 1. \tag{2.43}
$$

The nucleon's momentum is approximately equipartitioned between quarks and gluons, as the fraction carried by the quarks is measured to be around 0.5 [29, 32, 42].

2.6 The Gribov-Regge Theory

In the Gribov-Regge Theory, high energy hadron-hadron interactions are mediated by objects called Reggeons. The scattering amplitude has the following dependence:

$$A(s,t) \propto s^{\alpha_R(t)}, \tag{2.44}$$

where s and t are the squared center-of-mass energy and the squared four-momentum transfer of the collision, respectively, and $\alpha_R(t)$ is the total angular momentum of the exchanged reggeon with mass defined by $m_R^2 = t$, also known as a Regge trajectory [44–48].

The observed meson resonances, such as ρ, ω, f_2, a_2 etc., are found on such trajectories, which are linear:

$$\alpha_R(t) = \alpha_R(0) + \alpha'_R \cdot t, \tag{2.45}$$

with $\alpha_R(0) \approx 0.5$ and $\alpha'_R \approx 0.9$ GeV^{-2} [44–47].

The following proportionality of the total cross-section is found via the optical theorem:

$$\sigma_{\mathrm{TOT}} \propto s^{\alpha_R(0)-1}, \tag{2.46}$$

which is in clear contradiction with the observed slow rise of σ_{TOT} with s in the high collision energy region. In order to describe the experimental data, an additional trajectory was introduced:

$$\alpha_P(t) = \alpha_P(0) + \alpha'_P \cdot t, \tag{2.47}$$

called the Pomeron trajectory, with $\alpha_P(0) \approx 1.08$ and $\alpha'_P \approx 0.25$ GeV^{-2}. The objects on this trajectory are called soft Pomerons, in order to differentiate them from the hard Pomerons ($\alpha_P(0) \approx 1.3$ $\alpha'_P \approx 0.05$ GeV^{-2}) which are used to describe high momentum transfer interactions. The quantum numbers of the Pomerons are those of the vacuum [44–49].

2.7 Phenomenology of hadronic collisions

High energy hadron-hadron collisions can be either elastic or inelastic, with the latter category further split into diffractive and non-diffractive inelastic events [50].

Diffractive events proceed via colour singlet (Pomeron) exchanges, leading to the dissociation of one (single diffraction) or both (double diffraction) of the beam hadrons into high mass states which subsequently decay into the final-state hadrons. There is also a class of events called central-diffractive in which a double pomeron exchange takes place and both protons survive. In diffractive events, large rapidity gaps are usually observed [49–52].

The non-diffractive inelastic events involve colour exchange and can be either soft or hard, depending on whether high transverse momentum final state particles are absent or present, respectively. The latter case is an experimental signature of high momentum transfer (hard) partonic scatterings [50, 53]. The partons involved in these processes may emit gluons both before and after the collision, which may further branch and lead to so-called parton showers. The gluon emission by partons before the collision is similar to the phenomenon of bremsstrahlung from QED and the showers they generate are referred to as initial state radiation (ISR). Conversely, the final state radiation (FSR) is represented by showers generated after the collision [24, 29, 32, 50, 54–56]. Besides the valence quarks, hadrons also contain a multitude of sea quarks and gluons, as discussed in Section 2.5. Thus, a hadronic collision may result in many concurrent partonic scatterings collectively known as multi-parton interactions (MPI). According to the momentum transfer between the partons, the MPI can be split into soft and hard contributions. The partons that do not participate in the MPI form the so-called beam remnants, which together with the soft MPI constitute the underlying event (UE) [50, 57, 58].

The parton branching stops when the squared momentum transfer scales drop to a value of around ~ 1 GeV^2, referred to as the hadronization scale or the infrared shower cutoff. At this stage, the partons combine into colour singlet states, namely hadrons, a process suggestively called hadronization. While perturbative QCD calculations are applicable at the scales of hard partonic scatterings and showers, this is not the case for hadronization and thus, phenomenological models have been developed for its description [24, 32].

One such model is the Lund string fragmentation model described in the following. As discussed in Section 2.2, gluon self-coupling leads to the phenomenon of confinement. Thus, the colour field lines between a quark and an antiquark at a distance r form a tubular region which acts like a string with a potential of the form $V(r) = kr$, with $k \sim 1$ GeV/fm ~ 0.2 GeV^2. Gluons may also be incorporated into strings as kinks (transverse excitations). The strings break via the production of $q\overline{q}$ pairs through quantum mechanical tunelling with probability:

$$P\left(m_{\perp q}^2\right) \propto \exp\left(\frac{-\pi m_{\perp q}^2}{k}\right), \quad \text{with } m_{\perp q}^2 = m_q^2 + p_{\perp q}^2, \tag{2.48}$$

where the subscript q refers to a specific quark flavour, m_q is the produced quark mass and $p_\perp$ is its transverse momentum. This yields the relative production probabilities of $u\overline{u} : d\overline{d} : s\overline{s} : c\overline{c} \approx 1 : 1 : 0.3 : 10^{-11}$. Thus, heavy flavour production in hadronization is strongly suppressed. Denoting the initial string ends by $q_0\overline{q}_0$, when a $q_1\overline{q}_1$ is produced, the $q_0\overline{q}_1$ and $q_1\overline{q}_0$ systems are formed, which either become hadrons or strings that fragment further [24, 59, 60]. This iterative process continues until all of the initial string energy has been converted into hadrons and is governed by the Lund symmetric fragmentation function [1, 24, 59, 61]:

$$f(z) \propto \frac{1}{z}(1-z)^a \exp\left(-\frac{b\left(m_h^2 + p_{\perp h}^2\right)}{z}\right), \tag{2.49}$$

where a and b are experimentally constrained parameters [1, 61, 62], z is the fraction of the string momentum carried by the hadron, m_h and $p_{\perp h}$ are the mass and transverse momentum of the hadron, respectively [24, 59]. Baryons are produced by allowing string breaking through diquark-antidiquark pair creation. Other models for baryon production have also been developed [1, 24, 58]. Besides the parameters introduced above, there are many others which control the hadronization process and are tuned to describe experimental data. Examples of such parameters are the s quark and diquark suppression factors, namely the production probabilities of the former relative to the one of u or d quarks [1, 24, 62].

Another hadronization model is the so-called cluster model, which is based on the assumption that during the showering process, partons are preconfined to colour singlet configurations called clusters. When the infrared shower cutoff is reached, the gluons undergo $g \to q\overline{q}$ splittings and clusters containing exclusively $q\overline{q}$ pairs are formed. If the clusters have masses below a cutoff value of around 3-4 GeV, they will decay directly into one or two hadrons, with the most prevalent case being the latter. Otherwise, they decay into two other clusters. The fundamental parameters of this model are the infrared shower cutoff, the QCD scale (Λ_{QCD}), the cluster mass cutoff and the single-hadron cluster decay probability [24, 63].

2.8 Monte Carlo event generators

Owing to the complexity of particle production in high energy hadronic collisions, various Monte Carlo event generators have been developed in order to obtain predictions. In the following, the QCD based collider physics generator PYTHIA [1] and three Gribov-Regge Theory based generators developed for the study of high energy cosmic ray collisions, namely EPOS [2], QGSJET [3] and SIBYLL [4], included in the CRMC (Cosmic Ray Monte Carlo) package [64], are described, along with recent tuning procedures involving LHC data.

2.8.1 PYTHIA

PYTHIA is a complex hadronic collisions generator and is widely used in collider physics. It can also generate lepton-lepton and nucleus-nucleus collisions. In the case of hadron-hadron collisions, the generator covers a wide range of event types, e.g. elastic and diffractive scatterings, soft and hard QCD events, heavy flavour production, weak boson production etc. [1, 16, 58] The diffractive events include single and double diffraction by default and central diffraction is available as an option [62]. The hard partonic processes are treated using leading order (LO) QCD matrix elements (ME) with LO or, optionally, higher order (NLO, NNLO) PDF sets [16, 58, 62, 65, 66]. The parton showering is computed in the leading log (LL) approximation and various techniques of matching and merging the showers with the hard parton scatterings are implemented [16, 58, 65]. PYTHIA also treats MPI (both soft and hard) and beam remnants [1, 16, 58]. Several colour reconnection (CR) models based on string length minimization are implemented. The so-called QCD-based CR model treats colour reconnections beyond the leading colour (LC) approximation and allows for baryon production via the formation of Y-shaped string junctions [58, 67, 68]. The Lund string fragmentation model is used for the hadronization stage [1, 58].

Two recent versions of PYTHIA are 8.186 [69] and 8.219 [58]. Tunes 2C and 2M are obtained using minimum bias (MB) and underlying event (UE) observables measured at the CDF and D0 experiments from the Tevatron [70]. Minimum bias events are defined as events selected with a relaxed triggering scheme [50]. The parameters constrained using the aforementioned measurements are the values of the strong coupling constant for hard partonic processes and showers, and several parameters related to MPI and colour reconnections [70]. The PDF sets used are CTEQ6L1 and MRST LO** for 2C and 2M, respectively [62, 70]. Tune 4C was the default tune starting with version 8.150 and is developed from 2C by lowering the diffractive cross-section and constraining the MPI and colour reconnection parameters in order for the generator predictions to agree with MB and UE measurements from ALICE and ATLAS like charged particle multiplicities, rapidity distributions, transverse momentum distributions etc., at collision energies ranging from $\sqrt{s} = 0.9$ to 7 TeV [16, 62, 70]. The Monash 2013 tune (default in version 8.219) uses the NNPDF2.3 QCD+QED LO PDF set [58, 61, 62] and it involved a much larger set of parameters and a wider range of measurements, compared to the previous tunes, as detailed in [61]. The hadronization parameters related to flavour selection have been constrained using hadron production rates in e^+e^- collisions obtained from a combination of values published in the PDG (Particle Data Group) [24], measurements from the LEP experiments and to a lesser extent, from the SLD experiment. These production rates include the ones for ϕ mesons, strange baryons and also heavy flavour hadrons. The MPI parameters are constrained using MB and UE measurements from the ATLAS, CMS and TOTEM experiments. The effects of the tune are, among others, an increase in strange hadron production, a decrease in vector meson production and an increase in charged hadron production in the forward region in MB events, each of $\sim 10\%$ relative to tune 4C. The increase in strange hadron production leads to a very good description of the rapidity densities of K^0_S measured at CMS. The description of strange baryon production is also improved, but not significantly, as it is still underestimated by as much as $\sim 40\%$ [61].

2.8.2 EPOS

EPOS treats proton-proton, proton-nucleus and nucleus-nucleus collisions using an effective field theory which combines elements of QCD and the parton model with the

Gribov-Regge Theory, suggestively called the Parton-Based Gribov-Regge Theory [2, 71]. Three types of processes contribute to the inelastic cross-section, defined according to the squared momentum transfers involved, namely soft, semi-hard, and hard Pomeron exchanges [2, 71, 72]. The soft contribution is represented by partonic scatterings in the non-perturbative region of QCD, i.e. $Q^2 < Q_0^2$, with $Q_0^2 \sim 1$ GeV^2 [71]. The hard contribution is represented by a parton ladder, namely a hard partonic scattering and its associated parton showering, both at scales of $Q^2 > Q_0^2$ [2, 71–74]. This is mostly the case for scatterings between valence quarks, as they have large x on average. Scatterings in which at least one of the partons have small x, which is usually the case for sea quarks and gluons, are called semi-hard and are represented by parton ladders connected to soft Pomerons at the small x parton ends [71].

Pomerons exchanged during inelastic hadronic collisions are referred to as cut Pomerons and contain two strings which fragment into hadrons [2, 71, 72, 74]. The cut Pomerons are connected to the beam remnants via two colour singlet legs. The legs are part of the remnants and contain the conjugates of the string ends. Another source of hadron production is the decay of the beam remnants [72]. Multiple partonic scatterings can take place during a hadronic collision and the energy scales of each of the scatterings are taken into account in cross-section calculations, leading to a consistent treatment of particle production and interaction cross-sections, with energy conservation considered in both cases, in contrast with other models [2, 16, 71, 72, 74]. In the case of very high energy hadronic collisions, many partonic scatterings take place in parallel and the individual parton showers may interact, a process described via Pomeron-Pomeron interactions [3, 16, 75–78]. In EPOS, lowest order Pomeron-Pomeron interactions are implemented [71].

The hadronization is treated collectively in high string density regions, called "core" regions, in which strings overlap and via normal string fragmentation in regions with lower string densities, called "corona". This approach is found only in EPOS, as no other hadronic collisions generator implements "core" hadronization [2]. The overlapping strings form clusters which undergo outward longitudinal and transverse collective flow if the mass of the core and the individual masses of the clusters, respectively, exceed 3 GeV/c^2. When the energy density of the clusters reaches the freeze out density, a statistical hadronization procedure commences [2, 79]. An important aspect of the statistical hadronization is that the suppression of strangeness production is much lower than in normal string fragmentation [2].

The name of the EPOS generator comes from **E**nergy conserving quantum mechanical approach, based on **P**artons, parton ladders, strings, **Off**-shell remnants, and **S**plitting of parton ladders [73, 74].

EPOS LHC, as the name suggests, is a version tuned to measurements from LHC experiments. The measurements mentioned in the following refer to *pp* collisions at $\sqrt{s} = 7$ TeV unless otherwise stated. The parameters of EPOS LHC are constrained by the cross-section measurements from TOTEM, which, compared to the previous version, EPOS 1.99, significantly improves the description of the charged particle pseudorapidity distribution measured at the ALICE experiment. The collective flow has been reparameterized in order to increase the probability of high multiplicity events in *pp* collisions. This leads to a better description of the charged multiplicity distribution measured at the ATLAS experiment. The string fragmentation parameters are constrained to measurements from e^+e^- collisions, leading to a reasonably good description of the kaon-pion and proton-pion ratios measured in bins of charged particle multiplicity at the CMS experiment. The statistical hadronization in the "core" region allows for a good description of the strange baryon yields measured at CMS. The parameters controlling radial flow are tuned using charged particle transverse momentum distributions from pp collisions at $\sqrt{s} = 0.9$ and 7 TeV measured at ATLAS. The transverse momentum distributions of $p/\overline{p}$, $K^{\pm}$, $\pi^{\pm}$, Λ^0 and $\Xi^{\pm}$ measured at CMS are well described by EPOS LHC [2, 16].

2.8.3 QGSJET

Another model for hadronic (nuclear) collisions based on the Gribov-Regge Theory is QGSJET. Similarly to the case of EPOS, the inelastic interactions proceed via "soft" and "semi-hard" cut Pomerons containing two strings. The "soft" Pomeron describes scatterings with squared momentum transfers below the perturbative cut-off, Q_0^2. The "semi-hard" Pomeron consists of a parton ladder with "soft" Pomeron ends and represents a hard partonic scattering with its associated showering taking place partially in the perturbative QCD region [3, 16, 75–78]. The QGSJET model was initially inspired from the Quark-Gluon String Model (QGSM) in which Pomerons are equivalent to non-perturbative double gluon exchanges [16, 75, 80]. In QGSM, the beam nucleons are treated as q-qq systems and the gluons are exchanged between $q_{1(2)}$ and $qq_{2(1)}$, where the 1 and 2 subscripts indicate from which of the nucleons are the q (qq) coming from, leading to the formation of two strings which fragment into the final state hadrons [16, 80]. In QGSJET, only "soft" Pomerons interact, including those contained in "semi-hard" ones. This is motivated by the assumption that the interactions between showers take place predominantly in the non-perturbative QCD region [76–78]. Starting with version QGSJET-II, the generator takes into account enhanced Pomeron-Pomeron diagrams, with "net" diagrams in QGSJET-II-03 and including "loop" diagrams in QGSJET-II-04 [3, 16, 75–78].

The collisions of cosmic rays with the nuclei from the atmosphere initiate so-called extensive air showers (EAS) and the number of muons produced in such events and detected at ground level is used to infer the nature of the cosmic rays. This number is sensitive to the charged hadron multiplicity, nucleon production and to a lesser extent, strange hadron production. In QGSJET-II-04, the value of Q_0^2 has been increased to 3.0 GeV^2 from 2.5 GeV^2 in QGSJET-II-03 [3, 16, 77, 81], leading to a significantly better description of the charged hadron pseudorapidity distributions from pp collisions at $\sqrt{s} = 7$ TeV measured at the CMS experiment. The hadronization parameters have been tuned to the transverse momentum distribution of $\overline{p}$ from pp collisions at $\sqrt{s} = 0.9$ TeV measured at the ALICE experiment, the description of which required concurrent decrease of nucleon production and hardening of the nucleon p_T spectrum. The K_S^0 and Λ^0 rapidity distributions from pp collisions at $\sqrt{s} = 0.9$ and 7 TeV measured at the CMS experiment are largely underestimated by QGSJET-II-03. Thus, in order to obtain a good description of the aforementioned distributions, strange hadron production has been increased in version QGSJET-II-04 [16, 81].

2.8.4 SIBYLL

The SIBYLL generator uses the Gribov-Regge Theory for "soft" scatterings and the minijet model for "hard" scatterings. Similarly to the other Gribov-Regge based models presented in this section, the "soft" and "hard" scatterings are separated through a cutoff value of the transverse momentum of the partons [16, 82]. Starting with version 2.1 this cutoff value is parameterized as a function of the collision energy [82, 83]:

$$\begin{gathered} p_{\perp}^{min}(s) = p_{\perp}^{0} + \Lambda \exp\left[c\sqrt{\ln\left(s/\mathrm{GeV}^2\right)}\right], \\ \text{with } p_{\perp}^{0} = 1\mathrm{GeV}\ , \Lambda = 0.065\ \mathrm{GeV} \text{ and } c = 0.9, \end{gathered} \tag{2.50}$$

yielding $p_{\perp}^{min}$ (7 TeV) $\approx$ 3.87 GeV, for example. In contrast, this cut off value was a constant $p_{\perp}^{min} = \sqrt{5}$ GeV in SIBYLL 1.7. The dual parton model (DPM) implementation for soft interactions is carried over from version 1.7, in which two strings are formed between the valence quarks of the beam hadrons, namely between a quark from one hadron and a diquark (antiquark) from the other, in a very similar manner to the previously described QGSM. The Gribov-Regge parameterization of the soft scattering cross-section considers both Reggeon and Pomeron exchanges [4, 16, 82, 84, 85]. For the hard scattering cross-sections, LO QCD calculations are employed. The partons participating in a hard scattering form a so-called minijet pair. The flavours of the initial partons are not preserved after the hard scattering, all minijet pairs being regarded as consisting of two gluons. A double string is formed between the scattered gluons [82, 84, 85]. Through the implementation of the Gribov-Regge parameterization in version 2.1, additional soft scatterings involving sea partons are allowed with string formation analogous to the minijet case [82, 84]. The string fragmentation is treated using the Lund model [16, 82]. SIBYLL uses an effective PDF which in version 1.7 had an approximate slope of $\sim x^{-1}$ in the low x region, while in version 2.1 another parameterization is used, with a slope of $\sim x^{-1.3}$, in accordance with PDFs measured at HERA [82, 83].

In SIBYLL 2.3, beam remnants with masses exceeding the masses of the beam hadrons by 0.2 GeV/c^2 are fragmented [4]. The suppression of π^0 production relative to ρ^0 in the forward region observed in fixed-target π^+p collisions at 250 GeV/c at the NA22 experiment is not predicted by version 2.1, in which a constant scalar to vector meson suppression factor in string fragmentation of 0.3 is implemented. In version 2.3, the vector meson production is enchanced in the forward region via the excited remnant model and the generator is tuned to reproduce the aforementioned measurements [4, 83, 84, 86]. SIBYLL 2.3 is also tuned using pion and kaon yields from fixed-target pp collisions at 158 GeV/c measured at the NA49 experiment [4]. The inelastic pp cross-section at $\sqrt{s} = 7$ TeV measured at the TOTEM experiment is used for the tuning of version 2.3, as the prediction of version 2.1 overestimated this measurement [16, 87]. Baryon production is governed by the diquark suppression factor, which is equal to 0.4 in version 2.1. There are two distinct constant values of this parameter in version 2.3, one used in the case of minijet strings and another in all the other cases [16, 87]. This leads to a good description of the average $\overline{p}$ multiplicity measured at CMS at different collision energies and an improvement of the predictions relative to version 2.1 even for measurements from fixed-target experiments at $\sqrt{s}$ of the order of tens of GeV. The p_T^{min} parameterization was modified in version 2.3, leading to a highly improved description of the p_T spectra of charged hadron measured at CMS at $\sqrt{s} = 0.9$, 2.36 and 7 TeV [16, 87]. In SIBYLL 2.1, only light flavour (u, d, s) hadrons are produced [87]. A model for charm hadron production is implemented in SIBYLL 2.3, with its parameters tuned to D meson cross-sections measured at the ALICE and LHCb experiments in pp collisions at up to $\sqrt{s} = 7$ TeV [87].

The LHCb experiment at the LHC

3.1 The Large Hadron Collider at CERN

The Large Hadron Collider (LHC) is the most powerful particle accelerator to date and it is located at CERN (fr: Conseil Européen pour la Recherche Nucléaire, en: European Organization for Nuclear Research), spanning across the French-Swiss border near Geneva, Switzerland. The accelerator ring has a circumference of approximately 27 km and it is located at around 100 m underground. The LHC is host to four major experiments, namely ATLAS, ALICE, CMS and LHCb, but also to the TOTEM and LHCf experiments [88, 89]. A schematic view of the CERN accelerator complex showing the LHC and the experiments thereat is shown in Figure 3.1.

The protons are accelerated in several stages at LHC, as follows: protons are obtained by stripping hydrogen atoms using an electric field, then the linear accelerator Linac 2 accelerates the protons up to 50 MeV, the protons are injected into the Proton Synchrotron Booster (PSB) which accelerates them up to 1.4 GeV, The Proton Synchrotron (PS) accelerates the protons up to 25 GeV, The Super Proton Synchrotron (SPS) accelerates the protons up to 450 GeV after which they are injected into the LHC which accelerates the protons to a maximum energy of 6.5 TeV per beam [88].

3.2 Introduction to beam dynamics at the LHC

A simplistic description of the acceleration of the protons inside the LHC accelerator ring is given in the following. The coordinate system used for circular accelerators is shown in Figure 3.2. The coordinates transverse to the beam are x (horizontal) and y (vertical), and the longitudinal coordinates are s and θ, the longitudinal phase [90].

The circular motion of the protons in the accelerator ring is maintained by a series of dipole magnets which act in the horizontal (xs) plane. For the focusing of the beam a series of quadrupole magnets which focus in the vertical (horizontal) plane called focusing quadrupoles (QF) and defocus in the horizontal (vertical) plane called defocusing quadrupoles (QD). A series QF-QD-QF is called a FODO cell [90].

The focusing force varies along the accelerator ring and the equation of motion around the ring, called the Hills equation, is:

$$\frac{d^2x}{ds^2} + K(s)x = 0. \tag{3.1}$$

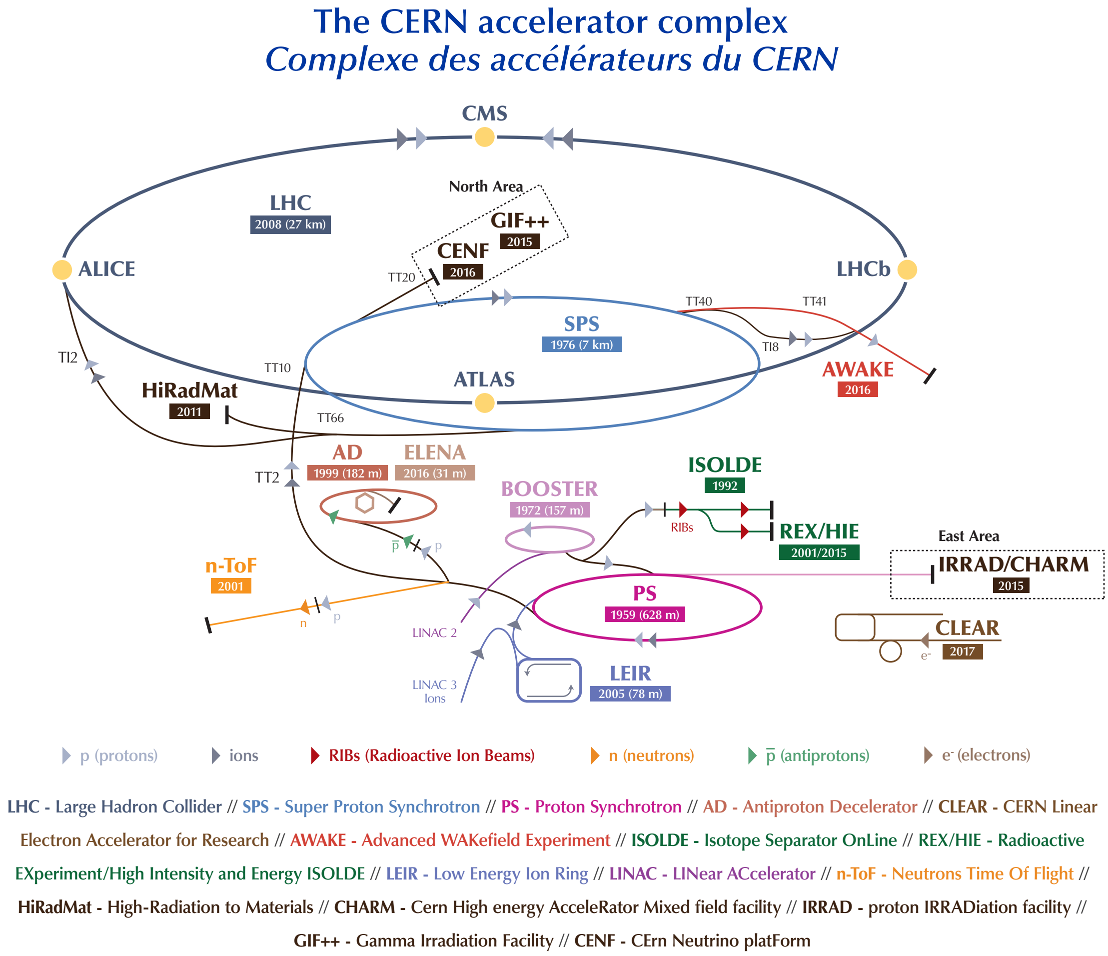

Figure 3.1: Schematic view of the CERN accelerator complex with the positions of the experiments. The image is the property of CERN and it is used in this work for a better understanding of the text. © CERN.

The solution to the Hills equation is of the form:

$$x = \sqrt{\varepsilon\beta(s)}\cos\left(\Psi(s)+\phi\right),$$
$$\text{and } x' = \frac{dx}{ds} = -\sqrt{\frac{\varepsilon}{\beta(s)}}\sin\left(\Psi(s)+\phi\right), \text{ as } \frac{d\Psi(s)}{ds} = \frac{1}{\beta(s)}, \tag{3.2}$$

where x is the displacement from the central orbit, $K(s)$ is the quadrupole field gradient, ε is the transverse emittance, a constant dependant on the initial conditions, $\beta(s)$ is the amplitude modulation and $\Psi(s)$ is the phase advance, both dependant on the focusing force [90].

The transverse emittance is defined as the area of an ellipse in the transverse phase space which contains a fraction, expressed as a percentage, of the total number of particles. For example, an emittance of 95% is an area in which 95% of the particles are found. The projection of the emittance on the x axis, $2\sqrt{\varepsilon\beta}$, is the transverse size of the beam, as shown in Figure 3.2. As the amplitude, $\beta(s)$, varies along the accelerator ring, so will the transverse beam size [90].

At LHC the central orbit passes on average through the center of the quadrupoles and the nominal momentum is determined by the integrated field of the dipole magnets:

$$p = e \oint \rho(s)B(s)ds = \frac{e}{2\pi}(BL)_d, \tag{3.3}$$

where e is the elementary electric charge, $\rho(s)$ is the radius of the orbit, $B(s)$ is the magnetic field and $(BL)_d$ is the integrated field of all the dipole magnets around the circumference of the accelerator ring [91].

The forces exerted by the dipole magnets on particles with different momenta have different magnitudes and so, the circular motion of the particles will have different radii of curvature. This leads to the particles passing through the quadrupole magnets at different positions on the x axis, the effect being as if passing through a dipole magnet. Thus, two particles of different momenta will have orbits of different lengths [90]. A schematic of the passage of two particles with different momenta through a dipole field is shown in Figure 3.2.

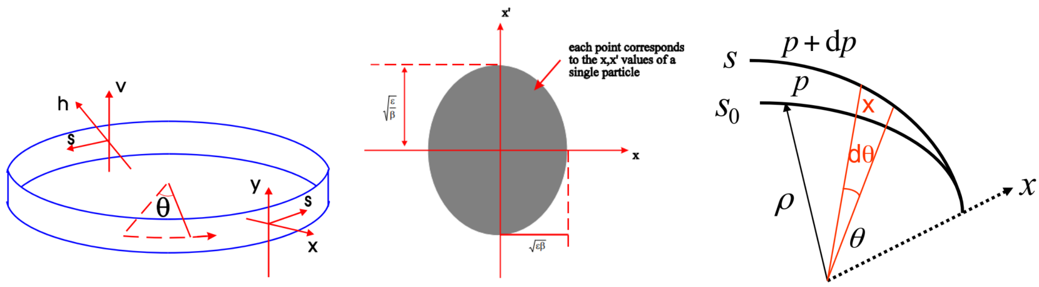

Figure 3.2: Circular accelerator coordinate system (left), transverse phase space plot for many particles (center) [90] and schematic of motion of different momenta particles through a dipole field (right) [93].

The change in orbit length is:

$$dr = \frac{dp}{p} \oint \frac{D(s)}{\rho(s)}ds, \text{ with } D(s) = \frac{dx}{dp}p \tag{3.4}$$

where $D(s)$ is the dispersion function [90, 92, 93].

The momentum compaction factor is defined as the ratio of the fractional change in orbit length and fractional change in momentum:

$$\alpha_p = \frac{dr/r}{dp/p} = \frac{1}{r} \oint \frac{D(s)}{\rho(s)}ds. \tag{3.5}$$

It follows that the fractional change of the revolution frequency as a function of that of momentum is:

$$\frac{df}{f} = \left(\frac{1}{\gamma^2} - \alpha_p\right)\frac{dp}{p} = \eta\frac{dp}{p}, \tag{3.6}$$

where η is the slip factor [90, 92, 93]. For LHC the momentum compaction factor is $\alpha_p \approx 3.2 \times 10^{-4}$ and $\eta \approx -\alpha$ as $\gamma \approx 10^3 - 10^4$ [91].

There is a value of the energy, named transition energy, for which:

$$\eta = 0 \rightarrow \frac{1}{\gamma_{tr}^2} = \alpha_p \rightarrow \gamma_{tr} = \sqrt{\frac{1}{\alpha_p}}. \tag{3.7}$$

For particles below the transition energy ($\eta > 0$) the net effect of an increase of momentum will be of an increase of the revolution frequency and vice versa for particles above transition ($\eta < 0$, the case for LHC). This is explained by the fact that at $\beta \approx 1$, the effect of massification is comparatively larger than the increase in velocity, leading to larger orbit lengths [90, 92, 93].

In a synchrotron the acceleration is done via the use of an alternating electric field. The frequency of the alternating electric field and the magnetic fields are modulated taking into account the change in revolution frequency [90, 92, 93]. At the LHC the energy of the particles is high enough for the RF frequency to be kept constant (details in [92, 93]).

For the acceleration of particles, the LHC uses the so-called RF (RadioFrequency) system, composed of resonant cavities on which alternating electric fields of a maximum of 5 MV/m ($V = 2$ MV) and a frequency of $f_{RF} = 400$ MHz, from which the name comes from. Each of the two beams of the LHC is equiped with 8 cavities grouped in two criomodules installed on linear segments of the accelerator ring [88].

In order for the protons to be accelerated, the electric field must be positive at the moment of passage through the cavity. For this to happen, the frequency of the alternating electric field must be an integer multiple of the revolution frequency, $f = \beta c/L$, of the protons inside the ring. This integer multiple is known as the the harmonic factor, h. As the protons accelerated at LHC have $\beta \approx 1$ and the circumference of the ring is $L = 26\,659$ m [88, 90]:

$$h = \frac{f_{RF}}{f} = \frac{f_{RF} \cdot L}{c} = 35\,640. \tag{3.8}$$

As mentioned earlier, the momentum is determined by the size of the ring and the magnetic fields:

$$p = eB\rho \rightarrow \frac{dp}{dt} = e\rho\dot{B} \rightarrow dp = e\rho\dot{B}dt. \tag{3.9}$$

For one turn around the accelerator ring:

$$\Delta p = e\rho\dot{B}T = \frac{e\rho\dot{B}L}{v} \text{ and } \Delta E = v\Delta p = e\rho\dot{B}L. \tag{3.10}$$

where T is the period of revolution. This gain in energy is equal to the work done by the RF electric field on the particle, so:

$$\Delta E = \Delta W = e\rho\dot{B}L = e\hat{V}\sin\phi_s, \tag{3.11}$$

where $\hat{V}$ is the RF voltage and ϕ_s is the synchronous phase. Clearly, the rate of acceleration is controlled by the rate of change of the dipole magnets [92–95]. Actually, there are also sources of energy loss like synchrotron radiation, so the change in energy per turn can be written as:

$$\Delta E = e\hat{V}\sin\phi_s - U(E), \tag{3.12}$$

where U(E) is the energy loss [95].

A particle is synchronised with the RF system if the field is always null when it arrives at the cavities or in other words, $\sin\phi_s = 0 \leftrightarrow h = 1$. The unsynchronised particles will oscillate longitudinally around the synchronised particles. These oscillations are called synchrotron oscillations and a schematic of them is shown in Figure 3.3 [90].

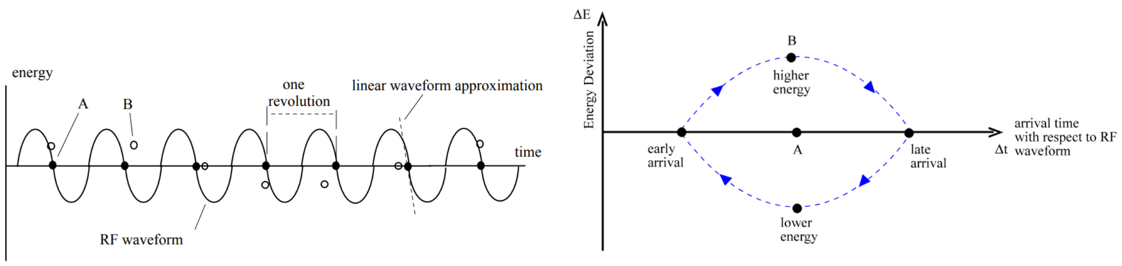

Figure 3.3: Schematic of synchrotron oscillations (left) and longitudinal phase space plot for unsynchronised particles (right) [90].

The synchronised particles and those that oscillate around them form a so-called bunch. For a set of electric field and harmonic factor values there is a cutoff value of the energy of particles beyond which their oscillation around the synchronised particle can no longer be maintained and they escape the bunch, being lost in the accelerator ring. The path of the particle with the cutoff energy in the longitudinal phase space forms a so-called bucket or separatrix. The bunch is contained in this bucket and there are h buckets along the accelerator ring [90]. The number of buckets occupied with bunches at LHC is 2 808 [88]. Schematic representations in longitudinal phase space of bunches and separatrixes are given in Figure 3.4.

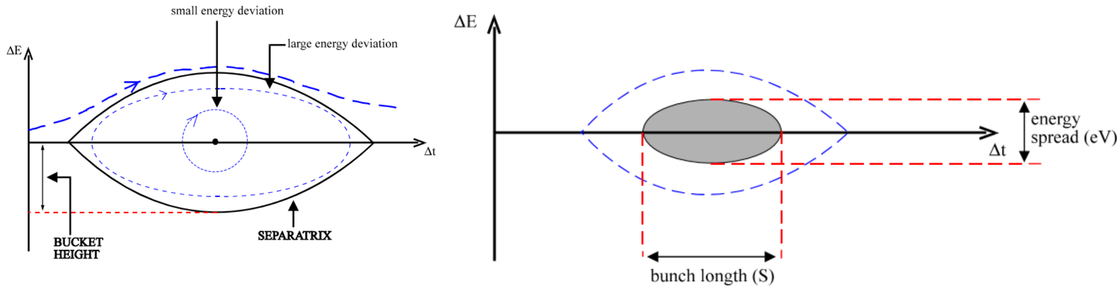

Figure 3.4: Schematics of a separatrix (left) and a bunch (right) in longitudinal phase space [90].

As can be seen, the net effect of the RF system is of forming bunches and, as discussed, the rate of acceleration of protons is proportional to the rate of increase of the dipole magnetic fields [90].

Another important quantity for accelerators is the beam current, which at LHC is determined via the use of two DC current transformers (DCCT) and two fast beam current transformers (FBCT) for each beam. The maximum beam current at LHC is:

$$I_{beam} = 0.58 \text{ A}, \text{ so } N_p = \frac{I_{beam}}{feN_b} = \frac{I_{beam}L}{eN_bc} = 1.15 \cdot 10^{-11}, \tag{3.13}$$

where N_p is the number of protons in the beam and $N_b = 2\,808$ is the number of bunches per beam [89].

The amplitude function at the interaction point, β^*, is defined as the distance from the interaction point at which the beam transverse size doubles and at LHC, $\beta^* = 0.55$ m [89].

The normalised emittance is defined as:

$$\varepsilon_n = \beta\gamma\varepsilon, \tag{3.14}$$

and it is invariant under longitudinal boosts. At LHC, $\varepsilon_n = 3.75$ μm [89, 96].

3.3 Luminosity

The interaction rate at a fixed target experiment is:

$$\frac{dN}{dt} = \Phi n_T \Delta x \sigma = \mathcal{L}\sigma \text{ and } \Phi = \phi A_b = n_b v_b A_b, \tag{3.15}$$

where Φ [s^{-1}] is the projectile flux at the surface of the target, ϕ [cm^{-2} s^{-1}] the projectile flux density, n_T [cm^{-3}] and n_b [cm^{-3}] are the densities of scattering centers (e.g. nucleons of a material) and beam particles, respectively, v_b [m s^{-1}] the velocity of the beam particles, A_b [m^2] the transverse area of the beam, Δx [cm] is the target depth, σ [cm^2] is the cross-section for the process of interest and $\mathcal{L}$ [cm^{-2} s^{-1}] is the luminosity. Thus, the luminosity can be defined as a surface density of collisions per unit of time necessary to obtain an interaction rate dN/dt for the process with cross-section σ [97, 98].

In the case of a collider experiment, where two oppositely moving beams collide, the luminosity is given by:

$$\begin{gathered}\mathcal{L} = N_1 N_2 f N_b K \int \rho_1(\vec{r},t)\rho_2(\vec{r},t)\ d^3\vec{r}\ dt, \\ \text{with } \vec{r} = (x,y,s) \text{ and } \int \rho_i(\vec{r},t)\ d^3\vec{r}\ dt = 1,\end{gathered} \tag{3.16}$$

where N_1 and N_2 are the number of particles per bunch for each beam, N_b is the number of bunches, f is the revolution frequency and $\rho_i(\vec{r},t)$ the bunch density distributions [97, 99, 100]. In order to account for the reciprocal movement between the beams, the Møller kinematical factor, K, is introduced:

$$K = \sqrt{(\vec{v_1} - \vec{v_2})^2 - \frac{(\vec{v_1} \times \vec{v_2})^2}{c^2}}, \tag{3.17}$$

where $\vec{v_1}$ and $\vec{v_2}$ and the velocities of the particles from their respective beams [97, 100, 101]. In the case of LHC, where $|\vec{v}_i| \approx c$, and head-on collisions, $\vec{v}_1 = -\vec{v}_2$, this factor reduces to $K \approx 2c$ [97, 99, 100].

Substituting t with the distance to the collision point, $s_0 = ct$ [97, 102]:

$$\mathcal{L} = 2N_1 N_2 f N_b \int_{-\infty}^{+\infty} \rho_1\left(x,y,s,-s_0\right)\rho_2\left(x,y,s,s_0\right) dxdydsds_0. \tag{3.18}$$

Assuming that the bunch density distributions are uncorrelated in all dimensions, the bunch profiles have a Gaussian PDF and the bunch longitudinal dimensions are equal, $\sigma_{1s} = \sigma_{2s}$, the following expression is obtained:

$$\mathcal{L} = \frac{N_1 N_2 f N_b}{2\pi\sqrt{\sigma_{1x}^2 + \sigma_{2x}^2}\sqrt{\sigma_{1y}^2 + \sigma_{2y}^2}} \text{ or } \mathcal{L} = \frac{N_1 N_2 f N_b}{2\pi\sigma_x\sigma_y} = \gamma\frac{N_1 N_2 f N_b}{4\pi\beta^*\varepsilon_n}, \tag{3.19}$$

where $\sigma_{x,y}$ are the effective transverse bunch sizes, β^* and ε_n are the amplitude function at the interaction point and the normalised transverse emittance introduced in the previous section [97, 100, 103].

The luminosity expression from Equation (3.16) can be rewritten as:

$$\mathcal{L}_0 = C \cdot \int \rho_1(u)\rho_2(u)du, \tag{3.20}$$

where C is a constant and again, assuming no correlation between the different dimensions [97, 102, 104].

If the beams are not collided head-on, but with an offset, δu, in the transverse plane:

$$\mathcal{L}(\delta u) = C \cdot \int \rho_1(u)\rho_2(u - \delta u)du \rightarrow \frac{\mathcal{L}(\delta u)}{\mathcal{L}_0} = \frac{\int \rho_1(u)\rho_2(u - \delta u)du}{\int \rho_1(u)\rho_2(u)du},$$
$$\text{which reduces to } \frac{\mathcal{L}(\delta u)}{\mathcal{L}_0} = e^{-\frac{\delta u^2}{2\sigma_u^2}} \rightarrow \mathcal{L}(\delta u) = \mathcal{L}_0 e^{-\frac{\delta u^2}{2\sigma_u^2}} = \mathcal{L}_0 \cdot T, \tag{3.21}$$

where $u = x, y$ is a coordinate in transverse space [97, 102, 104–107].

Experimentally, the luminosity is determined from:

$$\mu_{\text{vis}} = \frac{\mathcal{L}\sigma_{\text{vis}}}{fN_b}, \tag{3.22}$$

where the $\mu_{\text{vis}} = \varepsilon\mu_{\text{inel}}$ is the rate of interaction per bunch crossing visible to the detector or in other words, the true rate multiplied by the detector efficiency, and $\sigma_{\text{vis}} = \varepsilon\sigma_{\text{inel}}$ is the visible cross-section for the measured process [104, 108].

The two most important methods for absolute luminosity determination used at LHC and succesfully applied at the LHCb experiment are the "van der Meer scan" and Beam-Gas Imaging methods [99, 100, 102, 104–110].

Through the van der Meer (VDM) scan method, the effective bunch transverse dimensions are determined by measuring the visible interaction rates at different offsets in x and y coordinates:

$$\frac{\mu_{\text{vis}}(\delta u)}{\mu_{\text{vis}}^{\text{MAX}}} = e^{-\frac{\delta u^2}{2\sigma_u^2}} \Rightarrow \frac{\int \mu_{\text{vis}}(\delta u)d\delta u}{\mu_{\text{vis}}^{\text{MAX}}} = 2\pi\sigma_x\sigma_y, \tag{3.23}$$

where $\mu_{\text{vis}}^{\text{MAX}} = \mu_{\text{vis}}(u_0)$ is the visible rate at the nominal beam positions. If δu is small enough and the entire bunch width is scanned (from $\mu_{\text{vis}}^{\text{MAX}}$ to 0), the distribution of $\mu_{\text{vis}}(\delta u)$ is measured and the effective beam dimensions precisely determined by a fit to the distribution [99, 100, 102, 104–110].

As the other terms in Equation (3.19) are known, namely f, the revolution frequency, N_b, the number of bunches, and $N_{1,2}$ the bunch populations determined, as mentioned in the previous section, from the beam currents measured by the DCCT and FBCT transformers [99, 109]. An example of the interaction rate distribution obtained with a VDM scan at LHCb is shown in Figure 3.5.

The Beam-Gas Imaging (BGI) method is based on the interactions of the beams with the residual gas in the beampipe. The interaction vertices from *be* (beam-empty) and *eb* (empty-beam) crossings are reconstructed using the tracking system and so, the transverse bunch profiles are determined along with the eventual offsets and crossing-angles [99, 100, 109, 110]. A plot of the reconstructed vertices from beam-gas interactions at LHCb is shown in Figure 3.5.

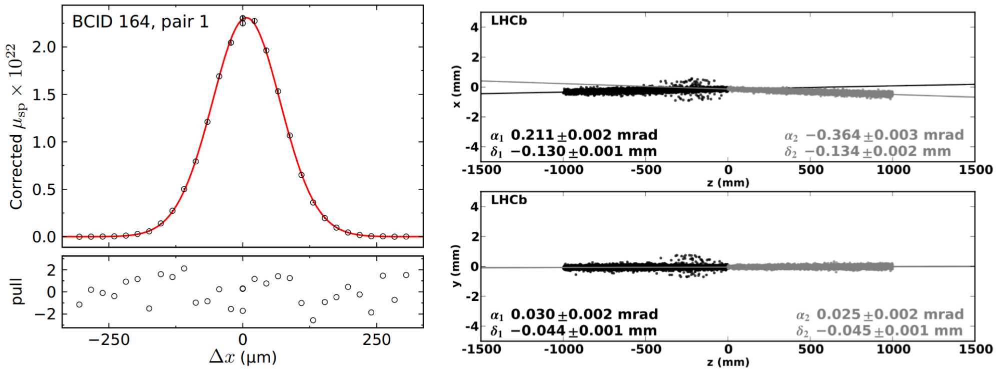

Figure 3.5: Distribution of interaction rates as a function of transverse offset from a VDM scan (left) [99] and a plot of reconstructed vertices from beam-gas interactions (right) [109] obtained at LHCb.

If one considers small beam crossing angles, ϕ, small σ_x and $\sigma_s \gg \sigma_{x,y}$, which is the case for LHC:

$$\mathcal{L} = \frac{N_1 N_2 f N_b}{2\pi\sigma_x\sigma_y} \cdot S, \text{ with } S \approx \frac{1}{\sqrt{1 + \left(\frac{\sigma_s}{\sigma_x}\frac{\phi}{2}\right)^2}}, \tag{3.24}$$

where S is the geometrical luminosity reduction factor [97, 103]. In the case of an offset and beam crossing at an angle at the same time, an additional reduction term is introduced (details in [97, 102]):

$$\mathcal{L}(\delta u) = \mathcal{L}_0 \cdot S \cdot T \cdot U. \tag{3.25}$$

From Equation (3.15) it follows that:

$$dN = \mathcal{L}(t)\sigma dt \rightarrow \int dN = \sigma \int \mathcal{L}(t)dt \rightarrow N = \mathcal{L}_{int}\sigma, \tag{3.26}$$

where N is the total number of observed events, σ the cross-section for the respective process and $\mathcal{L}_{int}$ is the time integrated luminosity [97].

3.4 Overview and motivation of LHCb

The LHCb experiment is dedicated to precision measurements of Standard Model parameters and searches for New Physics beyond the Standard Model. The latter is realised through the study of rare beauty and charm hadron decays by measuring branching fractions and CP violating phases. While this is the main scope of the experiment, it is not exclusive and the LHCb Collaboration is active and publishing measurements in many different areas like soft QCD, electroweak bosons production, exotic hadrons, and particle production in pPb collisions [8, 17].

The experiment is located at Intersection Point 8 (IP8), the location of the former DELPHI experiment at LEP. The LHC ring and the locations of the four major experiments are shown schematically in Figure 3.6. The LHCb detector assembly acts like a single arm forward spectrometer with an angular acceptance from 10 mrad to 300 and 250 mrad in the bending and non-bending planes, respectively, which corresponds to an acceptance in pseudorapidity of approximately $2 \leq \eta \leq 5$. This design is motivated by the fact that a large fraction of $b\bar{b}$ quark pairs are preferentially produced in this region, as shown in Figure 3.6, in which a two-dimensional plot of the pseudorapidities of $b\bar{b}$ quarks from a simulated sample of pp collisions at $\sqrt{s} = 14$ TeV is shown [8, 17].

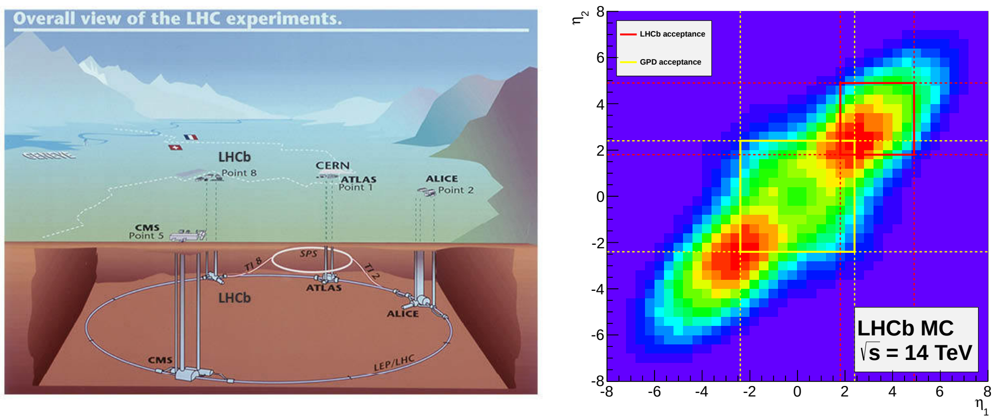

Figure 3.6: Locations of the four major experiments at the LHC (left) and the two-dimensional pseudorapidity plot of $b\bar{b}$ production phase space in simulated pp collisions at $\sqrt{s} = 14$ TeV with the LHCb acceptance highlighted using a red square. © CERN.

The nominal luminosity at the LHC is of the order of 10^{34} cm^{-2} s^{-1} [97], but the LHCb experiment runs at a luminosity of the order of 10^{32} cm^{-2} s^{-1}, as to minimize the number of pp collisions per bunch crossing and so, reduce the occupancy and radiation damage in the detector. This is achieved by the separate modulation of the beam focus at IP8. The efficiencies of the detectors depend strongly on the occupancy, so the lower luminosities allow for more precise measurements [8, 17]. Plots of integrated luminosities recorded at LHCb are shown in Figure 3.7.

The detector is composed of several specialized subsystems: a high performance tracking system with a 4 Tm integrated field warm dipole magnet, a particle identification system based on two Ring Imaging Cherenkov (RICH) detectors, electromagnetic and hadronic calorimeters, a muon detection system, and a trigger system, all of which will be described in the following, with an emphasis on the tracking system [8, 17]. A schematic of the detector assembly with all the subsystems is presented in Figure 3.8.

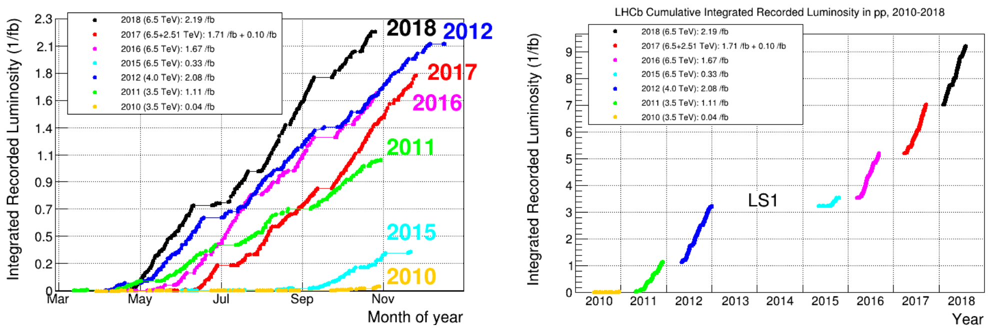

Figure 3.7: Integrated luminosities plot (left) and cumulative integrated luminosity plot (right) recorded at LHCb [111].

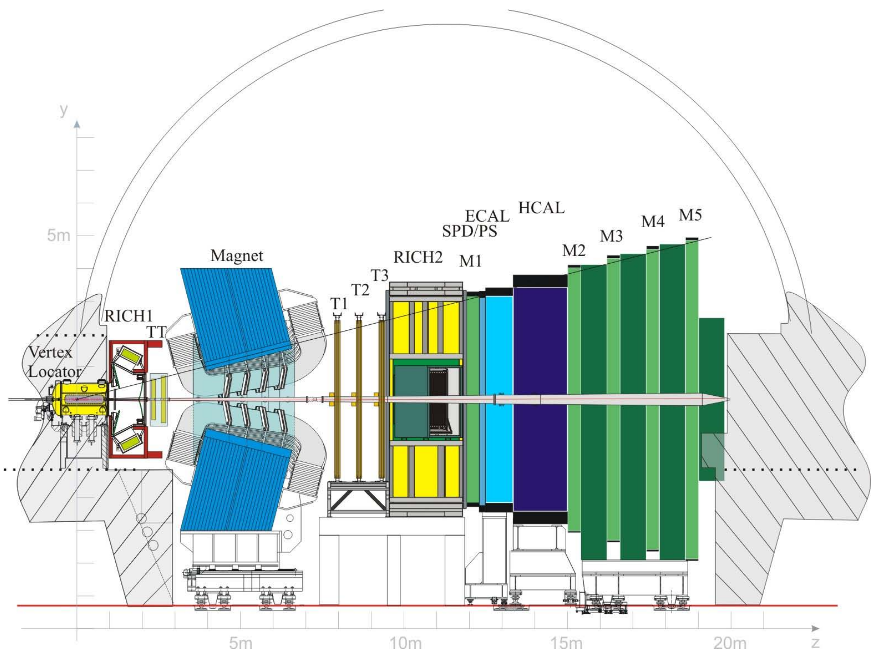

Figure 3.8: Schematic represenation of the LHCb detector assembly. © CERN.

3.5 The LHCb detector assembly and performance

3.5.1 The LHCb coordinate system

The LHCb coordinate system is a right-handed Cartesian coordinate system with the interaction point at its origin. The z axis is parallel to the beam line and points towards the detector. The x axis is in the horizontal plane and points towards the exterior of the accelerator ring, as opposed to the case of the LHC system of coordinates. The y axis points upwards and forms an angle of 3.601 mrad with the vertical direction [112]. A schematic of the LHCb coordinate system alongside the LHC and civil engineering systems is given in Figure 3.9.

The stereo angle at LHCb is defined as being positive for rotations from positive x to positive y and a schematic of this is shown in Figure 3.9 [113].

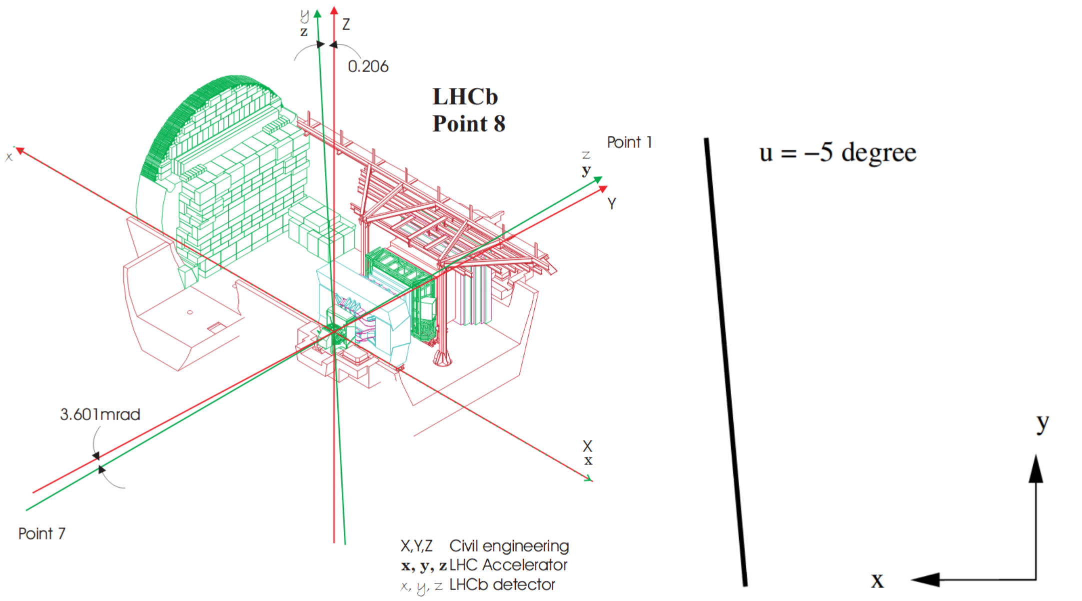

Figure 3.9: The LHCb coordinate system alongside the LHC and civil engineering systems (left) [112] and a schematic of the stereo angle convention (right) [113].

3.5.2 The beampipe

The beampipe is 19 m long and consists of the VELO window and four conical sections. The first three sections from the interaction point have a cumulated length of about 12 m, corresponding to the critical transparency zone and for this reason are made from beryllium, while the last section is made from stainless steel [8].

The ultra-high vacuum necessary for the optimal operation of the experiment is obtained by coating the beampipe and VELO RF-boxes with sputtered non-evaporable getter (NEG) and using sputter-ion pumps at both ends of the beampipe for non-getterable gases [8].

The particle flux around the beampipe is monitored with two stations, one upstream and one downstream of the interaction point, each with eight chemical-vapor deposition (CVD) diamond sensors. The two stations form the Beam Conditions Monitor (BCM), which is connected to both the control system of the LHCb experiment and to that of the LHC and will request dump of the beams in case of accidents [8].

3.5.3 The magnet

The LHCb spectrometer magnet is a warm dipole magnet with an integrated field of 4 Tm for 10 m length tracks, 11 m $\times$ 8 m $\times$ 5 m spatial dimensions and a total mass of around 1 600 tons, the magnetic field being vertically oriented for bending charged particle trajectories in the horizontal plane and thus, allowing momentum measurements [8, 17]. The design was constrained by the need of very low field inside the RICH detectors (below 2 mT) and as high as possible in the upstream region between the VELO and TT. The tracking regions are defined as upstream (VELO-TT) and downstream (T1-T3) according to the position relative to the magnet, namely between the interaction point and the magnet, and beyond the magnet. The integrated field is around 0.12 Tm in the VELO-TT region and around 3.6 Tm beyond the TT [8]. A schematic of the LHCb magnet and a plot of the magnetic field along the z axis are shown in Figure 3.10.

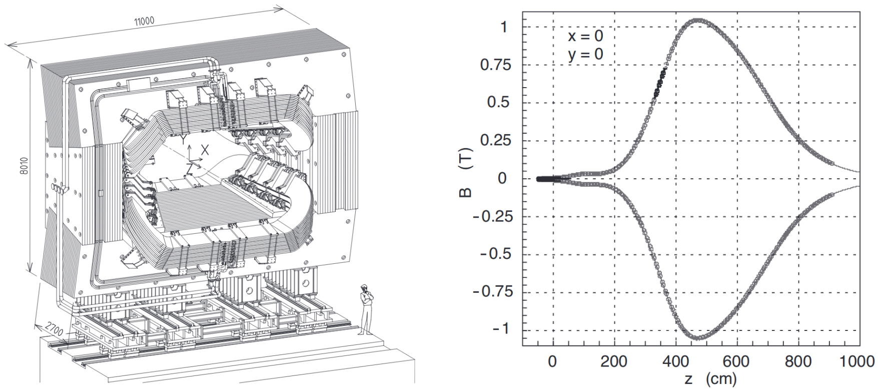

Figure 3.10: Schematic of the LHCb magnet (left) and plot of magnetic field along the z axis (right) [8].

3.5.4 Beam crossing schemes

The magnet configuration in the proximity of IP8 is as follows: two separation (recombination) dipole magnets, D1 and D2, and a low-β quadrupole triplet, Q1-Q3, with nested dipole orbit correctors, all of which are superconducting magnets, on each side of the IP8, and three warm dipole compensator magnets [114–116]. A schematic of the magnet configuration to the right of IP8 is shown in Figure 3.11.

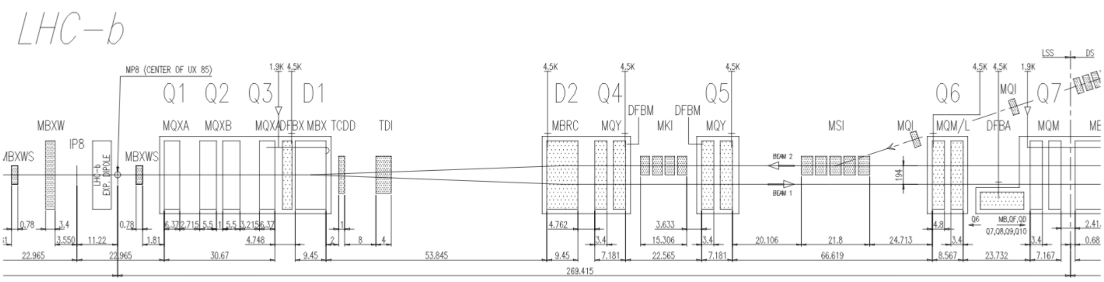

Figure 3.11: Schematic of the magnet configuration to the right of IP8 [115].

The beams are brought together in the common beampipe through horizontal trajectory kicks from the D1-D2 dipole magnets. The individual beam trajectories are bent towards the center of the LHC ring, the angle between them being negative by convention. Schematics of the beam trajectories are show in Figure 3.12. The beams need to be separated until they reach the central interaction point, otherwise a large number of parasitic interactions would occur. This is done via the use of the orbit correctors which apply a so called external crossing angle to the beams. The nominal sign of this angle is negative. A schematic of beam trajectories with a negative external crossing angle is shown in Figure 3.13. If the sign of this angle is reversed, an additional crossing point is generated [114]. The LHCb spectrometer magnet and the three compensator magnets create an orbit bump which leads to a so called internal crossing angle. The nominal negative powering of the spectrometer corresponds to a downward orientation of the magnetic field and a negative internal crossing angle. If the powering of the magnet is positive, then the internal crossing angle will also be positive and a compensation with a much larger negative external crossing angle is necessary [114]. Schematics of the orbit bump due to the spectrometer and compensator magnets, as well as a schematic of beam trajectories with negative external angles and different powerings of the spectrometer magnet are shown in Figure 3.13.

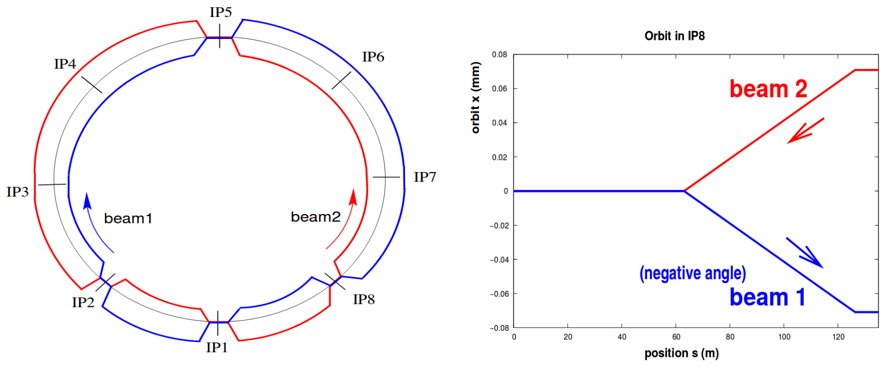

Figure 3.12: Schematic of the beam trajectories (left) and crossing angle convention (right) [114].

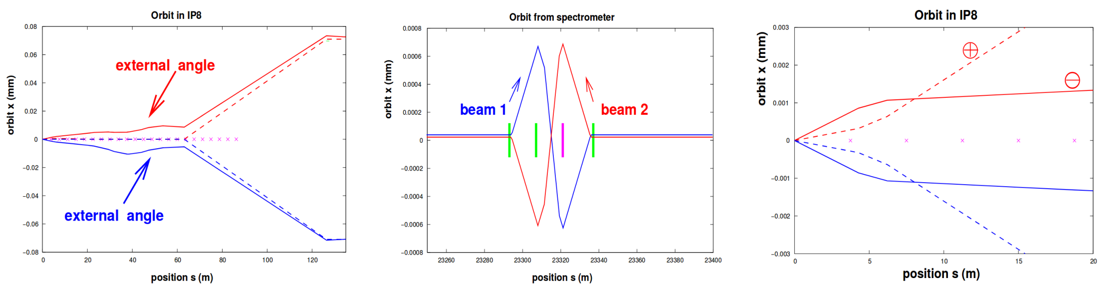

Figure 3.13: Schematic of the beam trajectories with external crossing angle (left), orbit bump from spectrometer and compensator magnets (center), and beam trajectories with negative external crossing angles for negative and positive powering of the spectrometer magnet (right) [114].

3.5.5 Tracking system

The tracking system of LHCb provides precise reconstruction of tracks and vertices, having very good impact parameter, decay time and momentum resolutions. The system is composed of the Vertex Locator (VELO), the Tracker Turicensis (TT) upstream of the spectrometer magnet and three tracking stations downstream of the magnet, T1-T3 [8, 17]. The individual components, as well as their performance, are described in the following.

3.5.5.1 Vertex Locator (VELO)

The Vertex Locator (VELO), as the name suggests, is dedicated to the precise reconstruction of tracks in the vicinity of the interaction region, which are used, in turn, for a precise reconstruction of the primary and displaced (production/decay) vertices. It has an acceptance in pseudorapidity of $1.6 < \eta < 4.9$ with the conditions that the distance of the primary vertex (PV) from the nominal interaction point (IP) to be $|z| < 10.6$ cm and the track has at least three hits in the VELO sensors [8].

The detector consists of silicon microstrip sensors placed along the z axis around the beampipe and perpendicular to it. These sensors measure the r (distance from the z axis) and ϕ (azimuthal angle) coordinates, and there are 42 modules with R-sensors on one side and ϕ-sensors on the other. The modules are equally split between the left and right sides of the beampipe, with a distance of 1.5 cm between a module of one half and the corresponding module from the other half. The linear density of the first 16 modules (for each half) is constant and the last five modules are further apart from each other. The distance from the IP to the 19th module is around 65 cm and the full length of the detector is around 1 m. During the injection of the beams each half is retracted by around 3 cm in order to protect the sensors and during data taking the halves of the VELO slightly overlap. Each sensor has 2 048 readout sectors and the silicon strip sensors have a thickness of 300 μm with varying pitches from around 40 μm to around 100 μm [8, 17]. A detailed description of the sensors can be found in [8]. Schematics of the VELO and its sensors are shown in Figure 3.14.

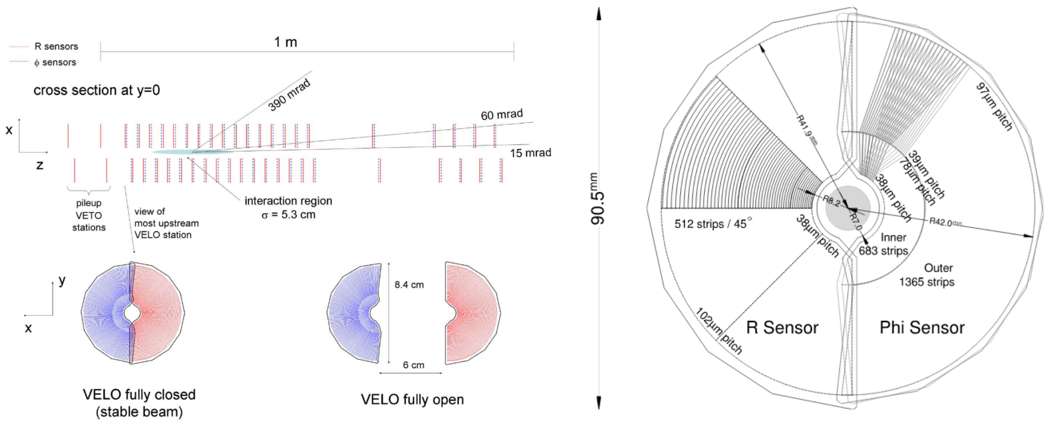

Figure 3.14: Schematic of the VELO (left) and its sensors (right) [8].

The performance of the VELO sensors has been studied and a fraction of 0.6% of the strips were found to be inefficient, while 0.02% were noisy [17, 117]. The hit resolution (for $p > 10$ GeV/c tracks) shows a linear dependence on the strip pitch and also a strong dependence on the projected angle of the track, with the best hit resolution of 4 μm being obtained for an 8° projected angle and 40 μm pitch [17, 117]. The projected angle is defined as the angle between the component of the track perpendicular to the plane of the strips and the track projection on the plane perpendicular to the strip length [118].

3.5.5.2 Silicon Tracker (ST)

The Silicon Tracker (ST) is based on silicon microstrip sensors and is composed of the Tracker Turicensis (TT), placed upstream of the magnet, and three cross-shaped detectors at the center of the downstream T1-T3 tracking stations, collectively known as the Inner Tracker (IT). Each station (TT, T1-T3) has four detection layers with a $x-u-v-x$ configuration, in which the microstrips are vertically oriented for the x layers and rotated with a stereo angle of negative and positive 5° for the u and v stations, respectively [8, 17].

The TT has the physical dimensions of about 150 cm × 130 cm, the active area being around 8.4 m^2, and its layer configuration is split down the middle with around 27 cm between the $x-u$ and $v-x$ halves. The microstrip sensors have a thickness of 500 μm and a pitch of 183 μm. Each sensor has the dimensions of 9.64 cm × 9.44 cm and contains 512 readout strips. The sensors are arranged in half-modules above and below the beampipe, each containing 7 sensors. There are 15 and 17 pairs of half-modules for each of the $x-u$ and $v-x$ layers, respectively [8, 17]. A schematic of the v layer of TT is shown in Figure 3.15.

The sensors used for the IT have 384 readout strips with a pitch of 198 μm and are arranged in modules of one or two sensors. The sensors have the dimensions of 7.6 cm × 11 cm and a thickness of 320 μm (410 μm) for modules with one sensor (two sensors). There are 7 of each type of module on either side of the beampipe, with the two-sensor modules left and right of the beampipe, and the one-sensor modules above and below the beampipe. The total active area of the IT amounts to around 4.0 m^2 [8, 17]. A schematic of the x layer of the T2 station of the IT is shown in Figure 3.15.

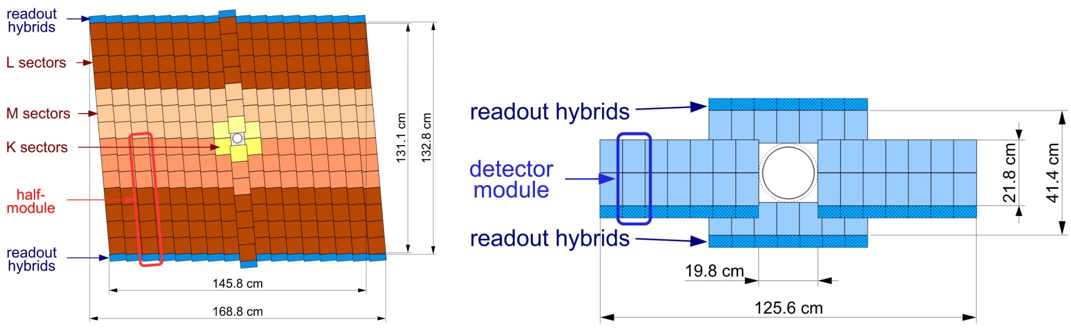

Figure 3.15: Schematic of the v layer of TT (left) and x layer of the T2 station of IT (right) [8].

The hit efficiencies in the TT and IT were determined to be a minimum of 99.7% and the hit resolutions vary between 50 μm and 55 μm, values obtained for tracks with $p > 10$ GeV/c [17].

3.5.5.3 Outer Tracker (OT)

The Outer Tracker (OT) is a gas drift-tube tracker using a mixture of Ar (70%), CO_2 (28.5%) and O_2 (1.5%). The drift-tubes (also called straw-tubes) have an inner diameter of 4.9 mm and are arranged into modules with two staggered layers of 64 straws each. The modules are of two types, namely F-type with a length of 485 cm in which the straws are split longitudinally and therefore have a total of 256 straws, and a shorter S-type with about half the length of the previous module type and half the number of straws. Similarly to the IT, the OT has 4 layers per T station, arranged in the same $x - u - v - x$ configuration. The stations are split in half vertically and the layers of each half are grouped two by two into so called C-frames. There are 12 C-frames and they are incorporated into the OT bridge, a stainless steel frame with rails which allows them to be individually moved away from the beampipe along the x axis. The half layers contain 7 F-type and 4 S-type modules each for a total of 168 long and 96 short modules for the OT with a cumulated number of around 55 300 straw-tubes. Each station has an active area of 597.1 cm $\times$ 485.0 cm $\approx$ 29.0 m^2 [8, 17]. Schematics of the OT design and sensors are given in Figure 3.16.

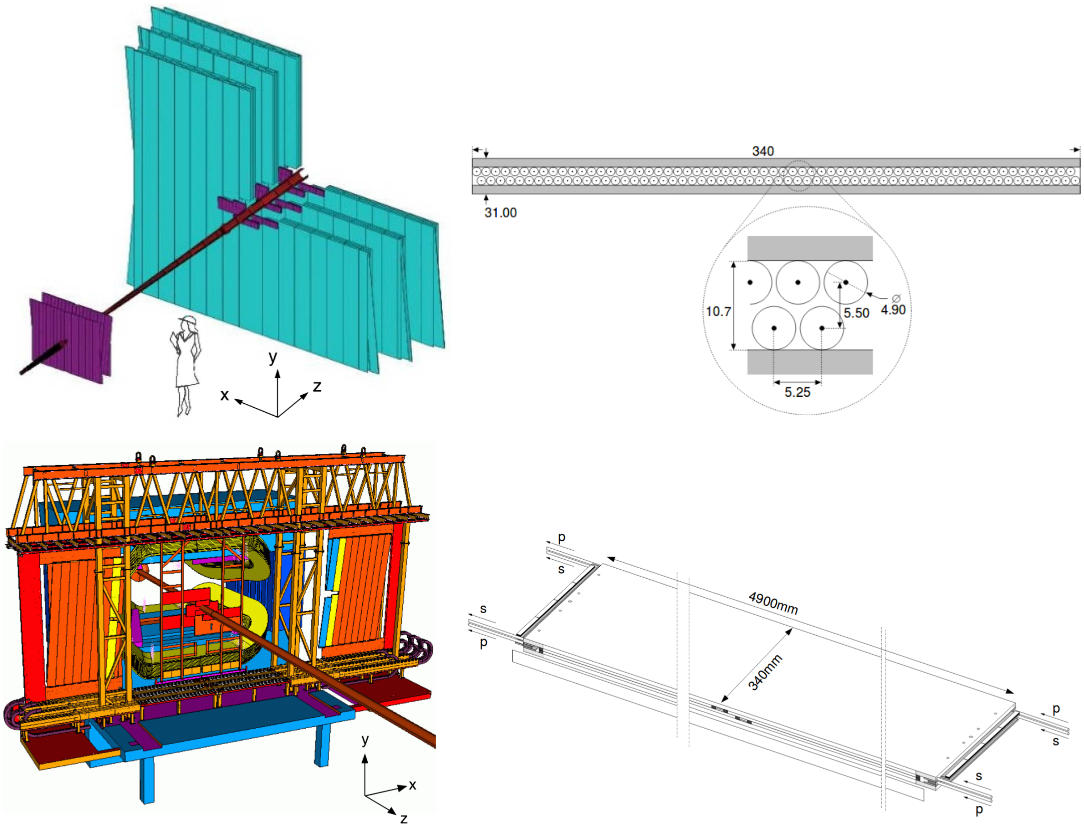

Figure 3.16: Schematic of the OT stations in light blue with the ST stations in purple (top-left), 3D view of the OT bridge with the C-frames retracted (bottom-left), cross section of a module with zoom showing the straw-tubes (top-right) and schematic of a long straw-tube module (bottom-right) [8].

The drift-time in a straw-tube is a maximum of about 36 ns corresponding to hits at the edge of the tube. The hit efficiency has a rapid increase at the edge of the tube towards the wire, reaching around 99.2% for distances smaller than 1.25 mm (half the radius of the tube) to the wire and the hit resolution is 205 μm. These values were determined using tracks with $p > 10$ GeV/c [17].

3.5.6 Particle identification system

The particle identification (PID) system at LHCb is composed of two RICH (Ring Imaging Cherenkov) detectors, RICH1 and RICH2, a set of calorimeters, namely the Scintillating Pad Detector (SPD), the PreShower detector (PS), an electromagnetic calorimeter (ECAL), and a hadronic calorimeter (HCAL), and a muon identification system with 5 stations, M1-M5 [8, 17]. A brief description of all of the PID system sub-components will be given in the following.

3.5.6.1 RICH detectors

The detection principle of the RICH detectors is based on the physical phenomenon called Cherenkov radiation which is described in the following. When charged particles traverse a medium of refractive index, n, with a velocity, v, larger than the phase velocity of light in the respective medium, light is emitted. Consider equidistant emission points along the trajectory of such a particle. The lightwaves will form a coherent wavefront behind the particle and they will travel at the speed of light in the respective medium, c/n, so the distance covered in an arbitrary amount of time, t, will be ct/n. In the same amount of time, the particle has travelled a distance $vt = \beta ct$. The wavefront will be the tangent to the circles described by the waves at time t and the angle formed by the radii with the trajectory of the particle is called the Cherenkov angle, at which photons are emitted. The rotation of this angle in a plane perpendicular to the particle trajectory defines a cone of emission of light. The image formed by this light cone on a screen perpendicular to the height of the cone will be of a circle, or ring, from which the name Ring Imaging Cherenkov Detector comes from [24, 119]. The Cherenkov angle will be:

$$\cos\theta_c = \frac{ct/n}{\beta ct} = \frac{1}{\beta n} \rightarrow \theta_c = \arccos\frac{1}{\beta n}, \tag{3.27}$$

so the velocity of the particles can be obtained from the measurement of θ_c, given that the refractive index of the medium, n, is known.

In order to unambiguously identify a particle, its mass and the sign of its electric charge need to be determined. The ring patterns are associated with reconstructed tracks from the tracking system [8, 17, 120, 121] and the masses of the particles are obtained from:

$$p = mv \rightarrow p = m\beta c \rightarrow p = m_0\gamma\beta c \rightarrow m_0 = \frac{p}{\gamma\beta c}, \tag{3.28}$$

where the momentum, p, as well as the sign of the electric charge, is determined from the bending of the particle trajectory in the field of the spectrometer magnet

[119]. The track reconstruction procedures are described in Section 3.6 and details can be found in [122, 123]. An event display showing the ring patterns in RICH1 and a plot showing the Cherenkov angle for different particles are shown in Figure 3.17.

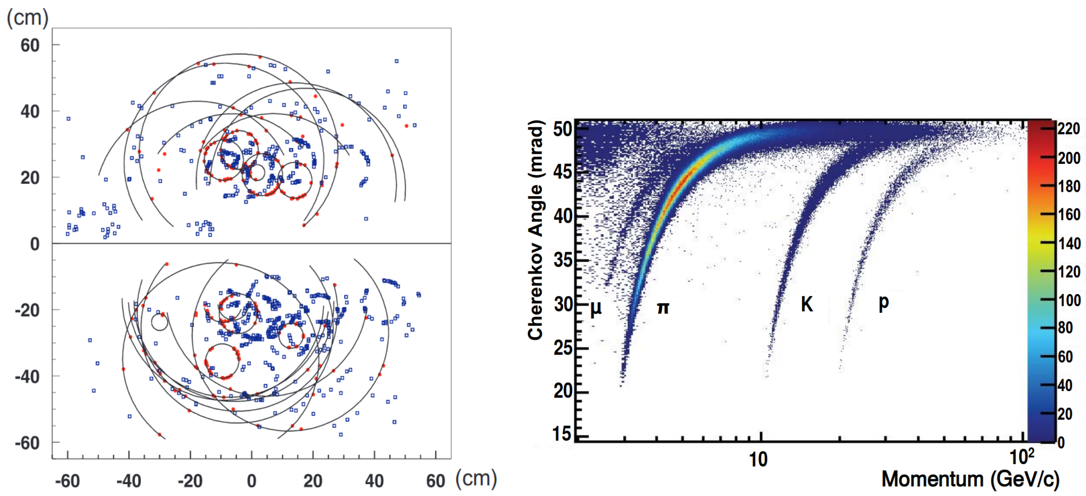

Figure 3.17: Event display in RICH1 (left) [8] and a two-dimensional plot of the Cherenkov angle versus the momentum of the particle (right) [17].

The RICH1 detector is used for the identification of charged hadrons with momenta in the range $\sim 2-60$ GeV/c and is installed upstream of the spectrometer magnet with its location along the beampipe defined by $990 < z < 2\,165$ mm, between the VELO and TT. The radiators consist of Aerogel and C_4F_{10}, and the Cherenkov photons emitted in the range $200 < \lambda < 600$ nm are detected using Hybrid Photon Detectors (HPD). The RICH1 covers the 25 mrad to 300 (250) mrad region in the horizontal (vertical) plane and its optical system is alligned vertically, being composed of one pair of spherical mirror surfaces and another pair of flat mirror planes with one surface/plane positioned above and one below the beampipe as can be seen in Figure 3.18 in which a schematic of the RICH1 detector is shown. The spherical mirror surfaces are inside the acceptance and each set contains two CFRP (carbon fibre reinforced polymer) substrate mirrors, with supports outside the acceptance. Each flat mirror plane contains eight glass substrate mirrors and is located outside the acceptance. The HPDs are arranged in two magnetically shielded planes outside the acceptance, one above and one below the beampipe, each containing 98 HPDs and forming an angle of 1.091 rad with the y axis [8, 17].

The RICH2 detector, which is dedicated to the identification of higher momentum charged hadrons in the range $15-100$ GeV/c, uses CF_4 as radiator, is placed between the T3 and M1 stations in the $9\,500 < z < 11\,832$ mm region, and has a narrower angular acceptance, between 15 mrad and 120 (100) mrad in the horizontal (vertical) plane. The optical system is alligned horizontally with pairs of spherical and flat mirror surfaces with glass substrates to the left and right of the beamline. Each of the flat mirrors is actually a set of 20 smaller rectangular mirrors and are located outside the acceptance, while each of the spherical surfaces are composed of 26 hexagonal mirrors and are placed inside the acceptance. The HPD detectors are located to the left and right of the beampipe, outside of the acceptance, and are placed in iron shielding boxes [8, 17]. Schematics of the RICH2 detector are shown in Figure 3.19.

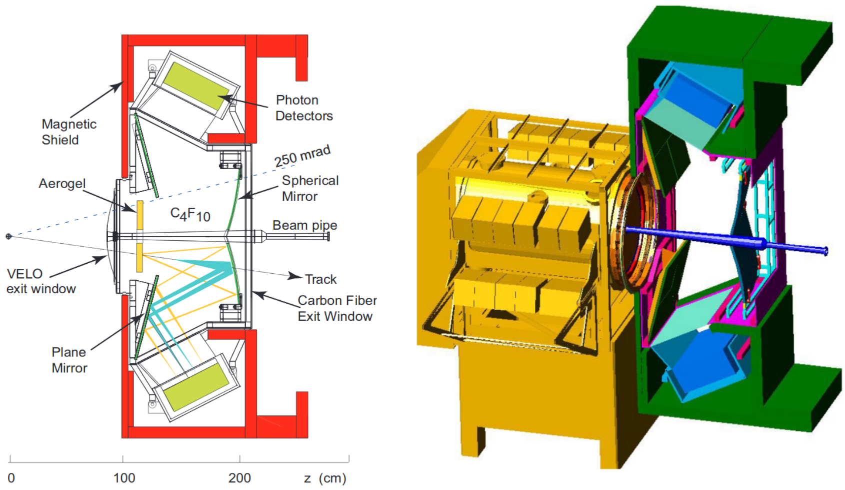

Figure 3.18: Schematic of the RICH1 detector (left) and a 3D render (right) [8].

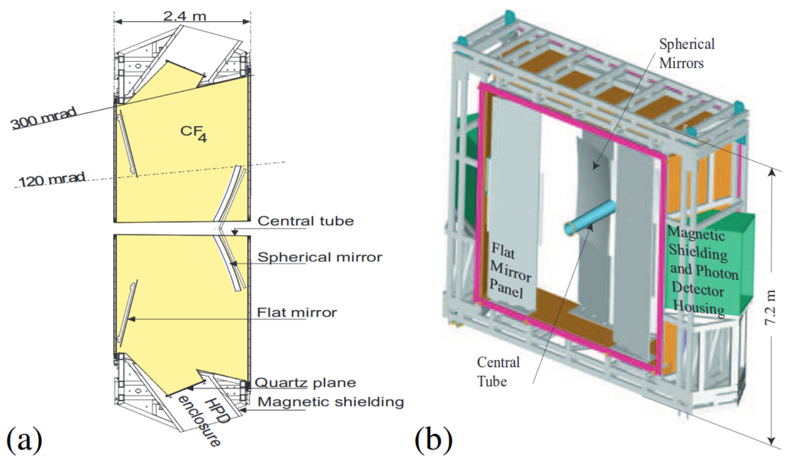

Figure 3.19: Schematic of the RICH2 detector (left) and a 3D view (right) [8].

The performance of the RICH detectors is quantified through the Cherenkov angle resolution and photoelectron yield, the average number of detected photons per track, of the radiators. The Cherenkov angle resolutions (and photoelectron yields in a typical LHCb event) for the C_4F_{10}, CF_4 and Aerogel radiators are around 1.6 mrad (20), 0.68 mrad (16) and 5.6 mrad (5), respectively [17].

The identification procedure starts with assigning particle hypotheses corresponding to all long lived and stable charged particles, namely electron, muon, pion, kaon and proton, for the reconstructed tracks and then the likelihoods for each case are computed based on the matching of the expected pixel patterns with the observed ones. The procedure is carried out simultaneously for all tracks in the event and is called the global pattern recognition. The likelihoods are then compared and the hypothesis corresponding to the highest value is chosen [8, 17, 120, 121]. The efficiency of kaon identification with the RICH based system is around 95% with around 5% probability of mis-identifying a pion as a kaon [124]. The performance of the RICH based identification system is detailed in [17].

3.5.6.2 Calorimeters

The calorimeter system is located upstream of the RICH2 detector, between the M1 and M2 muon stations, and is composed, in order from M1, of the Scintillating Pad Detector (SPD), PreShower Detector (PS), Electromagnetic Calorimeter (ECAL) and Hadronic Calorimeter (HCAL). The component calorimeters use scintillation pads and the light produced in the pads reaches Photo-Multiplier Tubes (PMT) via wavelength-shifting (WLS) fibres. The particle flux decreases rapidly towards the outer limit of the acceptance, the hit density in this region being two orders of magnitude lower than the one at the inner limit (towards the beampipe). As a consequence, the calorimeters are segmented laterally into zones with different cell dimensions, three zones for the SPD/PS and ECAL, and two zones for HCAL, as shown in Figure 3.20 [8, 17].

The ECAL is composed of alternating layers of lead and scintillating pads with a total thickness of 25 radiation lengths or 42 cm. The PS detector allows the reduction of background coming from charged pions by providing longitudinal segmentation of the electromagnetic showers and the role of the SPD is of selecting charged particles, thus improving the separation of electrons and photons. The scintillation pads of the SPD and PS are very similar and they both use multianode PMTs (MAPMT) for readout, while the ECAL and HCAL use individual PMTs. A lead converter with a thickness of 15 mm, corresponding to 2.5 radiation lengths, is installed between the SPD and PS. The HCAL has a thickness of 1.65 m, corresponding to 5.6 nuclear interaction lengths (definition in Section 5.13), and consists of alternating tiles of iron absorbers and scintillators arranged longitudinally in the zy plane as shown in Figure 3.20, whereas the scintillating pads of the other calorimeters are in the xy plane, perpendicular to the beampipe [8, 17].

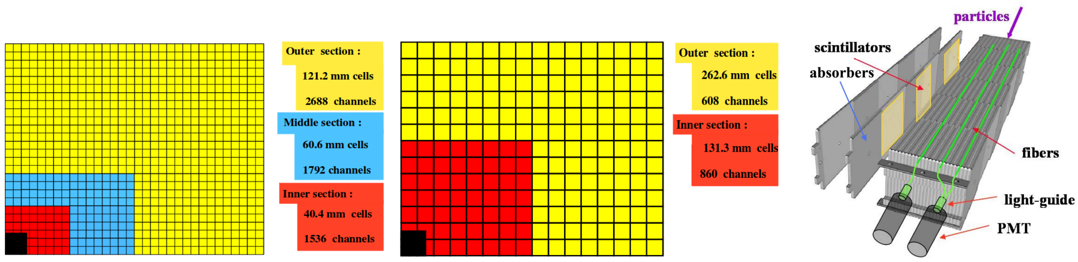

Figure 3.20: Schematic of a quadrant of the scintillation pads used for the SPD/PS and ECAL (left), HCAL (center) and 3D view of the HCAL (right) [8].

The performance of the calorimeters is amply discussed in [17]. The energy resolution of the ECAL is approximately given by $\sigma_E/E = 1\% + 10\%/\sqrt{E}$ [8, 124] and the one of HCAL is $\sigma_E/E = (9 \pm 2)\% + (69 \pm 5)\%/\sqrt{E}$ with E expressed in GeV [8].

The neutral and charged particles are discerned through the absence or presence of tracks associated with the energy deposits in the calorimeters. Photons are reconstructed using the energy deposits in the PS and ECAL. The low transverse momenta neutral pions ($p_T < 2$ GeV/c) are reconstructed with a mass resolution of around 8 MeV/c^2 as pairs of separated photons and are called resolved π^0. The high p_T neutral pions are called "merged" π^0 and may be misidentified with photons, due to the fact that the deposits from the daughter photons are not sufficiently separated. The shapes of the energy deposits are used to discern between the two. The efficiency of photon identification is around 95% with a 45% rejection of merged π^0 background. The electron identification is done using input from the PS, ECAL and HCAL with an efficiency of around 90% for $\sim$ 5% rate of mis-identification [8, 17, 124]. Similarly to the RICH identification procedure, the reconstructed tracks are extrapolated towards the calorimeters and particle hypotheses for electrons and hadrons are constructed. The difference in log-likelihoods of the two hypotheses are computed for each calorimeter and then summed, based on the degree of matching between the observed energy deposits and the extrapolated tracks. Besides the identification and reconstruction of particles, the calorimeter system provides input for the Level 0 (L0) trigger by selecting high transverse energy candidates [17].

3.5.6.3 Muon detection system

The muon detection system has an angular acceptance from 20 (16) mrad to 306 (258) mrad in the horizontal (vertical) plane and consists of five stations, M1-M5, with a total active area of around 435 m^2. The first station is placed upstream of the calorimeters and the rest downstream, each being segmented into four regions, R1-R4, starting from the beampipe, with a 1:2:4:8 relative scaling of the linear dimensions. This segmentation was chosen in order to have similar occupancy levels accros the regions. The detection system is based on 1 380 gas chambers divided into rectangular logical pads (details in [8]), of which 1 368 are Multi-Wire Proportional Chambers (MWPC) and 12 are Gas Electron Multiplier (GEM) chambers. The GEM chambers are installed in region R1 of M1, being chosen for their higher radiation tolerance as the particle flux in this region is larger. The M2-M5 stations are separated between them by iron absorbers with a thickness of 80 cm, which together with the calorimeters amount to around 20 radiation lengths. Only muons with momenta above 3 GeV/c reach the M2-M3 stations, while in order to traverse all stations they must have a minimum of $p \approx 6$ GeV/c [8, 17, 125]. A schematic of the muon system, as well as schematics showing the segmentation of the stations into regions and logical pads are shown in Figure 3.21.

The spatial resolution in the x and y coordinates is defined by the dimensions of the logical pads, which increase from R1 to R4 with the same scaling of progressive doubling and projectively from M2 to M5, with the x dimensions a factor of 2 smaller and larger for M2-M3 and M4-M5, respectively, than the projected size on M1. As the resolution is better in the case of the M1-M3 stations, they are used for determining the muon candidate direction and transverse momentum, the resolution for the latter being around 20%. The lower spatial resolution M4-M5 stations are mainly used for the selection of penetrating muons [8, 17, 125].

The muon identification starts with the extrapolation of tracks reconstructed with the tracking system towards the muon system and searching for hits around the extrapolated trajectory in a rectangular region in the xy plane called field of interest (FOI). The dimensions of the FOI are parameterized as a function of momentum for each region and station. The minimum number of stations with hits required to define a muon candidate depends on momentum as follows: M2-M3 for $3 < p < 6$ GeV/c, M2-M3 and M4 or M5 for $6 < p < 10$ GeV/c, and all of the stations downstream of the calorimeters for $p > 10$ GeV/c. The next step consists of constructing muon and non-muon hypotheses for which likelihoods are computed based on the distance from the closest hit to the extrapolated track [8, 17, 125]. The muon identification efficiency is around 97% with 1-3% probability of mis-identification of pions as muons [124]. For the improvement of particle identification, the previously mentioned likelihoods are combined with likelihoods computed with input from the RICH and calorimeter systems [8, 17, 125].

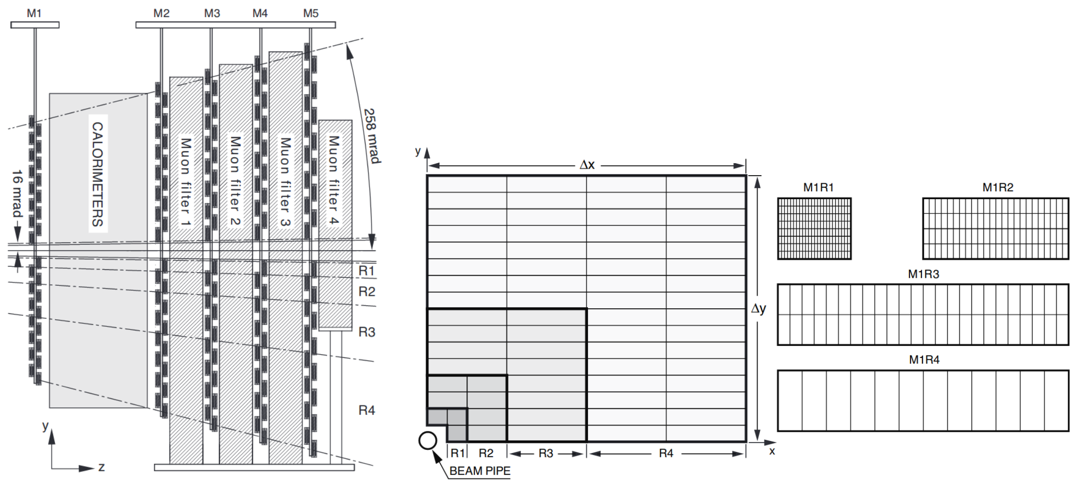

Figure 3.21: Schematics of the muon system (left), segmentation of the stations into regions (center) and logical pads (right) [8].

3.5.7 Triggers

The purpose of the LHCb trigger system is to enrich the data samples with interesting events that contain, for example, rare B meson decays, in order to facilitate the offline analysis. There are two trigger levels, namely Level-0 (L0) and High Level Trigger (HLT) which is further divided into two stages, HLT1 and HLT2 [8, 17]. A schematic of the trigger structure in Run I (2010-2012) and Run II (2015-2018) of data-taking [126] is shown in Figure 3.22.

3.5.7.1 Level-0

The Level-0 (L0) trigger is a hardware trigger built from custom electronics and reduces the event rate from around 40 MHz, the nominal LHC bunch crossing frequency, to around 1.1 MHz, corresponding to the maximum readout frequency of the detector [8, 17]. It has three components, namely the pile-up system, the Calorimeter Trigger and the muon trigger, as shown schematically in Figure 3.23. All of these components provide information to the Level-0 Decision Unit (DU) which delivers the final trigger decision per bunch crossing [8].

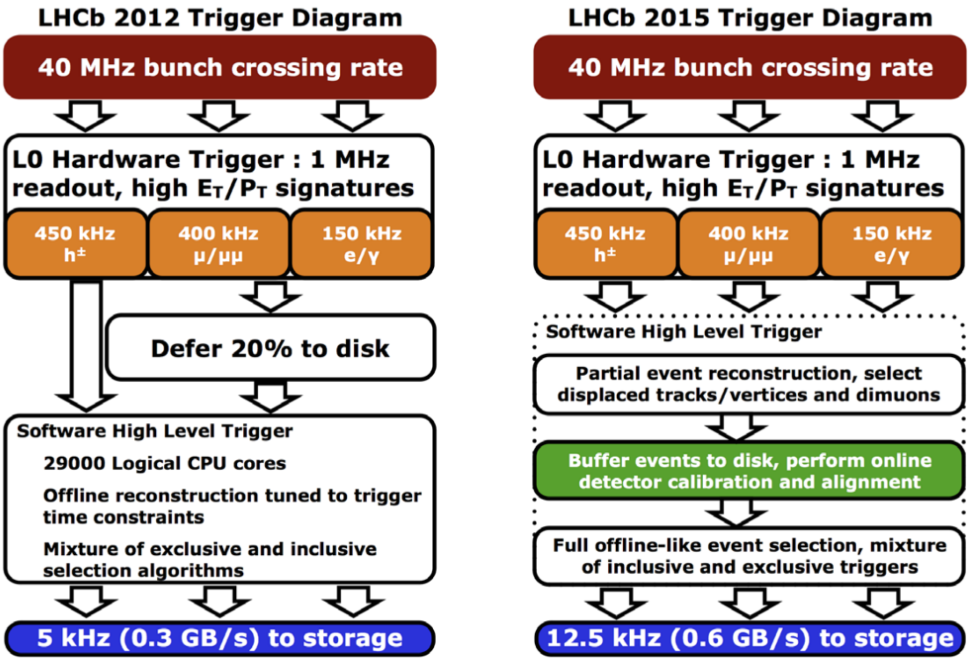

Figure 3.22: Schematic of the LHCb trigger structure in Run I (2010-2012) and Run II (2015-2018) [126].

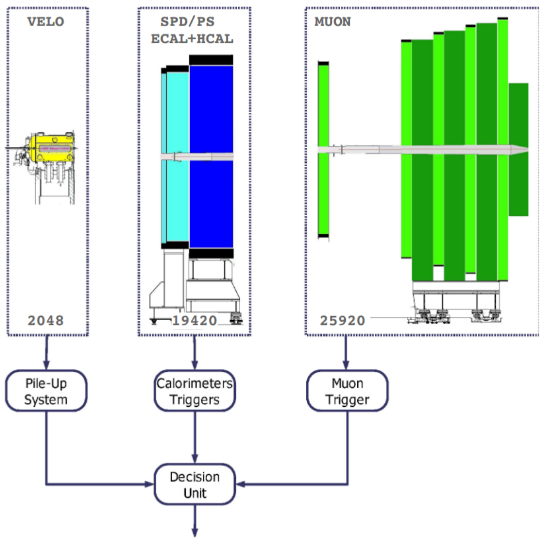

Figure 3.23: Schematic of the Level-0 trigger structure [8].

The pile-up system is composed of four R-sensors and is located upstream of the VELO. It is used to discern between bunch crossings with single and multiple visible interactions and to provide measurements of the positions of primary vertices on the z axis, as well as of the charged track multiplicity in the backward region [8].

High transverse momentum (and energy) is a signature property of B meson decay products and such, the Calorimeter Trigger is used to determine the highest transverse energy, E_T, deposits associated with electrons, photons and hadrons, while the muon trigger determines the first and second highest transverse momentum, p_T, muons. The total transverse energy deposited in the HCAL is used as a discriminator against bunch crossings without visible interactions and the number of SPD hits is used as a measure of the track multiplicity [8].

3.5.7.2 High Level Trigger

The High Level Trigger (HLT) is a software trigger written in C++ and running on the Event Filter Farm (EFF) which consists of around 30 000 cores organized into around 2 000 computing nodes [8, 17]. As mentioned, the HLT has two stages, namely HLT1 and HLT2 which will be described in the following.

Given the limited processing power of the EFF and the fact that the offline reconstruction is CPU intensive, the 1 MHz L0 output frequency is reduced by selecting interesting events via the use of partial event information and simpler algorithms. In the HLT1 stage, a set of algorithms are run in parallel on so-called alleys. The alleys correspond to the different types of L0 objects, i.e. highest p_T muons, highest E_T hadrons, photons, or electrons, and the algorithms search for the presence (or absence in the case of photons and π^0) of tracks in the VELO and T stations correspoding to the respective objects, a process known as L0 confirmation. This process reduces the frequency to around 30 kHz [8].

In the HLT2 stage, the offline reconstruction algorithms without the Kalman filter (details in section 3.6) are applied and the obtained tracks are combined to form particle candidates by using the invariant mass of the system as a discriminating variable and relaxed cuts on momentum and impact parameter. Afterwards, inclusive and exclusive criteria are used to select interesting decays. The final output frequency is reduced to around 5 kHz and 12.5 kHz for Run I and Run II, respectively [126, 127]. A schematic of the full trigger chain showing the HLT1 alleys and the HLT2 selections are shown in Figure 3.24.

A detailed description of the trigger performance is given in [17, 126, 127]. The efficiency of the trigger is around 90% for dimuon channels and around 30% for decays with multiple hadrons in the final state [17, 124].

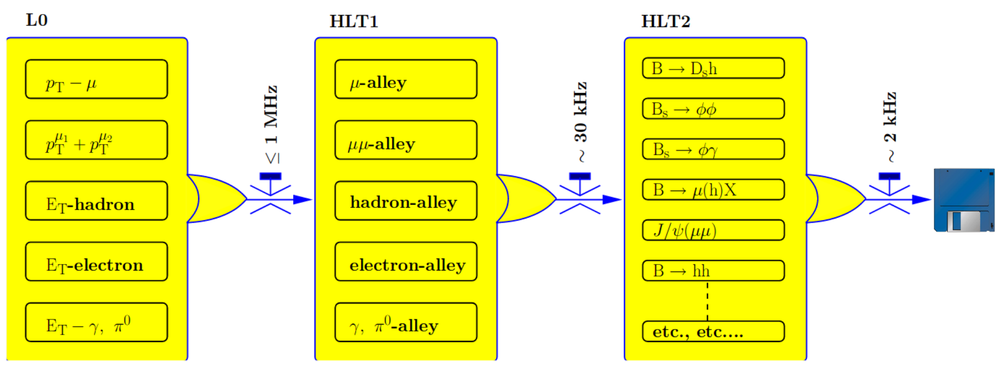

Figure 3.24: Schematic of the LHCb trigger chain [8].

3.6 Tracking at LHCb

A track consists of a set of segments spanning between the measurement planes in which hits in the tracking detectors are found. The magnetic field is low enough in the vicinity of the tracking stations to approximate the segments in the upstream (VELO-TT) and downstream (T stations) regions as being linear segments tangent to the trajectory of the particle, as can be seen in Figure 3.25 in which the magnetic field along the z axis is shown [122, 123, 128]. In the case of large distances between the measurements planes, like the distance between the TT and T stations, the curvature due to the magnetic field is taken into account. As all measurement planes are perpendicular to the beampipe, the track parameters are given as a function of the position on the z axis [122, 123]. There are five track parameters which form the state vector:

$$\vec{x} = \begin{pmatrix} x \\ y \\ t_x \\ t_y \\ q/p \end{pmatrix}; \; t_x = \frac{dx}{dz}; \; t_y = \frac{dy}{dz}; \tag{3.29}$$

where x, y are the positions on the respective axes, t_x and t_y are the slopes at the respective positions, and q/p is the ratio of the charge of the particle and its momentum, with $q = \pm 1$. The state vector and its corresponding 5×5 covariance matrix, C, are collectively known as the track state [122, 123].

The equation of motion of a charged particle in a magnetic field is:

$$\frac{d\vec{p}}{dt} = q\vec{v} \times \vec{B} \Rightarrow d\vec{p} = q\vec{v} \times \vec{B}dt = qd\vec{r} \times \vec{B} \Rightarrow \vec{p} = q \int d\vec{r} \times \vec{B}, \tag{3.30}$$

where q is the electric charge of the particle and $\int d\vec{r} \times \vec{B}$ is the integrated magnetic field along the trajectory of the particle [122]. As the magnetic field map is known and the trajectory of the particle is approximated by the track, the sign of the charge and the momentum, and thus the q/p parameter, can be determined.

3.6.1 Track fit

In order to obtain the best estimates for the track parameters, the tracks are fitted using a Kalman filter [122, 123], an iterative procedure equivalent to a least-squares fit, but not as CPU intensive when large covariance matrices are involved. The Kalman filter has three steps, namely prediction, filter and smoother [122, 123].

In the first step, a prediction of the track state at a measurement plane k, is made from the track state at a previous plane $k - 1$. The prediction for the first measurement plane is made using an estimate from a fit made by the track finding algorithms [122, 123].

In the filter step, the information from a measurement at the current plane, m_k, is added and a new state called a filtered state is obtained via χ^2 minimisation. The filtered state will actually be given by a correction of the predicted state with the product of the predicted residual (difference between the state and the measurement) and a so-called gain matrix. The cycle of prediction and filtering is repeated for each measurement. After all the measurements have been added, the filtered state at the last measurement plane is the best estimate for the respective state. The default direction of the prediction-filter sequence at LHCb is towards $-z$ [122, 123].

The smoother step updates the states at all the other measurement planes in the opposite direction [122, 123].

The Kalman filter takes into account the presence of the magnetic field and effects of the passage of particles through the detector material, namely multiple scattering and energy loss via ionization. The detector structure is approximated by material walls with the same thickness in terms of interaction lengths. The average scattering angle is zero and such, multiple scattering does not affect the values of the track parameters, but it increases the values of the covariance matrix elements. The particles traversing the detector are considered as minimum ionizing particles and the energy loss in the material layers is estimated with the Bette-Bloch formula. Then, the q/p parameter is corrected accordingly in the propagation through the detector [122, 123].

The magnetic field throughout the LHCb detector has components along all axes and is inhomogeneous. The equation of motion can be obtained by differentiating the state vector with respect to the z coordinate, instead of time, which yields a set of analitically unsolvable differential equations. An adaptive 5^{th} order Runge-Kutta extrapolation method is used to numerically solve the set of equations, a procedure which requires the full magnetic field map [122, 123]. A detailed description of the fit procedure is given in [122, 123].

3.6.2 Track types at LHCb

Several types of tracks are defined at LHCb according to the regions of the detector or the different subdetectors that they traverse:

- **Long tracks**: They traverse the entire tracking system, containing hits in VELO and the T stations, and may contain hits in the TT. These tracks have the best momentum resolution and are widely used in analyses.

- **Upstream tracks**: Contain hits in VELO and TT and can be used for background studies for the RICH1.

- **Downstream tracks**: Contain hits in the TT and T stations. They are used for the analysis of long-lived particles like V^0 particles, a large fraction of which decay after the VELO.

- **VELO tracks**: Contain hits only in VELO. They are usually large polar angle or backward tracks and are used for the reconstruction of primary vertices.

- **T tracks**: Contain hits only in the T stations and can be used for particle identification with RICH2 [8, 17, 122, 129].

The different track types are schematically shown in Figure 3.25. In order for the tracks to be reconstructible, they must satisfy a combination of conditions determined by the subdetectors in which they require hits. The conditions are based on the minimum number of hits in the subdetectors and are as follows:

- VELO: hits in 3 R sensors and 3 ϕ sensors.
- TT: hits in 3 layers.
- T stations: 1 hit in x and 1 in u or v layers for each station [17, 129].

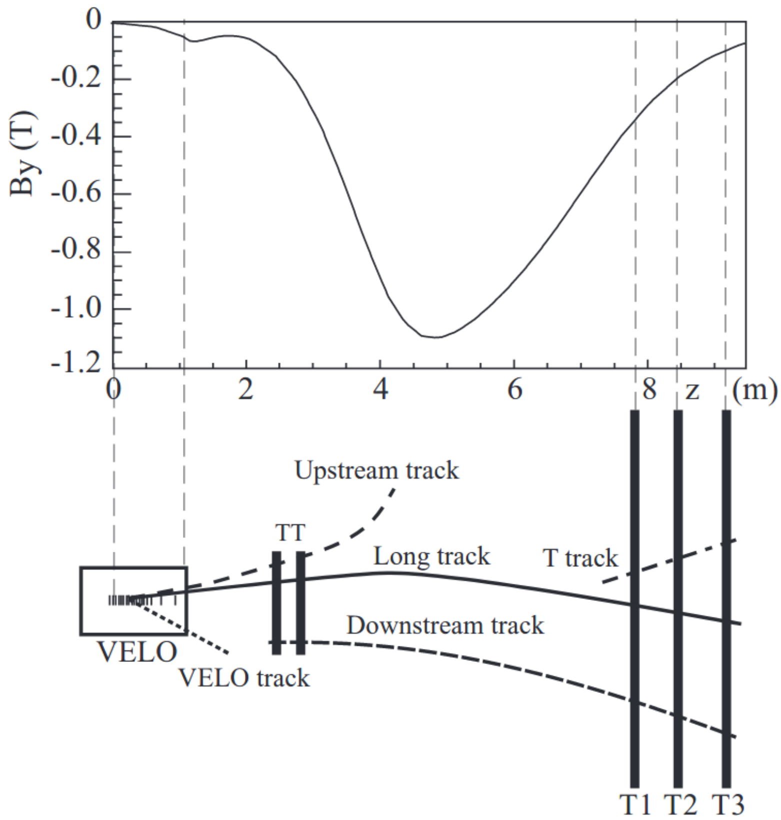

Figure 3.25: The magnetic field along the z axis and schematics showing the different track types used at LHCb [8].

The tracks are found by a set of track finding algorithms as described in the following. The first algorithm, called VELO seeding, searches for straight track segments in the VELO which will be used as seeds for other tracking algorithms. The next algorithm starts with combining a hit in the T stations with the VELO seeds. The momentum of this preliminary trajectory is computed and other hits in the T stations along it are searched for, in order to define a long track. This algorithm is suggestively called forward tracking. Similarly to the VELO seeding, the T seeding algorithm searches for straight segments in the T stations. There is an additional algorithm for finding long tracks called track matching, which matches T seeds with VELO seeds. After a long track is found, compatible TT hits are searched for and added, improving the momentum resolution of long tracks [17, 122, 128]. The remaining T and VELO seeds are matched to TT hits found along their projections, forming downstream and upstream tracks, respectively. The seeds that are not incorporated into one of the aforementioned track types are categorized as VELO and T tracks [17, 122].

A track is considered as succesfully reconstructed if at least 70% of its hits are produced by a single charged particle, and a "ghost" (fake) track otherwise [8, 122, 129, 130]. The ghost tracks are mostly long tracks constructed from mismatched VELO and T seeds [8]. The reconstruction efficiency is defined as the ratio between the number of reconstructed tracks and the number of reconstructible tracks [122, 129]. If a track is incorporated into another track, e.g. a VELO track into a long track, then it is an "ancestor" track of the latter. Tracks that share at least than 70% of their hits are considered as "clones" [129]. The ghost (fake) rate is defined as the ratio between the number of ghost tracks and the total number of reconstructed tracks, and is an important measure of the performance of the track finding algorithms [122, 129]. In a typical minimum bias event, the ghost rate is around 6.5%, but it can reach values as high as around 20% in high multiplicity events [8].

After all the tracks are found, an algorithm that removes clones is run, suggestively named "clone killer" [131].

3.6.3 Primary Vertex reconstruction

The precise determination of the position at which the proton-proton collisions take place, known as the Primary Vertex (PV), is fundamental for the measurements conducted at LHCb. The PV reconstruction consists of two steps, namely seeding and fitting [132, 133].

The seeding starts by searching for so-called "close" tracks among the tracks that have segments in the VELO. For each track in the event, the distance of closest approach (DOCA) of the other tracks to the former is determined and if this distance is less than 1 mm, the tracks are said to be "close" and are grouped together to form a PV seed, with a minimum of four tracks being required. Afterwards, the point of closest approach (POCA) is determined for each pair of tracks that form the seed, along with the mean position of the points. If the distance from a POCA to the mean is larger than 5 mm, the point is removed and the mean of the remaining points is computed. This process is repeated until all POCAs fall within 5 mm of their mean and, if enough points remain, a weighted mean is computed, which will be assigned as the PV candidate position. The tracks used in the reconstruction of one PV candidate are not considered for the reconstruction of another one. The order of the seed processing is from high to low multiplicity, in order to reduce the reconstruction of secondary vertices as PVs [132, 133].

In the fitting step, the position of the PV is found using an adaptive least squares method with Tukey biweights to minimize its χ^2:

$$\chi^2_{\mathrm{PV}} = \sum_{i=1}^{n_{\mathrm{tracks}}} \chi^2_{\mathrm{IP},i} \cdot w_i, \quad \text{with} \quad w_i = \begin{cases} (1 - \chi^2_{\mathrm{IP},i}/C_T^2)^2, & \text{if } \chi^2_{\mathrm{IP},i} < C_T \\ 0, & \text{if } \chi^2_{\mathrm{IP},i} > C_T \end{cases} \tag{3.31}$$

where $\chi^2_{\mathrm{IP},i}$ is the χ^2 of the impact parameter (IP) of track i with respect to the PV and C_T is the Tukey constant. The selection of this method is motivated by the fact that it minimizes the contribution of the tracks from secondary vertices and the number of ghost tracks, from which biases may arise [132, 133]. The IP is defined as the minimum distance between a track and a PV [17, 132]. The $\chi^2_{\mathrm{IP},i}$ is equal to the difference between the χ^2 of the PV found using a set of tracks which contains track i and the value obtained when tr ack i is removed from the set [132, 133].

In order for a track to be considered for the PV reconstruction it must satisfy the $\chi^2_{\mathrm{IP}} \leq 12$ condition. Besides the minimum number of tracks, $N^{\mathrm{PV}}_{\mathrm{Tracks}} = 4$, a radial distance of the PV of $r < 0.2$ mm is required to reconstruct a PV. The radial distance of the PV is defined as $r = \sqrt{x^2 + y^2}$, where x and y are the positions of the PV on the respective axes [133].

3.6.4 Tracking performance

The precision of most measurements at LHCb depends, in one form or another, on the performance of the track and PV reconstruction. For example, measurements of lifetime or flavour oscillations require a good and unbiased decay time resolution, while cross-section or branching fraction measurements require a precise determination of the track reconstruction efficiency [17, 128, 134]. The most important indicators of tracking performance are described in the following.

3.6.4.1 Long track reconstruction efficiency

The efficiencies of reconstructing charged particles that traverse the full tracking system as long tracks used in the LHCb analyses are obtained from Monte Carlo simulation and they might not reflect the experimental ones. This is due to the limited precision of the detector description and of the interaction cross-sections of particles with the detector material implemented in the simulation. Differences between the efficiencies obtained from MC simulation and the experimental ones may give rise to biases in the cross-section measurements. In order to avoid this, so-called "tag-and-probe" methods for determining the experimental track reconstruction efficiency have been developed [17, 128, 134].

These methods measure the track reconstruction efficiencies of the different subdetectors, which are then multiplied to obtain the long track reconstruction efficiency. In decays with two charged particles in the final state like $J/\psi \to \mu^+\mu^-$, $Z^0 \to \mu^+\mu^-$ or $K^0_S \to \pi^+\pi^-$ in which one of the daughter particles is reconstructed as a long track, the "tag", and the other daughter particle is only partially reconstructed, the "probe", the efficiency of the subdetectors in which the latter lacks hits can be estimated. If the probe shares a minimum fraction of its hits with a long track, the tracks are matched and the probe is defined as efficient. The probe tracks are required to contain an amount of momentum information that allows the construction of the invariant mass distribution of the mother particle with sufficient resolution to be used as a discriminant against backgrounds. The numbers of matched and unmatched probes are obtained from fits to the invariant mass distributions and the efficiency of the respective subdetector will be computed as the number of efficient probes divided by the total number of probes [17, 128, 134–137].

Three different methods based on $J/\psi \to \mu^+\mu^-$ decays, which are schematically shown in Figure 3.26, are used:

- **VELO method**: uses Upstream tracks as probes and measures the reconstruction efficiency of the VELO.
- **T-station method**: measures the efficiency of the T-stations by using probes with hits in the VELO and Muon stations.
- **Long method**: directly measures the combined efficiency of the VELO and T-stations with TT-Muon probes.

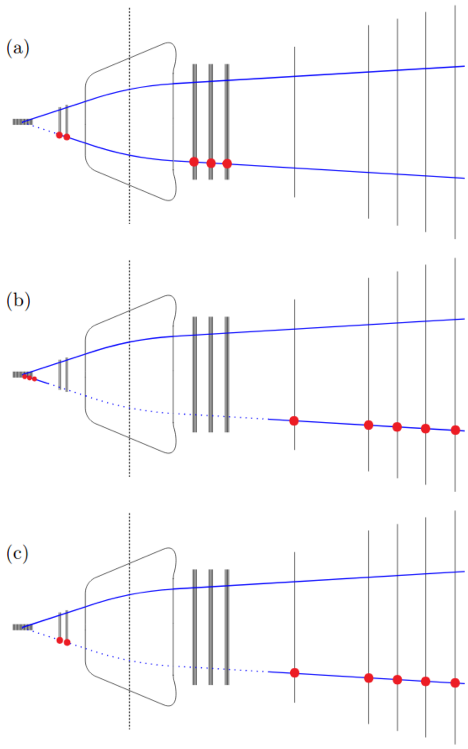

Figure 3.26: Schematics of the three "tag-and-probe" methods: (a) VELO method, (b) T-station method and (c) Long method. [128].

The efficiencies obtained with the VELO and T-station method are combined to form the long track reconstruction efficiency, a procedure suggestively named "Combined method". The final efficiency value is obtained as the weighted average of the Combined method and Long method efficiencies [128, 134–137].

The efficiency depends mainly on the path of the particles through the detector, their momentum and the occupancy in the detector. The occupancy in the detector is proportional to the total number of charged particles in an event. The variables which are strongly correlated with the occupancy are N_{Tracks}, the total number of unique tracks in an event, N_{PV}, the number of reconstructed primary vertices in an event and $N_{\text{SPD hits}}$, the number of hits in the SPD. The path of the particles through the detector is approximately given by their pseudorapidity, η. Ideally, the efficiencies should be computed as a function of all three variables: p, η and one variable correlated with the occupancy. As the statistics are not sufficient for this, the MC samples are reweighted so that the distribution of the considered occupancy correlated variable matches the experimental one, and then the efficiencies are computed as a function of p and η [134–137].

The LHCb Tracking Group has developed a tool for computing data and MC efficiency ratio tables, named "TrackCalib". These ratios are used to reweigh the MC samples used in various analyses which require efficiency corrections. The default variable for MC reweighting in TrackCalib is $N_{\text{SPD hits}}$. The choice of this variable can induce a bias in the ratios. The samples are reweighted using N_{PV} and the difference is taken as a systematic uncertainty, which for 2015 EM (early measurements) Data with a 50 ns bunch spacing and MC with simulation version Sim09b is 0.6% [134–136, 138].

The long track reconstruction efficiency for the aforementioned data is around 96% for tracks in the $10 < p < 100$ GeV/c and $1.9 < \eta < 4.9$ ranges [138]. The Data/MC ratio of efficiencies is given in Figure 3.27. For the $5 < p < 10$ GeV/c, $3.4 < \eta < 4.9$ and $100 < p < 200$ GeV/c, $1.9 < \eta < 3.4$ bins the statistics are too low to give a meaningful value, so the ratio is set to unity with an arbitrary 5% uncertainty. At $p > 10$ GeV the ratios are more or less close to unity. Only the statistical uncertainties are shown and for the most part are below 1% [138].

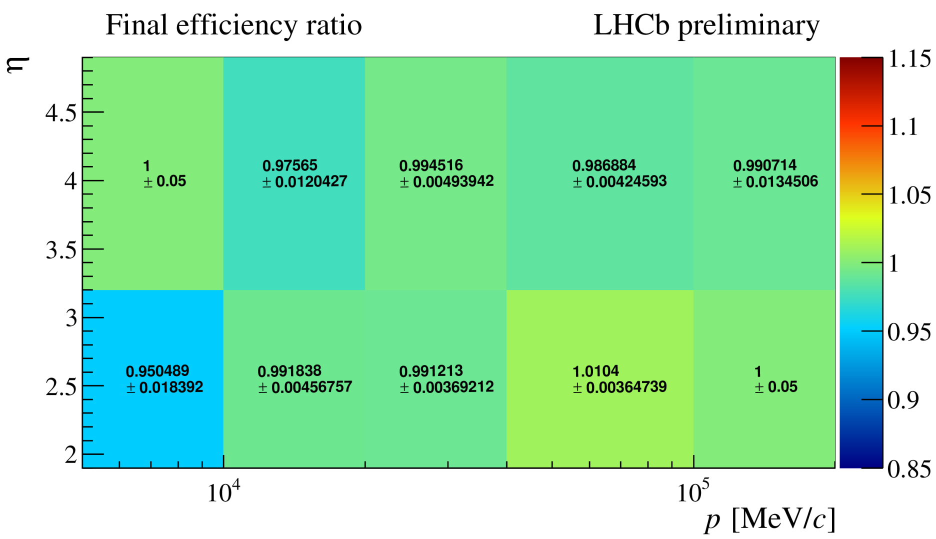

Figure 3.27: Data/MC long track reconstruction efficiency ratios for 2015 EM Data with 50 ns bunch spacing [138].

As these efficiency ratios are determined using muons, no information regarding hadronic interactions is included. The uncertainty on the material budget up to and including the last tracking station, and the one on the hadronic interaction cross-sections implemented in simulation amount to around 10%, which translates into a relative uncertainty on the survival probability of the charged hadrons and thus, on the long track reconstruction efficiency in the simulation. In order to use the efficiency ratios to correct track reconstruction efficiencies for hadrons, this uncertainty must be taken into account [128]. A detailed description of the hadronic interaction uncertainty is given in Sections 5.13.

3.6.4.2 Momentum resolution

The relative momentum resolution is obtained from the invariant mass distribution of the $J/\psi \to \pi^+\pi^-$ decays by using the following approximation:

$$\left(\frac{\delta p}{p}\right)^2 = 2\left(\frac{\sigma_m}{m}\right) - 2\left(\frac{p\sigma_\theta}{mc\theta}\right)^2, \tag{3.32}$$

where m and σ_m are the mean and the width of a Gaussian used as the signal function in the fit to the invariant mass distribution, θ is the opening angle between the tracks and σ_θ its associated uncertainty. The relative momentum resolution as a function of momentum is shown in Figure 3.28. The relative momentum resolution is around 0.5% in the $p < 20$ GeV/c range and rises to around 1% at $p \sim 200$ GeV/c [124, 128].

3.6.4.3 Mass resolution

The mass resolution has been determined for several dimuon decays like J/ψ, Υ resonances and Z^0. The relative mass resolution is around 0.5% in the mass range of the Υ resonances and below, as can be seen Figure 3.28. The mass resolution for $K^0_S \to \pi^+\pi^-$, in which the pions are both reconstructed as long or downstream tracks are 3.5 MeV/c^2 and 7 MeV/c^2, respectively, corresponding to around 0.7% and 1.4% relative mass resolutions [128].

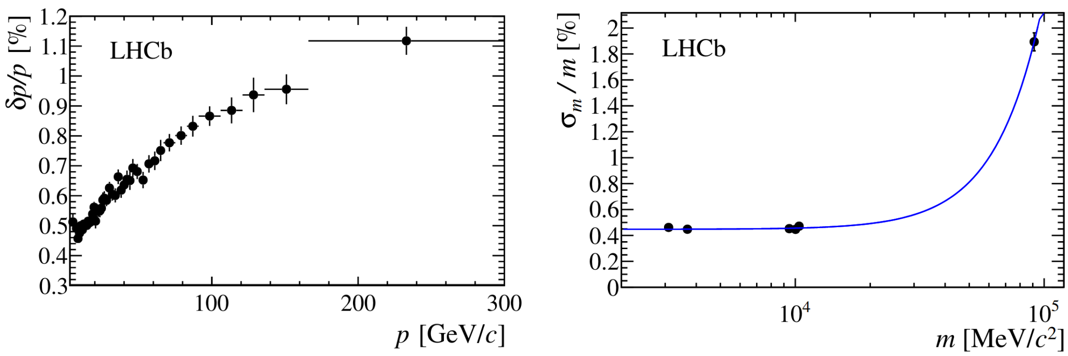

Figure 3.28: Plots of relative momentum resolution as a function of momentum (left) and relative mass resolution as a function of the invariant mass (right) [128].

3.6.4.4 Primary vertex resolution

The PV resolution is determined by reconstructing the PV using two independent sets of tracks from the same event. The resolution is given by the width of the distribution of the difference between the two PV positions, multiplied by a factor of $\sqrt{2}$, and presents a strong correlation with the track multiplicity. This can be seen in Figure 3.29 in which the PV resolution as a function of the track multiplicity is shown. Resolutions of around 13 μm in x and y, and around 71 μm in z are obtained for PV's reconstructed using 25 tracks [17].

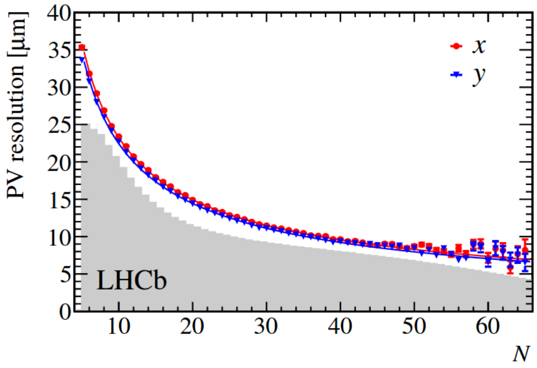

Figure 3.29: The PV resolution in transverse coordinates as a function of the track multiplicity. Only PV pairs reconstructed from sets with the same number of tracks are considered [17].

3.6.4.5 Impact parameter resolution

The impact parameter resolution is defined for its projections on the x and y axes, as these are normally distributed. The projection on x (and analogously for y) is:

$$\mathrm{IP}_x = x - x_{\mathrm{PV}} - (z - z_{\mathrm{PV}})t_x, \tag{3.33}$$

where x, z, and t_x are the track parameters at the point of closest approach to the PV, and x_{PV}, z_{PV} are the positions of the PV on the respective axes. The $\mathrm{IP}_{x,y}$ resolutions as a function of $1/p_T$ are shown in Figure 3.30, where a linear dependence due to multiple scattering can be seen. In order to minimize the contribution from the PV resolution, only PVs with $N^{\mathrm{PV}}_{\mathrm{Tracks}} \geq 25$ from events with a single PV are used. The best resolution is around 12 μm for both projections [17, 127].

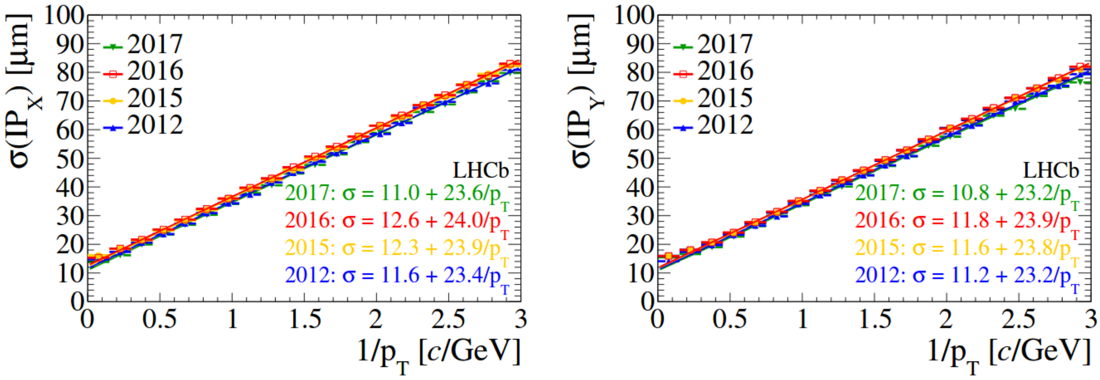

Figure 3.30: The $\mathrm{IP}_{x,y}$ resolutions as a function of $1/p_T$ [127].

3.6.4.6 Decay time resolution

The decay time is defined as:

$$t = \frac{Lm}{p}, \tag{3.34}$$

where L is the decay length, the distance between the production and decay vertices, and m, p are the measured invariant mass and momentum, respectively. The decay time resolution is determined using several B_S^0 decays. The prompt background candidates of these decays, called "fake" candidates, have a mean decay time of zero and so, the width of the distribution of their decay times reflects the resolution of the measurement. The decay time uncertainty is estimated from a fit to the decay vertex performed by the reconstruction algorithm and the "fake" candidates are sorted into bins of this uncertainty. The decay time resolution is computed for each decay time uncertainty bin and an average value is obtained. The resolutions obtained for different B_S^0 decays are given in Table 5.1. Plots of the decay time resolution as a function of momentum and decay time uncertainty for different data-taking periods are shown in Figure 3.31. The resolution presents a linear dependence of the decay time uncertainty and is independent of the momentum [17, 127, 139–142].

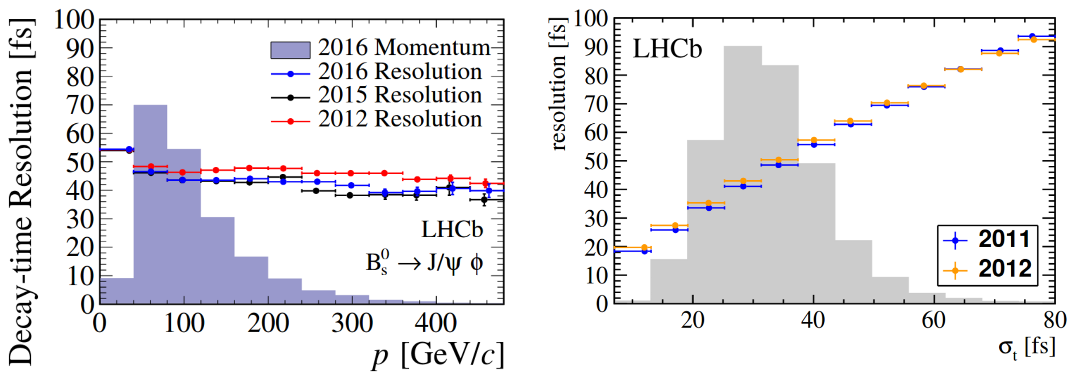

Figure 3.31: The decay time resolution as a function of momentum (left) [127] and as a function of decay time uncertainty (right) [17]. The momentum and decay time uncertainty distributions with an arbitrary scale are also shown.

Table 3.1: Decay time resolutions obtained using different B_S^0 decays.

Decay	Resolution [fs]	Source
$B_S^0 \to J/\psi(\to \mu^+\mu^-)\phi$	~ 45.0	[127]
$B_S^0 \to D_S^-\pi^+$	~ 44.0	[139]
$B_S^0 \to J/\psi(\to \mu^+\mu^-)K^+K^-$	~ 45.5	[140]
$B_S^0 \to J/\psi(\to \mu^+\mu^-)\pi^+\pi^-$	~ 41.5	[141]

3.7 The LHCb software applications

A wide range of software applications have been developed for LHCb, covering all aspects of the experiment, from reconstruction and data analysis to simulation and visualization. In order to permit a seamless communication between the different applications, they are built within a common Object Oriented framework called Gaudi [143–145]. The LHCb software applications are as follows:

- **Gauss** - the simulation application. It is used to generate collisions and simulate the interaction of particles with the detector [143, 144, 146–148]. The generation step is based on the PYTHIA 8.2 generator [58], but other generators are also available [146–148]. The particles produced in the collisions are decayed using EvtGen [149] or SHERPA [146, 148, 150]. The former is developed for accurate B meson decays [143, 146, 149] and interfaced with PHOTOS [151], which generates radiative decays of final state charged particles [147, 149]. The simulation of the detector and of the different processes of interaction within it are built using the Geant4 toolkit [152]. A number of tools are implemented to simulate the experimental conditions like, for example, the pile-up tool which allows for multiple collisions per bunch crossing, the beam tool which accounts for the beam crossing angle, and the smearing tool, which simulates the luminous region by setting the point of collision according to normal distributions in all spatial coordinates [148]. The application also provides information regarding the association between the hits in the detector and the particles that produced them, the so-called MC "truth" [143, 144]. The structure and data flow of the Gauss application, as well as the data flow from simulation to analysis are schematically shown in Figure 3.32.

- **Boole** - the digitization application. It simulates the detector response to the hits of particles generated with GAUSS and propagates the MC "truth" information [143].

- **Brunel** - the reconstruction application. It reconstructs hit clusters and tracks, integrating the algorithms described in Section 3.6. The output of the application is a so-called DST file and, besides the tracking objects, contains the information from the particle identification sub-systems. It can be run on both real or simulated data. In the case of simulated data, the MC "truth" is propagated to the reconstructed objects and writen to output [143].

- **DaVinci** - the analysis framework. It is used for the reconstruction of vertices, particle identification, constructing composite particles and applying off-line selections. It also provides access to the MC "truth". The C++ based LoKi toolkit is integrated, which provides a simplified, physics oriented language for the writing of analysis codes. The output can be either in the Ntuple format or a reduced DST (rDST) [143, 144].

- **Bender** - the interactive analysis application. It is based on Python and LoKi and provides an interactive browsing and analysis of data [143].

- **Panoramix** - the visualization application. It is used for the 3D interactive visualization of the detector simulation and of the reconstructed particles via a GUI (Graphical User Interface) [143, 144].

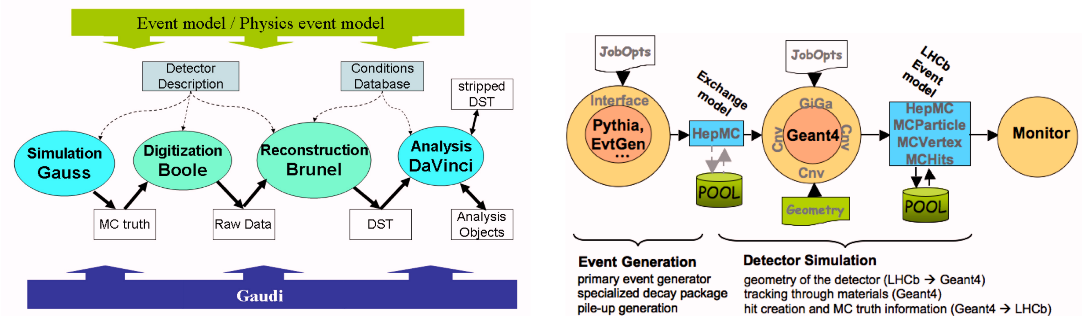

Figure 3.32: Schematics of the data flow between the LHCb software applications (left) and of the Gauss application (right) [143].

Study of Monte Carlo event generator predictions for observables in the "forward" region measured at LHCb and TOTEM in pp collisions at $\sqrt{s} = 7$ TeV

4.1 Introduction and motivation

In this chapter, the predictions of the Monte Carlo event generators with LHC tunes described in Section 2.8 are compared to measurements in the "forward" region from the LHCb and TOTEM experiments. The versions of the generators are as follows: PYTHIA 8.186, PYTHIA 8.219, both with default tunes, EPOS LHC, QGSJETII-04 and SIBYLL 2.3. In the case of the latter three, the implementations from the CRMC [64] package were used. The 8.186 version of PYTHIA with tune 2M (abbreviated to PYTHIA 8.1 2M) is used as a reference for non-LHC tunes. As mentioned in the Introduction, predictions in the "forward" region are sensitive to MPI and hadronization parameter values to a larger degree than those in the "central" region. The above generator tunes are based on minimum bias and underlying event observables mainly from the "central" region measured at the general purpose detector LHC experiments and thus, the parameters related to the "hard" processes of hadronic collisions can be considered to be fairly well constrained. The effects of these tuning procedures on the "forward" predictions are qualitately assessed using the following observables: charged energy flow, charged hadron multiplicities and densities, charged hadron production ratios and V^0 hadron production ratios, all measured in pp collisions at $\sqrt{s} = 7$ TeV [16]. The measurements are taken from [10–15].

The samples used in the study consist of 10 million events for each generator. In order to reduce the size of the output files, particles with $c\tau > 3$ m, where τ is the rest frame lifetime, are not decayed [16]. The generated charged particles from Sections 4.2 and 4.3 have lifetimes exceeding 10 ns, i.e. the stable (anti) protons and electrons, and the quasi-stable charged kaons, charged pions and muons [10].

With the exception of charged energy flow, all measurements involved prompt particles. The promptness definition, however, is not the same in all cases. For practical reasons, a universal condition of $\tau_{\text{ancestors}} \leq 10$ ps is set for the selection of generated particles, where $\tau_{\text{ancestors}}$ is the sum of the particle ancestors' lifetimes [16]. This is the condition used in [11, 12] and rejects particles with weakly decaying strange hadrons in their ancestry. An equivalent condition is used in [13]. Thus, prompt particles are produced directly in the hadronic collision or in decay chains in which the longest lived ancestor is a resonance (electromagnetic or strong) or a heavy flavour hadron (charm, beauty). In contrast, the condition from [14, 185] is equivalent to $\tau_{\text{ancestors}} \leq 10^{-17}$ s, rejecting particles with c and b hadrons as ancestors. This difference in the definition of prompt particles affects only the predictions of particle ratios from the generators which implement heavy flavour production, namely PYTHIA and SIBYLL. The overall effect is expected to be on the order of $\mathcal{O}(1\%)$. This was investigated and the results are given in Section 4.4.

So-called pull plots have been drawn for the figures in Sections 4.2 and 4.3, as to provide a measure for the quality of the predictions. The distributions of the Monte Carlo predictions in these figures are drawn without error bars for clarity. For the most part, the statistical uncertainties are on the order of $\mathcal{O}(0.1\%)$. The largest uncertainties are around 3%. The pull plots are the distributions of $(x_{\text{gen}} - x_{\text{exp}})/\sigma_{\text{exp}}$, where x_{gen} is the predicted value, x_{exp} is the measured value and σ_{exp} is the experimental uncertainty [16].

4.2 Energy flow

The charged energy flow is defined as the sum of the individual energies of (quasi-) stable charged particles per unit of pseudorapidity. The measurements cover 10 bins of $\Delta\eta = 0.3$ in the $1.9 \leq \eta \leq 4.9$ interval [10]. The energy flow in a given bin is computed as:

$$\frac{1}{N_{\text{int}}}\frac{dE_{\text{total}}}{d\eta} = \frac{1}{\Delta\eta}\left(\frac{1}{N_{int}}\sum_{i=1}^{N_{\text{part}},\eta} E_{i,\eta}\right), \tag{4.1}$$

where N_{int} is the number of inelastic pp collisions from the sample, N_{part}, η is the number of particles in the pseudorapidity bin and $E_{i,\eta}$ is the energy of the particles [10, 16].

The energy flow has been measured for several event classes and the corresponding selection criteria for the generated events are:

(a) Inclusive minimum bias (MB): $N_{\text{ch}} > 0$ in $1.9 \leq \eta \leq 4.9$;

(b) Diffractive enriched: (a) and $N_{\text{ch}} = 0$ in $-3.5 \leq \eta \leq -1.5$;

(c) Non-diffractive enriched: (a) and $N_{\text{ch}} > 0$ in $-3.5 \leq \eta \leq -1.5$;

(d) Hard scattering events: $N_{\text{ch}} > 0$ with $p_T > 3$ GeV/c in $1.9 \leq \eta \leq 4.9$;

where N_{ch} is the number of charged particles [10, 16, 153].

As their names suggest, the (b) and (c) event type samples do not contain exclusively diffractive and non-diffractive events, respectively. The sample "purity" is defined as the fraction of events of one type in the corresponding "enriched" sample [10]. The purities for PYTHIA 8.186 and 8.219 have been evaluated using the event information output [62] and are around 94% and 92% for the diffractive and non-diffractive enriched samples, respectively [16].

The transverse momentum distributions of the partons from the hardest $2 \rightarrow 2$ partonic scatterings in hard and so-called soft (neither hard, nor diffractive) events generated with PYTHIA 8.186 are shown in Figure 4.1. A reasonable degree of separation between the peaks is observed. The means and standard deviations of the distributions are $(\mu_{\mathrm{hard}}, \sigma_{\mathrm{hard}}) = (8.7, 4.5)$ and $(\mu_{\mathrm{soft}}, \sigma_{\mathrm{soft}}) = (4.2, 3.2)$ in GeV/c. Events that are included in both the diffractive enriched and hard scattering samples have been found, but their fractions from the respective samples are negligible [16].

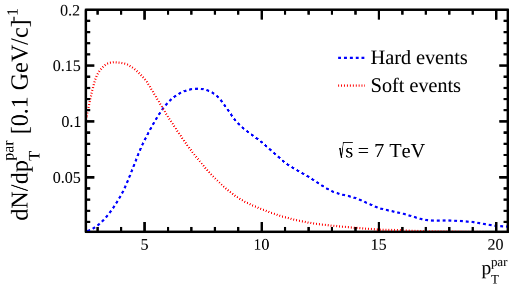

Figure 4.1: Transverse momentum distributions of the partons from the hardest $2 \rightarrow 2$ partonic scatterings [62] in hard and soft (see text above) events. Figure published in [16].

The fractions of inclusive minimum bias (MB) events from the number of generated inelastic events, as well as the fractions of the former included in the hard scattering and diffractive enriched samples are given in Table 4.1. The fractions of MB events and the ones corresponding to the diffractive enriched samples are similar between PYTHIA 8.186 and 8.219, while the fraction of hard scattering events of the latter is slightly smaller and closer to the one of EPOS. On the other hand, the MB and diffractive fractions of EPOS are smaller than those of PYTHIA 8.219. The hard scattering and diffractive fractions of QGSJETII-04 are significantly larger and smaller, respectively, than those of the other generators. In the case of SIBYLL 2.3, the MB fraction is the largest, the diffractive fraction is similar to the one of EPOS and the one of hard events is somewhat intermediate between EPOS and QGSJET [16].

Table 4.1: Fractions of inclusive minimum bias (N_{MB}) events from the number of generated inelastic events $N_{\mathrm{gen}} = 10^6$. The fractions of inclusive minimum bias events included in the hard scattering (N_{hard}) and diffractive enriched (N_{dif}) samples are also given. Table published in [16].

Generator	N_{MB}	N_{hard}	N_{dif}
PYTHIA 8.186	88.20 %	5.63 %	7.04 %
PYTHIA 8.219	88.11 %	5.05 %	7.10 %
EPOS LHC	84.92 %	4.87 %	6.26 %
QGSJETII-04	86.72 %	7.94 %	5.52 %
SIBYLL 2.3	89.55 %	6.43 %	6.47 %
PYTHIA 8.1 2M	86.89 %	5.08 %	7.97 %

The distributions of charged energy flow are shown in Figure 4.2. Predictions of previous versions of the generators without LHC tunes are shown in [10].

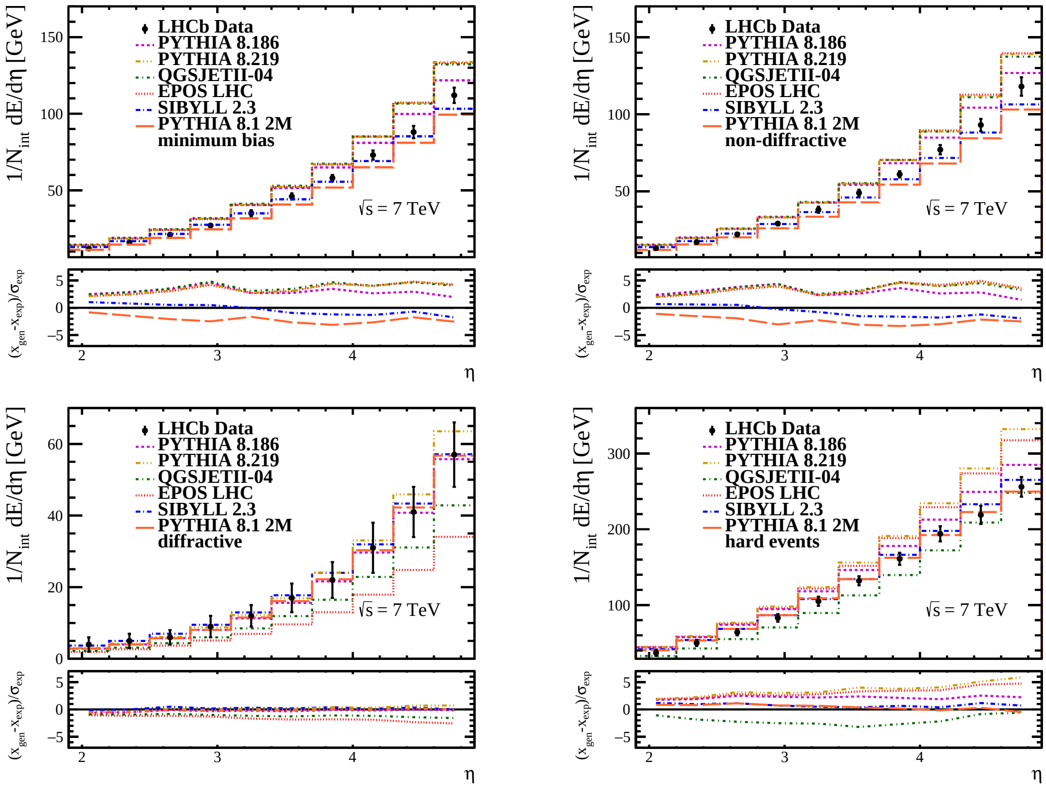

Figure 4.2: Distributions of charged energy flow in pp collisions at $\sqrt{s} = 7$ TeV. The error bars of the LHCb data points correspond to the systematic uncertainties. The statistical uncertainties of the measurements are negiligble [10]. Measurements from [10]. Figure published in [16].

The predictions of the various PYTHIA 6 versions show a good description in the central region and a general trend of underestimation in the forward region for the inclusive minimum bias, non-diffractive enriched and hard scattering event classes. In the case of the diffractive enriched class, a severe underestimation of up 50% is observed. Version 8.135 (with the default Tune 1 [62]), on the other hand, has exceptionally good descriptions of the measurements, except for the hard scattering events, for which an overestimation trend is observed. PYTHIA 8.1 2M has a similarly good description for the diffractive enriched class and also a good description, especially in the forward region, for hard scattering events. The measurements for the inclusive minimum bias and non-diffractive enriched classes are underestimated by PYTHIA 8.1 2M, more so in the forward region. PYTHIA 8.186 has a similar description to that of 8.1 2M in the case of the diffractive enriched class. Version 8.219's prediction is also similar in the central region, with slightly larger values in the forward region. The predictions of versions 8.186 and 8.219 largely overestimate the measurements for all of the other event classes. They are very similar in the central region, again with larger values in the forward region for the latter, which may be an effect of the $\sim$ 10% increase in charged particle production with the Monash 2013 tune [16].

The predictions of EPOS LHC are very close to those of PYTHIA 8.219, except in the case of the diffractive enriched class, for which the largest degree of underestimation amongst the LHC tuned generators is observed. EPOS 1.99's prediction for the latter class is similar to that of its successor, but the ones for the other event classes are very good, with a very slight overestimation trend beyond $\eta = 4.3$ [16].

For the inclusive minimum bias and non-diffractive enriched classes, QGSJET01 and QGSJETII-03 largely overestimate the measurements. The same is valid for QGSJETII-04, the predictions of which cluster together with the ones of EPOS LHC and PYTHIA 8.219. QGSJET01 has a reasonably good description for the diffractive enriched class in the central region and an underestimation trend in the forward region. The prediction of QGSJETII-03 is worse in the central region, but better beyond $\eta = 4.0$, with all of the values within one standard deviation of the measurements. QGSJETII-04 is similar to QGSJETII-03 in the $\eta < 4.0$ region and to QGSJET01 in the $\eta \geq 4$ one. The charged energy flow for hard scattering events is well described by QGSJET01 up to $\eta = 4.0$, beyond which an overestimation trend is observed. QGJSETII-03 has a reasonably good description in the central region, but generally underestimates the measurements in the forward region. QGSJETII-04 is the only LHC tuned generator to underestimate the measured charged energy flow for hard scattering events. The degree of underestimation by QGJSETII-04 is larger than that of QGJSETII-03 [16].

SIBYLL 2.1 is generally similar to EPOS 1.99 in the description of the charged energy flow for the inclusive minimum bias and non-diffractive enriched classes, with a slight underestimation trend in the case of the latter and a better description beyond $\eta = 4.3$ in both cases. Its prediction for the hard scattering events is similar in the central region to the ones of EPOS 1.99 and QGSJET01, but overestimates the measurements in the forward region. In the case of the diffractive enriched class, the prediction of SIBYLL 2.1 is very similar to the one of QGJSETII-03. The predictions of SIBYLL 2.3 are the best overall of the LHC tuned generators, with slight underestimation trends in the forward region for the inclusive minimum bias and non-diffractive enriched classes. Its predictions are similar to the ones of PYTHIA from Figure 4.2 for the diffractive enriched class and to the one of PYTHIA 8.1 2M for the hard scattering class [16].

4.3 Charged hadron multiplicities and densities

The transverse momentum, pseudorapidity and multiplicity distributions of prompt charged particles with $2.0 < \eta < 4.8$, $p \geq 2$ GeV/c and $p_T > 0.2$ GeV/c are shown in Figure 4.3. The predictions of the LHC tuned version of PYTHIA, EPOS and QGSJET cluster together and largely underestimate the measurements past $p_T = 0.7$ GeV/c, despite a somewhat good description at low p_T. These are joined by the prediction of SIBYLL 2.3 at around $p_T = 1.0$ GeV/c, which is similar to the one of PYTHIA 8.1 2M in the low p_T region, i.e. they both underestimate the measurements by up to around five standard deviations. In the case of the pseudorapidity distributions, the predictions of LHC tuned PYTHIA, EPOS LHC and QGJSETII-04 are close together and underestimate the measurements up to around $\eta = 3.5$, at which point PYTHIA 8.186 starts to describe the data relatively well, while the rest of the predictions continue with an overestimation trend. SIBYLL 2.3's prediction converges with the rest towards the central region, but a clear disagreement between it and the measurements is observed across the whole η range, again being similar to PYTHIA 8.1 2M. EPOS LHC seems to have the best description of the charged multiplicity distribution. QGSJETII-04, PYTHIA 8.186 and 8.219 show an excess of low multiplicity events with $n < 10$ to the detriment of higher multiplicity ones. This effect is severely more pronounced for SIBYLL 2.3 [16].

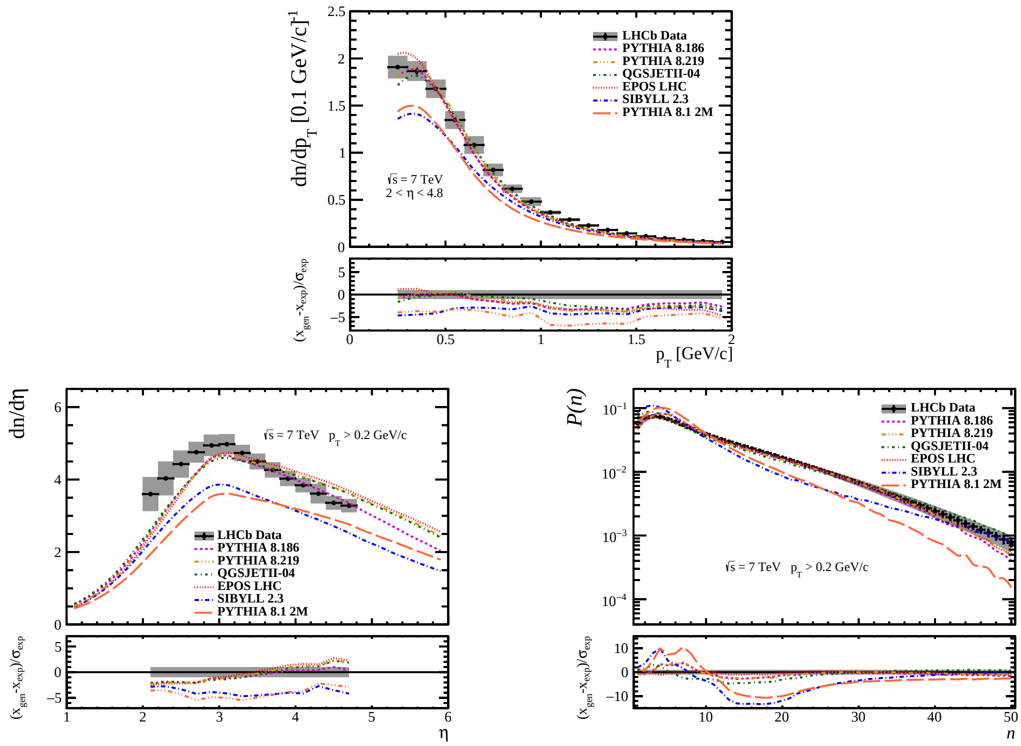

Figure 4.3: Transverse momentum, pseudorapidity and multiplicity distributions of prompt (quasi-) stable charged particles with $2.0 < \eta < 4.8$, $p \geq 2$ GeV/c and $p_T > 0.2$ GeV/c in pp collisions at $\sqrt{s} = 7$ TeV. The statistical and total (quadratic sum of statistical and systematic) uncertainties are represented using vertical bars and grey bands, respectively. Measurements from [11]. Figure published in [16].

The pseudorapidity and multiplicity distributions of prompt charged particles from minimum bias and "hard" events are shown in Figures 4.4 and 4.5, respectively. The minimum bias events are defined by $N_{\text{ch}} > 0$ in the $2.0 < \eta < 4.5$ region, while "hard" events have $N_{\text{ch}} > 0$ with $p_T > 1.0$ GeV/c and $2.5 < \eta < 4.5$ [12]. In the case of the pseudorapidity distributions, the best predictions for both types of event classes seem to be the ones of PYTHIA 8.219, followed closely by the ones of version 8.186. The predictions of these PYTHIA versions diverge in the forward region, which is expected, given that the charged particle production was increased in this region with the Monash 2013 tune. While EPOS LHC approaches the measurements to within one standard deviation in the central region, it shows a clear overestimation trend towards high η. QGSJETII-04 starts with underestimating the measurements for minimum bias events at low η, but converges with the prediction of PYTHIA 8.219 in the forward region. For the "hard" events class, QGSJETII-04 clearly underestimates the measurements, which is also the case of SIBYLL 2.3 for both event classes. The predictions of the latter two generators for "hard" events converge in the central region and a similar tendency is observed for minimum bias events, as well. The sudden rise of the values at $\eta = 2.5$ in Figure 4.5 is a consequence of the definition of “hard” events [16].

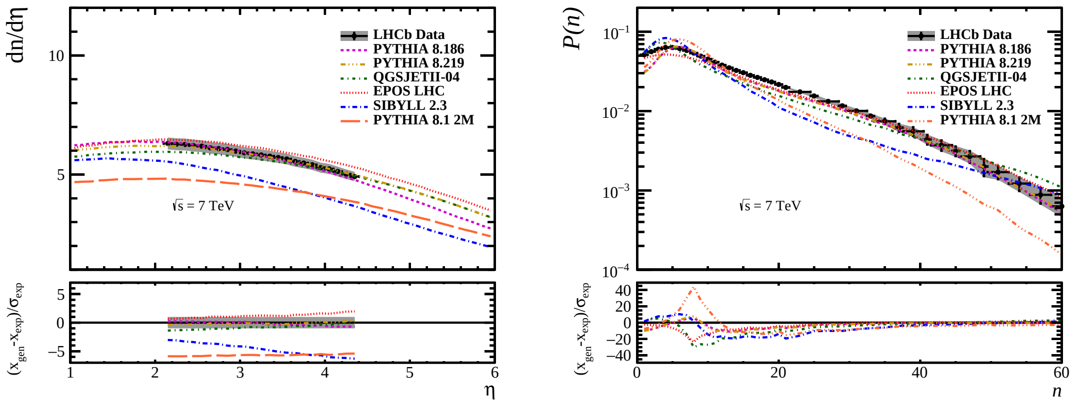

Figure 4.4: Pseudorapidity and multiplicity distributions of prompt (quasi-) stable charged particles from minimum bias events in pp collisions at $\sqrt{s} = 7$ TeV. The statistical and total (quadratic sum of statistical and systematic) uncertainties are represented using vertical bars and grey bands, respectively. Measurements from [12]. Figure published in [16].

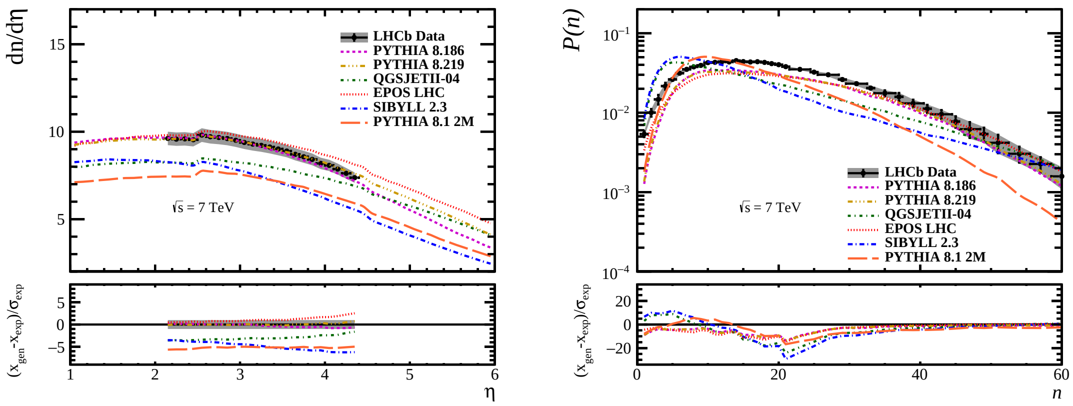

Figure 4.5: Pseudorapidity and multiplicity distributions of prompt (quasi-) stable charged particles from “hard” events in pp collisions at $\sqrt{s} = 7$ TeV. The statistical and total (quadratic sum of statistical and systematic) uncertainties are represented using vertical bars and grey bands, respectively. Measurements from [12]. Figure published in [16].

The multiplicity distributions are not well described by any of the generators. SIBYLL 2.3 and PYTHIA 8.1 2M show a clear excess of low multiplicity events for both classes. PYTHIA 8.186 and 8.219 predict a larger number of low multiplicity minimum bias events and the systematic underestimation in the low and mid multiplicity regions of “hard” events suggests an overestimation of the high multiplicity tails. The prediction of EPOS LHC for “hard” events is very close to the ones of PYTHIA 8.186 and 8.219. In the case of EPOS LHC, the low multiplicity minimum bias events are also underestimated and a similar behaviour of the prediction of QGSJETII-04 is observed. For “hard” events, QGSJETII-04 is similar to

SIBYLL 2.3. The predictions of PYTHIA 8.1 2M are clearly the furthest from the measurements overall [16].

The fractions of minimum bias events from the number of generated events and the ones of "hard" events from the former are given in Table 4.2. The values for the LHC tuned versions of PYTHIA are similar. The minimum bias fraction of SIBYLL 2.3 is close to the aforementioned ones, but the "hard" event fraction is higher. For EPOS LHC, the "hard" fraction is intermediate between those of PYTHIA and SIBYLL 2.3, while the minimum bias fraction is the lowest. The "hard" events fraction of QGSJETII-04 is significantly higher than the rest. PYTHIA with tune 2M clearly generates less "hard" events than the LHC tuned versions [16]

Table 4.2: Fractions of minimum bias events ($N_{\text{ch}} > 0$ in $2.0 < \eta < 4.5$) from N_{gen}. The fractions of "hard" events ($N_{\text{ch}} > 0$ with $p_T \geq 1$ GeV/c in $2.5 < \eta < 4.5$) from the number of minimum bias events are also given. Table published in [16].

Generator	minimum bias	hard events
PYTHIA 8.186	87.28 %	43.90 %
PYTHIA 8.219	87.17 %	42.83 %
EPOS LHC	83.81 %	44.86 %
QGSJETII-04	85.57 %	54.01 %
SIBYLL 2.3	88.19 %	46.68 %
PYTHIA 8.1 2M	85.87 %	37.37 %

The pseudorapidity distributions of charged particles with $p_T > 40$ MeV/c from events with $N_{\text{ch}} > 0$ in $5.3 \leq |\eta| \leq 6.5$ are shown in Figure 4.6. The measurements are reasonably well described by both QGSJETII-04 and PYTHIA 8.219. The prediction of EPOS LHC is also close up to $|\eta| = 6$, but it diverges upwards beyond this value. The rest of the generators underestimate the measurements. The description of PYTHIA is significantly improved with the Monash 2013 tune [16].

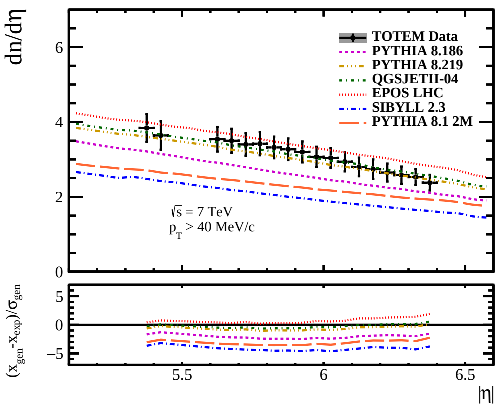

Figure 4.6: Pseudorapidity distributions of prompt (quasi-) stable charged particles with $p_T > 40$ MeV/c in pp collisions at $\sqrt{s} = 7$ TeV. The events have $N_{\text{ch}} > 0$ in $5.3 \leq |\eta| \leq 6.5$. The vertical bars represent the total (quadratic sum of statistical and systematic) uncertainty. Measurements from [13]. Figure published in [16].

4.4 Charged hadron and V^0 production ratios

The prompt $\overline{p}/p$, π^-/π^+ and K^-/K^+ production ratios as a function of pseudorapidity are shown in Figures 4.7 and 4.8. The ratios are more or less well described by all generators with few exceptions. The prediction of QGSJETII-04 for the π^-/π^+ ratio in the $p_T \geq 1.2$ GeV/c region shows a significant deviation from the measurements and thus, a charge asymmetry between the charged pions. The predictions cluster together and their separation seems to increase with p_T. All generator predictions show some amount of baryon number transport [16].

In Figure 4.8, the prompt $\left(K^+ + K^-\right) / \left(\pi^+ + \pi^-\right)$ production ratios are also shown. None of the generators correctly reproduce the measurements in all p_T regions. The predictions of SIBYLL 2.3 describe the ratios well in the $0.8 \leq p_T < 1.2$ GeV/c region and slightly worse in the $p_T < 0.8$ GeV/c regions. The next closest predictions to the measurements are the ones of EPOS LHC. In the lowest p_T region, the predictions of the generators converge towards high η. The prompt $(p + \overline{p}) / \left(\pi^+ + \pi^-\right)$ are shown in Figure 4.9. The best predictions for the ratios in the $p_T < 0.8$ GeV/c region seem to be the ones of PYTHIA. The predictions of the other generators are also close to the measurements. SIBYLL 2.3 has the closest prediction in the mid p_T region, but largely overestimates the measurements in the $p_T \geq 1.2$ GeV/c one, for which the best prediction is the one of EPOS LHC. The predictions of PYTHIA and QGSJETII-04 underestimate the measurements in these p_T regions. EPOS LHC also underestimates the measurements in the mid p_T region. The $(p + \overline{p}) / \left(K^+ + K^-\right)$ production ratios are shown in the same figure. The best description of the low p_T region measurements is the one of EPOS LHC, followed by the ones of SIBYLL 2.3 and QGSJETII-04. The prediction of PYTHIA 8.219 is close to these. In the mid and high p_T regions, the closest predictions are the ones of PYTHIA 8.219. The prediction of EPOS LHC clusters together with the one of SIBYLL 2.3 in the mid p_T region and with the one of PYTHIA 8.219 in the high p_T region. The measurements in the mid p_T region are somewhat between the predictions of QGSJETII-04 and EPOS LHC. The predictions of PYTHIA 8.186 and 8.1 2M cluster together and systematically overestimate the measurements in all p_T regions. The same is true for SIBYLL 2.3 in the high p_T region. The Monash 2013 tune improves the description of the K/π and p/K ratios [16].

QGSJETII-04's predictions in the high p_T regions of the ratios discussed in the previous paragraph have high positive slopes, while the measurements appear to be rather flat or even to be slowly decreasing towards high η. Some of the predictions of the other generators show similar behaviours and the slopes of the predictions with an increasing trend are not as high as in QGSJETII-04's case. The generated yields (normalized to unity) of protons, pions and kaons in the $p_T \geq 1.2$ GeV/c region are shown in Figure 4.10. The negative slope of the proton yields generated with QGSJETII-04 is much lower than the corresponding one for pions. This leads to the observed effect of high positive slopes of the predictions in the high p_T region. Moreover, the slope of the QGSJETII-04 pion yields is the highest among the generators, while the one of the proton yields is one of the lowest and the one for kaons is intermediate. These observations suggest that the decrease of the proton production towards the beampipe is too slow, the one of pions is too fast, or a combination of the two [16].

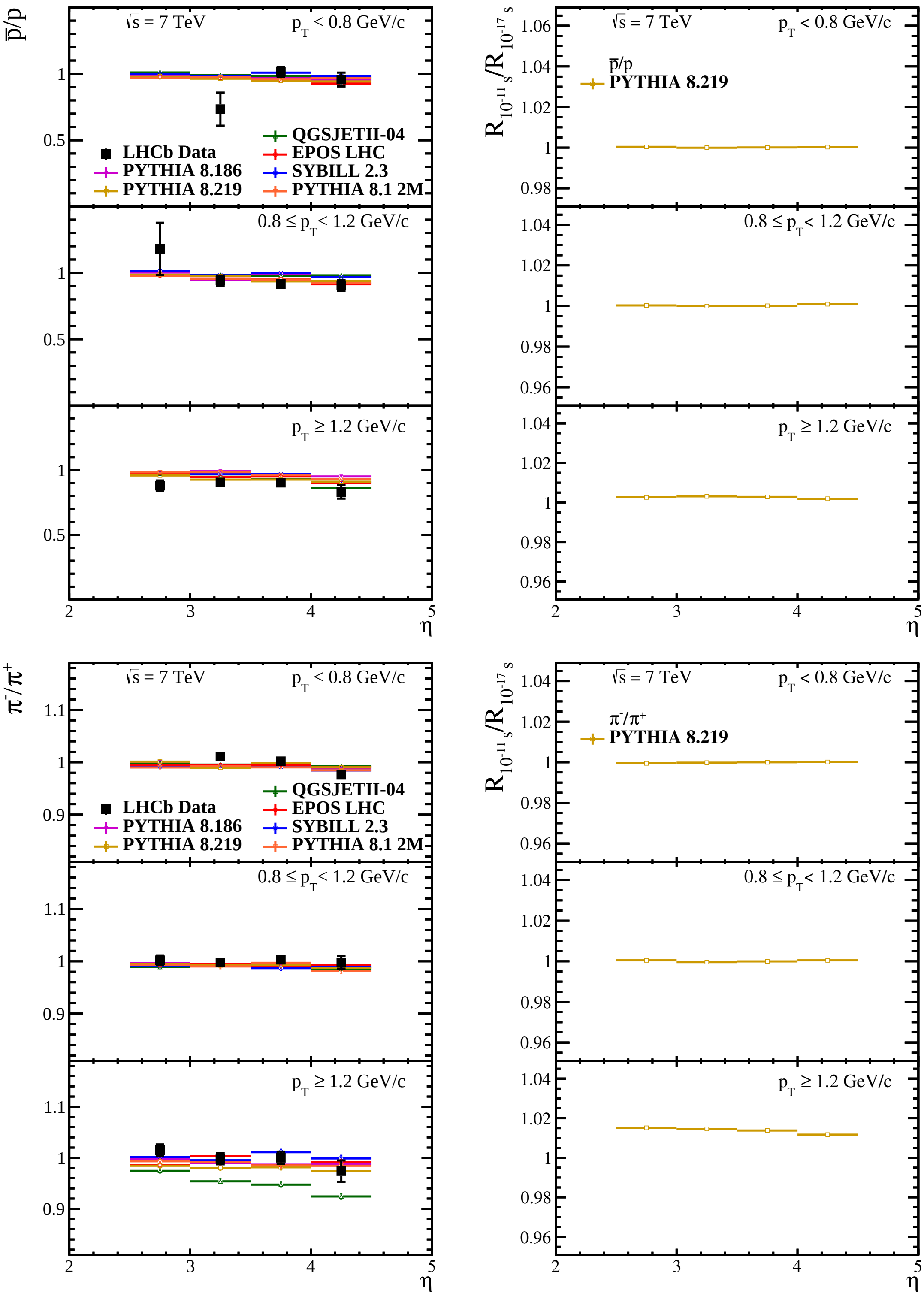

Figure 4.7: Production ratios of prompt charged hadrons with $p \geq 5$ GeV/c as a function of pseudorapidity in three p_T intervals in pp collisions at $\sqrt{s} = 7$ TeV (left). The total (quadratic sum of statistical and systematic) uncertainties of the measurements and the statistical uncertainties of the predictions are represented using vertical bars. Measurements from [14]. Plots published in [16]. The ratios between the values of PYTHIA 8.219 using $\tau_{\text{ancestors}} \leq 10^{-11}$ s and 10^{-17} s are also shown (right).

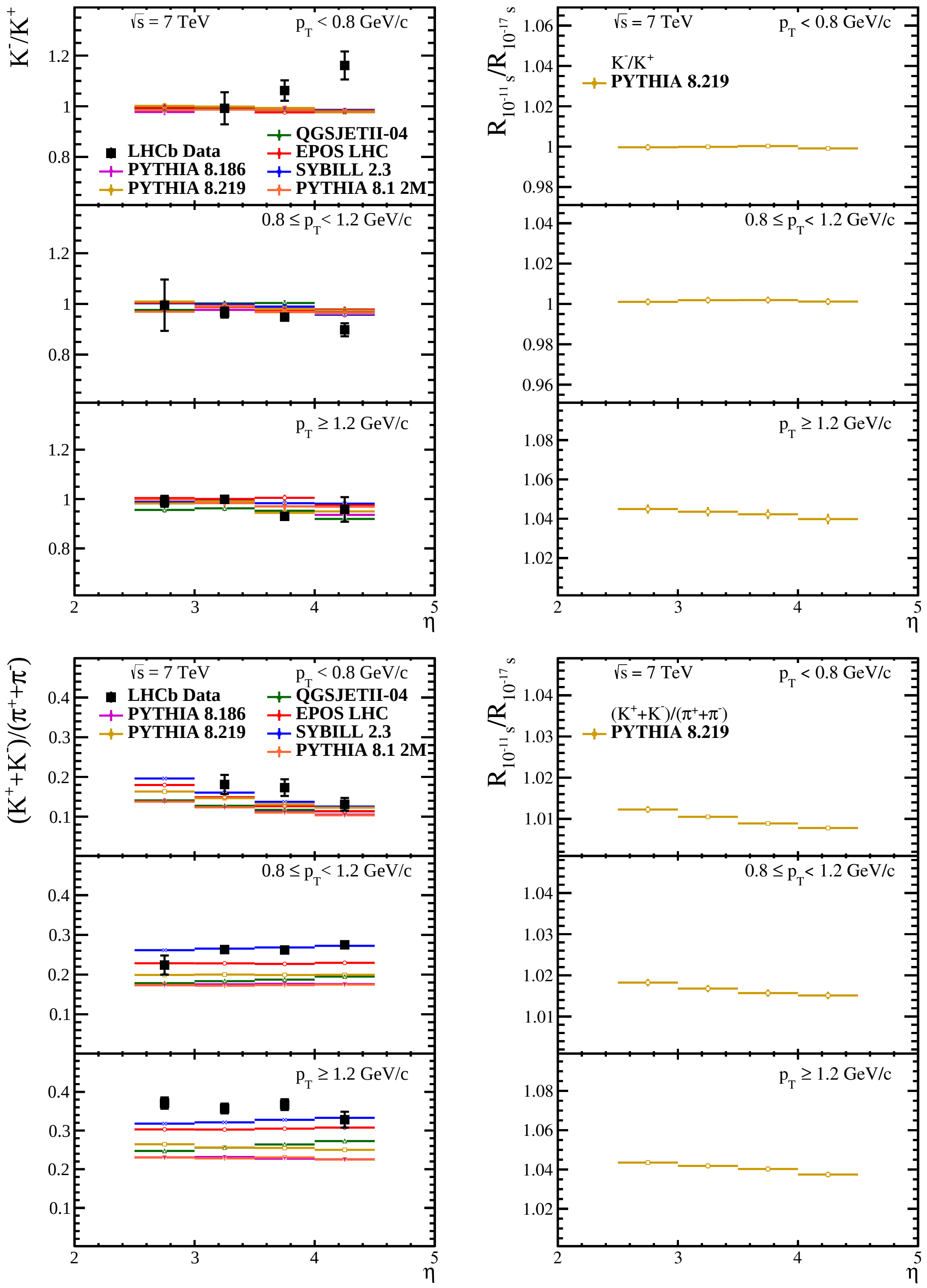

Figure 4.8: Production ratios of prompt charged hadrons with $p \geq 5$ GeV/c as a function of pseudorapidity in three p_T intervals in pp collisions at $\sqrt{s} = 7$ TeV (left). The total (quadratic sum of statistical and systematic) uncertainties of the measurements and the statistical uncertainties of the predictions are represented using vertical bars. Measurements from [14]. Plots published in [16]. The ratios between the values of PYTHIA 8.219 using $\tau_{\text{ancestors}} \leq 10^{-11}$ s and 10^{-17} s are also shown (right).

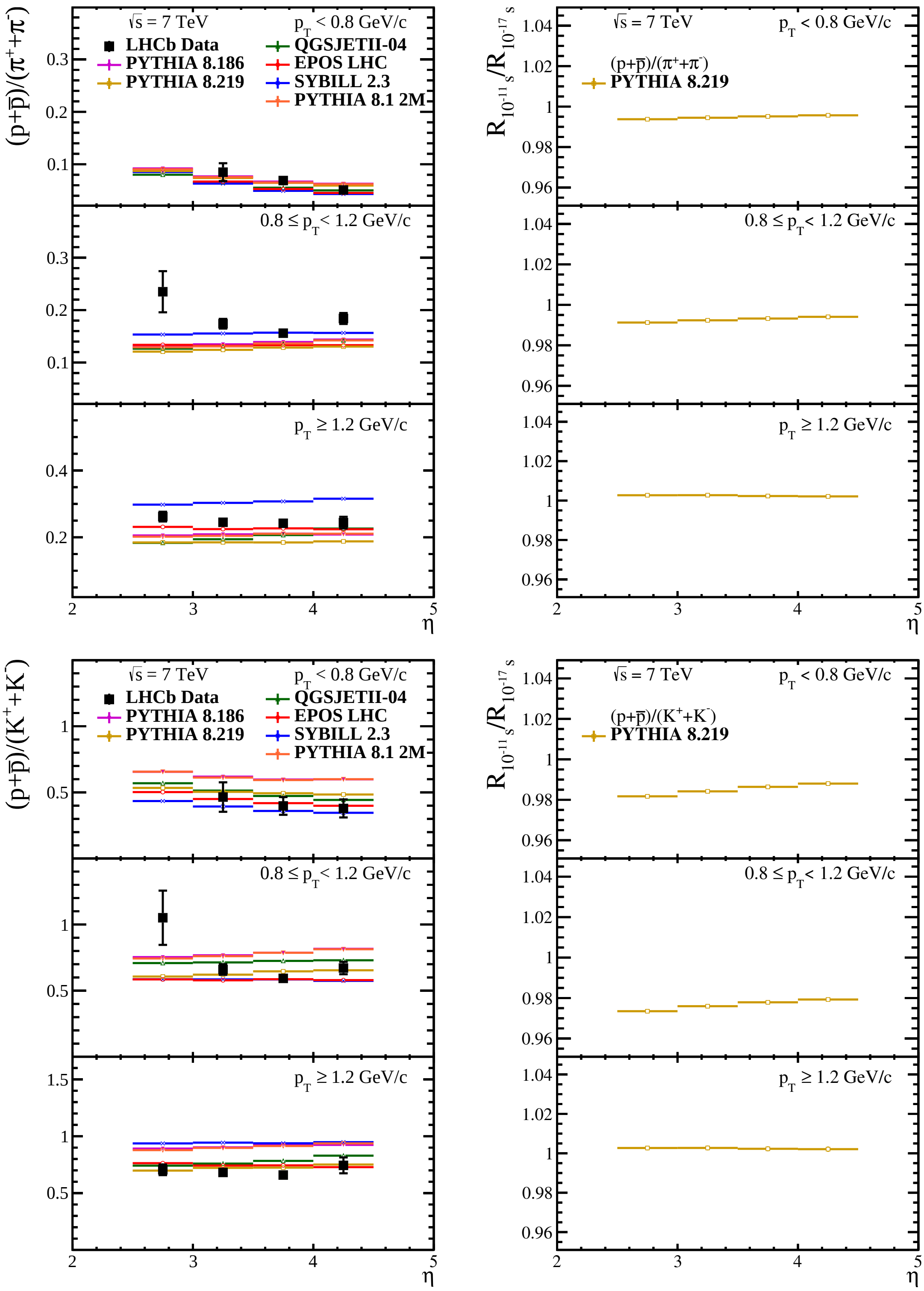

Figure 4.9: Production ratios of prompt charged hadrons with $p \geq 5$ GeV/c as a function of pseudorapidity in three p_T intervals in pp collisions at $\sqrt{s} = 7$ TeV (left). The total (quadratic sum of statistical and systematic) uncertainties of the measurements and the statistical uncertainties of the predictions are represented using vertical bars. Measurements from [14]. Plots published in [16]. The ratios between the values of PYTHIA 8.219 using $\tau_{\text{ancestors}} \leq 10^{-11}$ s and 10^{-17} s are also shown (right).

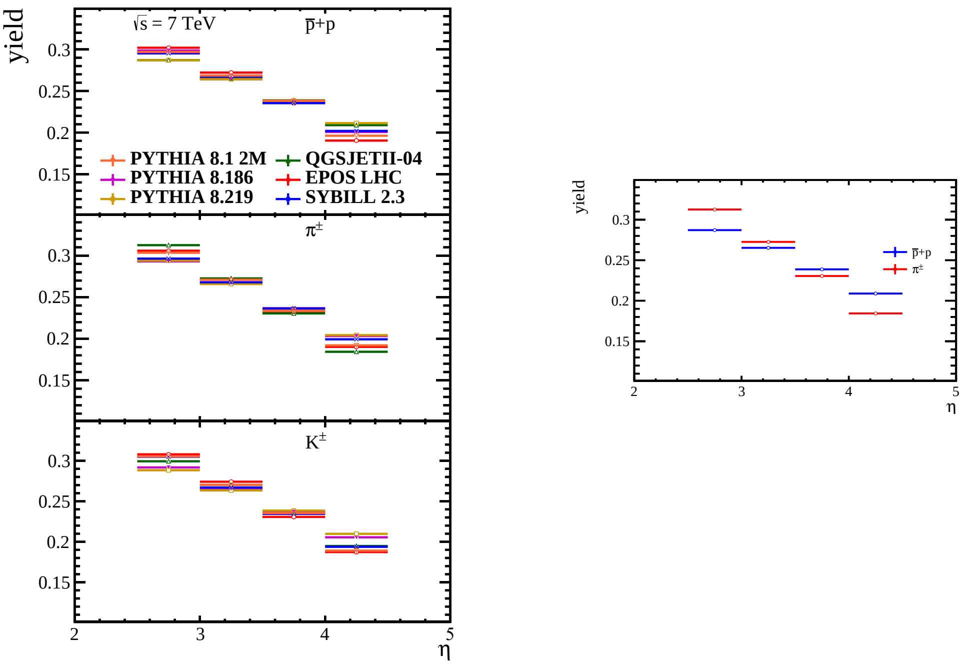

Figure 4.10: Normalized (to unity) yields of charged hadrons with $p \geq 5$ GeV/c in the $p_T \geq 1.2$ GeV/c region. The plot on the right shows the predictions of QGSJETII-04 for protons and pions. Plots published in [16].

The $\overline{\Lambda}/\Lambda$ and $\overline{\Lambda}/K^0_S$ production ratios as a function of rapidity and transverse momentum are shown in Figures 4.11-4.14.

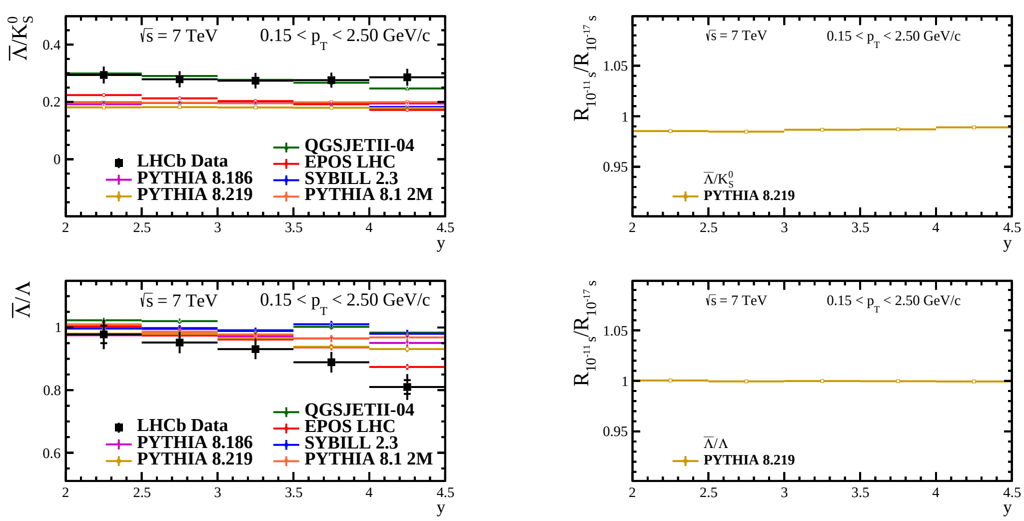

Figure 4.11: Production ratios of prompt V^0 hadrons as a function of rapidity in pp collisions at $\sqrt{s} = 7$ TeV (left). The vertical and small horizontal bars of the LHCb data points show the total and statistical uncertainties, respectively. The MC vertical bars represent the statistical uncertainties. Measurements from [15]. Plots published in [16]. The ratios between the values of PYTHIA 8.219 using $\tau_{\text{ancestors}} \leq 10^{-11}$ s and 10^{-17} s are also shown (right).

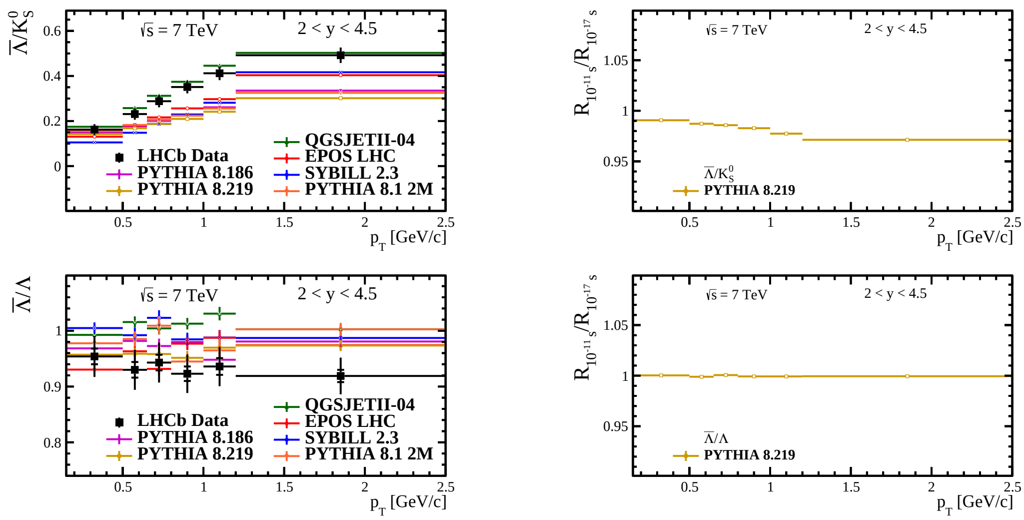

Figure 4.12: Production ratios of prompt V^0 hadrons as a function of p_T in pp collisions at $\sqrt{s} = 7$ TeV (left). The vertical and small horizontal bars of the LHCb data points show the total and statistical uncertainties, respectively. The statistical uncertainties of the predictions are shown using vertical bars. Measurements from [15]. Plots published in [16]. The ratios between the values of PYTHIA 8.219 using $\tau_{\text{ancestors}} \leq 10^{-11}$ s and 10^{-17} s are also shown (right).

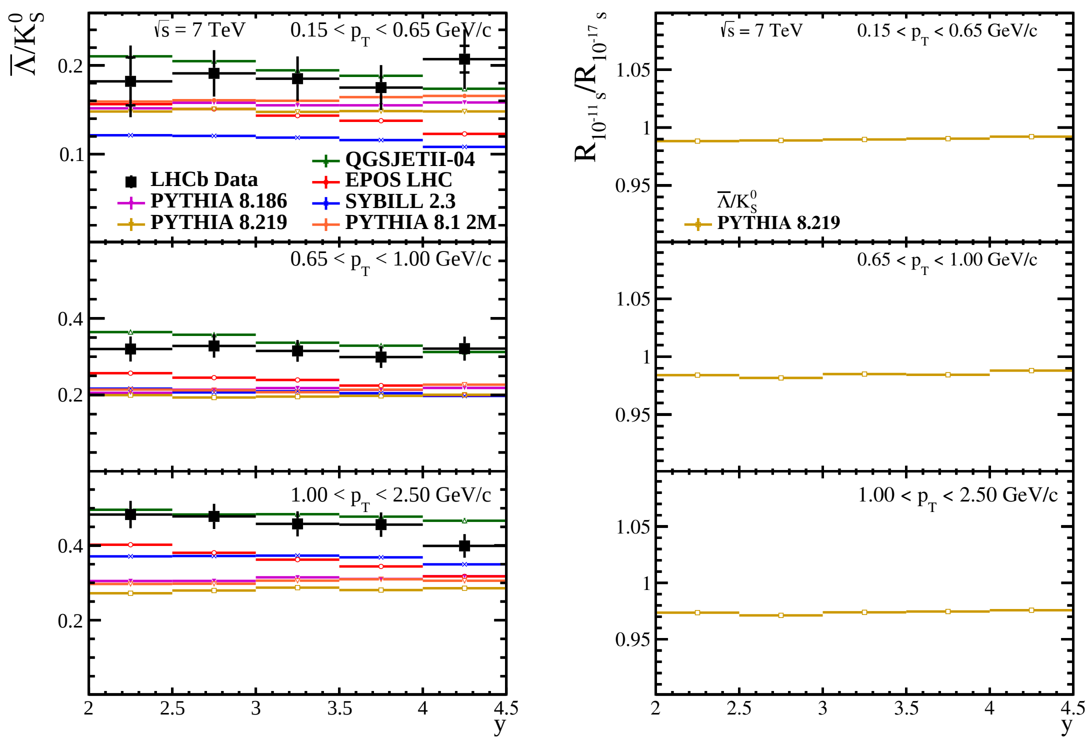

Figure 4.13: Production ratios of prompt V^0 hadrons as a function of rapidity in three p_T intervals in pp collisions at $\sqrt{s} = 7$ TeV (left). The vertical and small horizontal bars of the LHCb data points show the total and statistical uncertainties, respectively. The statistical uncertainties of the predictions are shown using vertical bars. Measurements from [15]. Plots published in [16]. The ratios between the values of PYTHIA 8.219 using $\tau_{\text{ancestors}} \leq 10^{-11}$ s and 10^{-17} s are also shown (right).

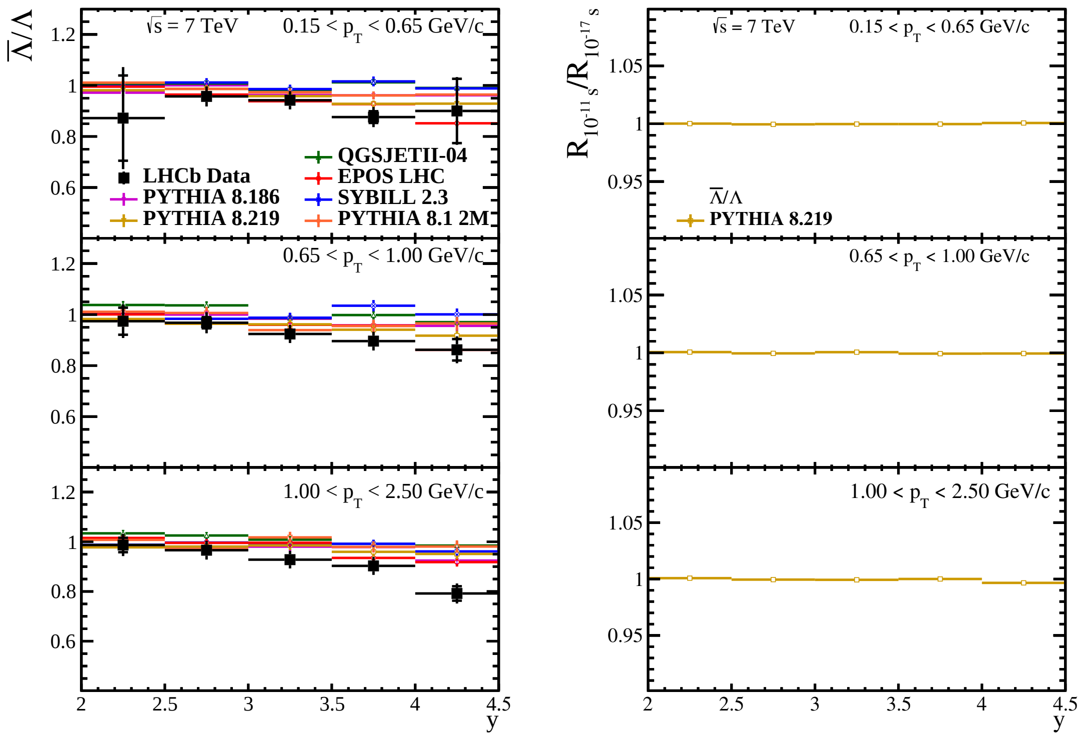

Figure 4.14: Production ratios of prompt V^0 hadrons as a function of rapidity in three p_T intervals in pp collisions at $\sqrt{s}$ = 7 TeV (left). The vertical and small horizontal bars of the LHCb data points show the total and statistical uncertainties, respectively. Measurements from [15]. Plots published in [16]. The ratios between the values of PYTHIA 8.219 using $\tau_{\text{ancestors}} \leq 10^{-11}$ s and 10^{-17} s are also shown (right).

QGSJETII-04 has an overall good description of the $\overline{\Lambda}/K^0_S$ production ratios and is the only one in this sense, as the other generators more or less underestimate the measurements. The closest predictions of the $\overline{\Lambda}/\Lambda$ ratios are the ones of EPOS LHC and PYTHIA 8.219, with both showing an overestimation trend towards high y and p_T, albeit to a smaller degree compared to the other generators [16]. Important to note is that the Y-shaped junction reconnection enhancement parameter from the PYTHIA CR model described in [68] is tuned to the Λ/K^0_S ratio as a function of rapidity in $0 \leq |y| \leq 2$ measured at CMS [68]. The effect in the forward region will be explored in a future study.

The promptness definition based on $\tau_{\text{ancestors}} \leq 10^{-11}$ instead of 10^{-17} induces no bias in the $\overline{p}/p$ and $\overline{\Lambda}/\Lambda$ ratios, and neither in the π^-/π^+ and K^-/K^+ ratios in the first two p_T intervals. In the high p_T interval, the ratios are increased by around 1-2% for π^-/π^+ and 4-5% for K^-/K^+. The increase in the case of the kaon/pion ratios rises from around 1% in the low p_T interval to around 4-5% in the highest p_T one. The proton/pion and proton/kaon ratios are decreased by around 1% and 3%, respectively, in the first two p_T intervals, while the effect in the highest p_T interval is negligible. The drop in the $\overline{\Lambda}/K^0_S$ ratios increases with transverse momentum from around 1% to around 3%. These differences do not induce significant changes in the interpretation of the plots.

4.5 Conclusions

The predictions of recent LHC tuned versions of the generators PYTHIA, EPOS, QGJSET, and SIBYLL for observables in the forward region, namely charged energy flow, charged hadron multiplicities and densities, and charged hadron and V^0 production ratios, have been studied. The versions of the generators are PYTHIA 8.186 with tune 4C and 8.219 with the Monash 2013 tune, EPOS LHC, QGSJETII-04 and SIBYLL 2.3. It was found that no generator correctly describes all of the measurements. The charged energy flow is best described by SIBYLL 2.3 and the next best description is the one PYTHIA 8.186, which is similar to the former in the case of the diffractive event class, but overestimates the measurements for the other event classes. The charged hadron pseudorapidity densities are generally well described by PYTHIA, while EPOS LHC shows a slightly worse overall description towards high η. QGJSETII-04 has a similar description to the previous ones for minimum bias events, but underestimates the measurements for "hard" events. Large underestimations are observed in the case of SIBYLL 2.3. The description of the multiplicity distributions is in general not good, with a few notable exceptions, namely the predictions of EPOS LHC and PYTHIA for minimum bias events. Again, the descriptions furthest from the measurements are the ones of SIBYLL 2.3. The charged hadron/antihadron ratios are generally well described by all generators, the predictions of which cluster together. The kaon/pion ratios are best described by SIBYLL 2.3, which also has a reasonably good description of the proton/pion and proton/kaon ratios at low and mid p_T. The best predictions for the proton/kaon ratios seem to be the ones of EPOS LHC, but those of PYTHIA 8.219 and QGSJETII-04 are close too. The closest predictions of the $\overline{\Lambda}/\Lambda$ ratios are those of EPOS LHC, followed by the ones of PYTHIA 8.219. QGSJETII-04 has a notably good description of the $\overline{\Lambda}/K^0_S$ ratios, while all the other generators underestimate the measurements [16].

In general, the tuning procedures which involved mostly "central" region measurements lead to better predictions even in the "forward" region. Nonetheless, specific tuning of the parameters using "forward" measurements like those from the LHCb and TOTEM experiments is required to further improve the predictions [16].

Prompt V^0 production cross-sections and ratios measured at LHCb in pp collisions at $\sqrt{s} = 13$ TeV

5.1 Introduction and motivation

In this chapter, preliminary results of the prompt V^0 production cross-sections and ratios in pp collisions at $\sqrt{s} = 13$ TeV measurements at the LHCb experiment are given, along with a detailed description of the analysis method. As discussed in Sections 2.7 and 2.8, the Monte Carlo event generators have many free parameters relating to hadronization, in which light quarks, namely u, d, and s, are produced in the vast majority of cases. The K_S^0 meson is a mixture of $d\bar{s}$ and $s\bar{d}$ flavour states, while the Λ^0 baryon is an uds state, so their production is sensitive to the strange quark suppression from the Lund string fragmentation model. The production of the latter depends also on baryon production parameters like the diquark suppression. The protons from the beams are uud states, so a surplus of states with positive baryon numbers containing u and d quarks is expected at high rapidities. Consequently, the $\overline{\Lambda^0}/\Lambda^0$ ratio as a function of y will be a measure of the net baryon number transport. In the case of the $\overline{\Lambda^0}/K_S^0$ ratio, the effect of the strange quark suppression approximately cancels out, so it is strongly correlated with the baryon-to-meson suppression parameter [15, 18]. Thus, the cross-sections and ratios measured in this analysis provide reference values for validation or tuning of several parameters of the Monte Carlo event generators.

5.2 Samples

The data samples used in this analysis are obtained from no bias data collected at LHCb in mid-2015, the "early measurements" period of Run II, in pp collisions from leading bunch crossings at $\sqrt{s} = 13$ TeV with a bunch spacing of 50 ns. The "no bias" term comes from the fact that the events to be recorded are randomly selected in an L0 triggering procedure which maximises their number. The leading bunch crossings are selected in the HLT stage and are defined as crossings in which a bunch from one beam meets a bunch from the other beam at the interaction point, given that in the previous two crossings this was not the case [154, 155]. The integrated luminosities of the data sets are taken from [155, 156] and are given in Table 5.1. The MC samples correspond to around 10 million events for each magnet polarity and are obtained using simulation version Sim09b. The collisions are generated using the LHCb tune of PYTHIA 8 with an average number of pp collisions per bunch crossing of $\nu = 1.6$. Both experimental and simulated data samples use the Reco15em reconstruction version. The samples are reffered to as MD (magnet down) and MU (magnet up) according to the orientation of the magnet field during data-taking [154, 155, 157]. The nominal samples used for various studies in this analysis are the MD ones and all plots or results are obtained from these, unless otherwise stated.

Besides the PV reconstruction cuts given in Section 3.6.3, the following reconstruction cuts are implemented:

- End vertex fit quality: $\chi^2_{\text{END\_VERTEX}} < 9$;
- Track fit quality: $\chi^2_{\text{Track}}/\text{NDOF} < 3$;
- A minimum of one PV is reconstructed.

Table 5.1: Data sets and integrated luminosities used in the analysis [155, 156].

Magnet polarity	Run	$\mathcal{L}[\mu b^{-1}]$	$d\mathcal{L}$
MD	157 577	206.2	4.0%
	157 588	233.1	3.9%
	157 697	287.4	3.9%
	157 702	117.4	3.9%
	157 706	285.5	3.9%
	157 805	135.5	3.9%
	157 809	226.3	3.9%
	157 815	226.2	3.9%
	Total	1 717.6	3.9%
MU	158 517	206.0	3.9%
	159 978	1 658,8	4.0%
	Total	1 864.8	4.0%

5.3 MC "truth" information

The Monte Carlo samples contain MC "truth" information like, for example, the "true" identity and momentum of the particles. The "true" designation refers to the values of the generated particles associated with the reconstructed ones. The Particle Data Group (PDG) has developed a scheme for translating the identity of particles into a series of digits for use with MC event generators or high energy physics data formats [24, 58]. Positive and negative numbers are assigned to particles and antiparticles, respectively. The quarks are numbered from 1 to 6 in increasing order of their masses. Mesons (baryons) are identified with a series of 3 (4) digits, with the first 2 (3) digits representing the quark content. The last digit is $n_J = 2J + 1$, where J is the hadron's spin. The scheme is described in detail in [24]. The "true" identities are stored for particles at several levels of the ancestry chain. Examples of "true" identity codes relevant for this analysis are given in Table 5.2. If the matching to a single generated particle failed, like in the case of "ghost" tracks, the identity is set to 0.

Table 5.2: Examples of identity codes.

Identity code	Particle
310	K_S^0
$\pm$3122	$\Lambda^0/\overline{\Lambda^0}$
$\pm$2112	$p/\overline{p}$
$\pm$211	π^+/π^-
0	details in text

5.4 Selection cuts

The selection of the V^0 candidates is inspired from several previous LHCb analyses like, for example, [158, 159]. Only long tracks are considered for this analysis. A V^0 candidate is formed if two long tracks which originate from the same vertex have an invariant mass in the $\pm$ 50 MeV/c^2 range around the values reported by the PDG (Particle Data Group) [24], when the mass hypothesis of the V^0 daughter particles is assigned to the respective tracks:

$$M_{V^0} = \sqrt{\left(\sqrt{p_1^2 + m_1^2} + \sqrt{p_2^2 + m_2^2}\right)^2 - (\vec{p_1} + \vec{p_2})^2} = M_{\mathrm{PDG}} \pm 50\ \mathrm{MeV/c^2}, \quad (5.1)$$

where M_{V^0} is the mass of the candidate, $p_{1,2}$ are the momenta of the tracks, $m_{1,2}$ are the masses of the daughters of the respective V^0 particle from the following decays:

$$\begin{aligned} K_S^0 &\to \pi^+\pi^-, \\ \Lambda^0 &\to p\pi^-, \\ \overline{\Lambda^0} &\to \overline{p}\pi^+. \end{aligned} \quad (5.2)$$

The mass range defined above is motivated by the presence of reconstruction effects which significantly widen the mass distributions of the V^0 hadrons.

The prompt signal candidates are defined as originating from the PV or from electromagnetic or strong decays of particles produced in the collision, which translates into a value of the sum of the lifetimes of their ancestors of $\tau_{\text{ancestors}} \leq 10^{-16}$ s. The non-prompt candidates have weakly decaying b, c or s hadrons in their ancestor chain or are produced in strong interactions of particles with the detector material [159].

The following selection cuts have been applied for the V^0 candidates:

- $\chi^2_{\text{IP}} < 100$ - This cut is rather loose, but it significantly improves the signal to background ratio, eliminating combinatorial background and non-prompt candidates. The effect of the cut can be seen in Figure 5.1, in which the distributions of $\ln(\chi^2_{\text{IP}})$ from the MC samples for prompt and non-prompt signal, as well as background candidates are shown. The contamination from the other V^0 species is also shown. The distributions of $\ln(\chi^2_{\text{IP}})$ from both the data and MC samples are shown in Figure 5.2.

- Decay in the forward region: $z_{\mathrm{PV}} < z_{\mathrm{dec}}$, where z_{PV} is the z coordinate of the primary vertex from which the candidate originated and z_{dec} is the z coordinate of the decay vertex of the candidate. The cut is very efficient in eliminating combinatorial background [158]. As a consequnce of the use of long tracks combined with the detector geometry, the momentum of a signal V^0 candidate points towards $+z$ and thus, $z_{\mathrm{PV}} < z_{\mathrm{dec}}$. The distributions of z_{PV}, z_{dec}, $z_{\mathrm{dec}} - z_{\mathrm{PV}}$, and N_{PV}, the number of reconstructed PVs, are shown in Figures 5.2-5.6 and their means are given in Table 5.3. The MC distributions are normalized to the ones from data. It can be clearly seen in Figure 5.5 that the signal candidates fall in the positive region and that the cut removes a significant fraction of the combinatorial background. The peaking structures around 0 are due to prompt backgrounds, combinations of particles originating from the PV. The combinatorial background is selected using the "true" identity ID = 0 and contains a fraction of signal candidates as detailed in Section 5.7.

- Fisher discriminant: $\mathrm{FD} = (\mathrm{IP}_1 \cdot \mathrm{IP}_2)/\mathrm{IP}_0 > 10$, where IP_1, IP_2 and IP_0 are the impact parameters, measured in mm, of the daughter particles and the mother particle, respectively [158, 159]. It is very efficient at rejecting combinatorial background and non-prompt candidates [18, 159]. This specific value of the cut has been optimised for candidates from 0.9 TeV and 7 TeV collisions in [159]. It can be seen in Figure 5.7 that the cut is applicable to this analysis as well. Slight differences in the distributions for data and MC are observed. The samples are produced with a relaxed cut of FD > 8 to allow for the estimation of the systematic uncertainties due to the selection based on FD.

- The mass windows are further constrained to $450 \leq M_{K^0_S} \leq 545$ MeV/c^2 and $1095 \leq M_{\Lambda^0/\overline{\Lambda^0}} \leq 1135$ MeV/c^2.

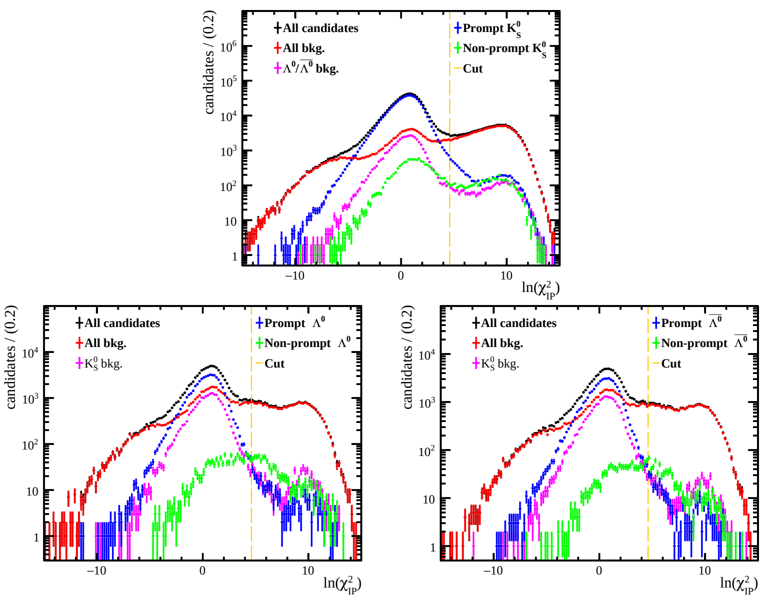

Figure 5.1: Distributions of $\ln\left(\chi^2_{\mathrm{IP}}\right)$ from the MC samples for different categories of signal and background candidates.

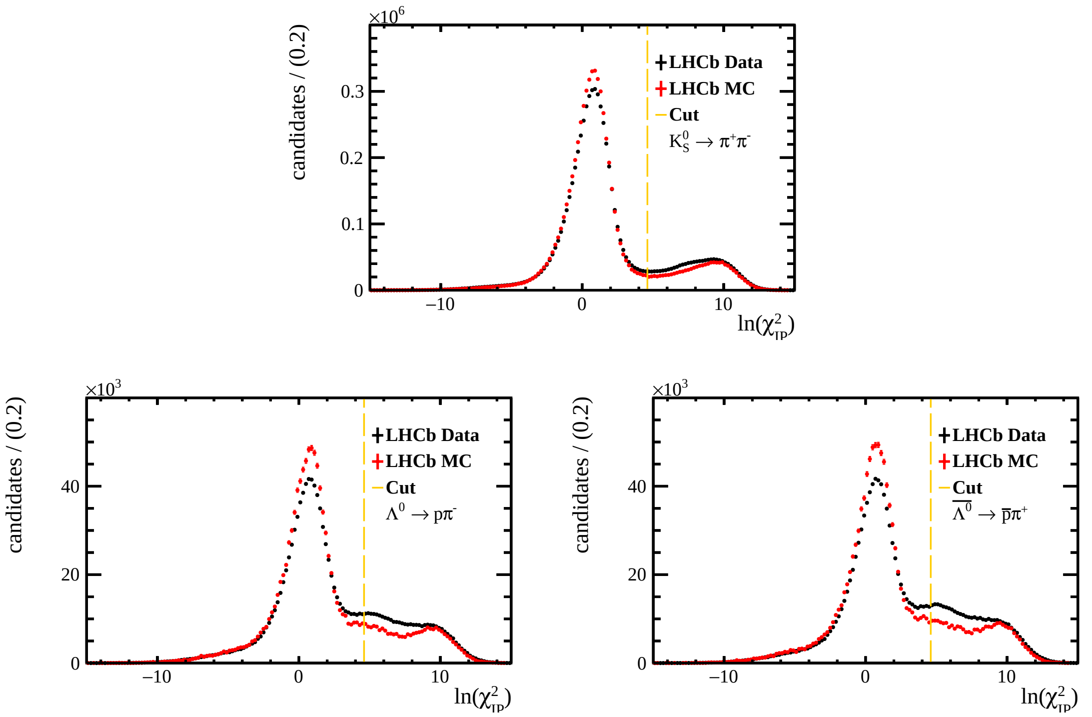

Figure 5.2: Distributions of $\ln\left(\chi^2_{\rm IP}\right)$ for data and MC.

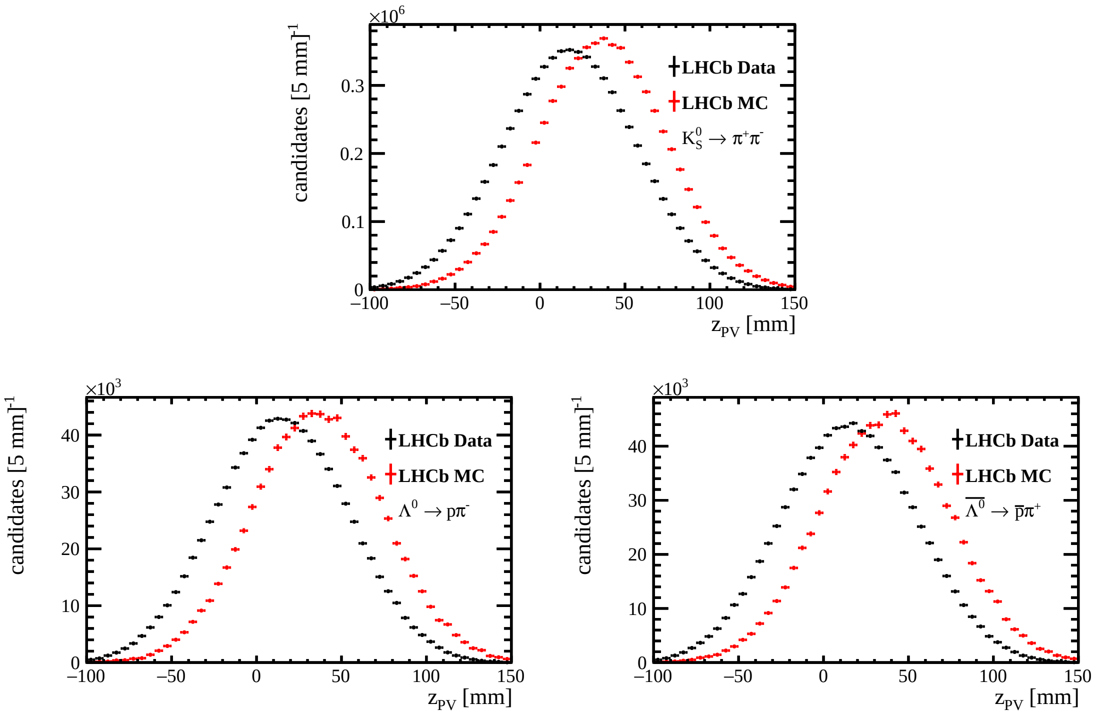

Figure 5.3: Distributions of $z_{\rm PV}$ for data and MC.

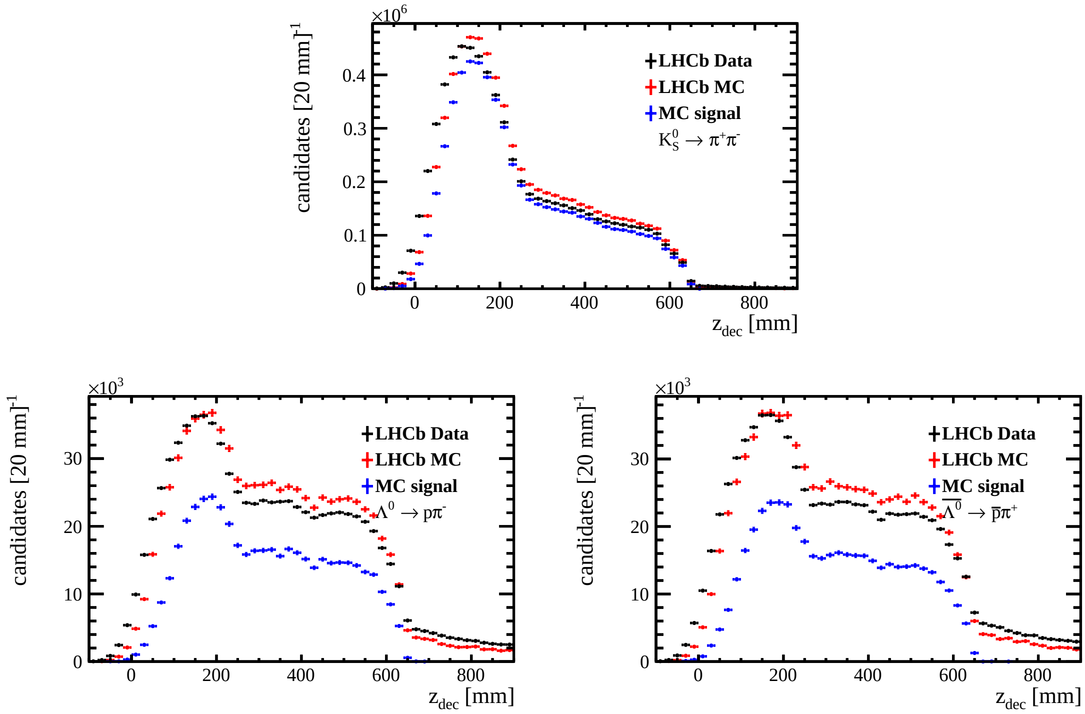

Figure 5.4: Distributions of z_{dec} for data and MC.

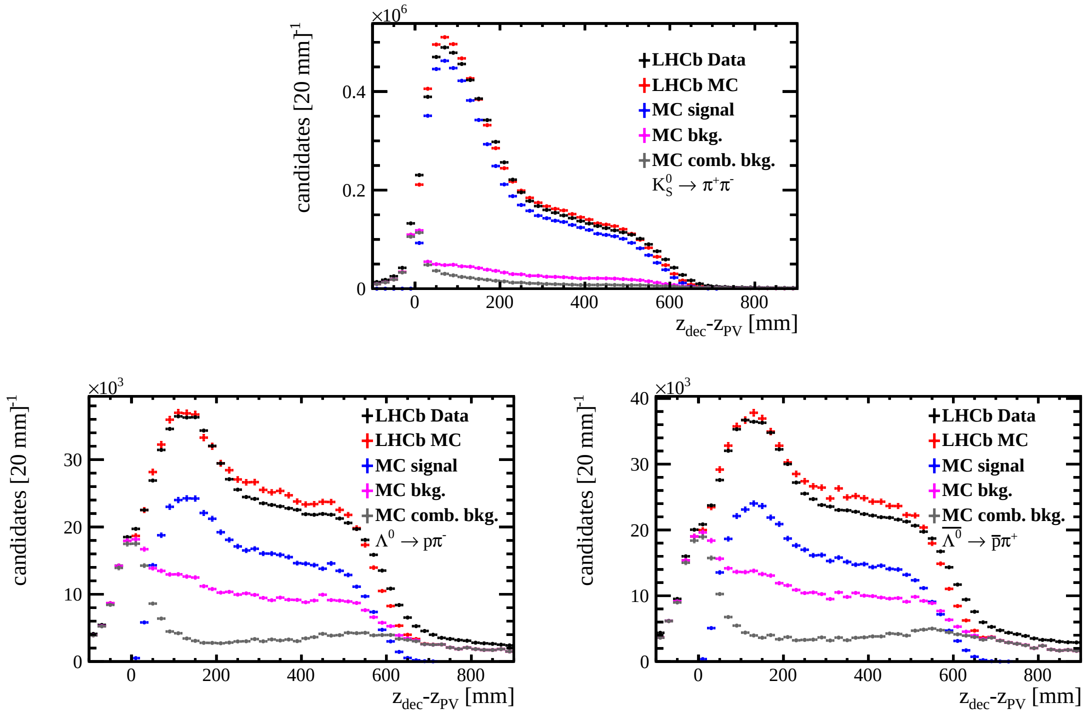

Figure 5.5: Distributions of $z_{\text{dec}} - z_{\text{PV}}$ for data and different categories of MC candidates.

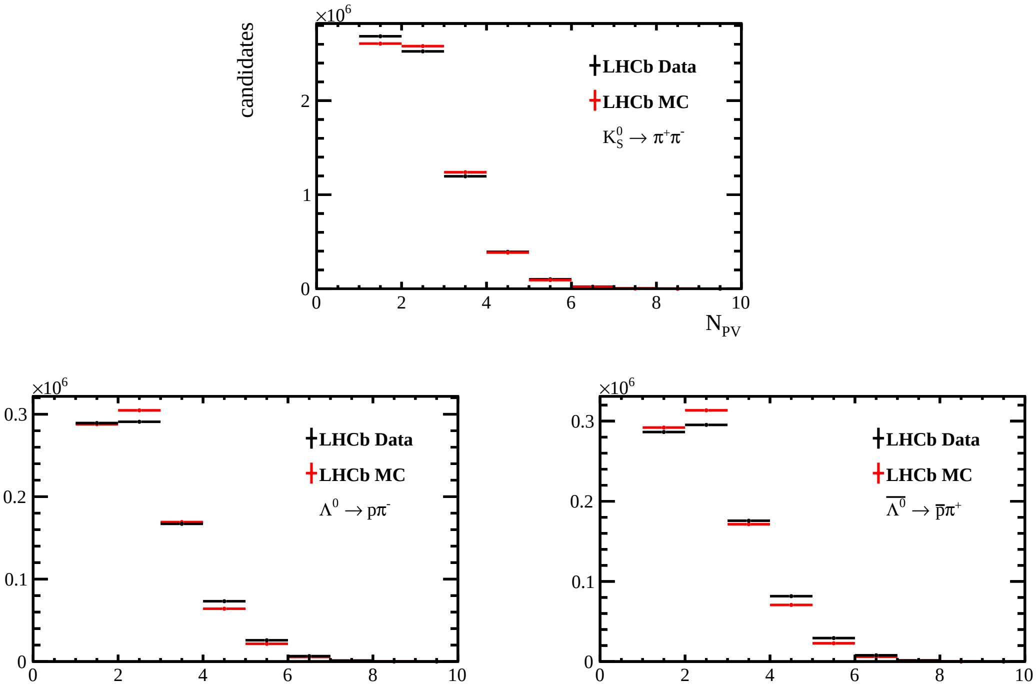

Figure 5.6: Distributions of N_{PV} for data and MC.

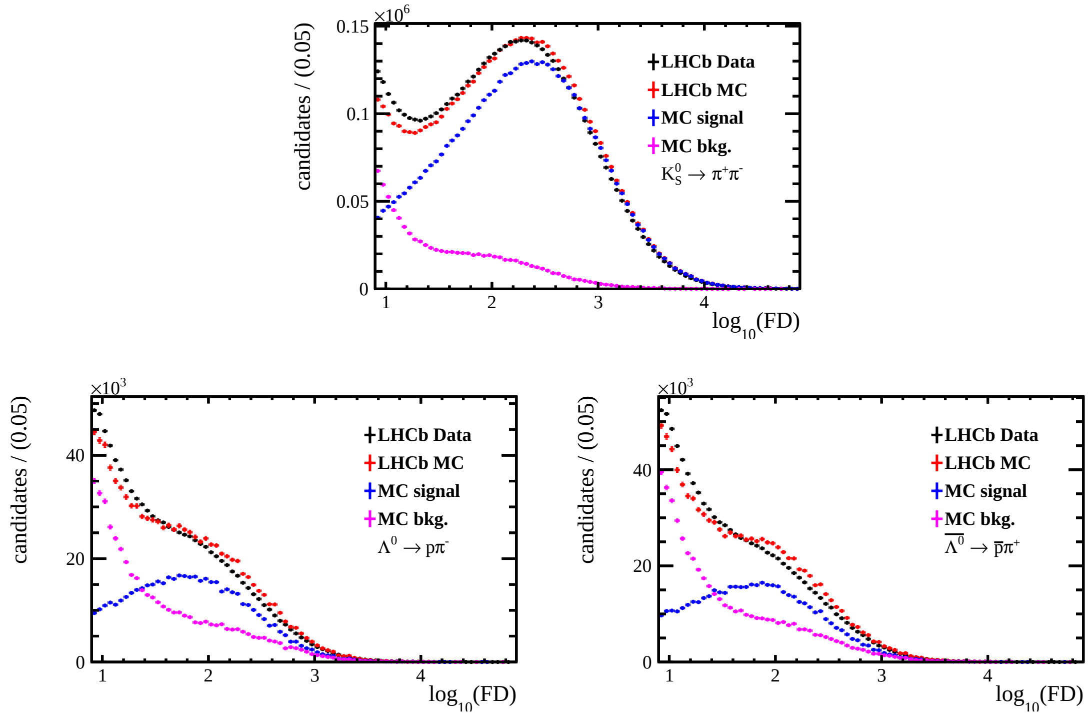

Figure 5.7: Distributions of $\log_{10}(\mathrm{FD})$ for data and MC. The signal and background distributions from MC are also shown.

Table 5.3: Mean values of different distributions.

Candidates	Sample	z_{PV} [mm]	z_{dec} [mm]	$z_{\mathrm{dec}} - z_{\mathrm{PV}}$ [mm]	N_{PV}
K_S^0	Data	17.535	234.559	209.364	1.957
	MC	36.417	249.528	206.948	1.966
Λ^0	Data	15.167	319.184	285.206	2.159
	MC	36.164	327.272	274.288	2.121
$\overline{\Lambda^0}$	Data	15.244	323.348	287.740	2.205
	MC	36.163	330.053	275.972	2.137

5.5 Boost to the CM frame

As discussed in Section 3.5.4, the proton beams are collided at an angle. The crossing angles of the proton beams are $\theta = -395$ µrad and $\theta = -105$ µrad for magnet down and magnet up polarities, respectively [160]. The crossing angle is in the horizontal (xz) plane and is the angle between the beam and the z axis with the convention that if the beams are inclined in the $-x$ direction (towards the center of the LHC ring) the angle is negative (see Section 3.5.4) [114]. In order to facilitate the comparison with results from other experiments or at different collision energies, the kinematical variables are boosted from the LHCb frame to the center-of-momentum (CM) frame of reference. This procedure is inspired from [159, 161, 162].

As the energy of the beam particles $E_{beam} = 6.5$ TeV and the crossing angles are known:

$$p_{CM} = 2p_{beam} \sin\theta, \tag{5.3}$$

$$\beta_{CM} = \frac{p_{CM}}{E_{CM}} = \frac{2p_{beam}\sin\theta}{2E_{beam}} \approx \sin\theta, \tag{5.4}$$

where the variables with the "CM" subscript belong to the center-of-momentum of the beams in the LHCb frame of reference. Using the small angle approximation:

$$\beta_{CM} \approx \theta \Rightarrow \gamma_{CM} \approx 1. \tag{5.5}$$

The Lorentz transformations will be:

$$E^* = \gamma_{CM}E - \beta_{CM}\gamma_{CM}p_x \approx E - \theta p_x, \tag{5.6}$$

$$p_x^* = \gamma_{CM}p_x - \beta_{CM}\gamma_{CM}E \approx p_x - \theta E. \tag{5.7}$$

where the variables with and without the star superscript are in the CM and LHCb frames, respectively [159, 161, 162].

In the LHCb frame, particles will be produced preferentially in the direction of p_{CM}, namely the $-x$ direction. The azimuthal angle ϕ is defined in the xy plane and is the angle formed by the momentum of the particles with the x axis, with positive values in the positive y region [89]. Thus, particles will be preferentially produced towards $\pm\pi$ rad, while in the CM frame the distribution of ϕ should be flat [159]. This can be seen in Figure 5.8 in which the distributions of the azimuthal angle ϕ of generated prompt V^0 is shown in both the LHCb and CM frames of reference. From here on, all kinematic variables will be given in the CM frame, unless otherwise stated.

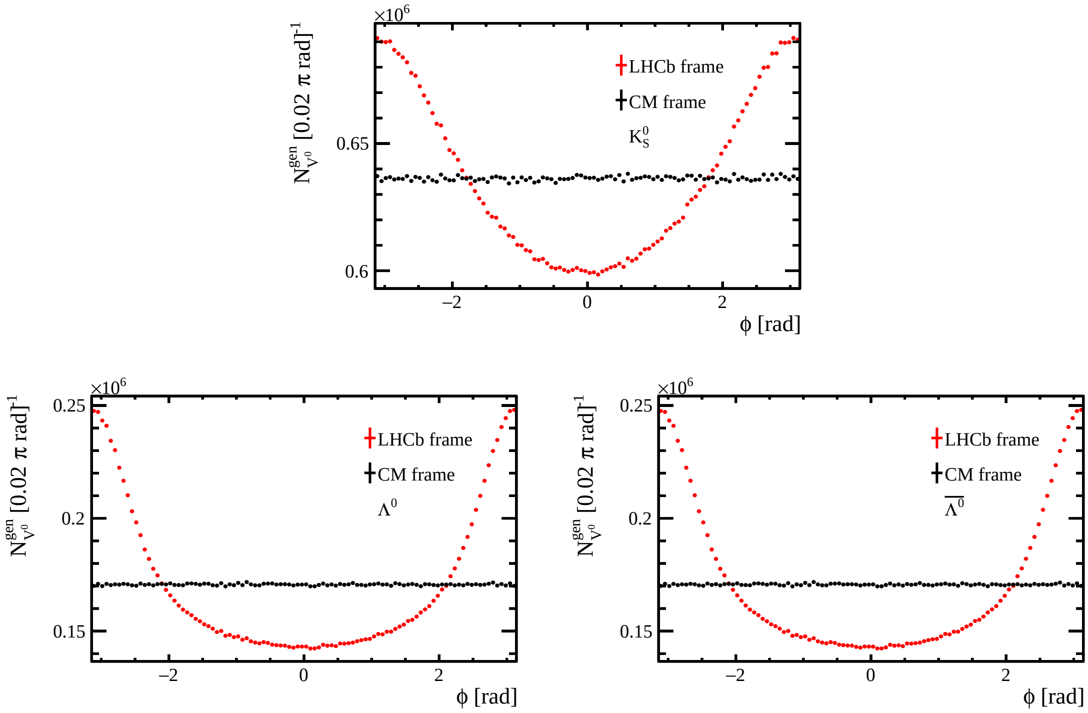

Figure 5.8: Distributions of ϕ for generated prompt V^0 in the LHCb and CM frames of reference.

5.6 Comparison of kinematic variables

The distributions of momentum, transverse momentum, rapidity, pseudorapidity and invariant mass for data and MC, normalized to the former, are given in Figures 5.9-5.14. All distributions are similar between data and MC, but slight differences are observed as detailed in the following.

The momentum distributions from data for K^0_S peak at around 8 GeV/c, while the spectra of $\Lambda^0/\overline{\Lambda^0}$ are harder and peak at around 14 GeV/c. The MC spectra are softer for all V^0 species, especially for K^0_S. The transverse momentum distributions from data peak at around 500 and 600 MeV/c for K^0_S and $\Lambda^0/\overline{\Lambda^0}$, respectively, with the spectra of the latter being harder. As was the case for momentum, the MC spectra are softer, more so for K^0_S. The rapidity distributions peak at around $y = 3.6$ and 3.4 for K^0_S and $\Lambda^0/\overline{\Lambda^0}$, respectively, and are reasonably well described by the MC. The pseudorapidity distributions have their peaks at around $\eta = 3.8$

and 4 for K_S^0 and $\Lambda^0/\overline{\Lambda^0}$, respectively, with the MC description being a bit worse than in the case of the rapidity distributions. As can be seen in the invariant mass plots, the signal to background ratio is a bit larger in MC than in data, which is expected.

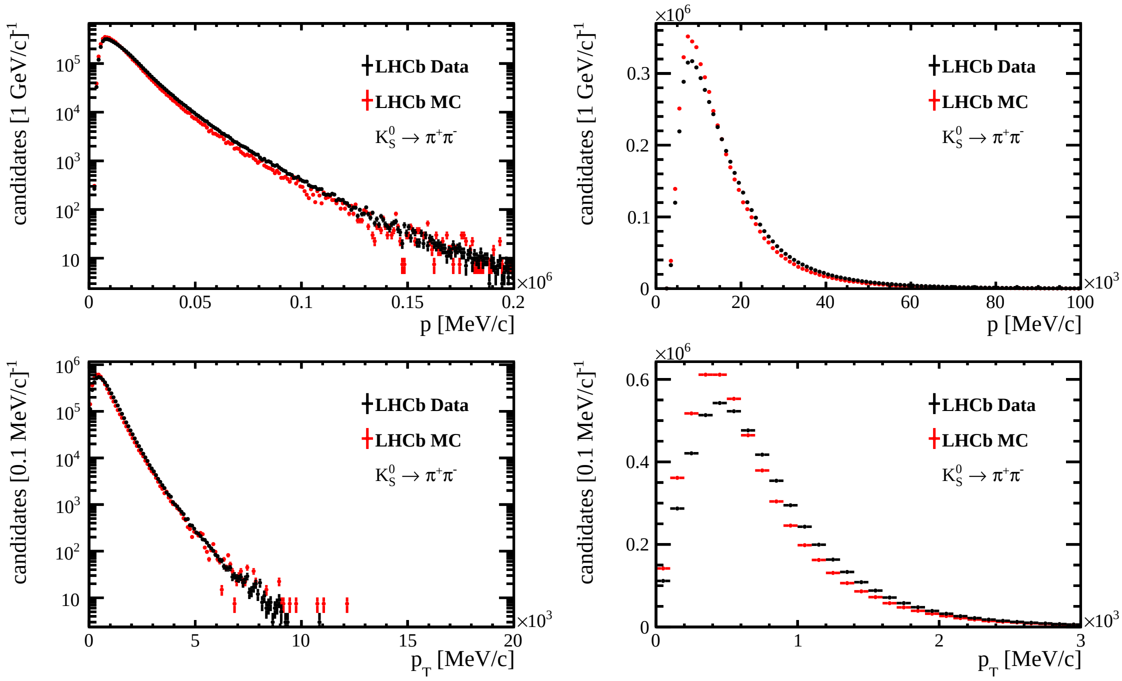

Figure 5.9: Distributions of momentum and transverse momentum for K_S^0 candidates.

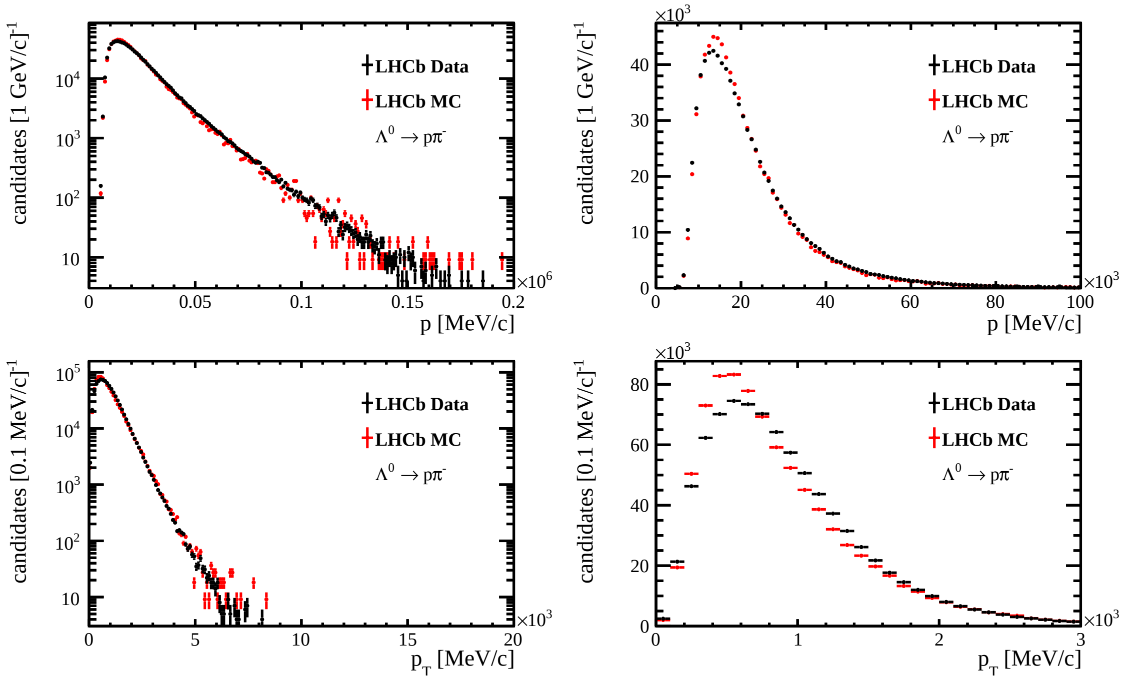

Figure 5.10: Distributions of momentum and transverse momentum for Λ^0 candidates.

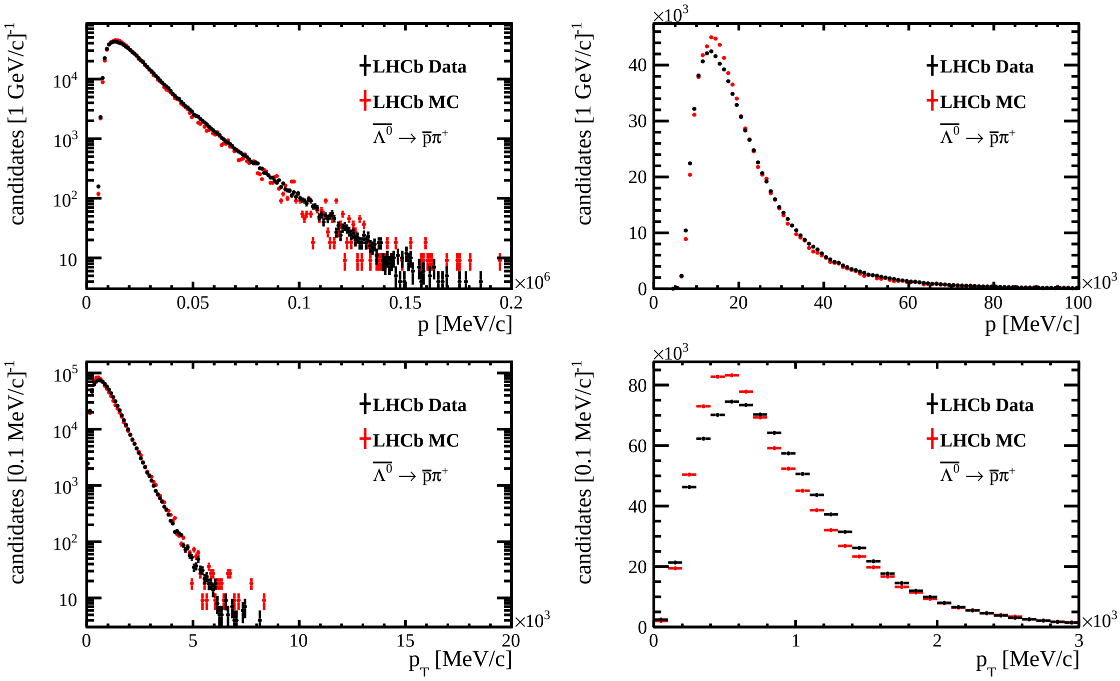

Figure 5.11: Distributions of momentum and transverse momentum for $\overline{\Lambda^0}$ candidates.

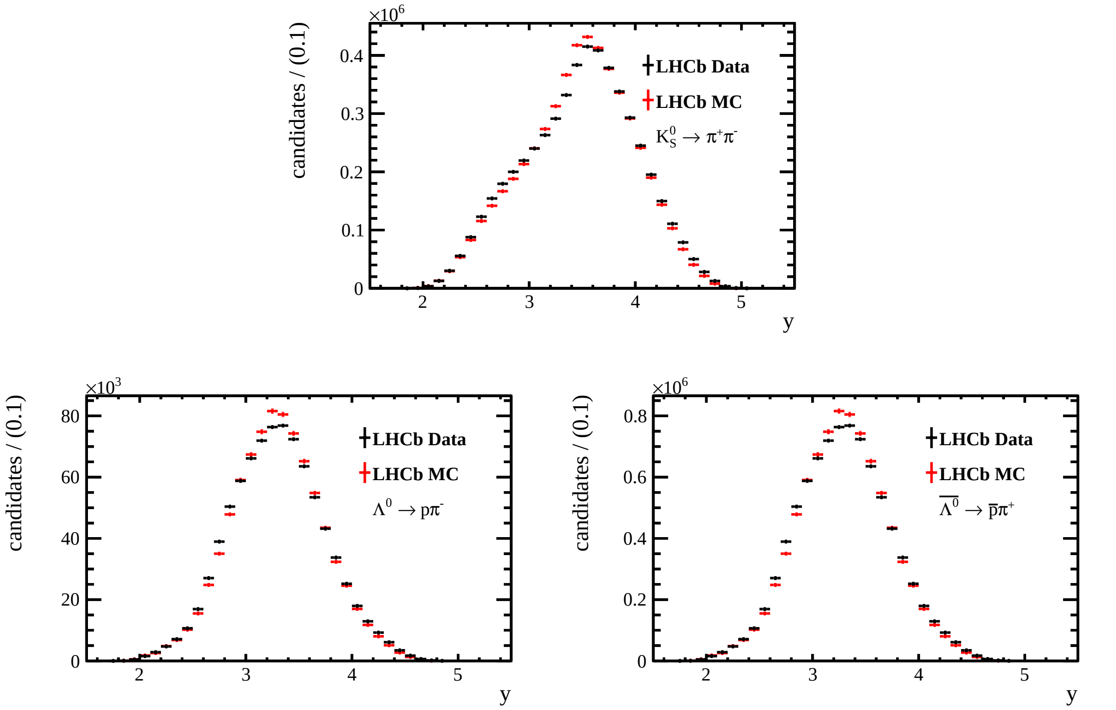

Figure 5.12: Distributions of rapidity for V^0 candidates.

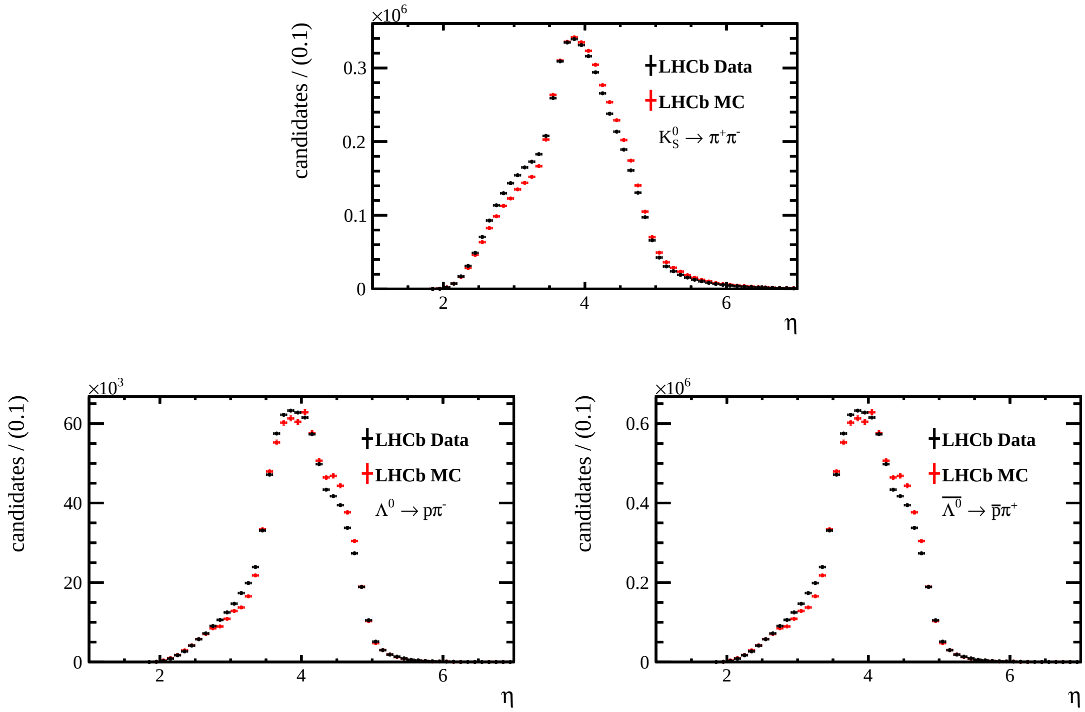

Figure 5.13: Distributions of pseudorapidity for V^0 candidates.

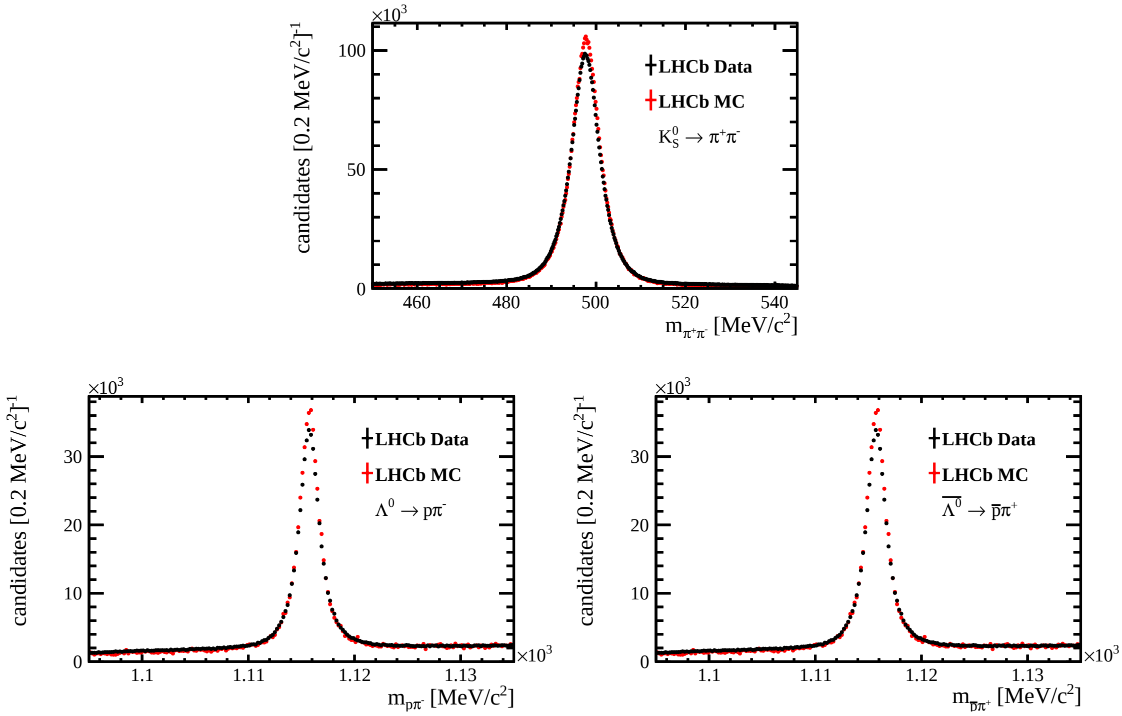

Figure 5.14: Distributions of invariant mass for V^0 candidates.

5.7 Background sources

The V^0 background sources have been studied using the "truth" information from MC. The following background categories have been defined:

- Contamination from other V^0 species.
- Contamination from other identified particles.
- Combinatorial background.

The selection of signal using the "true" identity ID = 310/ ± 3122 is not 100% efficient, as detailed in Section 5.8. For candidates formed from at least one "ghost" track, the identity ID = 0 is assigned. These candidates have a peaking mass distribution, as some "ghost" tracks may contain hits from daughters of the V^0 species of interest. The peaking has been found to come from combinations of "ghost" tracks with tracks that are identified as coming from a V^0. This type of candidates will be referred to as "ghost" signal. The mass distribution of candidates formed from two "ghost" tracks is not peaking (see Section 5.8), so the probability of both tracks to have sufficient hits and thus, momentum information, from V^0 daughters is very low. The candidates that are not associated with an identified particle or found by the "ghost" signal selection, form the combinatorial background. The invariant mass plots highlighting the different contributions are shown in Figures 5.15-5.17. It can be seen that the contamination from other V^0 species is comparable to the amount of combinatorial background. Important to note is that the shape of the background is consistent with a 2^{nd} or even higher order polynomial. The effect of the χ^2_{IP} cut is of eliminating a large fraction of the combinatorial background and almost the entire contamination from other identified particles.

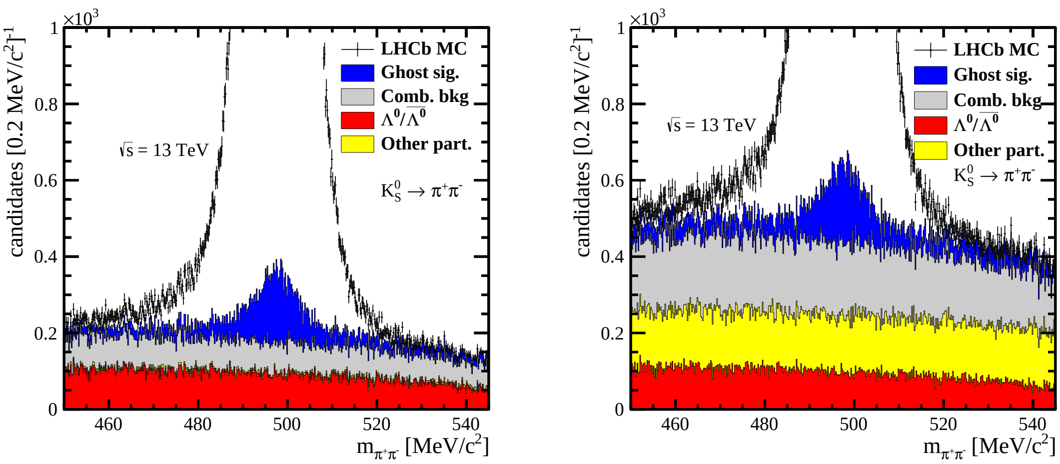

Figure 5.15: Invariant mass distributions for different categories of K^0_S candidates with (left) and without (right) the χ^2_{IP} cut.

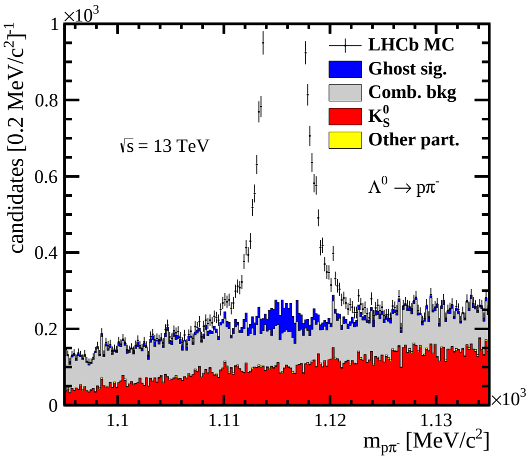

Figure 5.16: Invariant mass distributions for different categories of Λ^0 candidates with (left) and without (right) the χ^2_{IP} cut.

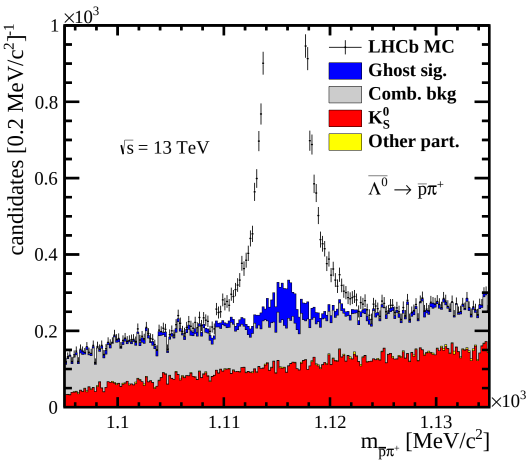

Figure 5.17: Invariant mass distributions for different categories of $\overline{\Lambda^0}$ candidates with (left) and without (right) the χ^2_{IP} cut.

The Armenteros-Podolanski plots are two-dimensional plots of the component of momentum of one daughter particle perpendicular to the V^0 candidates' momentum, q_T, versus the longitudinal momentum assymetry term $\alpha = (p_l^+ - p_l^-)/(p_l^+ + p_l^-)$, where p_l^+ and p_l^- are the components of momentum of the positive and negative daughter particles, respectively, parallel to the mother particle's momentum. In such plots, different ellipse arches are formed for each type of hadron, i.e. a broad central ellipse arch for K_S^0 and narrow ellipse arches to the right (positive α) and left (negative α) for Λ^0 and $\overline{\Lambda^0}$, respectively [18, 163]. The Armenteros-Podolanski plots for candidates in the full $M_{\text{PDG}} \pm 50$ MeV/c^2 range from an MC sample are shown in Figure 5.18, in which the cross-contamination of the V^0 candidates is clearly visible.

The transverse and longitudinal components of the daughter's momenta relative to the V^0's momentum are:

$$
\begin{aligned}
p_l^{\pm} &= p^{\pm}\cos\theta, \\
p_T^{\pm} &= p^{\pm}\sin\theta,
\end{aligned}
\tag{5.8}
$$

respectively, where $p^{\pm}$ is the daughter particle momentum and θ is the angle between the daughter and mother particles momenta. By using the properties of scalar and vector products:

$$
\begin{aligned}
P \cdot p^{\pm} = |P||p^{\pm}|\cos\theta \Rightarrow \cos\theta = \frac{P \cdot p^{\pm}}{|P||p^{\pm}|} \Rightarrow p_l^{\pm} = \frac{P \cdot p^{\pm}}{|P|}, \\
P \times p^{\pm} = |P||p^{\pm}|\sin\theta \Rightarrow \sin\theta = \frac{P \times p^{\pm}}{|P||p^{\pm}|} \Rightarrow p_T^{\pm} = \frac{P \times p^{\pm}}{|P|},
\end{aligned}
\tag{5.9}
$$

where P is the V^0's momentum.

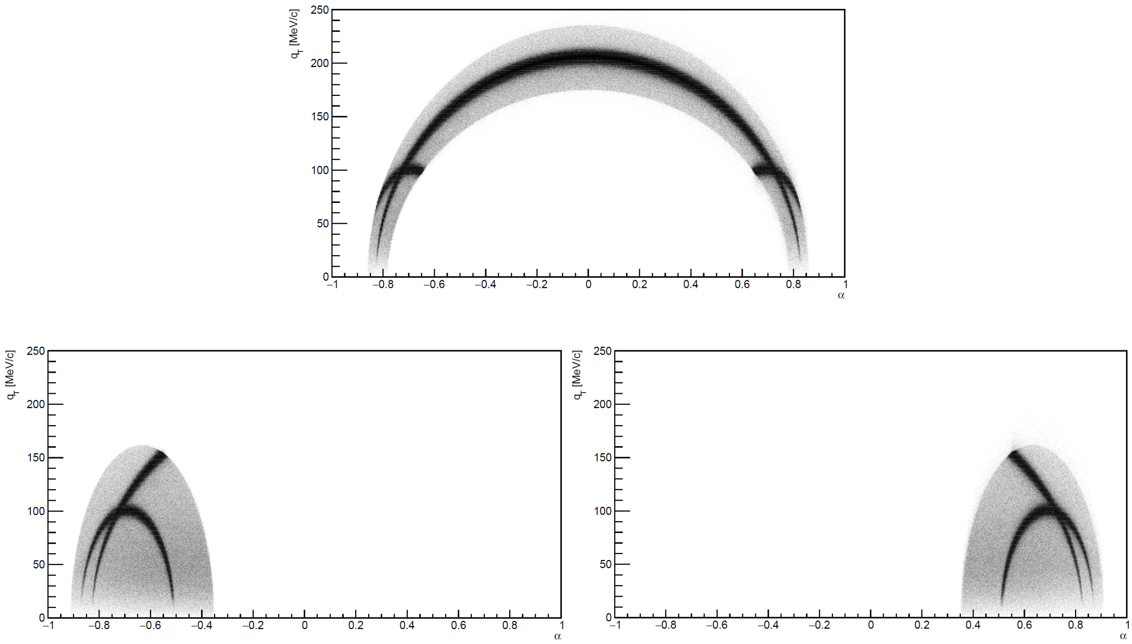

Figure 5.18: Armenteros-Podolanski plots for K_S^0 (top), $\overline{\Lambda^0}$ (bottom left) and Λ^0 (bottom right) candidates.

5.8 Efficiency of selecting signal with MC truth

The efficiency of selecting signal candidates using the "true" identity is obtained through a procedure inspired from [161, 162]. It is defined as the ratio of signal candidates with a correctly assigned identity code and the total number of signal candidates:

$$
\varepsilon_{\text{sig}} = \frac{N_{\text{sig}}}{N_{\text{sig}} + n_{\text{ghost}}},
\tag{5.10}
$$

where n_{ghost} is the yield obtained with a fit to the peaking mass distributions of "ghost" signal candidates defined in the previous section [161, 162]. The fitted distributions are shown in Figures 5.19-5.21 (top right). The signal function used in these fits is a sum of two Gaussians. The background candidates would be represented by combinations of tracks identified as being produced by a V^0 daughter and "ghost" tracks which do not contain sufficient hits from the other daughter. The shapes of these distributions should be similar to the ones for combinations between tracks identified as coming from a V^0 with tracks coming from other identified particles, which are shown in Figures 5.19-5.21 (bottom right). A 1$^{\text{st}}$ order Chebychev polynomial of the first kind is found to describe this distribution and is, consequently, used for the background in the "ghost" signal fit. As mentioned in the previous section, the mass distributions are not peaking for candidates of which both daughters are "ghosts" as can be seen in Figures 5.19-5.21 (bottom left). The signal and "ghost" yields, as well as the efficiencies, are given in Table 5.4.

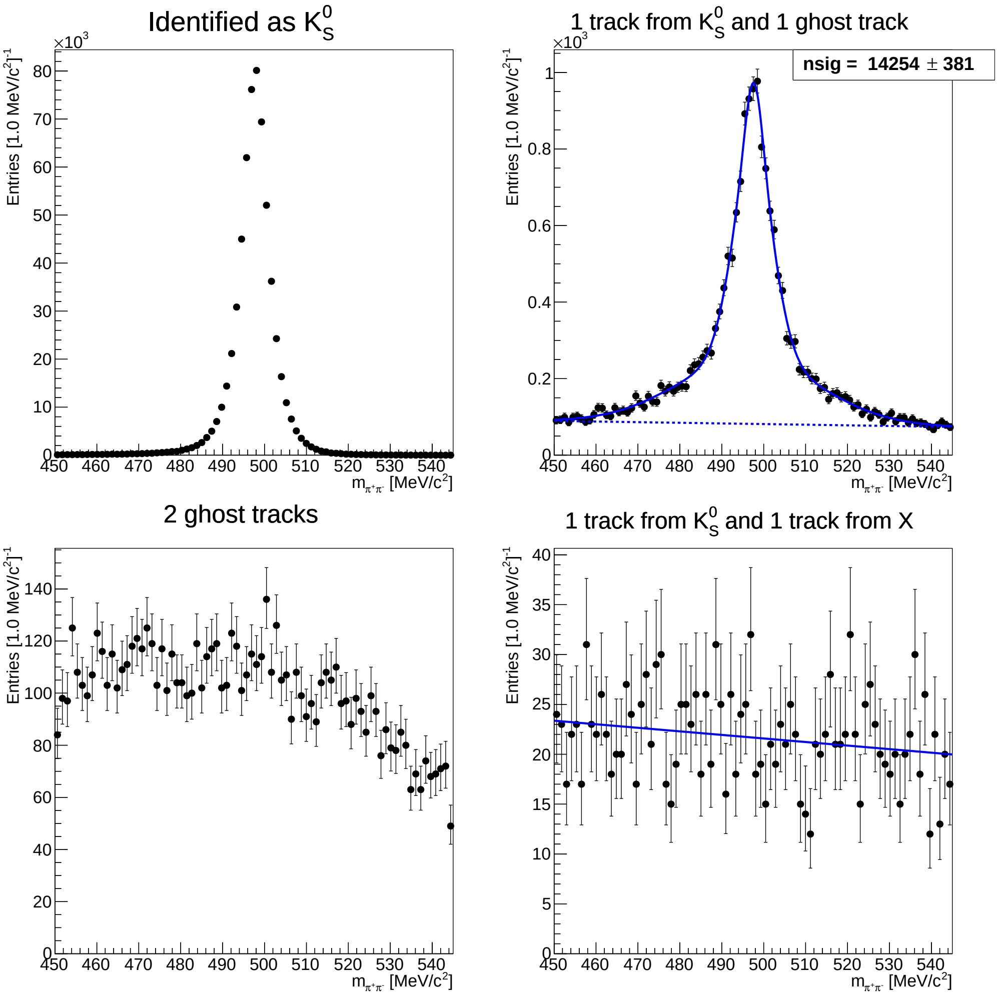

Figure 5.19: Invariant mass distributions for K^0_S candidates selected using "true" identity codes.

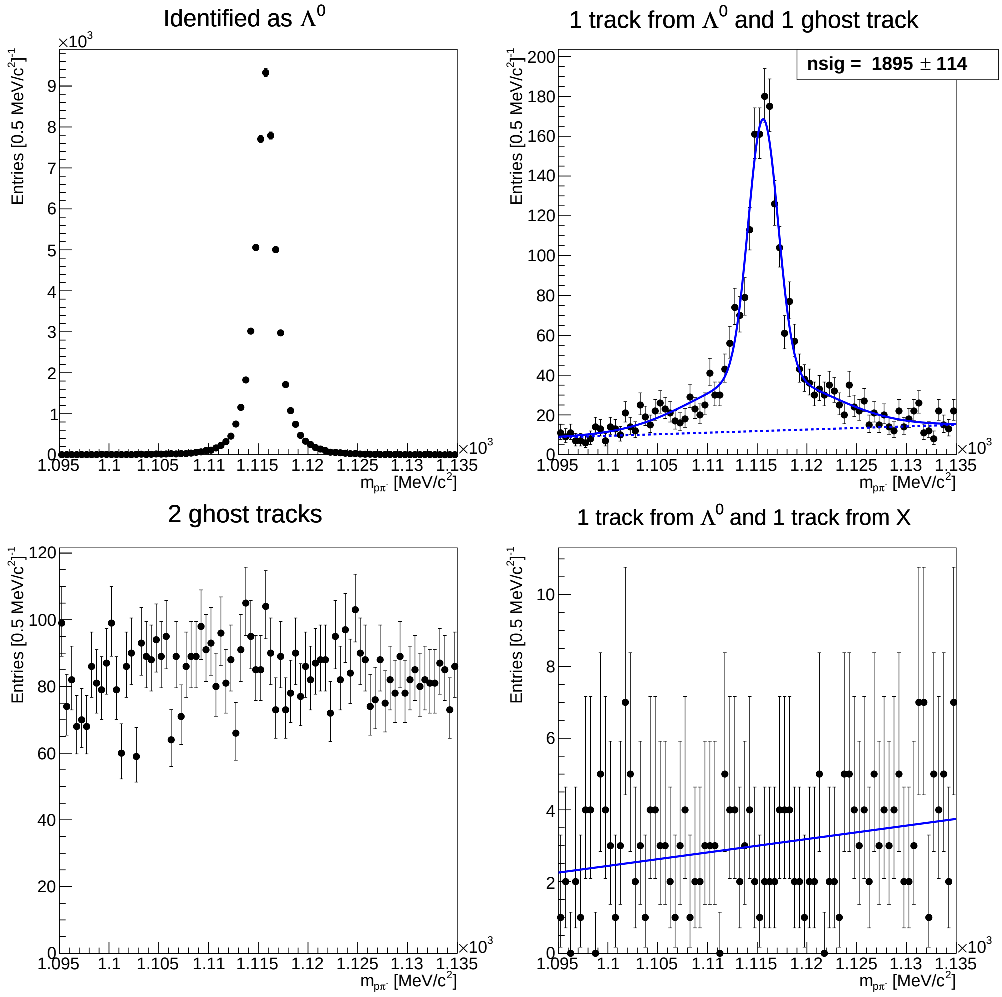

Figure 5.20: Invariant mass distributions for Λ^0 candidates selected using "true" identity codes.

Table 5.4: Yields and efficiencies of selecting signal with MC truth.

Candidates	N_{sig}	n_{ghost}	ε_{sig}
K_S^0	$605\,934 \pm 778.42$	$14\,253.50 \pm 380.99$	$97.70\% \pm 0.06\%$
Λ^0	$51\,852 \pm 227.71$	$1\,895.15 \pm 114.25$	$96.47\% \pm 0.21\%$
$\overline{\Lambda^0}$	$50\,336 \pm 224.37$	$2\,067.70 \pm 85.02$	$96.05\% \pm 0.16\%$

The efficiencies of selecting signal using the "true" identity codes are around 98% and 96% for K_S^0 and $\Lambda^0/\overline{\Lambda^0}$, respectively. This method, however, will not be used for the determination of the MC signal yields as detailed in the following sections.

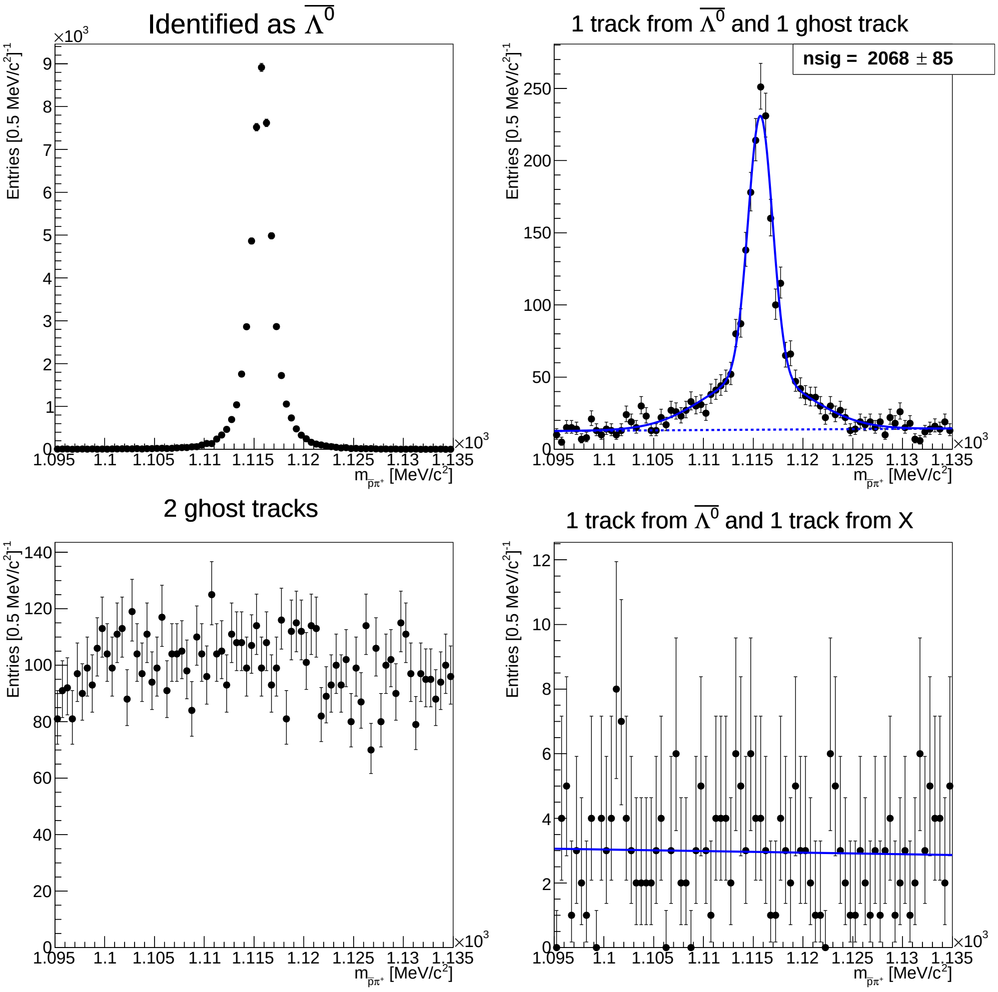

Figure 5.21: Invariant mass distributions for $\overline{\Lambda^0}$ candidates selected using "true" identity codes.

5.9 Variables of interest and analysis phase space

The inclusive cross-sections of producing V^0's in pp collisions are computed as:

$$\sigma(pp \to V^0 X) = \frac{N^{\text{Data}}}{\varepsilon \cdot \mathcal{L}} \tag{5.11}$$

and the ratios:

$$\frac{\overline{\Lambda^0}}{\Lambda^0} = \frac{\sigma(pp \to \overline{\Lambda^0} X)}{\sigma(pp \to \Lambda^0 X)}, \quad \frac{\overline{\Lambda^0}}{K_S^0} = \frac{\sigma(pp \to \overline{\Lambda^0} X)}{\sigma(pp \to K_S^0 X)}, \tag{5.12}$$

where N^{Data} is the raw (not corrected with efficiency) signal yield obtained from a fit to the invariant mass distributions from the data samples, as detailed in Section 5.14, $\mathcal{L}$ is the integrated luminosity of the sample and ε is the combined reconstruction and selection efficiency obtained from MC [15, 158, 159, 164]. The latter is defined as:

$$\varepsilon = \frac{N^{\mathrm{MC}}}{N^{\mathrm{gen}}}, \tag{5.13}$$

where N^{MC} is the yield obtained from the MC samples and N^{gen} is the number of generated prompt V^0 hadrons [158, 159]. This efficiency can be expressed as:

$$\varepsilon = \varepsilon_{\mathrm{PV}} \cdot \varepsilon_{\mathrm{reco}} \cdot \varepsilon_{\mathrm{sel}} \cdot \mathcal{B}(V^0 \to d^+ d^-), \tag{5.14}$$

where ε_{reco} is the efficiency to reconstruct a V^0 candidate given that a minimum of one PV is reconstructed, ε_{PV} is the efficiency to reconstruct a minimum of one PV, ε_{sel} is the efficiency of the selection cuts and $\mathcal{B}(V^0 \to d^+ d^-)$ is the branching fraction for the decays from Equation (5.2). Of course, there are several decay channels like radiative decays with a low energy photon in the final state [24] that may contaminate the samples, but they can be neglected, given their very small branching fractions [24]. The contamination from the data and MC samples from such decays would cancel out in most part when computing the cross-section, and thus no systematic shift is expected. Differences between the PV reconstruction efficiencies in data and MC may lead to systematic shifts in the cross-sections. This source of systematic uncertainties will be explored in a future study. The uncertainties on the branching fractions reported by PDG [24] will be propagated as systematic uncertainties. The only selection cut which is expected to lead to significant shifts in the measurements is the Fisher discriminant cut.

The raw signal yields obtained from the invariant mass fits are contaminated with non-prompt candidates, as detailed in Section 5.11. By using Equations 5.11 and 5.13:

$$\begin{aligned}\sigma_{\mathrm{meas}} &= \frac{N^{\mathrm{Data}}}{\varepsilon_{\mathrm{meas}} \cdot \mathcal{L}} = \frac{N^{\mathrm{Data}}}{N^{\mathrm{MC}}} \cdot \frac{N^{\mathrm{gen}}}{\mathcal{L}} = \frac{N^{\mathrm{gen}}}{\mathcal{L}} \cdot \frac{N^{\mathrm{Data}}}{N^{\mathrm{MC}}} \cdot \frac{N_p^{\mathrm{Data}}}{N_p^{\mathrm{MC}}} \cdot \frac{N_p^{\mathrm{MC}}}{N_p^{\mathrm{Data}}} \\ &= \sigma_p \cdot \frac{N^{\mathrm{Data}}}{N^{\mathrm{MC}}} \cdot \frac{N_p^{\mathrm{MC}}}{N_p^{\mathrm{Data}}} = \sigma_p \cdot \frac{f_p^{\mathrm{MC}}}{f_p^{\mathrm{Data}}} = \sigma_p \cdot \frac{1 - f_n^{\mathrm{MC}}}{1 - f_n^{\mathrm{Data}}} \Rightarrow \sigma_p = \sigma_{\mathrm{meas}} \cdot \frac{1 - f_n^{\mathrm{Data}}}{1 - f_n^{\mathrm{MC}}}\end{aligned} \tag{5.15}$$

where σ_{meas} and $\varepsilon_{\mathrm{meas}}$ are the measured cross-sections and efficiencies, computed using the raw yields from the invariant mass fits, σ_p is the actual cross-section for prompt V^0, $N_p^{\mathrm{Data,\ MC}}$ are the prompt candidate raw yields, $f_p^{\mathrm{Data,\ MC}}$ and $f_n^{\mathrm{Data,\ MC}}$ are the prompt and non-prompt fractions of candidates, respectively, from $N^{\mathrm{Data,\ MC}}$. As can be seen, differences between the non-prompt fractions from the data and MC samples lead to systematic shifts in the cross-sections. The procedure of evaluating the systematic uncertainties due to this effect is described in Section 5.11.

The reconstruction and selection efficiency can be corrected to obtain the one for prompt candidates:

$$\varepsilon_p = \frac{N_p^{\mathrm{MC}}}{N^{\mathrm{gen}}} \Rightarrow \varepsilon_p = \frac{N_p^{\mathrm{MC}}}{N^{\mathrm{gen}}} \cdot \frac{N^{\mathrm{MC}}}{N^{\mathrm{MC}}} = \frac{N^{\mathrm{MC}}}{N^{\mathrm{gen}}} \cdot f_p^{\mathrm{MC}} = \varepsilon \cdot (1 - f_n^{\mathrm{MC}}). \tag{5.16}$$

Obviously, this prompt efficiency can be used with Equation (5.11) to obtain:

$$\begin{aligned}\sigma_c &= \frac{N^{\mathrm{Data}}}{\varepsilon_p \cdot \mathcal{L}} = \frac{N^{\mathrm{Data}}}{N_p^{\mathrm{MC}}} \cdot \frac{N^{\mathrm{gen}}}{\mathcal{L}} = \frac{N^{\mathrm{gen}}}{\mathcal{L}} \cdot \frac{N^{\mathrm{Data}}}{N_p^{\mathrm{MC}}} \cdot \frac{N_p^{\mathrm{Data}}}{N_p^{\mathrm{MC}}} \cdot \frac{N_p^{\mathrm{MC}}}{N_p^{\mathrm{Data}}} \\ &= \sigma_p \cdot \frac{N^{\mathrm{Data}}}{N_p^{\mathrm{Data}}} = \sigma_p \cdot \frac{1}{f_p^{\mathrm{Data}}} = \sigma_p \cdot \frac{1}{1 - f_n^{\mathrm{Data}}} \Rightarrow \sigma_p = \sigma_c \cdot (1 - f_n^{\mathrm{Data}})\end{aligned} \tag{5.17}$$

where σ_c denotes the cross-section computed using the prompt efficiency. In the case of this analysis, f_n^{Data} can not be obtained directly from the data samples, as detailed in Section 5.11.

A two-dimensional phase space is considered for this analysis with transverse momentum and rapidity as the defining variables.

The transverse momentum is defined as the component of momentum transverse to the beamline or, in other words, the z axis:

$$p_T = \sqrt{p_x^2 + p_y^2}, \tag{5.18}$$

where $p_{x,y}$ are the components of momentum on the x and y axes [165].

Rapidity and the related quantity, pseudorapidity, are defined as:

$$\begin{aligned} y &= \frac{1}{2} \ln\left(\frac{E + p_z}{E - p_z}\right), \\ \eta &= \frac{1}{2} \ln\left(\frac{|p| + p_z}{|p| - p_z}\right) = -\ln\tan\frac{\theta}{2}, \end{aligned} \tag{5.19}$$

where it can be seen that they are equivalent at very high energies [165, 166].

This choice of variables is common for many high energy physics analyses, as transverse momentum and differences in rapidity are invariant under Lorentz boosts along the beamline [166] and thus, the results can be easily compared with the ones at other collision energies.

The analysis phase space is divided into a 6×6 array of symmetric bins in $2 \leq y < 5$ and $1 \leq \log(p_T[\mathrm{MeV/c}]) < 4$. The use of $\log(p_T)$ in the binning scheme is motivated by the fact that it provides low granularity in the high p_T region, characterized by low statistics, and high granularity in the low p_T region, in which a large fraction of the hadrons produced in soft QCD processes reside.

5.10 Bin migration effects

Due to the finite momentum resolution of the tracking system, the candidates may be reconstructed in other bins than the ones in which the real, or generated in the case of MC, values of their kinematic variables places them. This effect may lead to biased cross-section measurements and is evaluated for the MC candidates in the full $M_{\rm PDG} \pm 50$ MeV/c^2 range through a procedure inspired from [167]. Three quantities are defined, namely the net bin migration, $R_{\rm net}$, the loss towards other bins, $R_{\rm loss}$, and the contamination from other bins, $R_{\rm cont}$:

$$R_{\rm net} = \frac{N^{{\rm reco},i}_{{\rm gen},\forall}}{N^{{\rm reco},\forall}_{{\rm gen},i}}, \quad R_{\rm loss} = \frac{N^{{\rm reco},j\neq i}_{{\rm gen},i}}{N^{{\rm reco},\forall}_{{\rm gen},i}}, \qquad R_{\rm cont} = \frac{N^{{\rm reco},i}_{{\rm gen},j\neq i}}{N^{{\rm reco},i}_{{\rm gen},\forall}}, \tag{5.20}$$

where

- $N^{{\rm reco},i}_{{\rm gen},\forall}$ is the number of particles reconstructed in bin i, which is the sum of correctly reconstructed particles (the generated kinematic variables are in the same bin) and the particles generated in bins $j \neq i$ and incorrectly reconstructed in bin i;
- $N^{{\rm reco},\forall}_{{\rm gen},i}$ is the number of generated particles in bin i, and reconstructed either correctly in bin i or incorrectly in bins $j \neq i$.
- $N^{{\rm reco},j\neq i}_{{\rm gen},i}$ is the number of generated particles in bin i and incorrectly reconstructed in bins $j \neq i$
- $N^{{\rm reco},i}_{{\rm gen},j\neq i}$ is the number of generated particles in in bins $j \neq i$ and incorrectly reconstructed in bin i.

The results are shown in Figures 5.22-5.24. No significant deviation from unity is observed for the net bin migration. The effect is assumed to be similar for the data samples and thus, no systematic uncertainty is assigned.

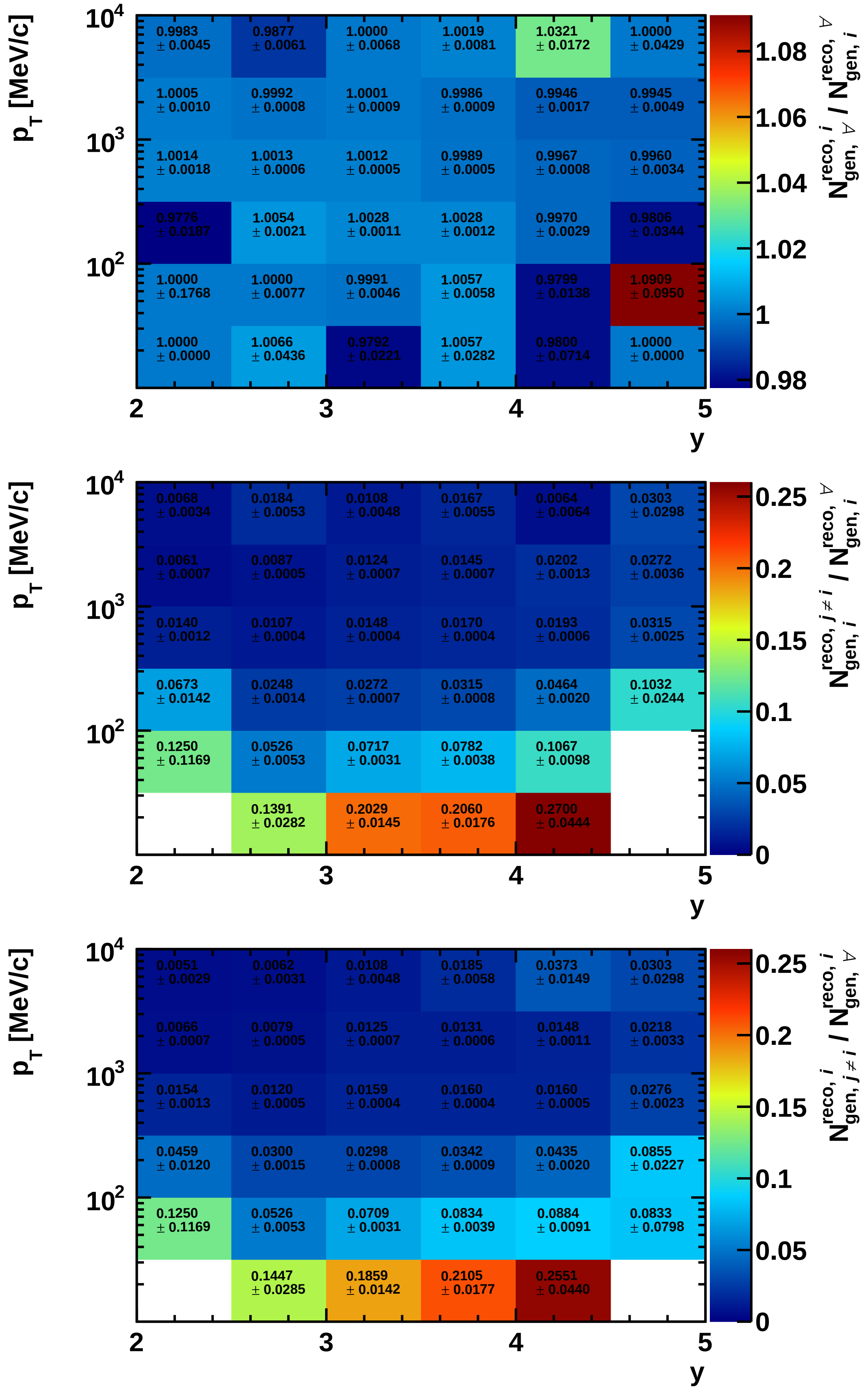

Figure 5.22: The net bin migration (top), loss towards other bins (middle) and contamination from other bins (bottom) for K^0_S.

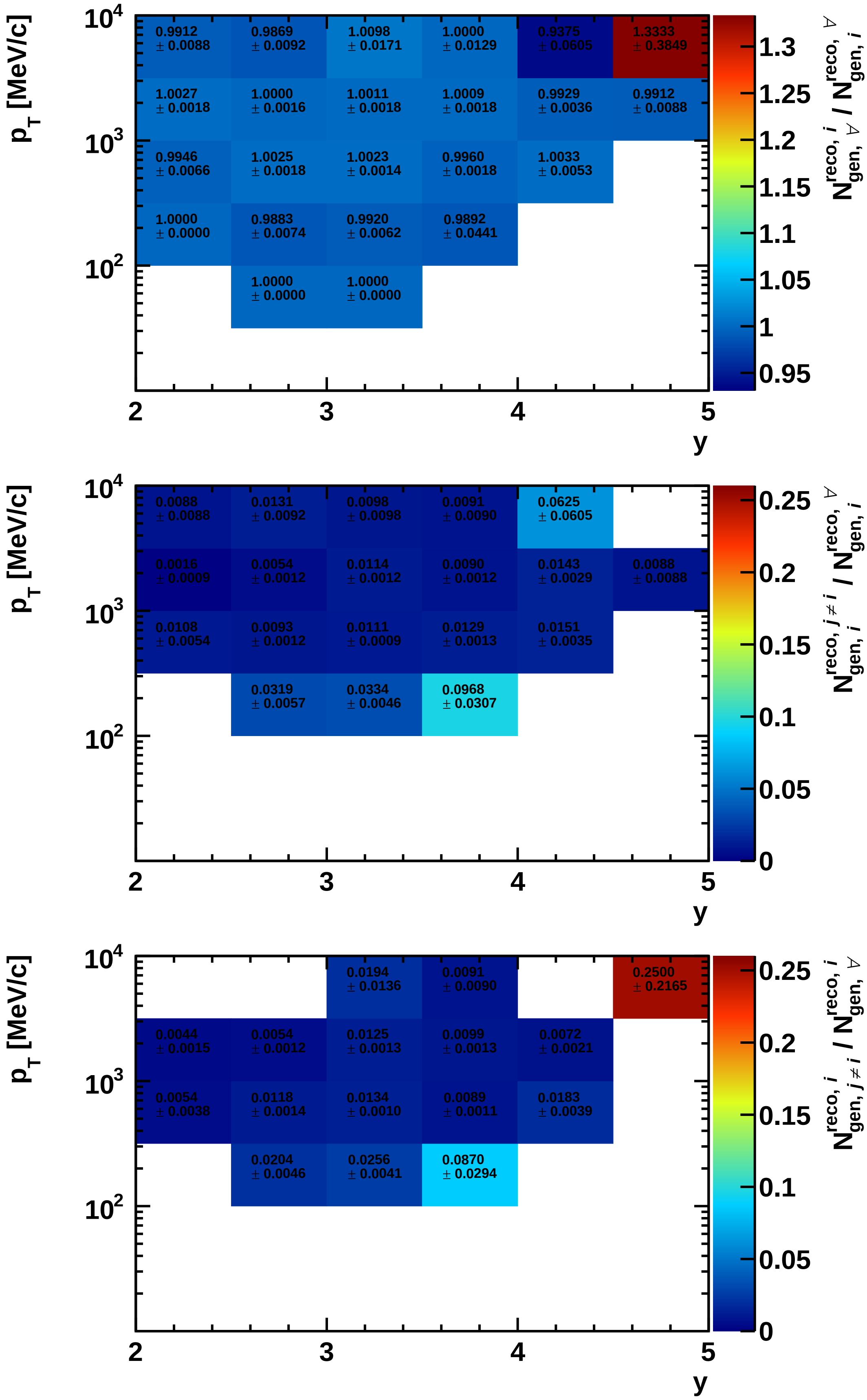

Figure 5.23: The net bin migration (top), loss towards other bins (middle) and contamination from other bins (bottom) for Λ^0.

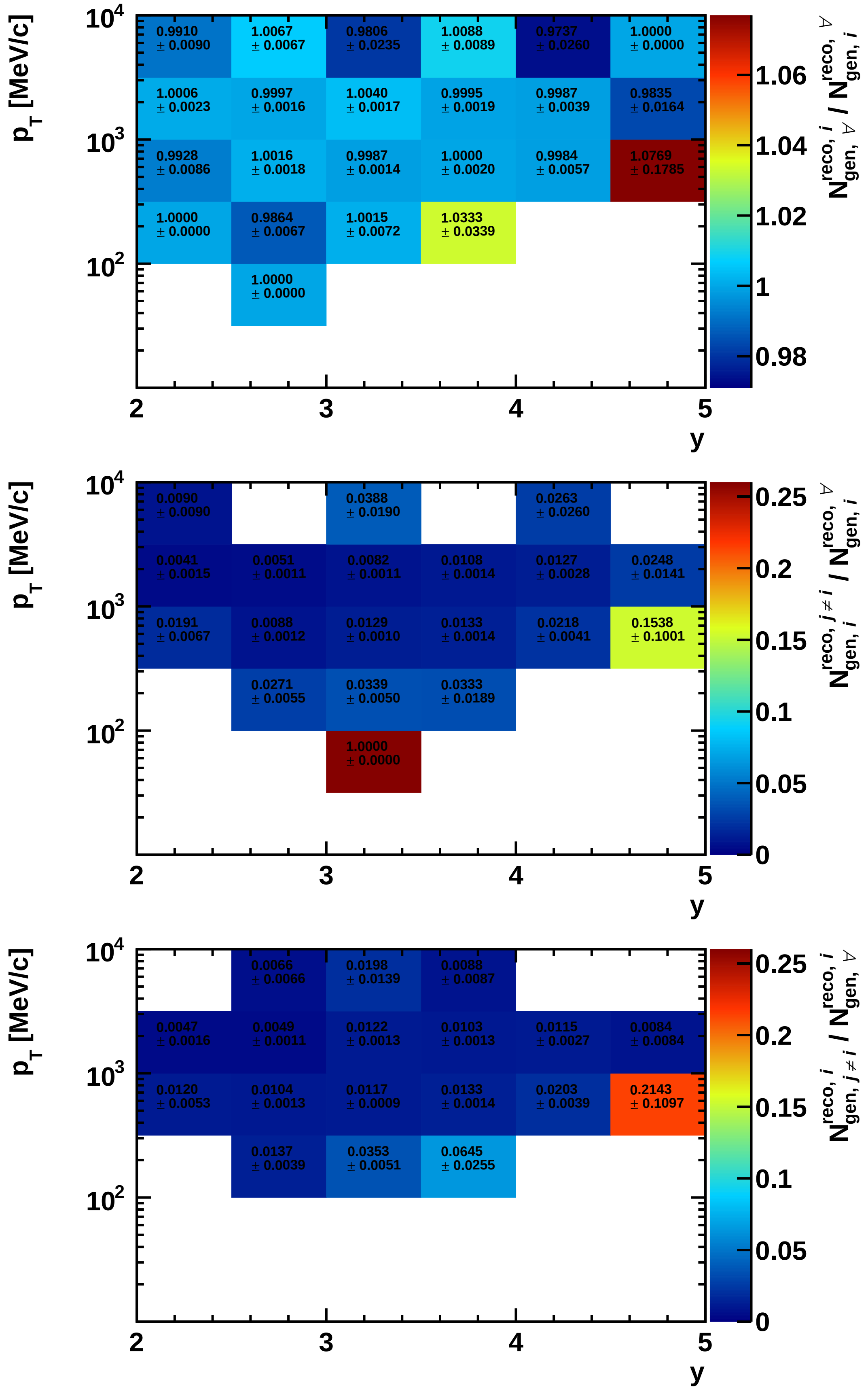

Figure 5.24: The net bin migration (top), loss towards other bins (middle) and contamination from other bins (bottom) for $\overline{\Lambda^0}$.

5.11 Non-prompt contamination

As mentioned in the previous sections, the raw signal yields are contaminated with non-prompt candidates. The momenta of these candidates generally do not point towards the PV and thus, their $\ln\left(\chi^2_{\mathrm{IP}}\right)$ distribution should be different than the one of prompt candidates [161, 162]. A procedure to determine the non-prompt fractions, inspired from [161, 162], making use of this fact is explored.

5.11.1 $\ln\left(\chi^2_{\mathbf{IP}}\right)$ method

Ideally, the non-prompt fractions from data and MC should be determined using the same method as to avoid biases. The method using the $\ln\left(\chi^2_{\mathrm{IP}}\right)$ distributions is first tested on MC, as the "truth" information permits its validation.

For each candidate category, namely prompt signal, non-prompt signal and background, a probability density function (PDF) is assigned. The prompt signal distribution is modelled using a composite function consisting of two asymmetric Gaussians, one on each side of their common mean, and two exponential tails:

$$f_{\mathrm{AGE}}\left(x;\mu,\sigma,\epsilon,\rho_L,\rho_R\right) = \begin{cases} e^{\frac{\rho_L^2}{2}+\rho_L\cdot\frac{x-\mu}{(1-\epsilon)\cdot\sigma}}, & x < \mu - \big(\rho_L\cdot\sigma\cdot(1-\epsilon)\big)\,, \\ e^{-\left(\frac{x-\mu}{\sqrt{2}\cdot\sigma\cdot(1-\epsilon)}\right)^2}, & \mu - \big(\rho_L\cdot\sigma\cdot(1-\epsilon)\big) \le x < \mu, \\ e^{-\left(\frac{x-\mu}{\sqrt{2}\cdot\sigma\cdot(1+\epsilon)}\right)^2}, & \mu \le x < \mu + \big(\rho_R\cdot\sigma\cdot(1+\epsilon)\big)\,, \\ e^{\frac{\rho_R^2}{2}-\rho_R\cdot\frac{x-\mu}{(1+\epsilon)\cdot\sigma}}, & x \ge \mu + \big(\rho_R\cdot\sigma\cdot(1+\epsilon)\big)\,, \end{cases} \tag{5.21}$$

where μ is the mode of the PDF, σ is the average width of the Gaussians with ϵ allowing an assymetry between them, and $\rho_{L,R}$ are the tail parameters [161, 162]. A Gaussian PDF is used for the non-prompt signal. For the background, a non-parametric PDF is obtained via kernel density estimation (KDE) [161, 162]. In the KDE procedure, a so-called kernel function is assigned for each data point. Usually, this is a symmetric function and contains a smoothing parameter which controls the level of detail of the modelling [168].

The background PDF is determined using candidates from the sidebands of the mass distributions, namely the single sideband of $535 \le m < 545$ MeV/c^2 for K^0_S, and the symmetric sidebands of $1095 < m \le 1105$ and $1125 \le m < 1135$ MeV/c^2 for $\Lambda^0/\overline{\Lambda}^0$. Then, a fit with a composite PDF, formed from the individual PDFs of three candidate categories, is performed in the remaining mass ranges. Fits to the invariant mass distributions are also performed, in order to determine the background yields.

To test the method, a random bin from the MC samples is chosen and the yields are compared to the ones obtained from fits to the distributions of prompt and non-prompt signal candidates selected using MC "truth". The results for K^0_S are shown in Figures 5.25 and 5.26. A non-prompt fraction of around 2.74% is obtained by using the yields from the fits to the distributions of candidates selected with MC "truth", compatible with the one obtained directly using the "truth" selection (see Section 5.11.2). The means of the distributions for selected prompt and non-prompt candidates are around 0.9 and 1.5, respectively, while the widths are around 1.2 and 1.7, respectively. The background PDF is very similar to the one of prompt candidates and so, large correlations between them are expected during the fit procedure. Moreover, the limited separation between the prompt and non-prompt distributions and the low statistics of the non-prompt candidates may lead to further correlations. The global fit does not converge, indeed, to values near the expected ones, as can be seen in Figure 5.25. The background yield in the signal region of the mass distribution is $\sim 5\,600$, whereas the value obtained from the global fit to the $\ln(\chi^2_{\mathrm{IP}})$ distribution is $\sim 2\,300$. Moreover, the value of the width reaches the upper limit set to 1.8. Several parameters in different combinations have been fixed to or constrained near the "true" values, like the mean and width of the non-prompt signal, or the background yield near the one estimated from the mass fits. The result for all combinations was the same lack of convergence towards the "true" signal yields. In order to remove the high correlations of the background and signal distributions, a "wrong" mass cut of 10 MeV/c^2 around the Λ^0 mass has been applied. As can be seen in Figure 5.26, the peaking structure of the background is eliminated. The global fits are still highly unstable and do not converge to reasonable values. In the example global fit shown, several parameters are reaching the imposed limits, namely the upper limits in the case of the non-prompt signal PDF and the lower limit on the background yield. The "wrong" mass is computed using Equation (5.1) by applying a different mass hypothesis to one of the daugther particles, namely the (anti-) proton hypothesis. The same procedure is carried out for Λ^0 and the results are shown in Figures 5.27 and 5.28. The "wrong" mass cut in this case is of 30 MeV/c^2 around the K^0_S mass. Although the separation between the means of the prompt and non-prompt signal distributions is larger, still no satisfactory results are obtained. In the case of the fit with no "wrong" mass cut applied, a background yield of $\sim 1\,200$ is obtained, whereas it should be $\sim 2\,100$, while the mean and signal yield of the non-prompt component reach the upper limits. The same parameters reach the lower limits in the case of the global $\ln(\chi^2_{\mathrm{IP}})$ fit from Figure 5.28. Thus, the method is deemed as not applicable to the current analysis.

5.11.2 Estimation from MC

An alternative to the method presented in the previous section is to estimate the non-prompt fractions using the MC "truth" selection and assume they reflect the fractions from data. The non-prompt fractions for the different V^0 candidates from the full analysis phase space are given in Table 5.5 and the ones for the individual phase space bins are given in Figure 5.29. These fractions are the weighted averages of the ones obtained from the MD and MU samples, where the weights are the ones used for the cross-sections, as detailed in Section 5.17. As can be seen, the fractions are low, indicating the high efficiency of the Fisher discriminant and $\ln(\chi^2_{\mathrm{IP}})$ cuts. The fractions of particles with the largest lifetimes in the ancestry chains of non-prompt V^0 are estimated from the MD sample and are given in Tables 5.6 and 5.7.

Around 90% of the non-prompt K^0_S are produced in the decays of charm mesons, with an additional 3% coming from decays of the Λ_c^+ baryon. The non-prompt fractions for K^0_S increase with transverse momentum and decrease with rapidity, which is expected as the p_T spectra of charm mesons is harder than that of strange mesons. The values span the approximate range of 1-6%.

Table 5.5: Non-prompt fractions for V^0 candidates in the full analysis phase space.

Candidates	Fraction
K^0_S	1.78%
Λ^0	2.40%
$\overline{\Lambda^0}$	2.24%

Table 5.6: Fraction of particles, including charge conjugates, with the largest lifetime from the ancestry chain of non-prompt K^0_S. The fraction of candidates produced in material interactions is also given.

Particle	Fraction
D^0	55.44%
D^+	23.70%
D_s^+	10.20%
Total	89.34%
Λ_c^+	3.11%
material	2.08%
other	5.47%

Table 5.7: Fraction of particles (charge conjugates) with the largest lifetime from the ancestry chain of non-prompt $\Lambda^0(\overline{\Lambda^0})$. The fraction of candidates produced in material interactions is also given.

Particle		Fraction		Fraction
Ξ^-	Λ^0	45.72%	$\overline{\Lambda^0}$	43.05%
Ξ^0	Λ^0	28.04%	$\overline{\Lambda^0}$	28.74%
Λ_c^+	Λ^0	20.39%	$\overline{\Lambda^0}$	20.72%
Ξ_c^0	Λ^0	1.32%	$\overline{\Lambda^0}$	1.71%
Ω^-	Λ^0	1.23%	$\overline{\Lambda^0}$	1.62%
Λ_b^0	Λ^0	0.90%	$\overline{\Lambda^0}$	1.11%
Total		97.60%		96.95%
material		1.40%		1.45%
other		1.00%		1.60%

In order to test the assumption that the values for K^0_S reflect the experimental ones, the cross-sections of the charm hadrons from data and MC are compared. The integrated values from different kinematic ranges are given in Table 5.8. The differential cross-sections as a function of p_T are shown in Figures 5.30-5.33 and the MC/Data ratios are given in Figures 5.34-5.37. The measurements are taken from [169]. As mentioned previously, the generation step of the MC production is based on PYTHIA 8.2. Thus, a sample containing $6 \cdot 10^6$ events is generated with the default tune of PYTHIA 8.219, and the charm hadron cross-sections are computed. Many of the integrated cross-sections are exceptionally well described by the MC, and the rest are within one standard deviation from the measurements. The differential cross-sections are also reasonably well described by the MC, with a slight underestimation trend at low p_T and a stronger overestimation trend towards high p_T. The deviations are generally within 30% and 50% in the $p_T < 5$ GeV/c and $p_T \geq 5$ GeV/c ranges, respectively. In some cases, the deviations become larger towards the upper limit of the p_T spectrum, but the uncertainties also increase and so, the significance remains at the same level or even drops.

As can be seen in Table 5.7, the vast majority of the non-prompt $\Lambda^0/\overline{\Lambda^0}$ are produced in the decays of heavier baryons, with around 75% coming from strange baryons and around 20% from Λ_c^+. The MC value of the integrated cross-section for Λ_c^+ is at around 40% of the measured value, but this large deviation amounts to only around 1.5 standard deviations. In [61], the predictions of PYTHIA 8.219 for the multiplicity distributions as a function of rapidity and p_T distributions of K_S^0, Λ^0 and Ξ^- in pp collisions at $\sqrt{s} = 7$ TeV are compared to measurements from CMS in the $|y| < 2$ region. It is observed that the multiplicities as a function of rapidity are well described for K_S^0, while the predictions for Λ^0 and Ξ^- are at around 65%-70% and 60% of the measured values, respectively [61]. These observations suggest that the strange quark production is well described, while the net baryon production is underestimated [61]. In the case that the underestimation factor is more or less the same for all baryons, as suggested by the aforementioned factors for Λ^0 and Ξ^-, the non-prompt fractions for Λ^0 should not be affected and thus, will reflect the experimental ones. The p_T distribution for K_S^0 is overestimated below ~ 0.5 GeV/c and underestimated above this value. The maximum deviation is observed in the $0 < p_T \leq 0.2$ GeV/c bin, namely around 30%, while above 1 GeV/c the deviations are, on average, around 25%. The distribution for Λ^0 is overestimated by a factor of around 2 in the lowest p_T bin. The predictions drop to values of around 70% of the measurements in the $1 < p_T < 2$ GeV/c region, and rise towards high p_T, overestimating the measuremets beyond ~ 4.5 GeV/c [61]. These findings are consistent with the results from [16] presented in Section 4.4 and partially with the ones from Section 5.20.

Table 5.8: Integrated charm hadron production cross-sections in different kinematic ranges in data and MC. The experimental values are measured at the LHCb experiment in pp collisions at $\sqrt{s} = 13$ TeV and are taken from [169]. The value for Λ_c^+ is obtained using the following relationship: $\sigma(pp \to \Lambda_c^+ X) = \sigma(pp \to c\bar{c}X) \cdot 2f(c \to \Lambda_c^+)$, where $\sigma(pp \to c\bar{c}X)$ is the integrated charm production cross-section taken from [169] and the fragmentation fraction, $f(c \to \Lambda_c^+)$, is taken from [170]. The MC values are obtained from a sample containing $6 \cdot 10^6$ events generated with PYTHIA 8.219.

Particle	p_T range	y range	σ [µb]	σ_{MC} [µb]
D^0	$0 < p_T < 8$ GeV/c	$2.0 < y < 4.5$	$2\,709 \pm 2 \pm 165$	$2\,707 \pm 6$
D^+	$0 < p_T < 8$ GeV/c	$2.0 < y < 4.5$	$1\,102 \pm 5 \pm 111$	$1\,100 \pm 4$
D^0	$1 < p_T < 8$ GeV/c	$2.0 < y < 4.5$	$2\,072 \pm 2 \pm 124$	$2\,129 \pm 5$
D^+	$1 < p_T < 8$ GeV/c	$2.0 < y < 4.5$	$834 \pm 2 \pm 78$	873 ± 3
D_s^+	$1 < p_T < 8$ GeV/c	$2.0 < y < 4.5$	$353 \pm 9 \pm 76$	371 ± 2
D^{*+}	$1 < p_T < 8$ GeV/c	$2.0 < y < 4.5$	$784 \pm 4 \pm 87$	769 ± 3
D^0	$0 < p_T < 8$ GeV/c	$2.5 < y < 4.0$	$1\,720 \pm 1 \pm 98$	$1\,635 \pm 5$
D^+	$0 < p_T < 8$ GeV/c	$2.5 < y < 4.0$	$706 \pm 4 \pm 66$	665 ± 3
D^0	$1 < p_T < 8$ GeV/c	$2.5 < y < 4.0$	$1\,313 \pm 1 \pm 73$	$1\,286 \pm 4$
D^+	$1 < p_T < 8$ GeV/c	$2.5 < y < 4.0$	$527 \pm 1 \pm 45$	527 ± 3
D_s^+	$1 < p_T < 8$ GeV/c	$2.5 < y < 4.0$	$227 \pm 2 \pm 24$	224 ± 2
D^{*+}	$1 < p_T < 8$ GeV/c	$2.5 < y < 4.0$	$493 \pm 2 \pm 41$	464 ± 2
Λ_c^+	$0 < p_T < 8$ GeV/c	$2.0 < y < 4.5$	$445 \pm 0 \pm 170$	179 ± 2

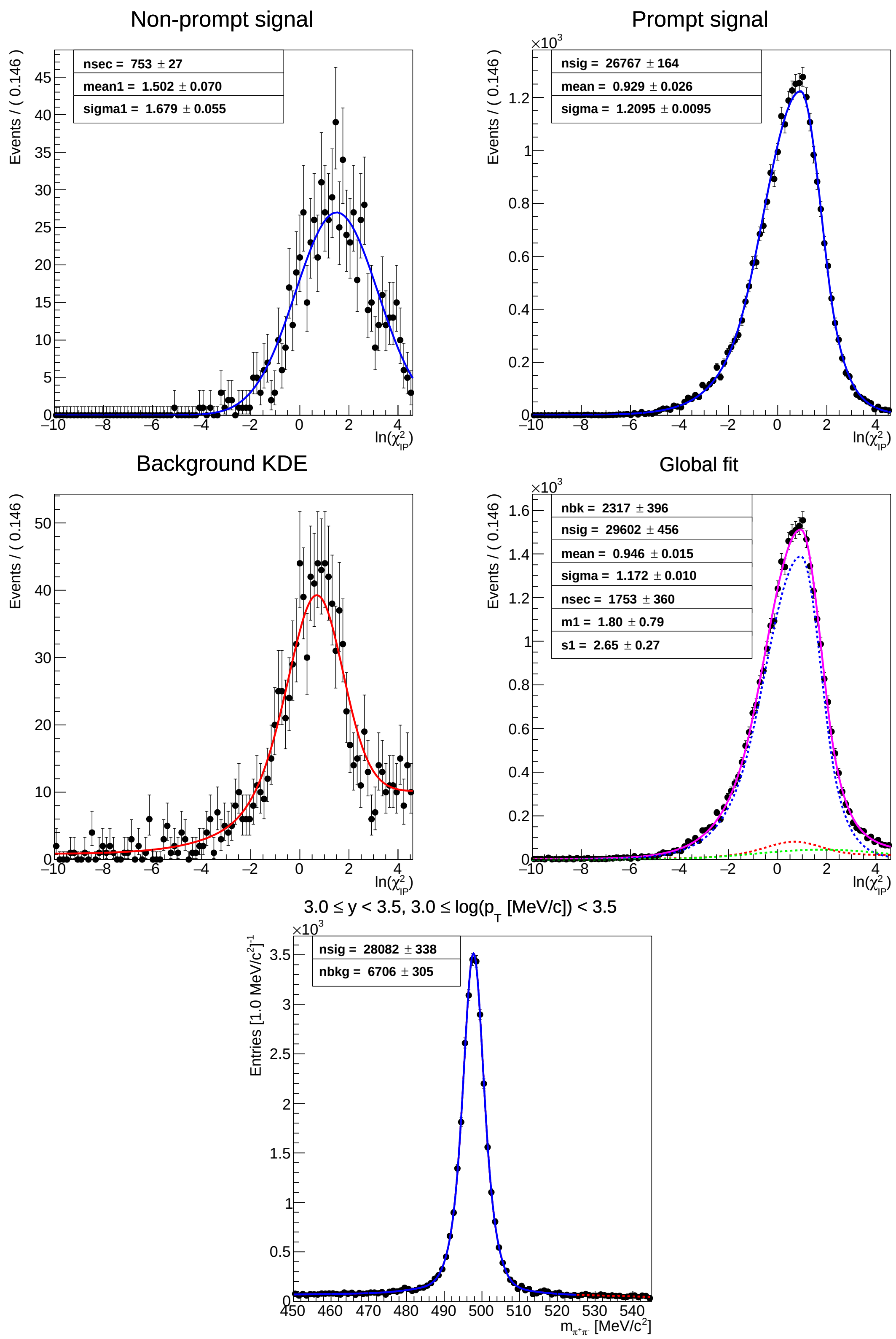

Figure 5.25: $\ln(\chi^2_{\text{IP}})$ fits for prompt and non-prompt K^0_S candidates selected using MC "truth", background KDE and global fit. The fit to the mass distribution is also shown (sideband shown with dashed red line). The PDFs from the global fit are: composite PDF (continuous magenta line), prompt signal (dashed blue line), non-prompt signal (dashed green line) and background (dashed red line).

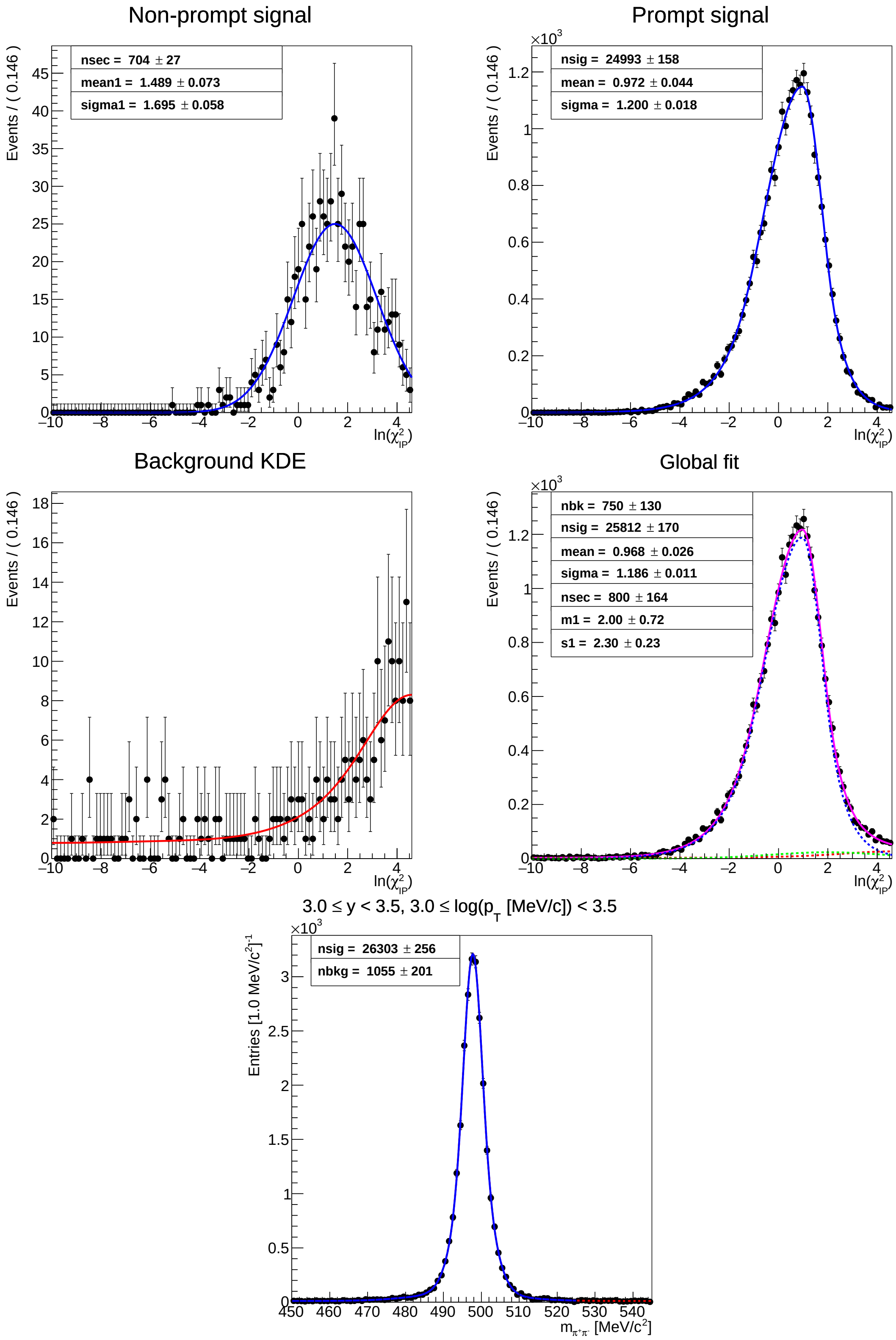

Figure 5.26: $\ln(\chi^2_{\rm IP})$ fits for prompt and non-prompt K^0_S candidates selected using MC "truth", background KDE and global fit. The fit to the mass distribution is also shown (sideband shown with dashed red line). A "wrong" mass cut of 10 MeV/c^2 around the mass of Λ^0 is applied. The PDFs from the global fit are: composite PDF (continuous magenta line), prompt signal (dashed blue line), non-prompt signal (dashed green line) and background (dashed red line).

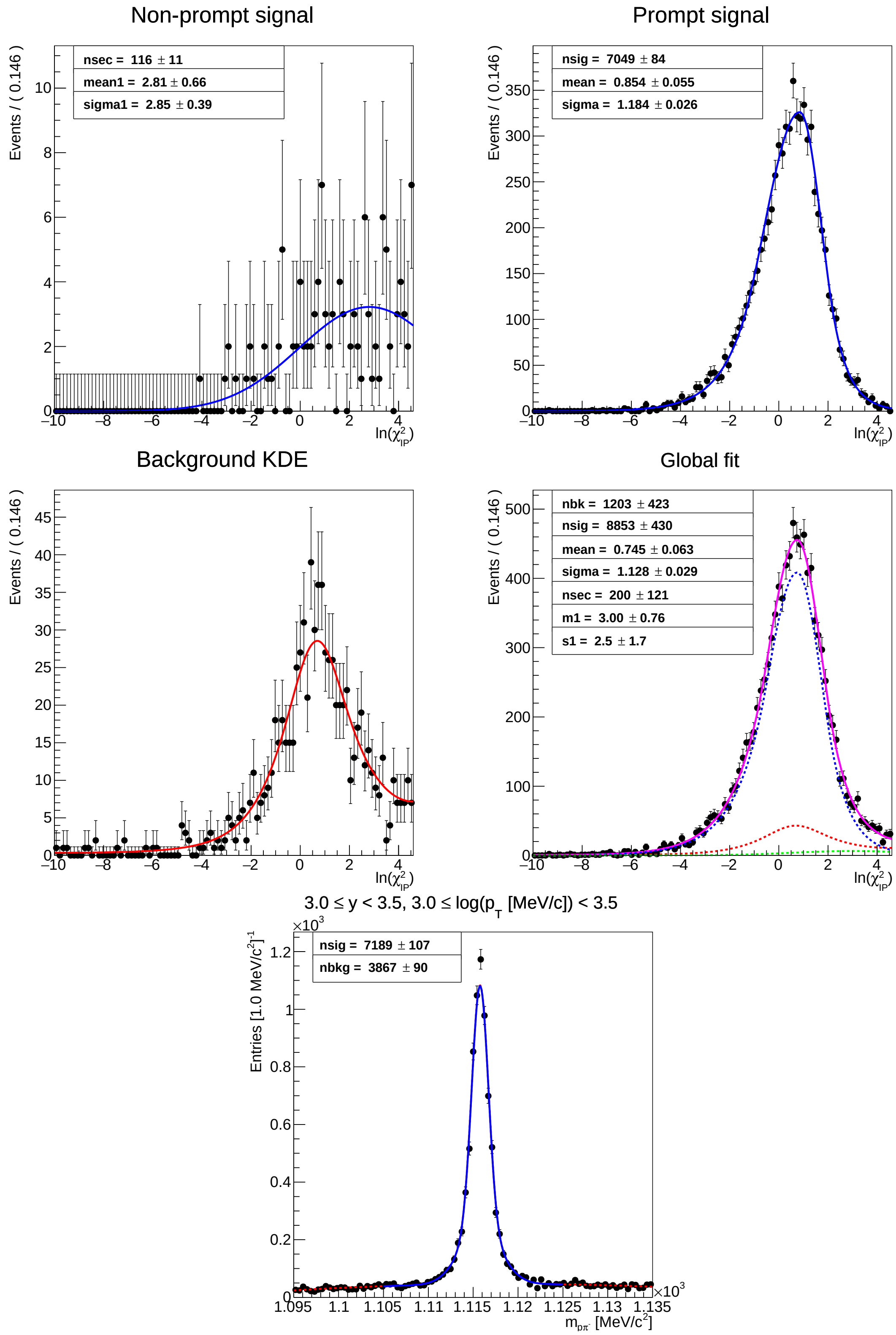

Figure 5.27: $\ln(\chi^2_{\rm IP})$ fits for prompt and non-prompt Λ^0 candidates selected using MC "truth", background KDE and global fit. The fit to the mass distribution is also shown (sidebands shown with dashed red line). The PDFs from the global fit are: composite PDF (continuous magenta line), prompt signal (dashed blue line), non-prompt signal (dashed green line) and background (dashed red line).

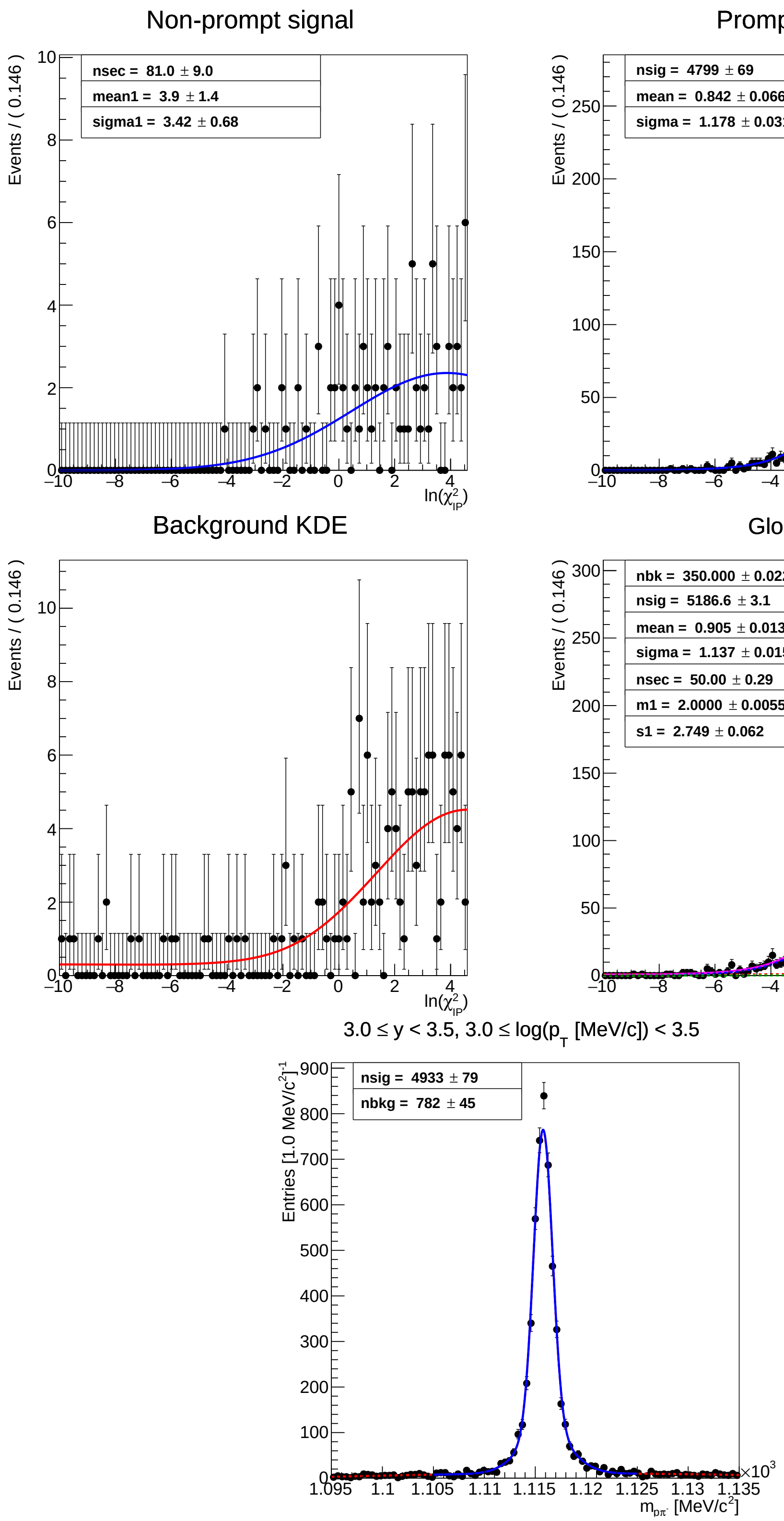

Figure 5.28: $\ln(\chi^2_{\mathrm{IP}})$ fits for prompt and non-prompt Λ^0 candidates selected using MC "truth", background KDE and global fit. The fit to the mass distribution is also shown (sidebands shown with dashed red line). A "wrong" mass cut of 30 MeV/c^2 around the mass of K^0_S is applied. The PDFs from the global fit are: composite PDF (continuous magenta line), prompt signal (dashed blue line), non-prompt signal (dashed green line) and background (dashed red line).

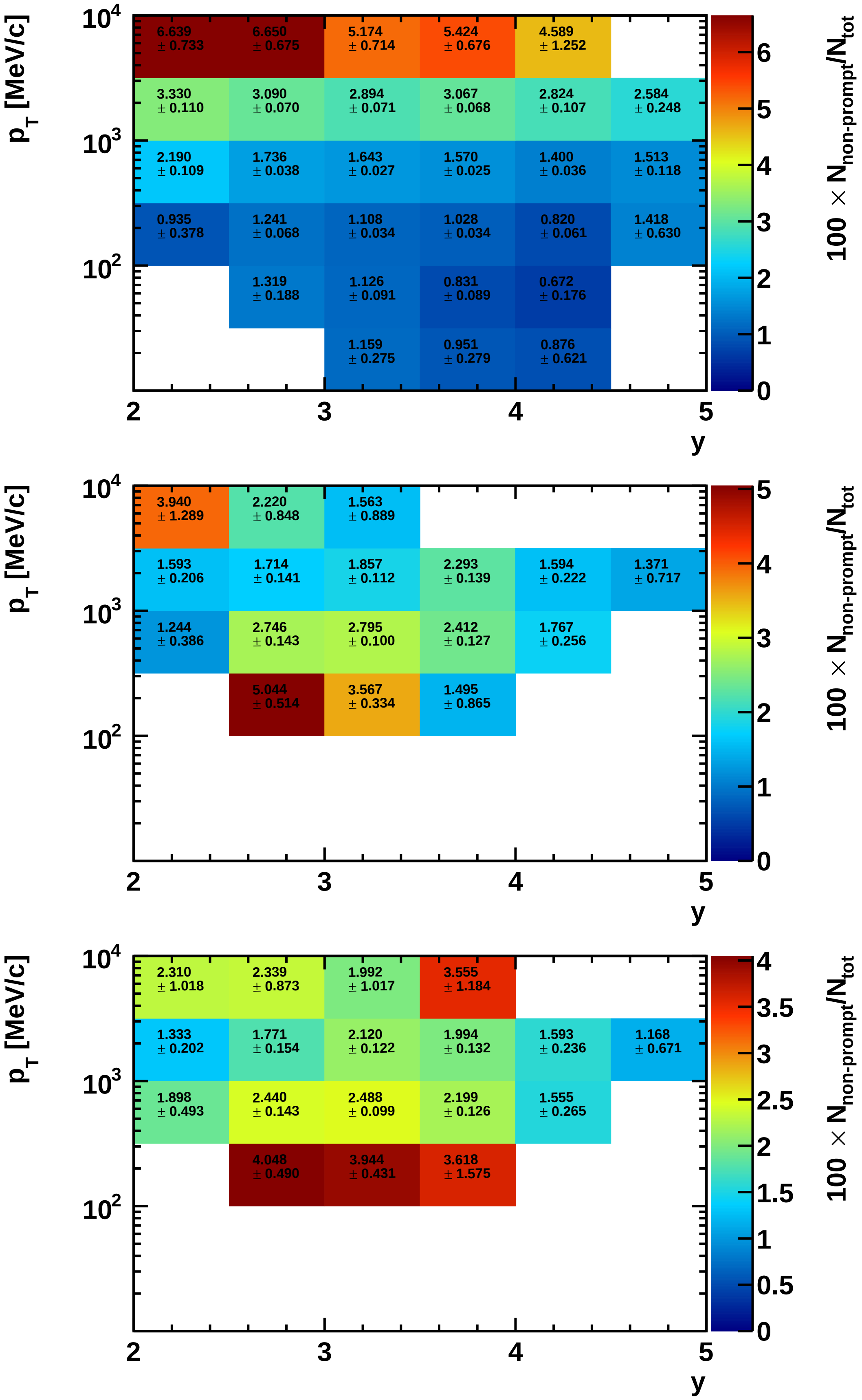

Figure 5.29: Non-prompt fractions estimated using MC "truth" for K_S^0 (top), Λ^0 (middle) and $\overline{\Lambda^0}$ (bottom).

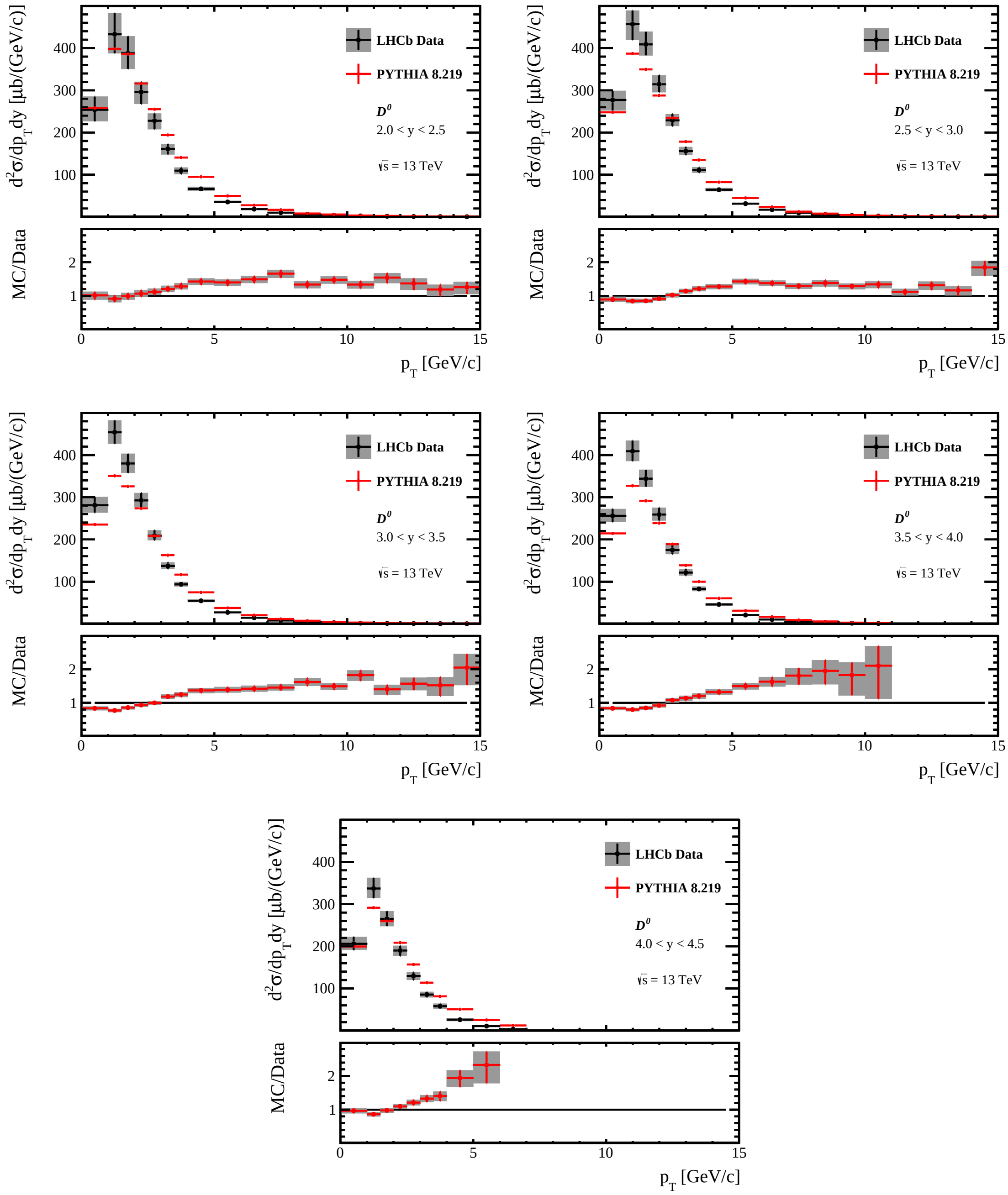

Figure 5.30: D^0 production cross-sections as a function of p_T in different rapidity bins. The data are taken from [169].

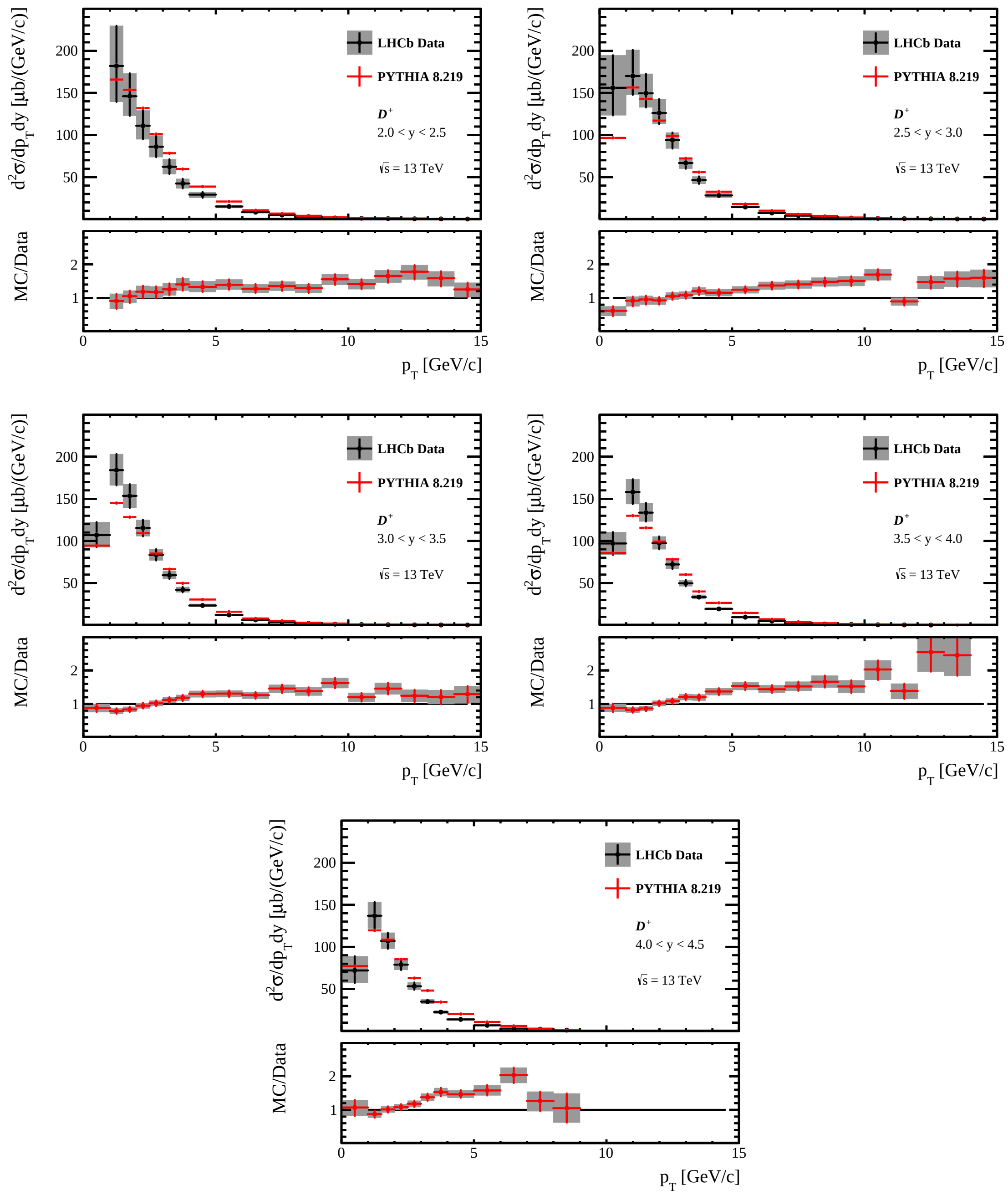

Figure 5.31: D^+ production cross-sections as a function of p_T in different rapidity bins. The data are taken from [169].

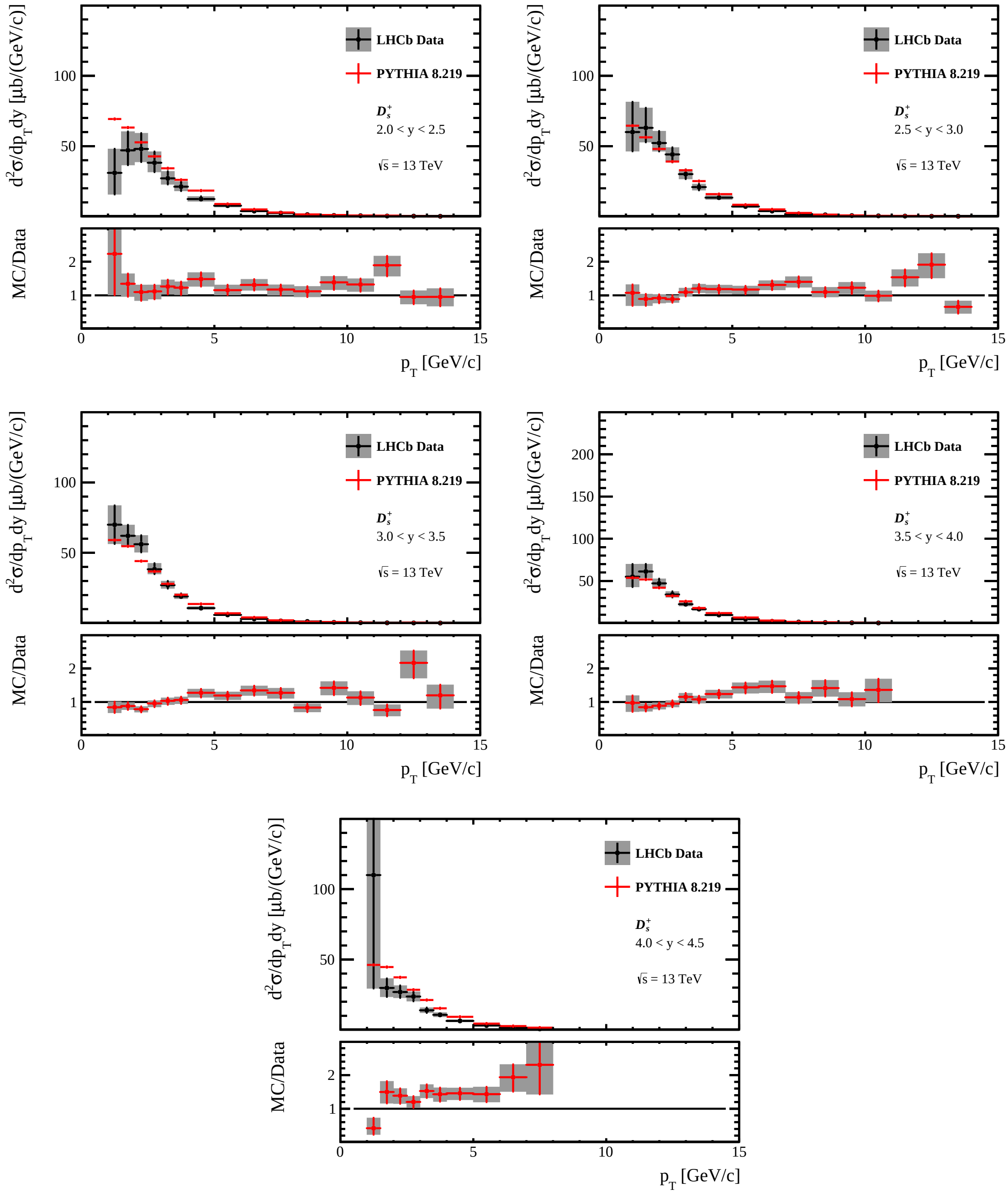

Figure 5.32: D_s^+ production cross-sections as a function of p_T in different rapidity bins. The data are taken from [169].

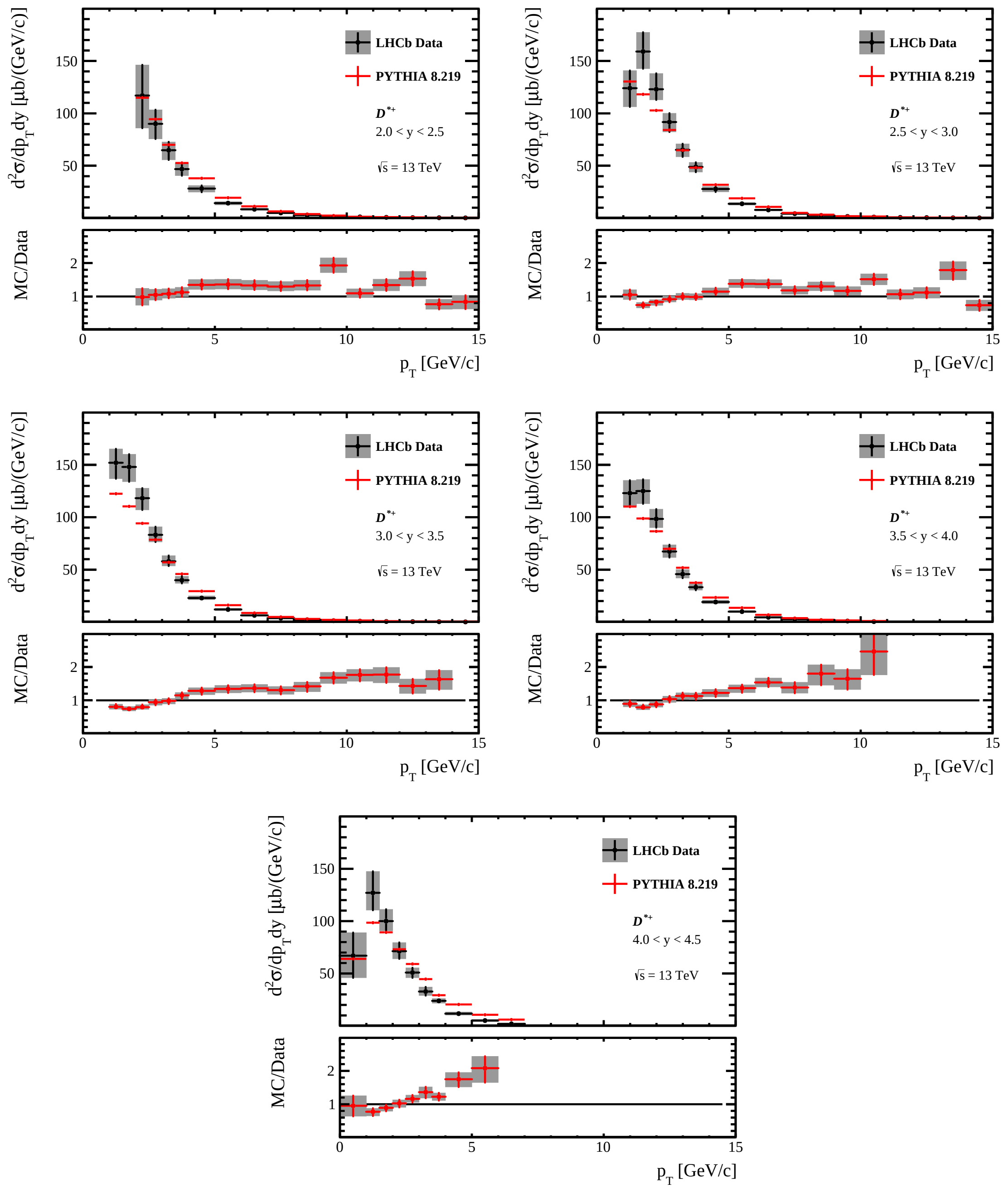

Figure 5.33: D^{*+} production cross-sections as a function of p_T in different rapidity bins. The data are taken from [169].

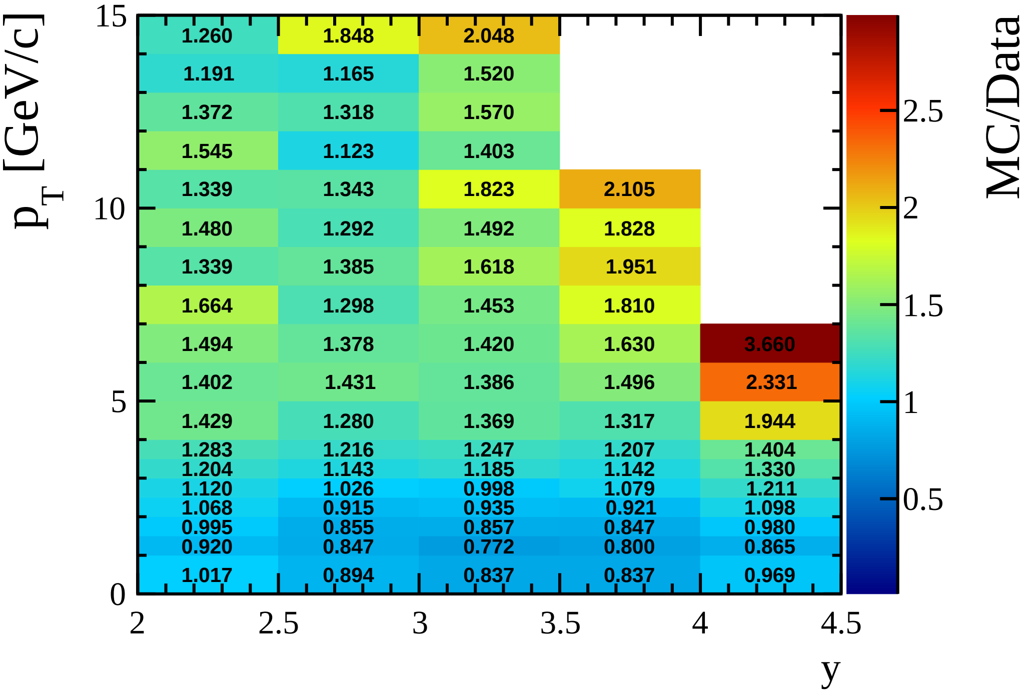

Figure 5.34: MC/Data production cross-section ratios for D^0. The data are taken from [169].

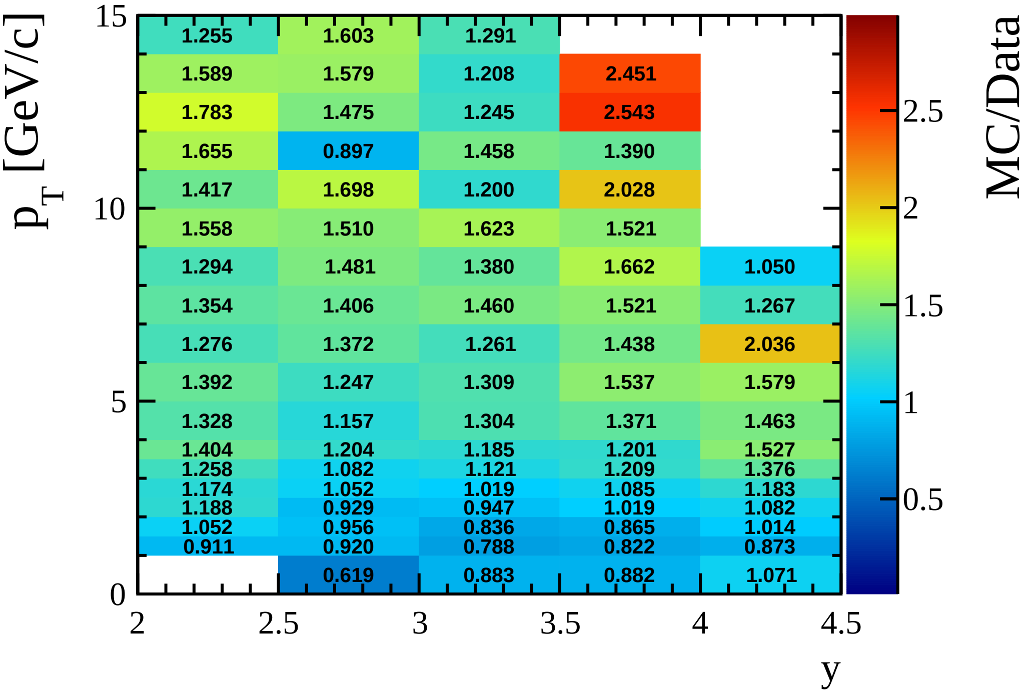

Figure 5.35: MC/Data production cross-section ratios for D^+. The data are taken from [169].

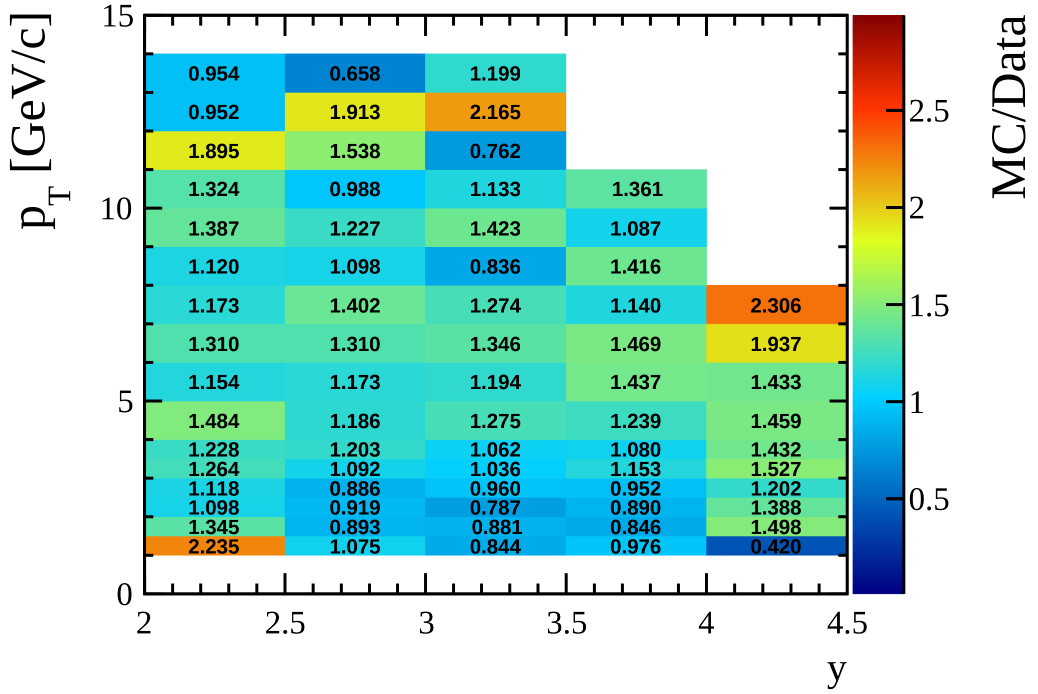

Figure 5.36: MC/Data production cross-section ratios for D_s^+. The data are taken from [169].

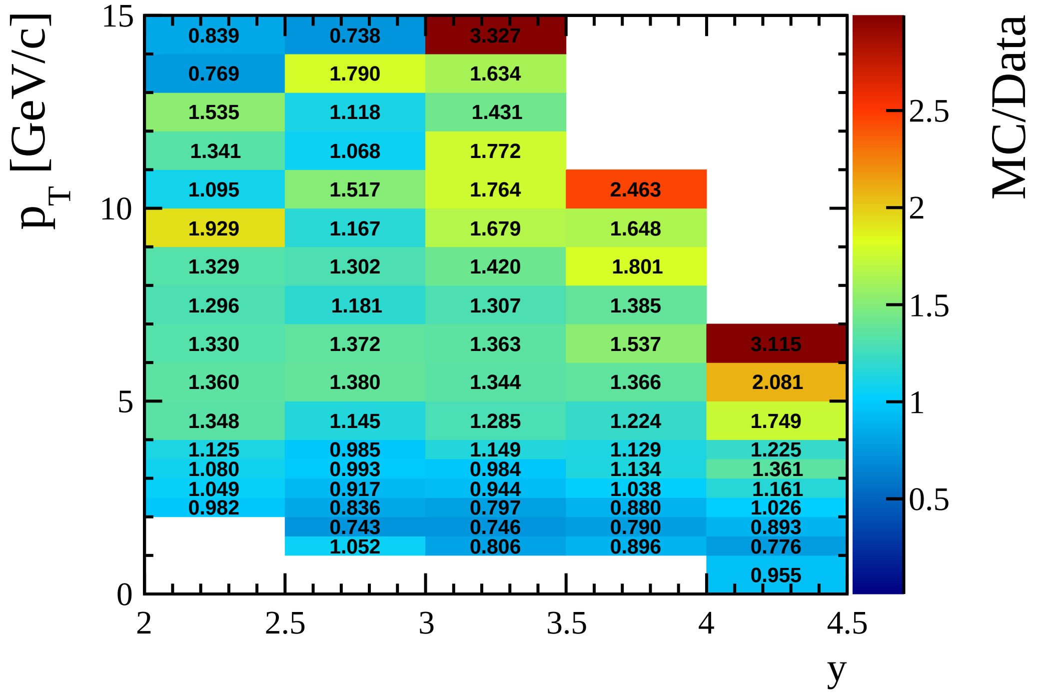

Figure 5.37: MC/Data production cross-section ratios for D^{*+}. The data are taken from [169].

5.12 Efficiency correction procedure

As detailed in Section 3.6.4.1, there are differences between the long track reconstruction efficiencies in data and MC. This may lead to systematic shifts in the cross-sections computed using the efficiencies estimated from MC. The efficiency ratios for the samples used in this analysis are given in Figure 3.27. These ratios are used to reweigh the candidates, in order to correct for the differing track reconstruction efficiencies.

The use of these ratios for the present analysis presents a caveat, as the muon "probes" are prompt, while this is not the case for the pions and (anti) protons originating from V^0 decays. Moreover, large fractions of the pions from K^0_S decays have momenta below 5 GeV/c, and more so in the case of $\Lambda^0/\overline{\Lambda^0}$ as can be seen in Figures 5.38 and 5.39. Almost the entirety of the (anti) protons from the $(\overline{\Lambda^0})$ Λ^0 have momenta in the range covered by the ratios from TrackCalib. There are also non-negligible tails beyond the upper limit of the η range. Of course, the fractions of daughter particles outside the TrackCalib phase space vary from an analysis phase space bin to another.

Another problem arises from the use of the ratios computed using muons as "probes", as these do not undergo hadronic interactions in the detector material, while hadrons do so. This will be the source of a systematic uncertainty, as detailed in Sections 5.13 and 5.22.4.

In a future study, in order to obtain more suitable efficiency ratios, tag-and-probe methods using V^0 daughters will be applied to the data from which the samples used in this analysis are obtained. The methods that are foreseen to be used will probe the efficiencies of the VELO and T stations by matching long tracks to upstream tracks and downstream tracks, respectively.

The MC candidates are reweighted with the ratios of $N_{\text{SPD hits}}$ between data and MC, in order to use the efficiency ratios provided by the TrackCalib tool. The $N_{\text{SPD hits}}$ distributions in data and MC and their ratios are shown in Figures 5.40 and 5.41. If the relative uncertainty of the ratio in a specific bin exceeds 30%, then the weight is set to 1 [135]. This is also the case if $N_{\text{SPD hits}} > 600$ [136].

The candidates are further reweighted with the efficiency ratios corresponding to the daughter particles, $w_{1,2}$. The final weights will be:

$$w = w_N \cdot w_1 \cdot w_2. \tag{5.22}$$

where w_N is the ratio of $N_{\text{SPD hits}}$ corresponding to the candidate. The distributions of these weights are given in Figure 5.42 and their average values in Table 5.9.

Table 5.9: Average weights, $\bar{w}$, for V^0 candidates from the MD samples. The average weights for signal candidates selected using MC "truth", $\bar{w}_{sig}$, are also given.

Candidates	$\bar{w}$	$\bar{w}_{sig}$
K^0_S	0.919	0.887
Λ^0	0.860	0.770
$\overline{\Lambda^0}$	0.843	0.746

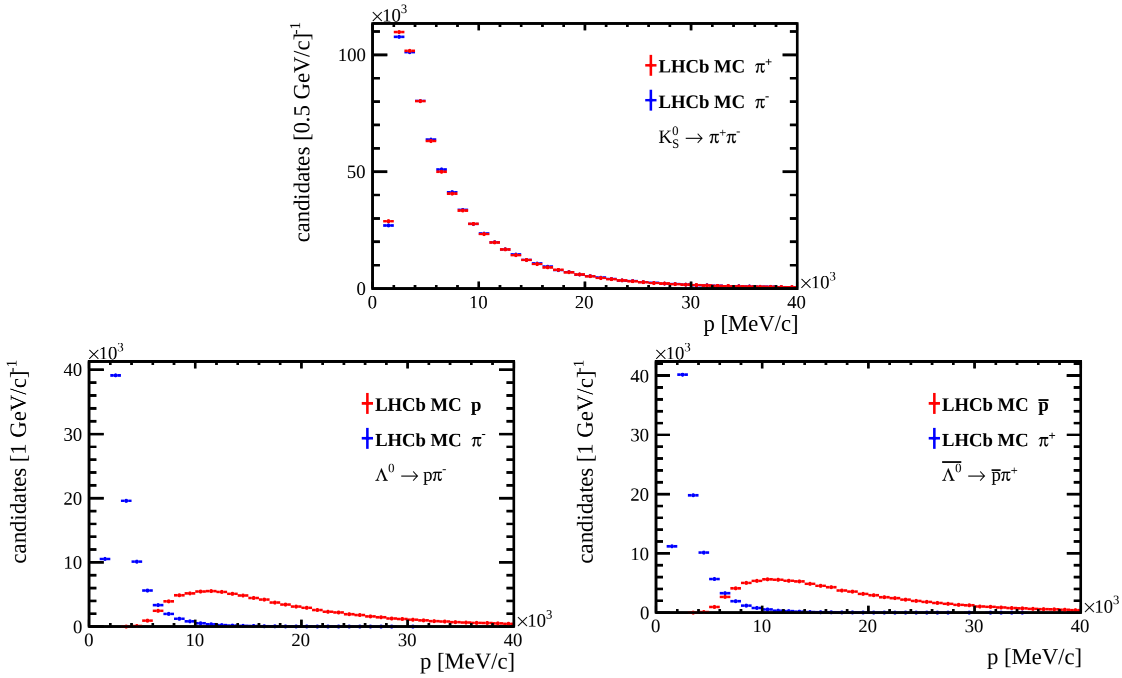

Figure 5.38: Momentum distributions of V^0 daughters.

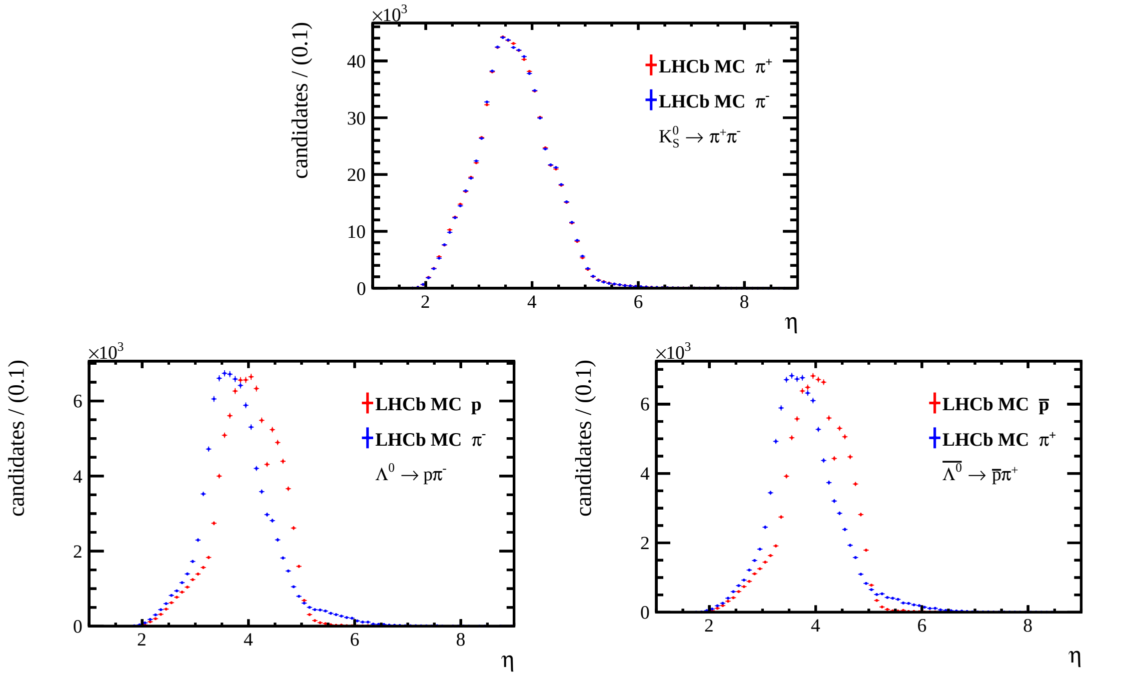

Figure 5.39: Pseudorapidity distributions of V^0 daughters.

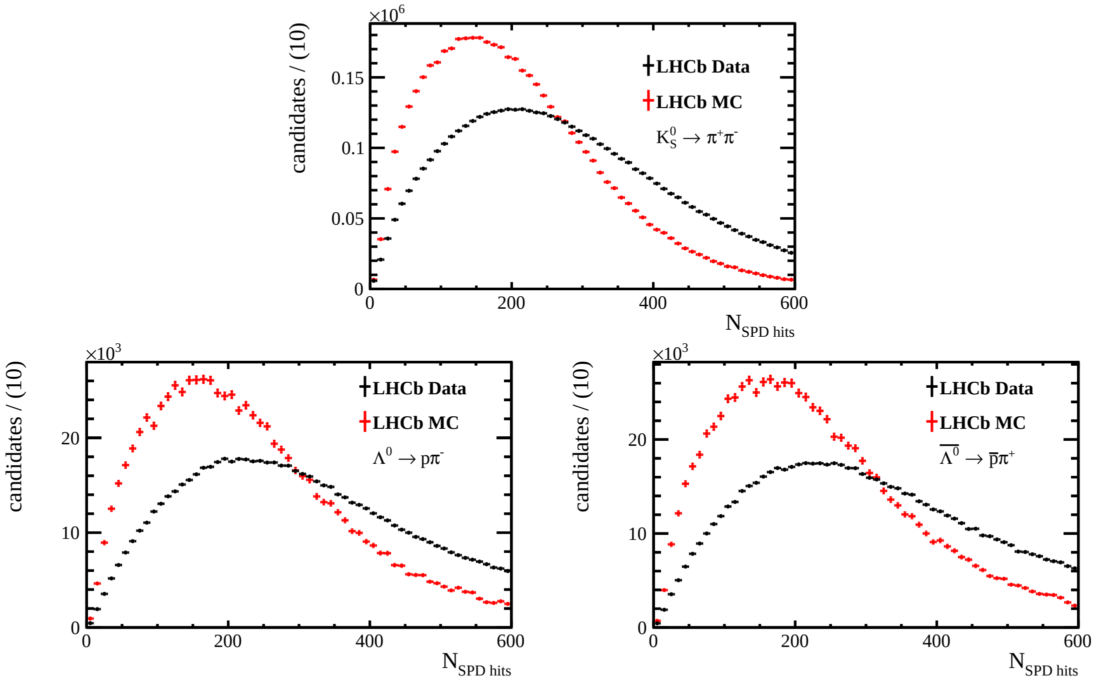

Figure 5.40: Distributions of $N_{\mathrm{SPD\ hits}}$ in data and MC.

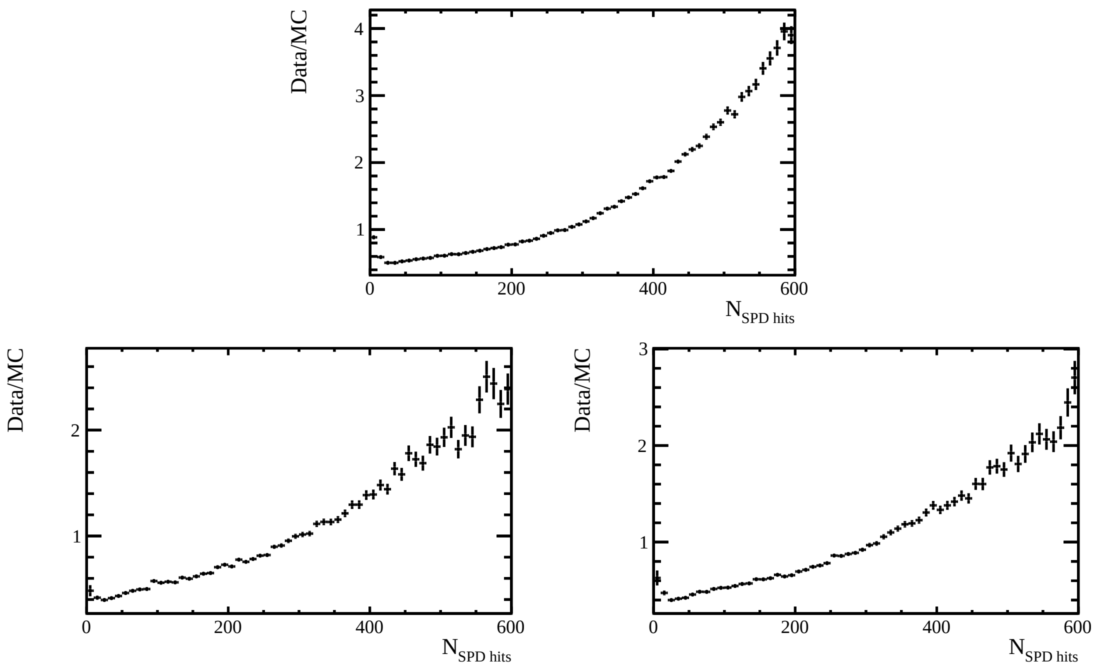

Figure 5.41: MC/Data ratios of $N_{\mathrm{SPD\ hits}}$.

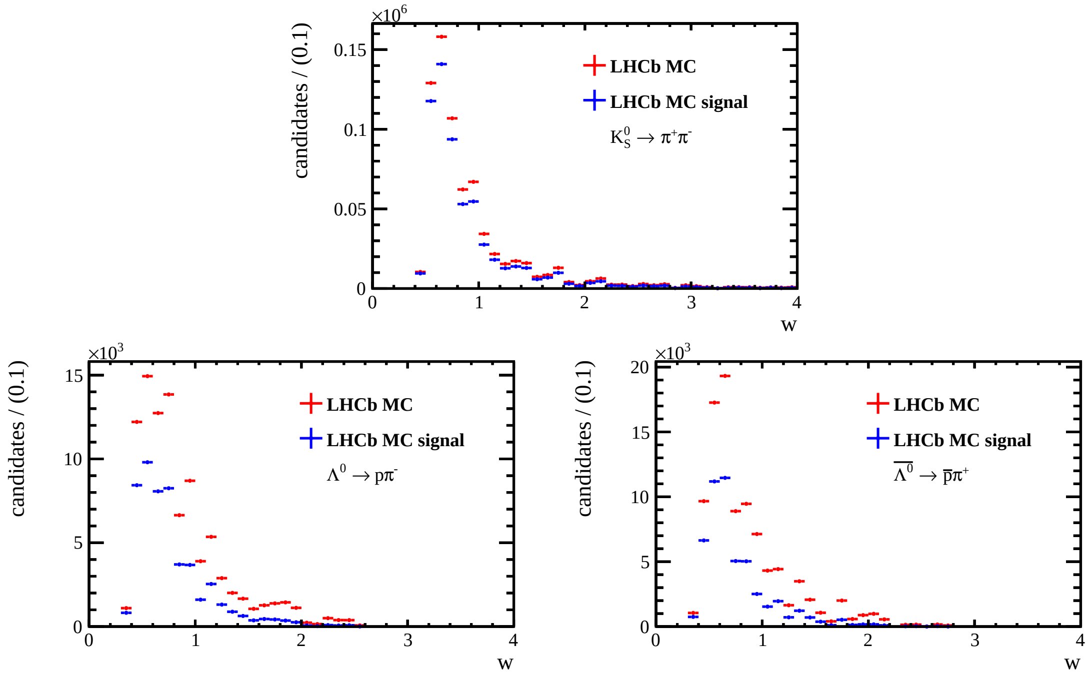

Figure 5.42: Distributions of efficiency correction weights for MC candidates. The distributions for signal candidates selected using MC "truth" are also shown.

5.13 Hadronic interactions in the detector

The reconstruction of V^0 hadrons and their daughter particles may be hindered by several processes, as detailed in the following. At low momenta, below 1 GeV/c, the energy loss of charged particles through ionization processes is large. Thus, they can rapidly lose all of their energy and not be reconstructed. This effect is not relevant, however, in the case of the present analysis, as particles have higher momenta in order to pass the magnetic field of the dipole magnet and so, to be possible to reconstruct them as long tracks. Particles can also undergo strong interactions with the nuclei of the detector material which may lead to their disapareance or large angle deviations from elastic and diffractive processes, which obviosuly prevents their reconstruction. The largest contribution is from the inelastic component, namely about 95% as revealed by an LHCb MC study of pions and kaons from $B \to J/\psi K^*$ decays [171].

These hadronic interactions are taken into account in the MC simulation, but as stated before, the precision of the detector description and the interaction cross-sections in the simulation is limited. The uncertainty on the material budget of the LHCb detector from the interaction point and up to the end of the last tracking station is about 10%. For the VELO, the uncertainty is about 6% [128]. The material budget can be expressed in terms of hadronic interaction lengths [171].

The nuclear collision length is defined as the mean distance travelled by a hadron (nucleus) in a medium before it undergoes a strong (nuclear) interaction or, in other words, the mean free path of a hadron (nucleus) with respect to strong (nuclear) interactions [172, 173]. It can also be understood as the distance travelled by a hadron for which the probability of it not undergoing a strong interaction is e^{-1} [171]. As the probability of survival is:

$$e^{-\mu x}, \quad \text{with } \mu = N\sigma = \frac{\rho N_A \sigma}{A}, \tag{5.23}$$

where x is the distance travelled through a medium, μ is the attenuation coefficient of the medium, σ is the interaction cross-section, $N = \rho N_A/A$ is the density of nuclei, ρ is the density of the material, A is the atomic mass number and N_A is Avogadro's number.

The nuclear collision length is obtained as follows:

$$e^{-\mu\lambda_N} = e^{-1} \to \lambda_N = \frac{1}{\mu} \to \lambda_N = \frac{A}{\rho N_A \sigma}. \tag{5.24}$$

The nuclear or hadronic interaction lengths take into account only inelastic processes [172, 173], so:

$$\lambda_I = \frac{A}{\rho N_A \sigma_{inel}} \to \lambda_I^{-1} = N\sigma_{inel}. \tag{5.25}$$

The material budget from the interaction point and up to the end of the last tracking station (T3) is about $0.2 \cdot \lambda_I$ in the $2 \leq \eta \leq 4.8$ region, while the of the VELO is about 5% of an interaction length [171]. These values are obtained from a material scan of the detector simulation. The hadronic interaction lengths of the different materials used by the simulation are computed using:

$$\lambda_I = \frac{k\sqrt[3]{A}}{\rho}, \tag{5.26}$$

where $k = 35\ g/cm^2$, which is an approximation valid in the ranges of $Z \geq 15$ and $\sqrt{s} \approx 1 - 100$ GeV/c [171, 172].

For ${}^{27}_{13}$Al, Equation (5.26) yields $\lambda_I = 388.8$ mm [171]. The value given in PDG is 397 mm and is obtained from simulation for 200 GeV/c neutrons [171, 174]. The hadronic interaction lengths are a function of the inelastic cross-sections, which are computed using the LHEP parameterization in the simulation [175].

In [175, 176], a study of material interactions is presented. In this study, a simplified geometry of the detector, consisting of an aluminium box of different widths, is used to simulate the passage of protons, pions and kaons of different energies in order to obtain the interaction probability. This probability is defined as the ratio of the number of particles which interacted within the box and the total number of particles sent through it:

$$P_{int} = \frac{N_{int}}{N_{tot}}. \tag{5.27}$$

In the thin target approximation [176], the interaction length can be obtained from the interaction probability:

$$e^{-\frac{x}{\lambda_I}} = 1 - P_{int} \rightarrow -\frac{x}{\lambda_I} = \ln(1 - P_{int}) \rightarrow \lambda_I = -\frac{x}{\ln(1 - P_{int})}, \tag{5.28}$$

where x is the target thickness.

The inelastic interaction probabilities of $p/\overline{p}$ and $\pi^{\pm}$, obtained for 1 mm boxes of aluminium and energies in the 1-100 GeV/c range from [176] are used to compute the corresponding interaction lengths. The inverses of these interaction lengths are plotted and fitted with functions which approximate the shapes of the cross-section distributions as a function of momentum from the LHEP parameterization, shown in [175]. The functions are given in Table 5.10 and the fits are shown in Figure 5.43. The functions are, afterwards, evaluated at the centers of the 1 GeV/c sized bins of the momentum histograms of the particles from the analysis samples. The obtained values values are inverted to obtain λ_I. The interaction probability of particles in the LHCb detector is estimated by:

$$P = 1 - e^{-\frac{f_{sim}\lambda_I^{sim}}{\lambda_I}}, \tag{5.29}$$

where f_{sim} is the material budget expressed as a fraction of the interaction length used in the material scan from the detector simulation, $\lambda_I^{sim} = 388.8$ mm.

Table 5.10: Functions used in the $1/\lambda_I$ fits from Figure 5.43.

Particle	Range [GeV/c^2]	$f(x)$	Range [GeV/c^2]	$f(x)$
$\pi^{\pm}$	1.0-5.0	$a + bx^3$	5.0-100.0	constant
p	1.0-2.5	$a + bx^3$	2.5-100.0	constant
$\overline{p}$	1.0-5.0	$a + bx^{-2}$	5.0-100.0	$a + bx^{-2}$

Given the dimensions of the VELO, its structure and the decay lengths given in Section 5.4, the average material budget traversed by the V^0's is estimated to be approximately 3% of λ_I^{sim}. Consequently, the daughter particles will, on average, traverse only around 18% of λ_I^{sim} of material budget until they reach the end of the last tracking station. For Λ_0 the inelastic cross-section is almost constant in the 1-100 GeV/c range and is about 300 µb [175]. The same value is considered for K_S^0. The interaction length is obtained with Equation (5.25) and then, the interaction probability with Equation (5.29). In the case of $\overline{\Lambda_0}$, the inelastic cross-section is the same as the one of antiprotons [175] and thus, the same procedure as for the latter is used.

The mean interaction probabilities, $\bar{P}$ over the momentum spectra of the particles are computed as the weighted average of the values at the center of the bins, the weights being the numbers of particles in the respective bins. The values obtained are summarized in Table 5.11.

The reconstruction efficiency can be expressed as a function of the survival probabilities, $p_{i=1,3}$, of the mother and daughter particles:

$$\varepsilon_{\mathrm{reco}} = \mathcal{C}\prod_{i=1}^{3} p_i, \quad \text{with } p_i = 1 - \bar{P}_i, \tag{5.30}$$

where $\mathcal{C}$ is a constant containing the detector and reconstruction algorithm efficiencies. The uncertainties on $\bar{P}_i$ are assumed to be fully correlated and are given in Table 5.11. The relative uncertainty on the reconstruction efficiency and so, on the cross-sections, due to hadronic interactions will be:

$$\sigma_{\mathrm{had}} = \sum_{i=1}^{3} \frac{\sigma_i}{1 - \bar{P}_i}. \tag{5.31}$$

The p and η distributions and so, σ_{had}, differ between phase space bins. The largest values are expected for $\overline{\Lambda^0}$ and are determined to be around 5.50%, compared to the 4.50% average value, so the use of the latter for all bins is justified.

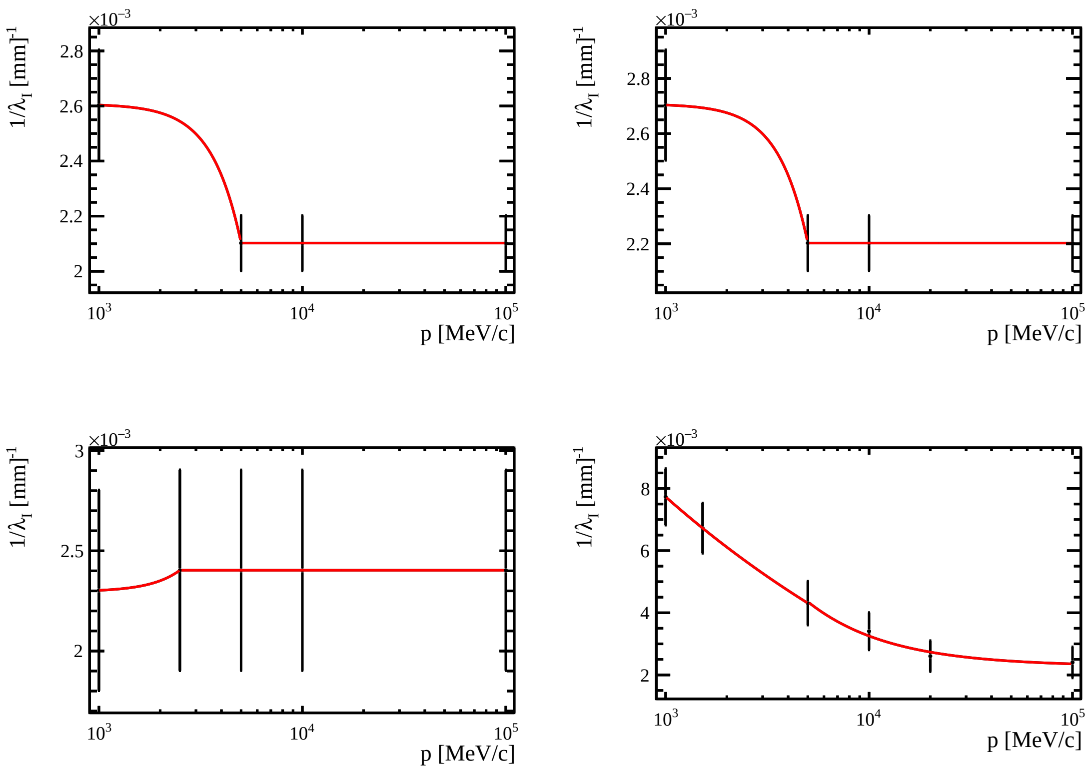

Figure 5.43: Fits to the inverse interaction lengths for π^+ (top left), π^- (top right), p (bottom left) and $\bar{p}$ (bottom right). The data are obtained from [176].

Table 5.11: Mean interaction probabilities and associated uncertainties.

V^0	Particles	$\bar{P}$	σ	σ_{had}
	π^+	14.58%	1.46%	
K^0_S	π^-	15.17%	1.52%	3.80%
	K^0_S	4.18%	0.25%	
	p	15.48%	1.55%	
Λ^0	π^-	16.20%	1.62%	4.00%
	Λ^0	4.18%	0.25%	
	$\overline{p}$	18.61%	1.86%	
$\overline{\Lambda^0}$	π^+	15.62%	1.56%	4.50%
	$\overline{\Lambda^0}$	5.91%	0.36%	

5.14 Invariant mass fits

The raw signal yields from the data samples are obtained from extended maximum likelihood (MLE) fits to the invariant mass distributions of the V^0 candidates using the RooFit package from ROOT [177, 178] with Strategy 2 for the best error estimates [179]. Unbinned fits have been used for the majority of the bins. In order to reduce the computation times, in the case of very high statistics, binned fits have been used. The signal functions are composed of one to three and four gaussians, for $\Lambda^0/\bar{\Lambda}^0$ and K^0_S, respectively, depending on the statistics from the phase space bins. The background functions used are Chebychev polynomial of the first kind of orders one to three. The order of the polynomial function is determined from fits in the sidebands and careful visual inspection of the mass distributions. In order to test the goodness of the fit, χ^2 and the corresponding p-values have been computed. The fits were required to have reasonable p-values. The mean values of the dominant Gaussians from the full analysis phase space fits are compatible with the masses from PDG [24] as can be seen in Table 5.12. The widths of the dominant Gaussians are taken as the mass resolutions. These are around 3.55 MeV/c^2 for K^0_S, compatible with the value from [128] given in Section 3.6.4.3, 1.40 MeV/c^2 for Λ^0 and 1.50 MeV/c^2 for $\overline{\Lambda^0}$. The full analysis phase space fits and fits from different phase space bins are shown in Figures 5.44 and 5.45.

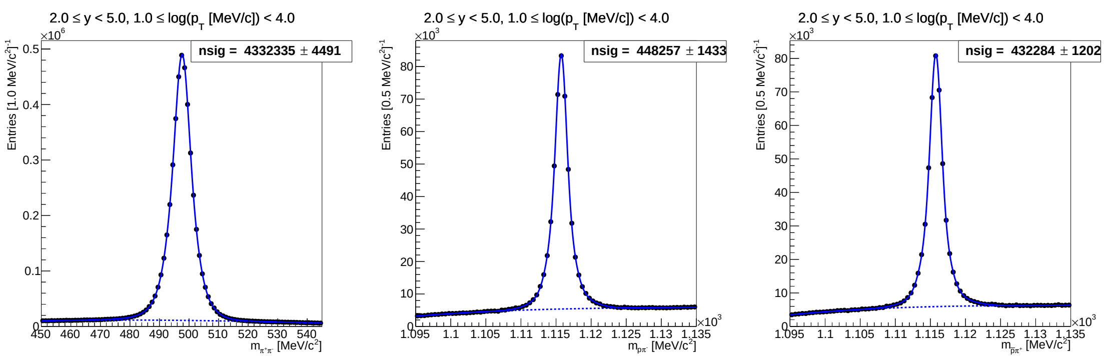

Figure 5.44: Full analysis phase space invariant mass fits for K^0_S, Λ^0 and $\overline{\Lambda^0}$ (left to right).

Table 5.12: Mean values of the dominant Gaussian from the full analysis phase space invariant mass fits and the masses from PDG [24].

V^0	μ_0 [MeV/c^2]	μ from PDG [MeV/c^2]
K_S^0	497.627 ± 0.010	497.611 ± 0.013
Λ^0	$1\,115.710 \pm 0.008$	$1\,115.683 \pm 0.006$
$\overline{\Lambda^0}$	$1\,115.740 \pm 0.008$	$1\,115.683 \pm 0.006$

The yields from the reweighted MC are obtained in a similar manner to the experimental ones, but using MLE fits with weighted likelihood functions. The parameter errors obtained with these fits do not reflect the statistics of the unweighted samples. In order to obtain better error estimates, the covariance matrix is corrected as follows:

$$V' = V\ C^{-1}\ V, \tag{5.32}$$

where V is the covariance matrix calculated from the weighted MLE fit and C is the covariance matrix calculated from a weighted MLE fit to the distribution of the candidates with the square of the weights applied instead. This procedure is applicable only if the weights are close to unity [180, 181], which is true for the ones used in this analysis (see Section 5.12).

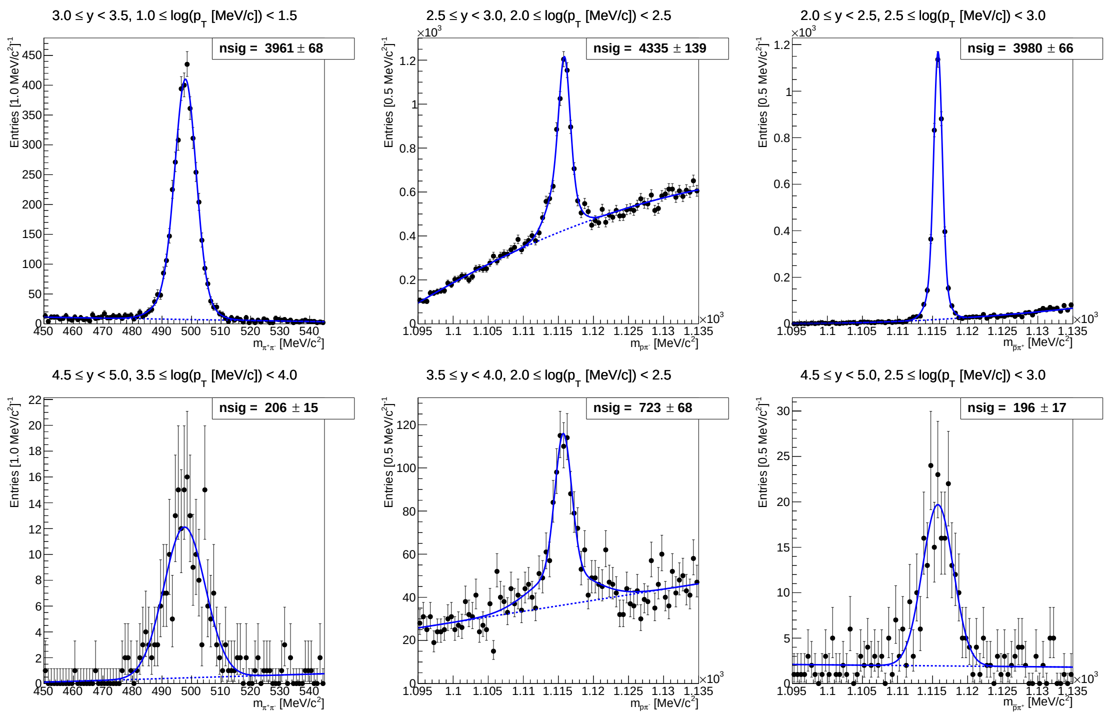

Figure 5.45: Invariant mass fits for K_S^0 (left), Λ^0 (middle) and $\overline{\Lambda^0}$ (right) in different phase space bins.

5.15 Raw signal yields

The data and MC raw signal yields obtained from the MD samples are shown in Figures 5.46 and 5.47. The highest yields are in the central bins of the phase space and decrease by as much as four orders of magnitude towards the edges. The difference between data and MC is of about an order of magnitude. In four and three bins for K^0_S and $\Lambda^0/\overline{\Lambda^0}$, respectively, in which the data yields are extracted, the MC statistics do not permit the same procedure.

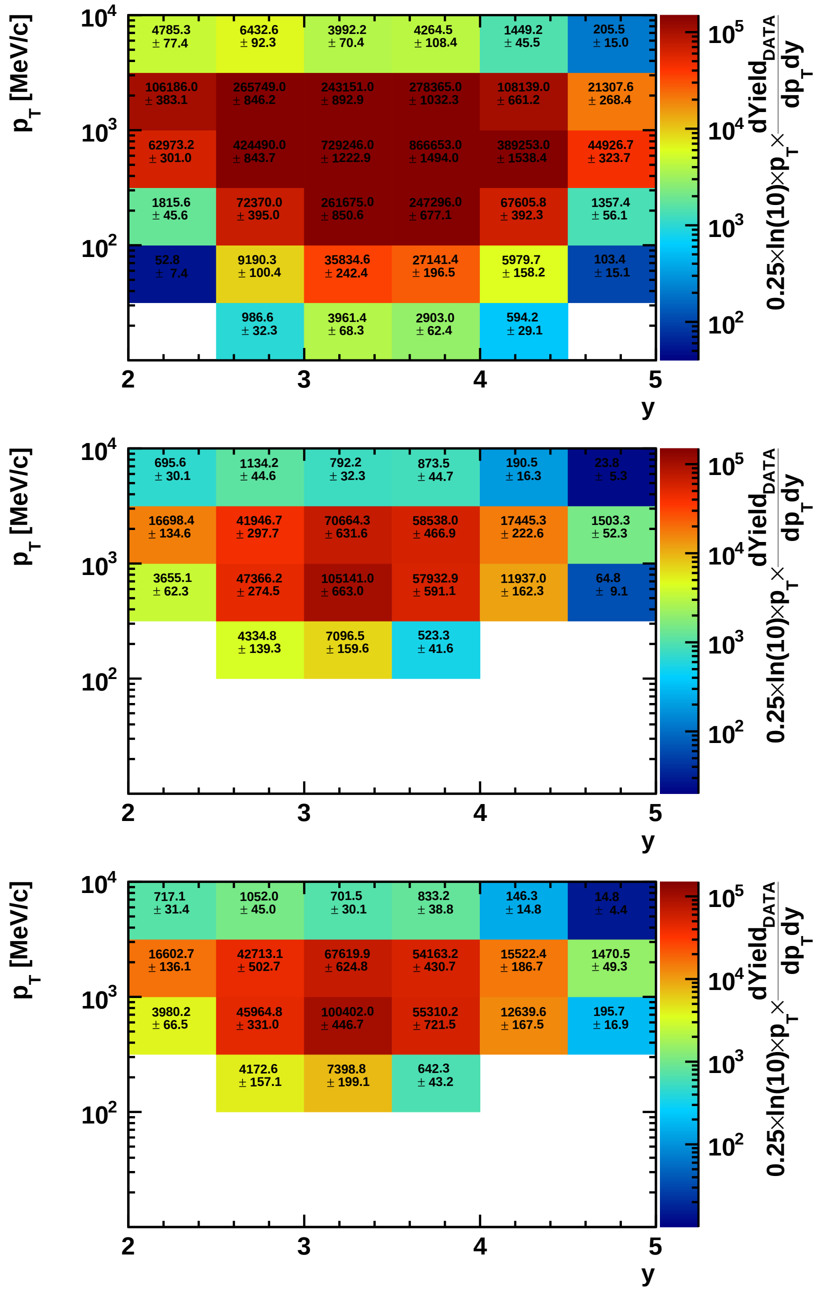

Figure 5.46: Data raw signal yields from the MD samples for K^0_S (top), Λ^0 (middle) and $\overline{\Lambda^0}$ (bottom). The uncertainties are statistical.

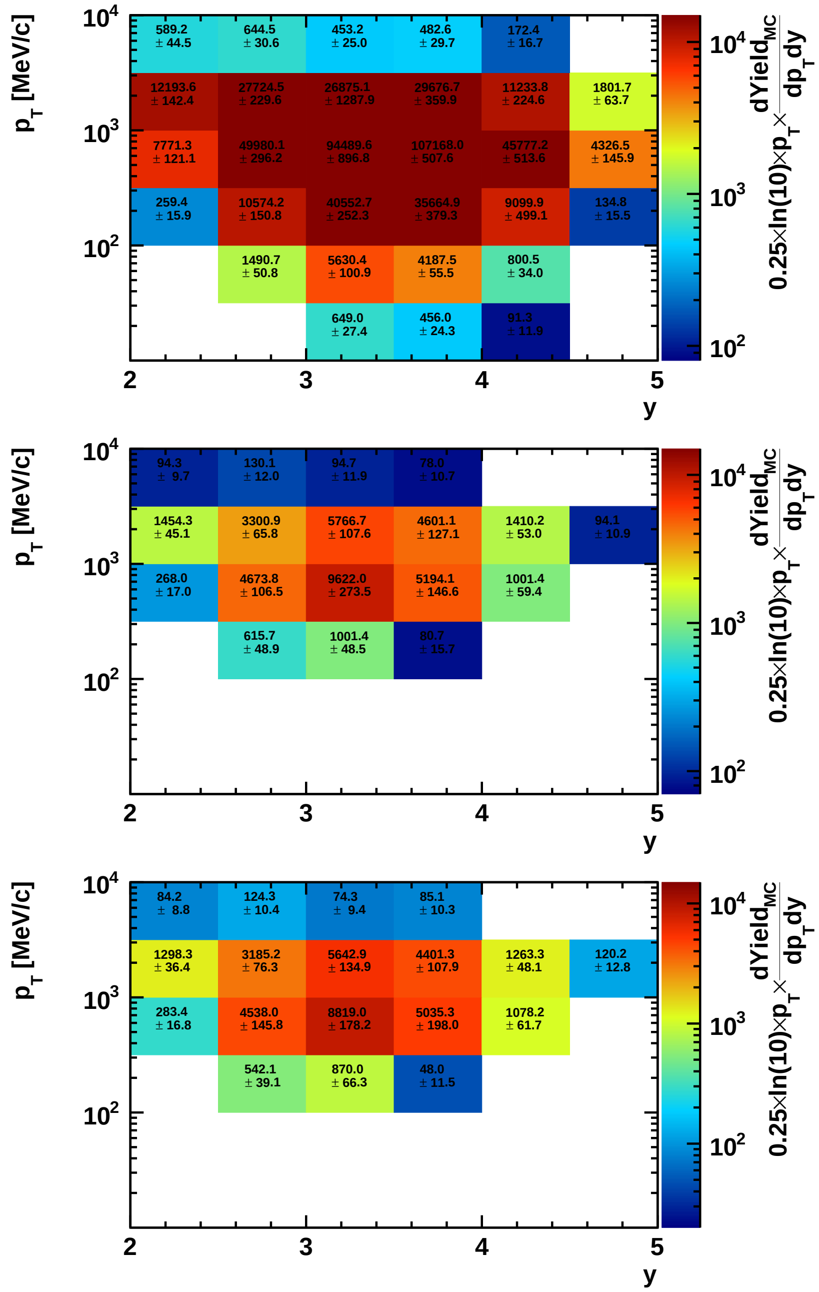

Figure 5.47: MC raw signal yields from the MD samples for K_S^0 (top), Λ^0 (middle) and $\overline{\Lambda^0}$ (bottom). The uncertainties are statistical.

5.16 Efficiencies

The reconstruction and selection efficiency maps are shown in Figure 5.48, where it can be seen that the highest efficiencies are in the central phase space region and decrease towards the edges. The values for K_S^0 and $\Lambda^0/\overline{\Lambda^0}$ in this region are around 6.0-9.0% and 3.0% , respectively. The efficiencies for K_S^0 remain high even in the low p_T region, which is not the case for $\Lambda^0/\overline{\Lambda^0}$. The efficiency for the full analysis phase space region is around 3.8%, 1.1% and 1.0% for K_S^0, Λ^0 and $\overline{\Lambda^0}$, respectively.

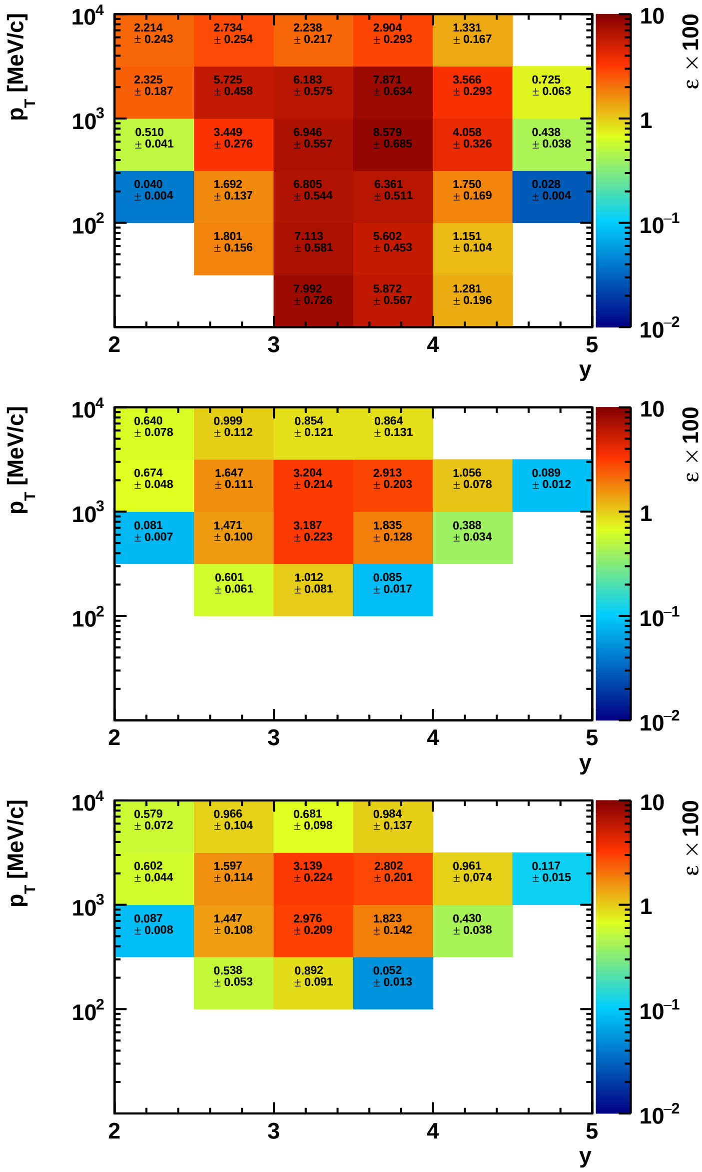

Figure 5.48: The MC reconstruction and selection efficiencies obtained from the MD samples for K^0_S (top), Λ^0 (middle) and $\overline{\Lambda^0}$ (bottom). The uncertainties do not contain the ones from the branching fractions.

5.17 Cross-sections

The reported cross-sections and ratios are the weighted averages of the values obtained from the MD and MU samples. The weights are computed as a function of the variances and covariances of the cross-sections:

$$w_2 = 1 - w_1 = \frac{\sigma_1^2 - \sigma_{21}}{\sigma_1^2 + \sigma_2^2 - 2\sigma_{21}}, \tag{5.33}$$

where the 1 and 2 subscripts refer to the MD and MU samples, respectively [159, 182].

The double differential production cross-sections are given in Figures 5.49 and 5.50, where the fact that the highest values are in the $2.5 \leq \log\left(p_T[\mathrm{MeV/c}]\right) < 3$ region and a decreasing trend towards high rapidities are observed. The full analysis phase space values are given in Table 5.13. The uncertainties are the quadratic sums of the statistical and systematic uncertainties, as detailed in Sections 5.21 and 5.22.

Table 5.13: Full analysis phase space cross-sections for V^0 hadrons.

Particle	σ [µb]
K^0_S	$64\,501.5 \pm 4\,787.3$
Λ^0	$22\,106.3 \pm 1\,656.5$
$\overline{\Lambda^0}$	$21\,013.7 \pm 1\,654.3$

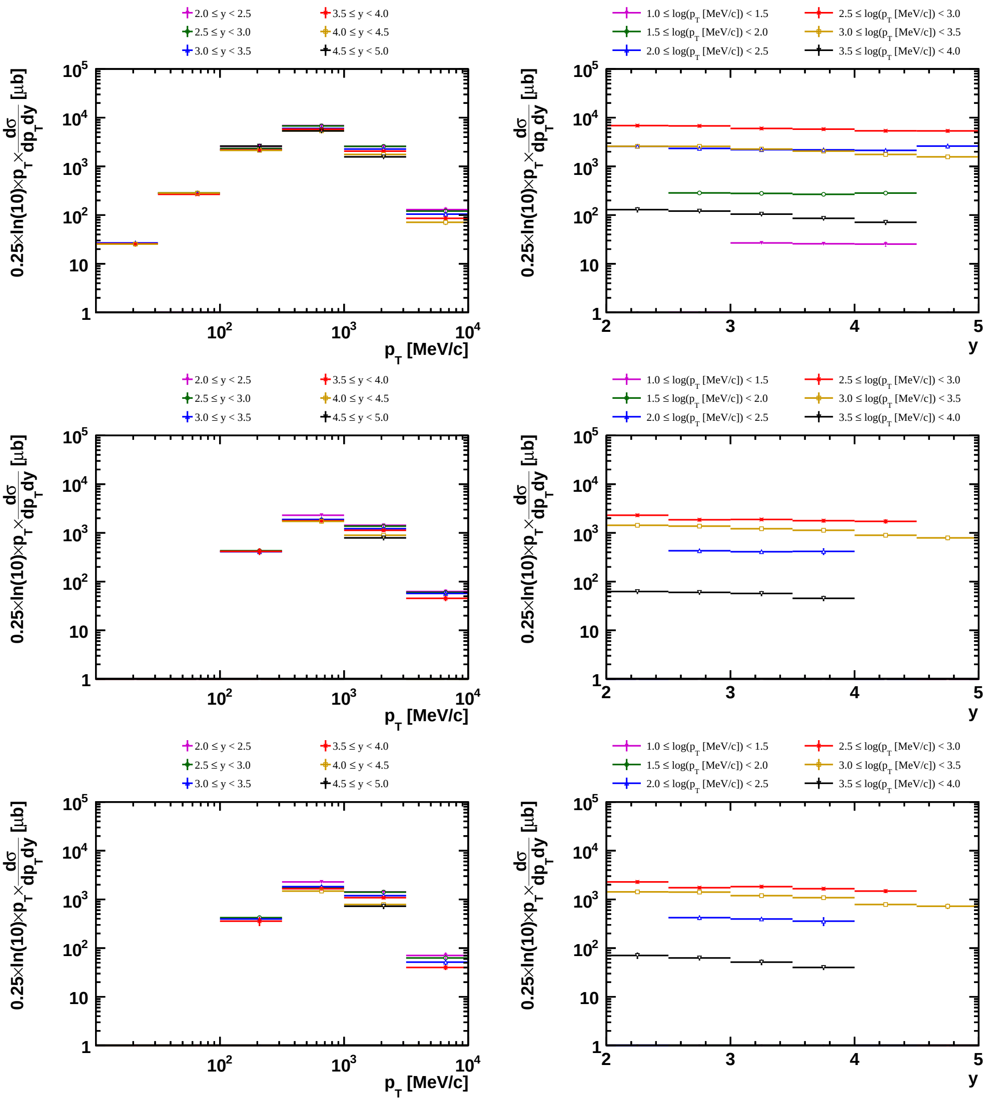

Figure 5.49: Double differential production cross-sections as a function of p_T and y for K^0_S (top), Λ^0 (middle) and $\overline{\Lambda^0}$ (bottom).

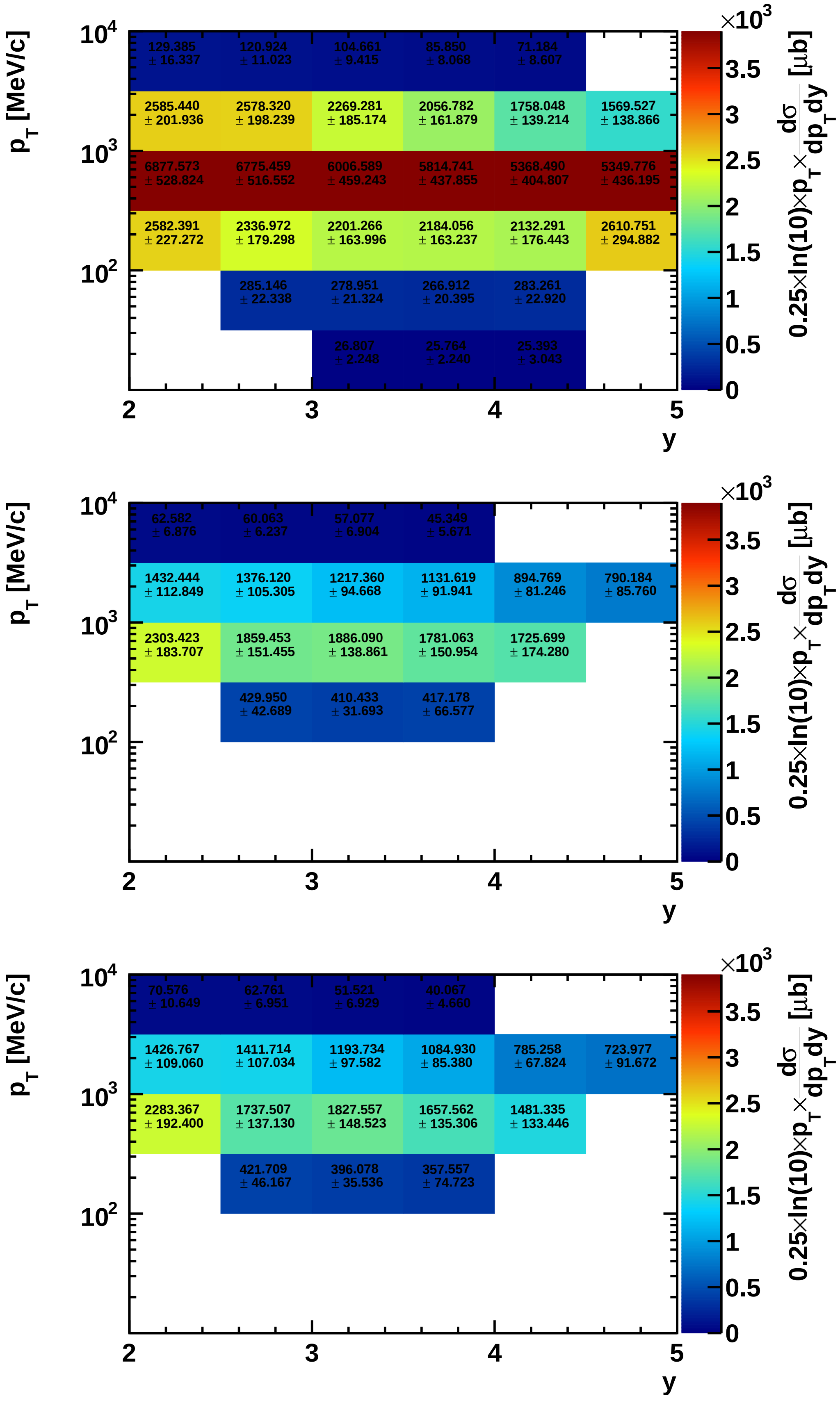

Figure 5.50: Production cross-sections for K_S^0 (top), Λ^0 (middle) and $\overline{\Lambda^0}$ (bottom).

The weights used for K^0_S are shown in Figure 5.51. The uncertainties taken into account in the computation of these weights, apart from the statistical ones, are the systematic uncertainties coming from the integrated luminosity and efficiency determination. The weights corresponding to the MU samples are generally larger and this is due to better statistics. This is also the case for $\Lambda^0/\overline{\Lambda^0}$ and the ratios, but, for brevity, the weights are not shown.

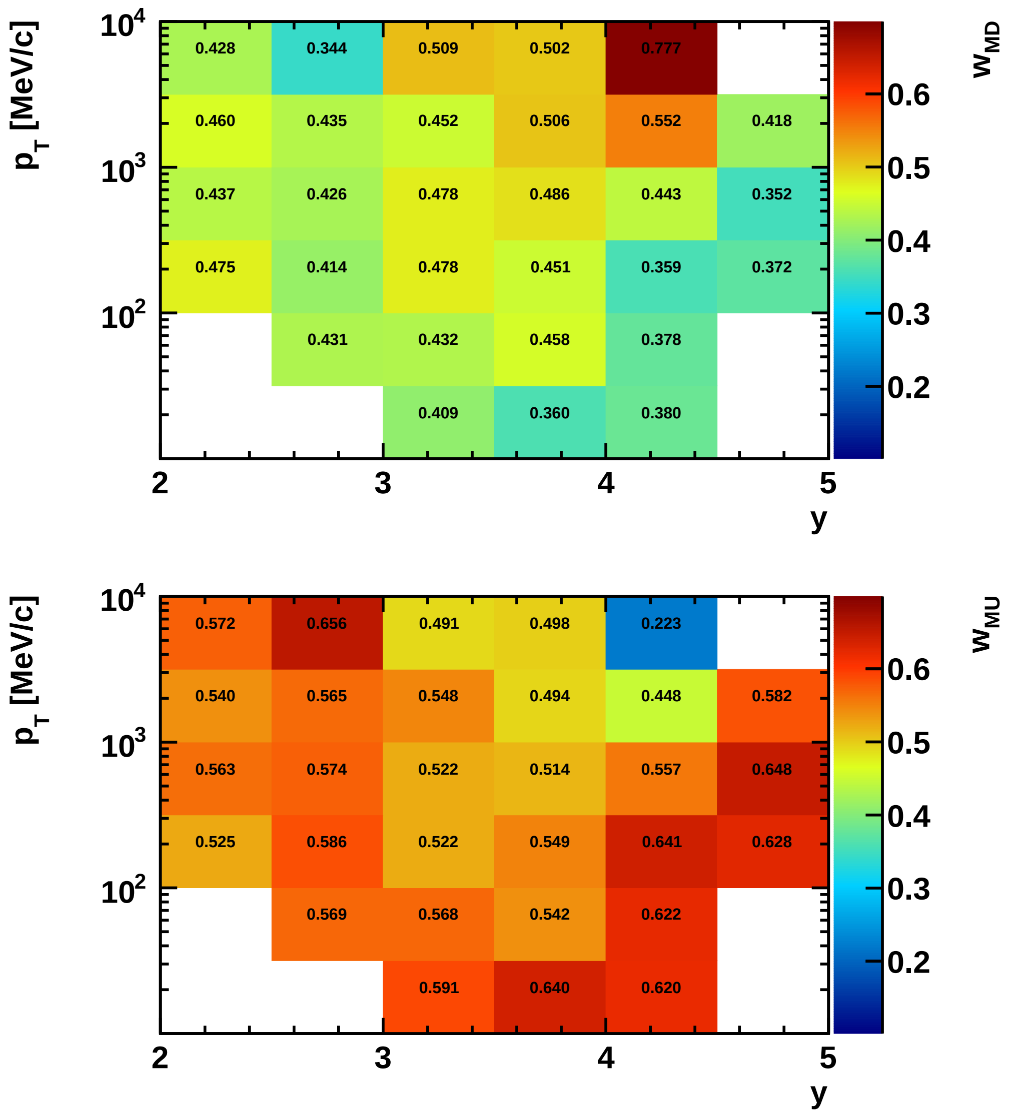

Figure 5.51: Weights used for the computation of the average cross-section for K^0_S.

5.18 Ratios

The V^0 ratios as a function of p_T and y are shown in Figures 5.52 and 5.53. The values for the full analysis phase space are given in Table 5.15. A clear baryon number transport is observed for the $\overline{\Lambda^0}/\Lambda^0$ ratios. The $\overline{\Lambda^0}/\Lambda^0$ ratios show a slight trend of decrease towards high rapidities. The highest values are found in the $2.5 \leq \log(p_T[\mathrm{MeV/c}]) < 3$ region, while a slight decrease towards higher p_T and a steeper decrease towards lower p_T are observed. The values tend to a maximum of around 0.55.

Table 5.14: Antibaryon-baryon and antibaryon-meson ratios in the full analysis phase space.

Ratio	R
$\overline{\Lambda^0}/\Lambda^0$	0.960 ± 0.052
$\overline{\Lambda^0}/K_S^0$	0.329 ± 0.023

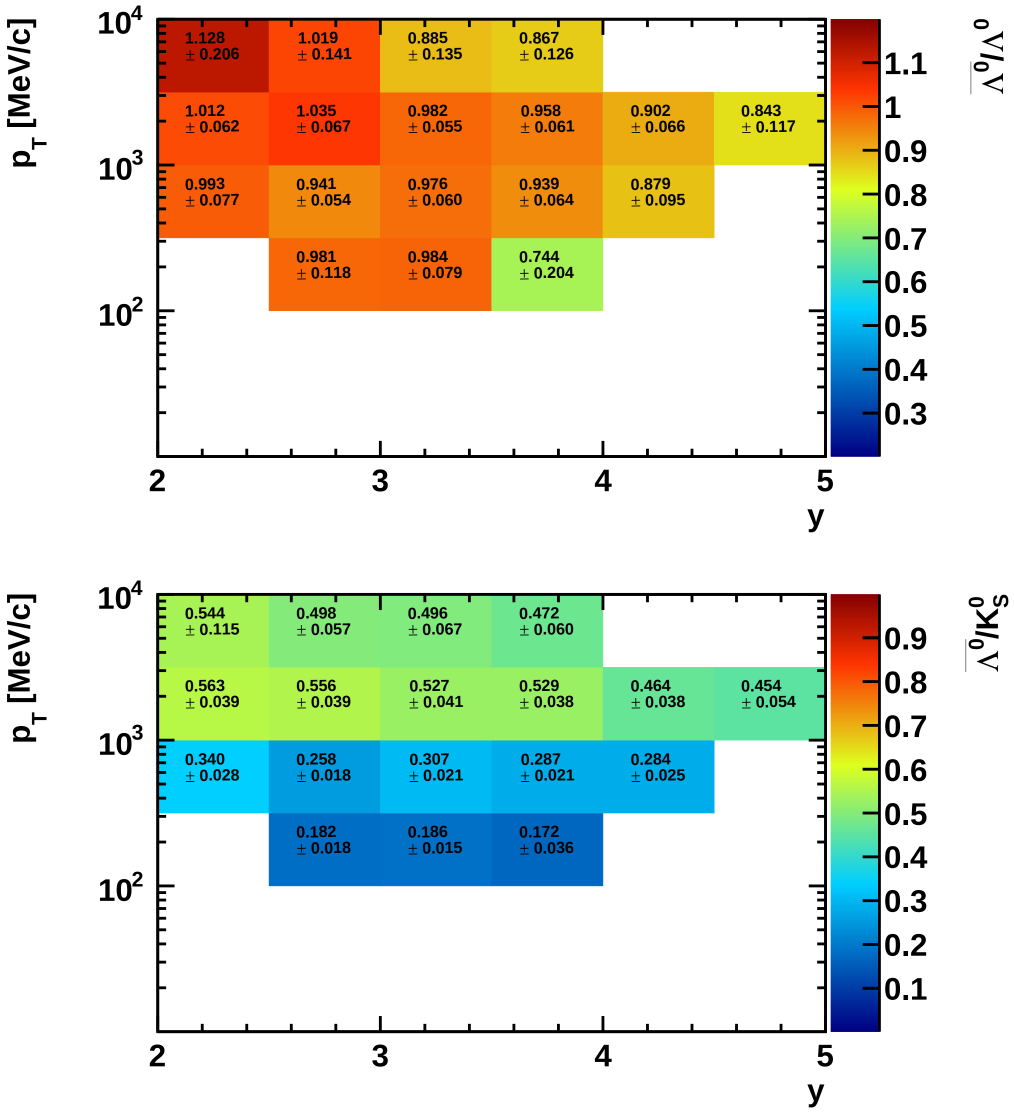

Figure 5.52: V^0 ratios.

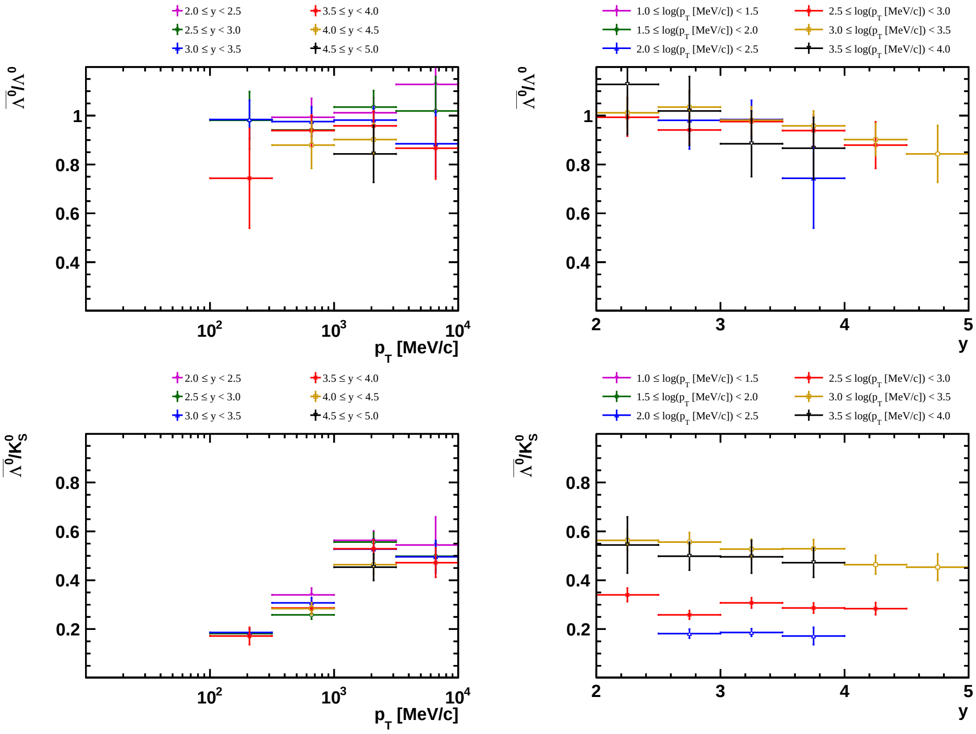

Figure 5.53: V^0 ratios as a function of p_T and y.

5.19 Comparison between magnet polarities

As discussed in Section 5.9, the cross-sections are computed as:

$$\sigma_{\mathrm{MD}} = \frac{N^{\mathrm{Data}}_{\mathrm{MD}}}{\varepsilon^{\mathrm{MC}}_{\mathrm{MD}} \cdot \mathcal{L}_{\mathrm{MD}}} \quad \text{and} \quad \sigma_{\mathrm{MU}} = \frac{N^{\mathrm{Data}}_{\mathrm{MU}}}{\varepsilon^{\mathrm{MC}}_{\mathrm{MU}} \cdot \mathcal{L}_{\mathrm{MU}}}, \tag{5.34}$$

where the subscripts indicate the magnet polarity, $N^{\mathrm{Data}}_{\mathrm{MD,MU}}$ are the raw signal yields, $\mathcal{L}_{\mathrm{MD,MU}}$ are the integrated luminosities, and $\varepsilon^{\mathrm{MC}}_{\mathrm{MD,MU}}$ are the reconstruction and selection efficiencies estimated from MC.

The ratio of the cross-sections measured with opposite magnet polarities will be:

$$\frac{\sigma_{\mathrm{MU}}}{\sigma_{\mathrm{MD}}} = \frac{\varepsilon^{\mathrm{MC}}_{\mathrm{MD}}}{\varepsilon^{\mathrm{MC}}_{\mathrm{MU}}} \cdot \frac{N^{\mathrm{Data}}_{\mathrm{MU}}}{\mathcal{L}_{\mathrm{MU}}} \cdot \frac{\mathcal{L}_{\mathrm{MD}}}{N^{\mathrm{Data}}_{\mathrm{MD}}}. \tag{5.35}$$

The integrated luminosities have uncertainties of 3.9% and 4.0% for the MD and MU samples, respectively. These are fully correlated [156] and so, the uncertainty on the cross-section ratio above due to the luminosity measurements is a negligible 0.1%. The raw signal yields may be biased due to the selection of the fit model, as detailed in Section 5.22.5. The corresponding systematic uncertainties are found to be below 1.0% for most bins in the case of K^0_S. and slightly higher for $\Lambda^0/\overline{\Lambda}^0$. These values are obtained using the MD samples. The ones for the MU samples are assumed to be similar, with no straightforward method of determining the correlation between them and the MD ones. The statistical uncertainties are given in Section 5.21. These are mostly below 1.0% for K^0_S. This is also the case for $\Lambda^0/\overline{\Lambda^0}$ in the center of the analysis phase space, but values of 2.0%-3.0% are found at the edges. Thus, the combined uncertainties on the cross-section ratios corresponding to the integrated luminosities and raw signal yields are on the order of a few percent. In this case, if the experimental efficiencies, $\varepsilon^{\text{Data}}_{\text{MD,MU}}$, are correctly estimated from MC, the cross-section ratios should be around unity with fluctuations on the order of $\mathcal{O}(0.01)$:

$$\frac{\sigma_{\text{MU}}}{\sigma_{\text{MD}}} \approx 1 \Leftrightarrow \frac{\varepsilon^{\text{Data}}_{\text{MD}}}{\varepsilon^{\text{Data}}_{\text{MU}}} \approx \frac{N^{\text{Data}}_{\text{MD}}}{\mathcal{L}_{\text{MD}}} \cdot \frac{\mathcal{L}_{\text{MU}}}{N^{\text{Data}}_{\text{MU}}}. \tag{5.36}$$

So, the ratio between the luminosity weighted raw signal yields provides an estimate of the ratio between the real experimental efficiencies.

Larger fluctuations would be driven by differences between the true experimental efficiencies and the ones estimated from MC. Combining the right-hand side of Equation (5.36) with Equation (5.35):

$$\frac{\sigma_{\text{MU}}}{\sigma_{\text{MD}}} \approx \frac{\varepsilon^{\text{MC}}_{\text{MD}}}{\varepsilon^{\text{MC}}_{\text{MU}}} \cdot \frac{\varepsilon^{\text{Data}}_{\text{MU}}}{\varepsilon^{\text{Data}}_{\text{MD}}}. \tag{5.37}$$

The cross-section, experimental and MC efficiency ratios are compared in Figure 5.54.

The V^0 decays with two charged particles in the final state are categorized according to the kinematics of the decay products in the presence of a magnetic field. If the trajectories of the daughters converge, the mother particles are called "cowboys" and if they diverge, then the mother particles are called "sailors". These scenarios interchange when the initial directions of the daughter particles are swaped or the magnet polarity is flipped [159, 183]. This effect might induce differences between the reconstruction efficiencies in the MD and MU configurations, as the charged particles will pass through different regions of the detector.

In the case of the symmetric decay of $K^0_S \to \pi^+\pi^-$, the aforementioned effect is negligible. However, given the highly asymmetric kinematics of the $\Lambda^0 \to p\pi^-$ and its charge conjugate counterpart decays, significant differences between the efficiencies are expected. When computing the ratio of the efficiencies for baryons and antibaryons with the magnet polarities flipped between them, the "cowboys" and "sailors" effect should cancel out [183]. These ratios are shown in Figure 5.54.

The remaining deviations from unity of the ratios of experimental efficiencies are generally compatible with the differences between the cross-sections of the interactions of the daughter particles with the detector material. The ratios of MC efficiencies have large deviations from the experimental ones in some phase space regions, especially in the case of $\overline{\Lambda^0}$, further motivating the need of developing tag-and-probe methods which use V^0 daughters, as discussed in Section 5.12.

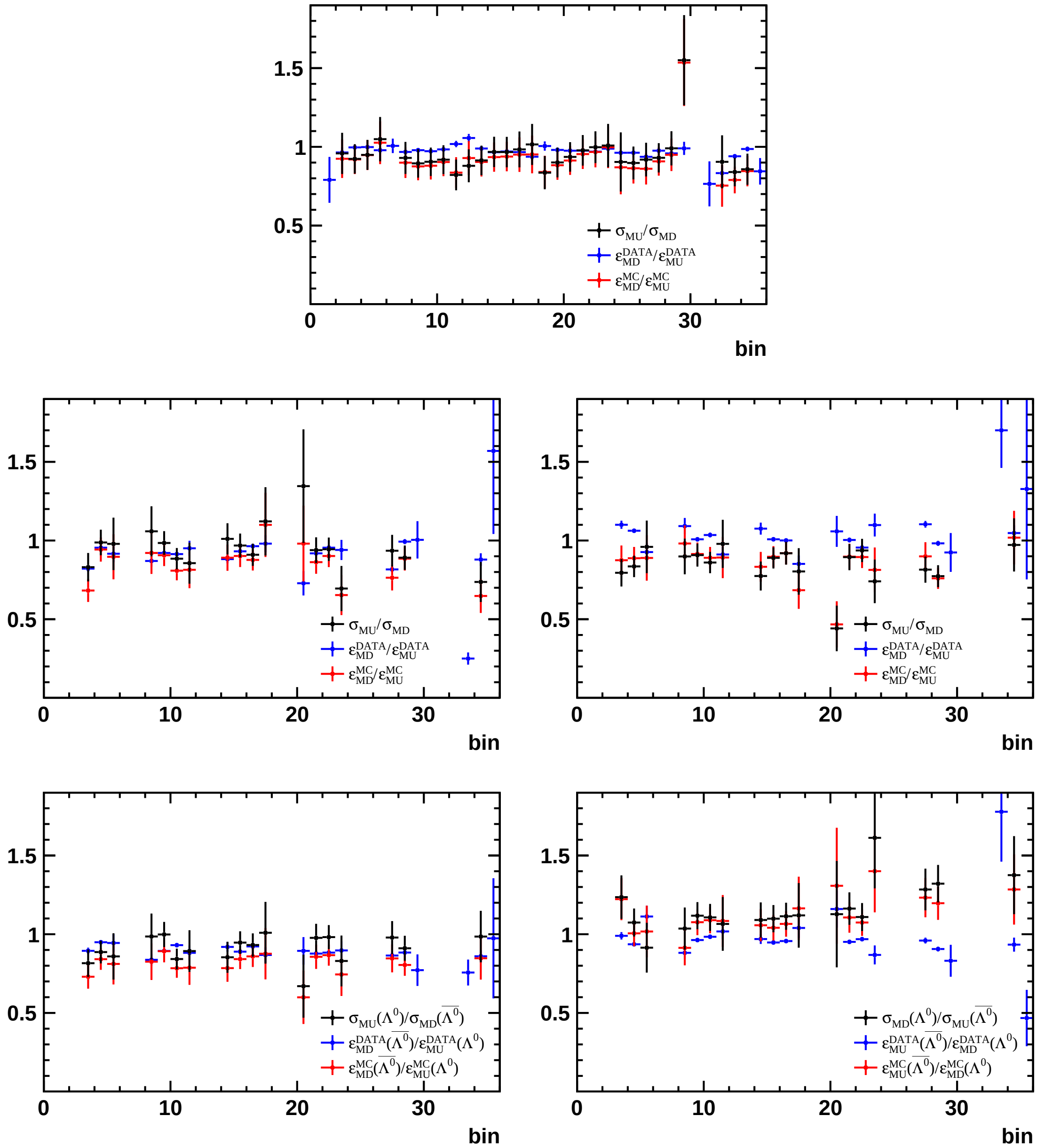

Figure 5.54: Cross-section and efficiency ratios for K_S^0 (top), Λ^0 (middle left) and $\overline{\Lambda^0}$ (middle right). The $\Lambda^0/\overline{\Lambda^0}$ ratios with the magnet polarity flipped are shown in the bottom plots. The $n \times m$, where $n = m = 6$, bin matrix is converted into a single row vector through looping over n and m, where n and m correspond to the y and $\log(p_T[\mathrm{MeV/c}])$ bins, respectively. The bin numbers correspond to $6(n-1)+m$. The statistical and systematic uncertainties from the luminosity and MC efficiency determination are propagated to the different ratios.

5.20 Generator predictions

The ratios between the cross-sections obtained from a sample generated with version 8.219 of PYTHIA and the measured ones are shown in Figures 5.55 and 5.56. The values for the full analysis phase space are given in Table 5.15. The full analysis phase space cross-section for K_S^0 is overestimated at a level of around 4.5%, which is within one standard deviation, while the predictions for $\Lambda^0/\overline{\Lambda^0}$ are at around 58% of the measured values.

It can be seen that the deviations for K_S^0 are within 10% and generally within one standard deviation in the $2.5 \le \log(p_T[\mathrm{MeV/c}]) < 4.0$ region. An overestimation trend is observed towards low p_T where the deviations reach a maximum of around 30%.

In the case of $\Lambda^0/\overline{\Lambda^0}$, the ratios drop from around 0.80-0.90 at low p_T to around 0.50 in the $3.0 \le \log(p_T[\mathrm{MeV/c}]) < 3.5$ region and rise again to values of 0.65-0.75 in the highest p_T bins.

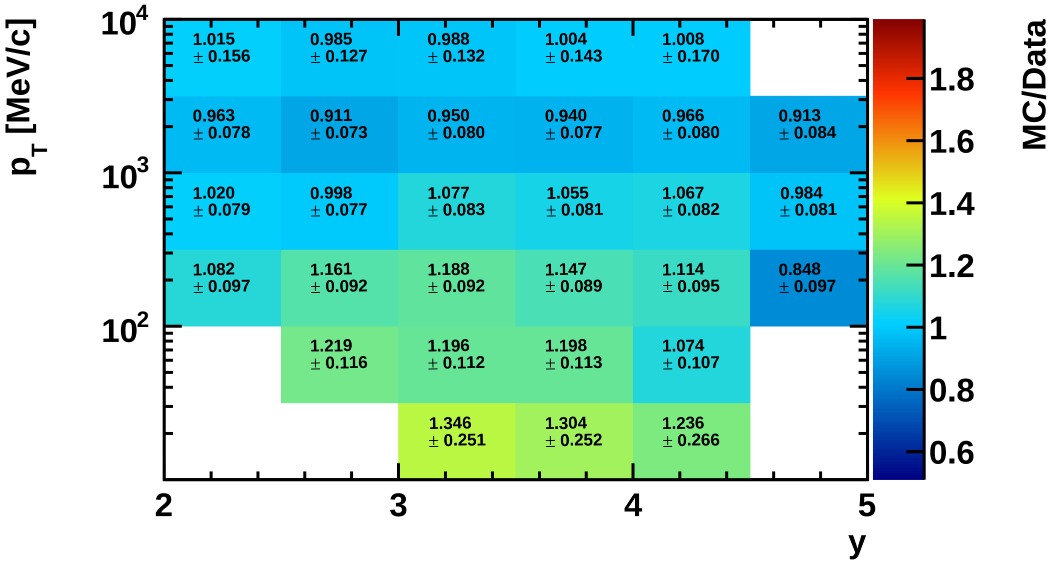

Figure 5.55: The MC/Data cross-section ratios for K_S^0.

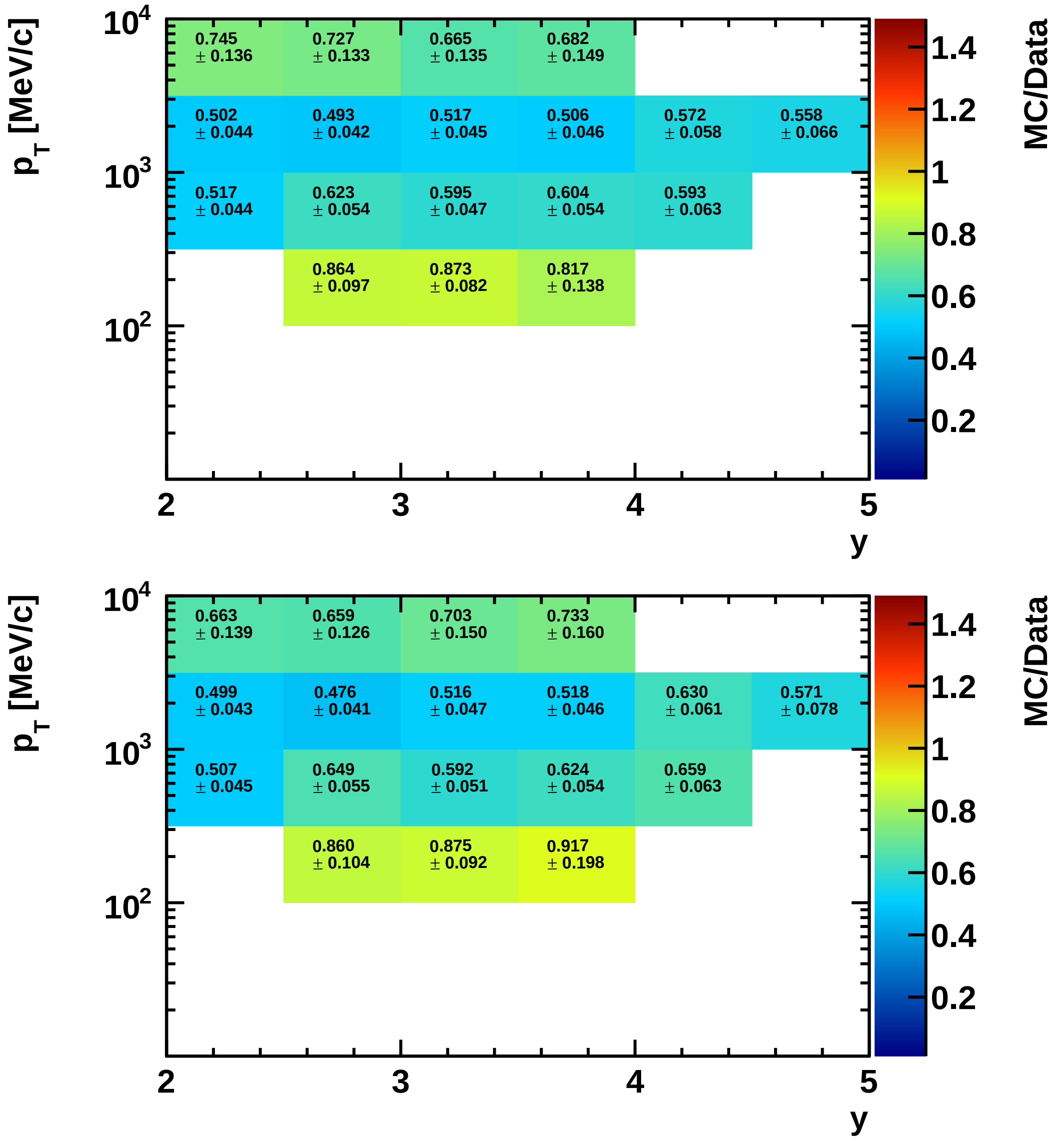

Figure 5.56: The MC/Data cross-section ratios for Λ^0 (top) and $\overline{\Lambda^0}$ (bottom).

Table 5.15: Full analysis phase space cross-sections for V^0 hadrons from data and MC.

Particle	σ [µb]	σ_{MC} [µb]	$\sigma_{\mathrm{MC}}/\sigma$
K_S^0	$64\,501.5 \pm 4\,787.3$	$67\,365.9 \pm 29.7$	1.0444 ± 0.0775
Λ^0	$22\,106.3 \pm 1\,656.5$	$12\,640.1 \pm 12.9$	0.5718 ± 0.0428
$\overline{\Lambda^0}$	$21\,013.7 \pm 1\,654.3$	$12\,208.4 \pm 12.6$	0.5810 ± 0.0457

5.21 Statistical uncertainties

The relative statistical uncertainties of the raw signal yields from data are propagated to the cross-section measurements and are shown in Figure 5.57. These are mostly at the per mille level for K_S^0, with values of around 1.0-3.0% being observed in the peripheral bins. A similar pattern is observed for $\Lambda^0/\overline{\Lambda^0}$, but with slightly higher uncertainties which reach a maximum of around 5.0%.

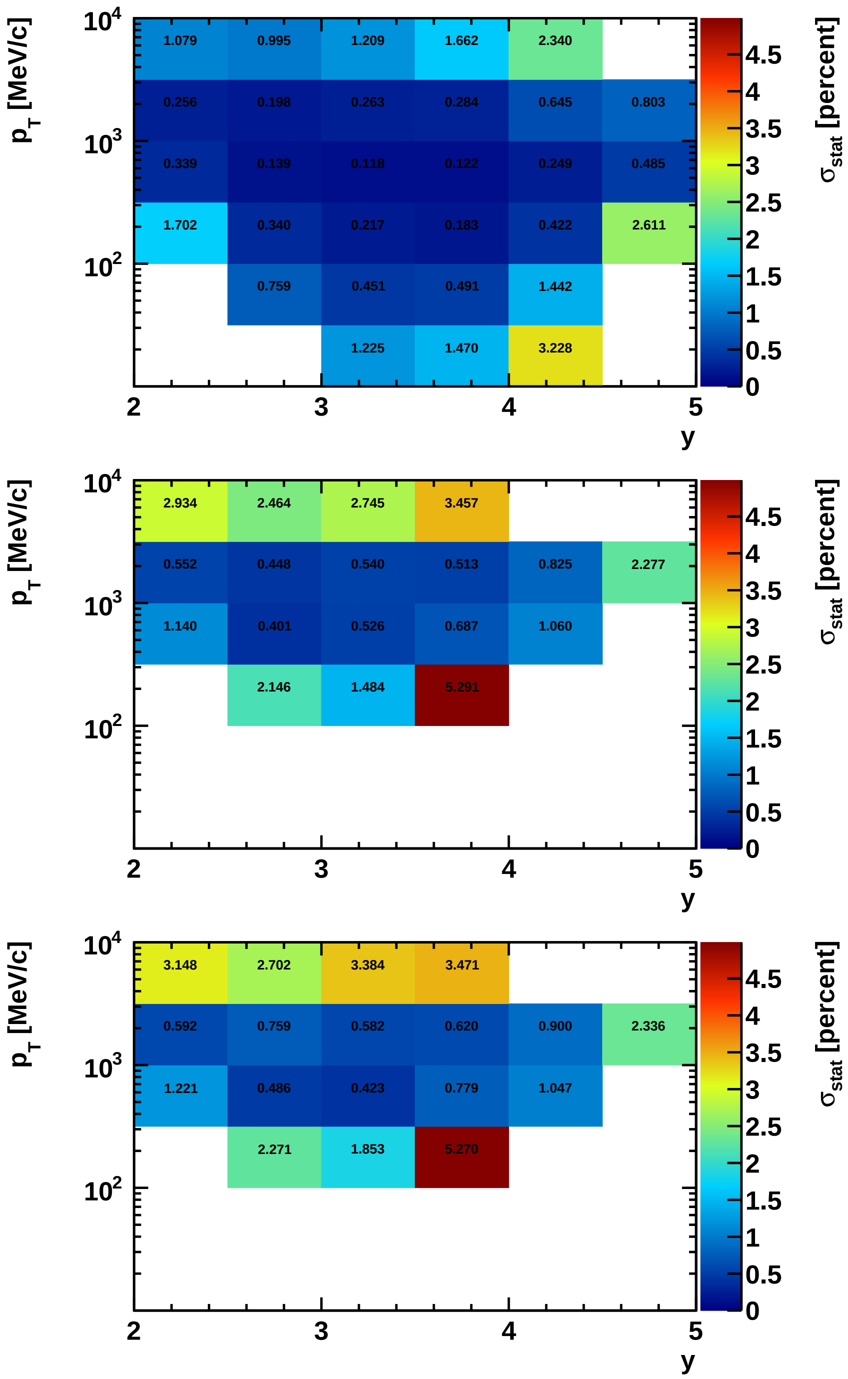

Figure 5.57: Relative statistical uncertainties for K_S^0 (top), Λ^0 (middle) and $\overline{\Lambda^0}$ (bottom).

5.22 Systematic uncertainties

5.22.1 MC statistics

The systematic uncertainties coming from the statistical ones of MC signal yields and numbers of generated particles used in the efficiency computation are given as relative uncertainties in Figure 5.58. The values are below 1.0% and around 1.0-2.0% in the central bins, rising to around 8.0% and 16.0% towards the edges of the phase space, for K^0_S and $\Lambda^0/\overline{\Lambda^0}$, respectively.

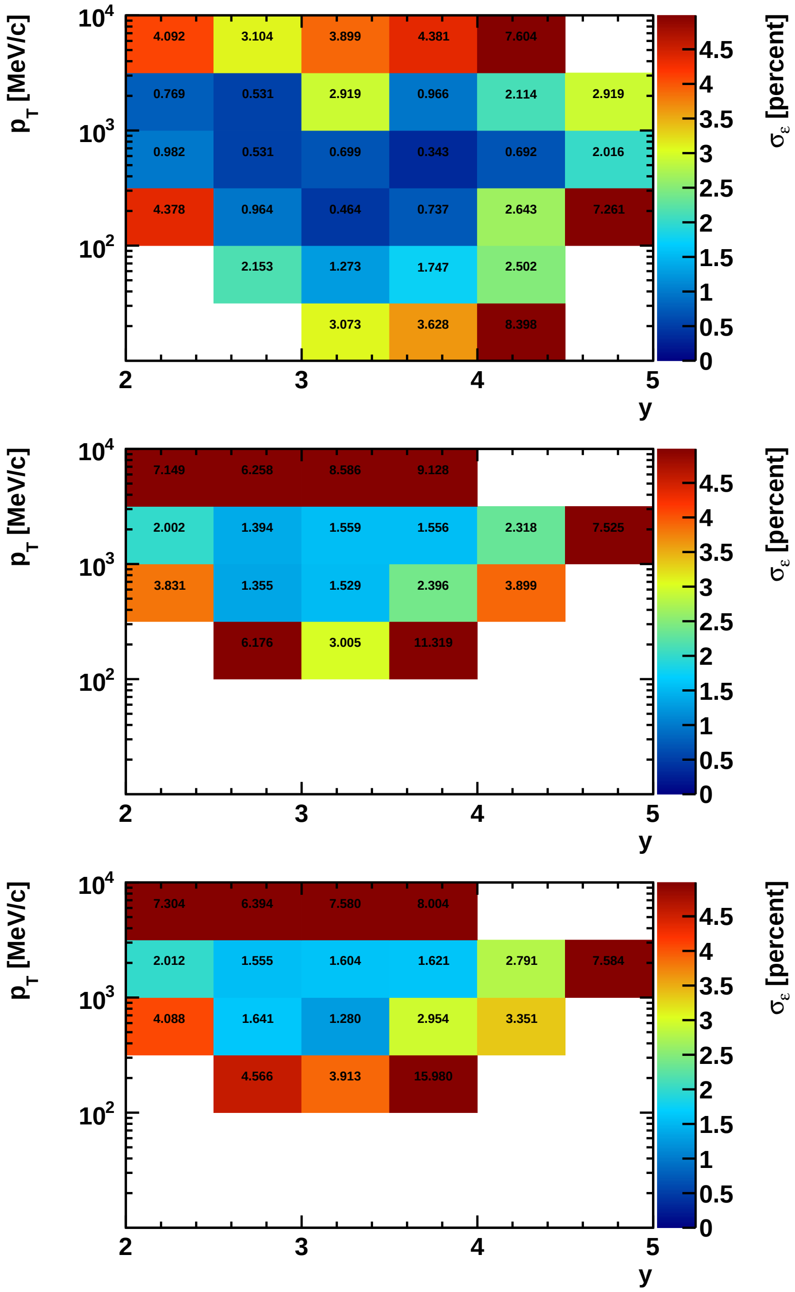

Figure 5.58: Relative systematic uncertainties from MC statistics for K^0_S (top), Λ^0 (middle) and $\overline{\Lambda^0}$ (bottom).

5.22.2 Integrated luminosity

The uncertainties on the integrated luminosities of 3.9% and 4.0% for the MD and MU samples, respectively, are fully correlated [156].

5.22.3 Efficiency correction

The systematic uncertainty due to the efficiency correction has three components:

- Uncorrelated uncertainties - the sum of statistical and systematic uncertainties from the different methods used to determine the ratios. These are the uncertainties given in the ratios plot [135, 161, 184]. An arbitrary conservative uncertainty of 5% has been assigned to tracks which are outside of the phase space covered by the efficiency ratios plot.
- A fully correlated uncertainty of 0.6% per track. This is obtained by recomputing the ratios after the reweighting of the MC samples to match the experimental distributions of N_{PV} and $N_{\mathrm{SPD\ hits}}$ and taking the largest difference as the systematic uncertainty [128, 135, 138, 161, 184].
- Uncertainty on hadronic interactions.

Preliminary values of 7% and 5%, which should be viewed as upper limits, are assigned for K_S^0 and $\Lambda^0/\overline{\Lambda^0}$ to account for the first two contributions. These values are justified by the fact that large fractions of the pions from K_S^0 are outside of the TrackCalib phase space and the (anti-) protons from $\Lambda^0/\overline{\Lambda^0}$ are mostly within the phase space covered by the ratios. More precise values for each phase space bin will be determined after the efficiency ratios will be obtained using V^0 daughters as described in Section 5.12.

In order to test the applicability of these preliminary values, a procedure inspired from [161, 184] is carried out for several bins. The first two contributions are propagated at the same time to the MC yields using a toy Monte Carlo method, consisting of 100 iterations. At the start of each iteration, the ratios used to weigh the tracks are randomly generated according to a gaussian function with the mean equal to the ratio from the plot and the standard deviation equal to the uncertainty of the ratio. Afterwards, another weight is randomly generated according to a gaussian with $\mu = 1$ and $\sigma = 0.006$, which is applied to each track. After each iteration, the yields are extracted and added to a histogram which is fitted with a gaussian function. The relative systematic uncertainty will be the ratio of the standard deviation and mean obtained from the fit [161, 184]. The results of this procedure are shown in Figure 5.59. The uncertainties are around 7.7% and 5.6% for K_S^0 and Λ^0, respectively, in bins with large fractions of daughters outside the TrackCalib phase space, while values of around 1.7% and 2.8% are obtained in bins with small fractions.

5.22.4 Hadronic interactions

As discussed in Section 5.13, the uncertainties on the cross-sections due to hadronic interactions are 3.8%, 4.0% and 4.5% for K_S^0, Λ^0 and $\overline{\Lambda^0}$, respectively. These are assumed to be fully correlated and thus, the uncertainties on the ratios will be 0.5% and 0.7% for the antibaryon-baryon and antibaryon-meson ratios, respectively.

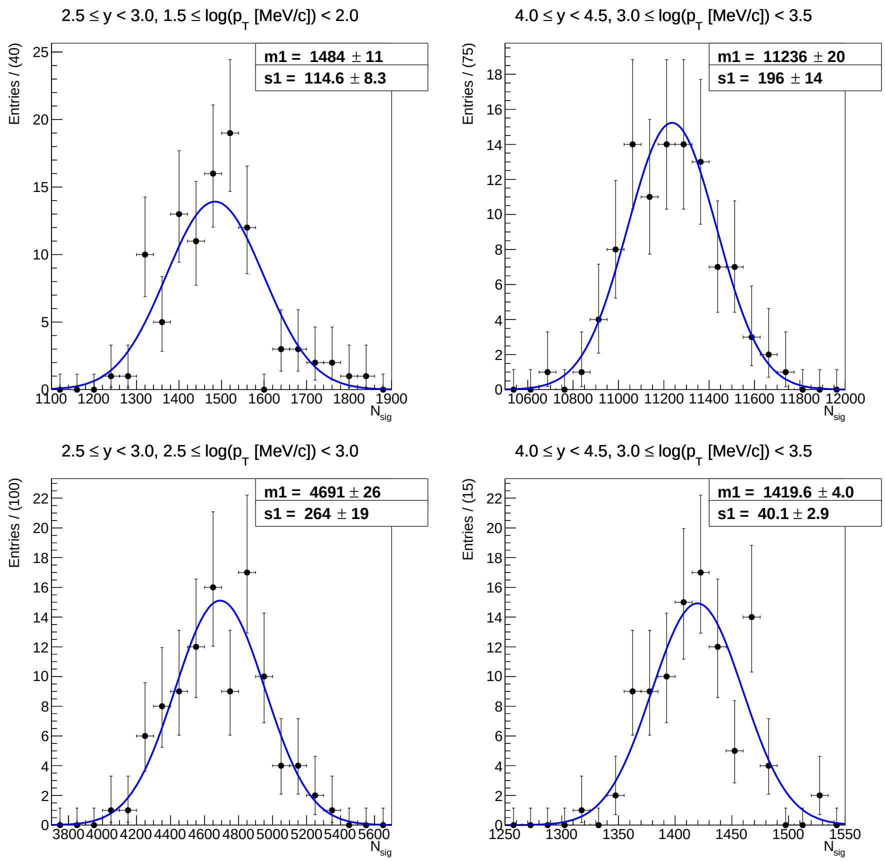

Figure 5.59: Fits to the distributions of signal yields obtained with the toy MC method in different phase space bins for K_S^0 (top) and Λ^0 (bottom).

5.22.5 Fit model

The n-Gaussian PDFs used to model the signal may not approximate the true distributions with sufficient accuracy. In order to estimate the systematic uncertainty due to the modelling, the data yields from the MD samples are obtained using two additional signal PDFs, namely Double-Sided Crystal Ball (DSCB) and ExpGaussExp (EGE) functions, both consisting of a Gaussian core and exponential tails:

$$f_{\mathrm{DSCB}}(x) = \begin{cases} e^{-\frac{1}{2}\cdot\alpha_L^2\cdot\left[\frac{\alpha_L}{n_L}\cdot\left(\frac{n_L}{\alpha_L}-\alpha_L-\left(\frac{x-\mu}{\sigma}\right)\right)\right]^{-n_L}}, & \dfrac{x-\mu}{\sigma} < -\alpha_L, \\ e^{-\frac{1}{2}\cdot\left(\frac{x-\mu}{\sigma}\right)^2}, & -\alpha_L \leq \dfrac{x-\mu}{\sigma} \leq \alpha_H, \\ e^{-\frac{1}{2}\cdot\alpha_H^2\cdot\left[\frac{\alpha_H}{n_H}\cdot\left(\frac{n_H}{\alpha_H}-\alpha_H+\left(\frac{x-\mu}{\sigma}\right)\right)\right]^{-n_H}}, & \dfrac{x-\mu}{\sigma} > \alpha_H, \end{cases} \tag{5.38}$$

$$f_{\mathrm{EGE}}\left(x\right) = \begin{cases} e^{\frac{k_L^2}{2} + k_L \cdot \left(\frac{x-\mu}{\sigma}\right)}, & \dfrac{x-\mu}{\sigma} < -k_L, \\ e^{-\frac{1}{2} \cdot \left(\frac{x-\mu}{\sigma}\right)^2}, & -k_L \leq \dfrac{x-\mu}{\sigma} \leq k_H, \\ e^{\frac{k_H^2}{2} - k_H \cdot \left(\frac{x-\mu}{\sigma}\right)}, & \dfrac{x-\mu}{\sigma} > k_H, \end{cases} \tag{5.39}$$

where μ is the mode of the distribution and σ is the width of the Gaussian [185, 186].

The largest deviation from the nominal value is taken as the uncertainty and the relative values are shown in Figure 5.60.

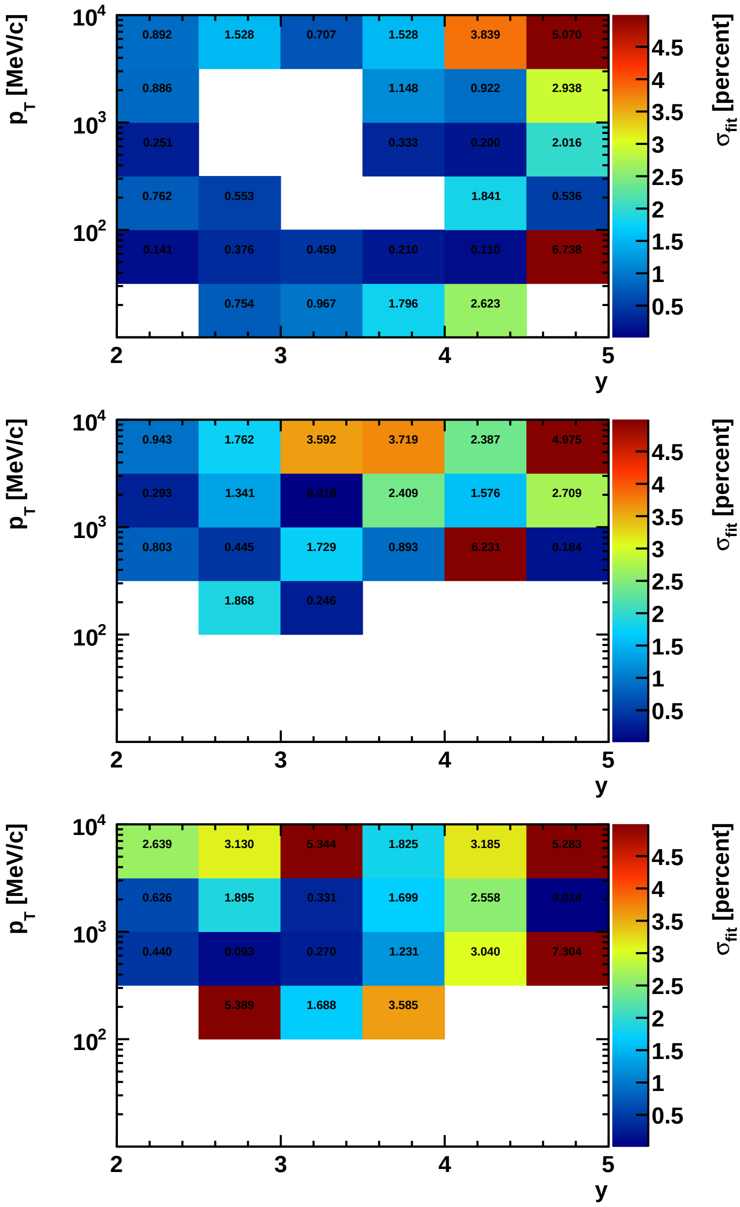

Figure 5.60: Relative systematic uncertainties from signal modelling K_S^0 (top), Λ^0 (middle) and $\overline{\Lambda^0}$ (bottom).

In some high statistics bins for K_S^0, the fits do not converge to reasonable values and thus, the uncertainty can not be estimated. This is also the case for the full analysis phase space fits for all V^0 species. As can be seen in Figure 5.60, the uncertainties in the neighbouring bins are generally at the per mille level, suggesting that the missing uncertainties are negligible. An increasing trend towards high rapidities is observed. There are also several bins for $\Lambda^0/\overline{\Lambda^0}$ in which the fits do not converge and so, in those with linear background shapes, the yields are computed using the sideband subtraction method.

The first step of the aforementioned method is of defining a signal region and so-called sidebands on each side of the former. The signal region is defined around the mass peak and should be wide enough to contain most of the signal candidates. The sidebands will mostly contain background candidates. If the background shape is linear and the width of each sideband is equal to half the width of the signal region, it can be simply shown that:

$$S = N_{\mathrm{sig}} - N_{\mathrm{sb}} \qquad \text{and} \qquad \sigma_S^2 = \sqrt{N_{\mathrm{sig}} + N_{\mathrm{sb}}}, \tag{5.40}$$

where S is the signal yield, N_{sig} is the number of candidates in the signal region, N_{sb} is the number of candidates in the sidebands and σ_S^2 is the uncertainty of the signal yield [187].

This method is not applicable in the case of the missing bins for K_S^0, due to the non-linearity of the background shapes. There is also a single bin for Λ^0 in which neither the fits converge, nor the sideband subtraction can be used.

In several bins, the MC yields can not be extracted and so, the computation of the cross-sections is not possible, as discussed in Section 5.15. The maximum values of the signal modelling uncertainties from bins in which the cross-sections are computed are around 4.0% and 6.0% for K_S^0 and $\Lambda^0/\overline{\Lambda^0}$, respectively.

5.22.6 Fisher discriminant

The systematic uncertainty due to the Fisher discriminant cut in estimated from the MD samples. The cross-sections and ratios are recomputed after the cut is relaxed to FD > 8 and the differences between these values and the nominal ones are taken as systematic uncertainties. The relative uncertainties and the ratios between the cross-sections obtained with the relaxed and nominal FD cuts are shown in Figures 5.61 and 5.62. The values for K_S^0 are below 2.0% with two exceptions in peripheral bins, namely 3.4% and around 8.5%, while the ones for Λ^0 are generally higher and range between 0.1% and 4.5% with two exceptional values of around 5.3% and 7.3%. There are relatively large differences between the values for $\overline{\Lambda^0}$ and Λ^0. As can be seen in Figure 5.62, in which the uncertainties represent the combined statistical ones of the data and MC yields, the values are within one standard deviation of each other and so, are consistent with statistical fluctuations.

For most bins, an increase in the values of the cross-sections with the relaxing of the FD cut is observed, suggesting that the cut affects signal candidates from data and MC differently. The ratios between yields from both data and MC samples with the relaxed and nominal cuts are shown in Figure 5.63, where it can be seen that the increase of the data yields is generally larger than in the case of MC.

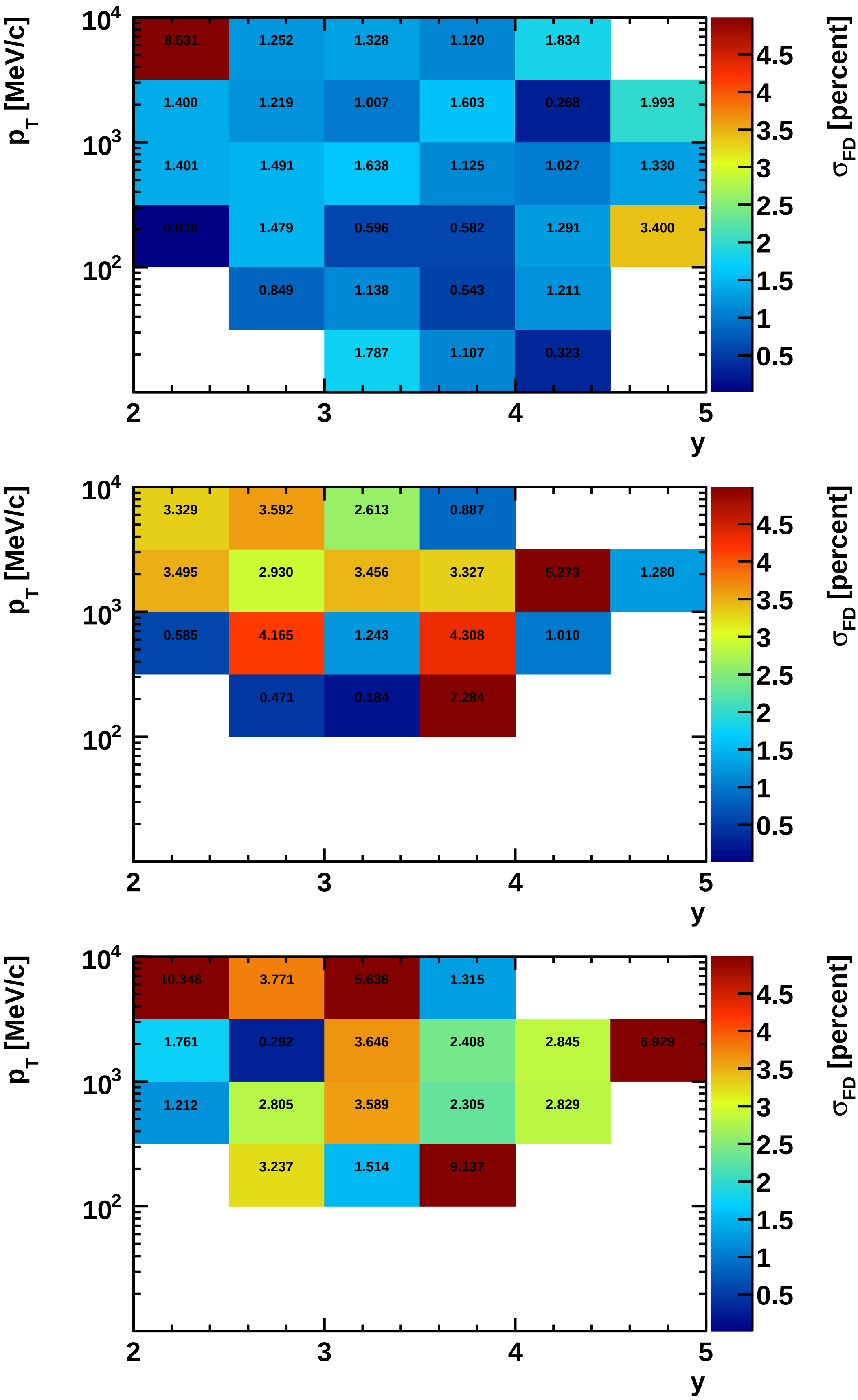

Figure 5.61: Relative systematic uncertainties from the Fisher discriminant cut for K^0_S (top), Λ^0 (middle) and $\overline{\Lambda^0}$ (bottom).

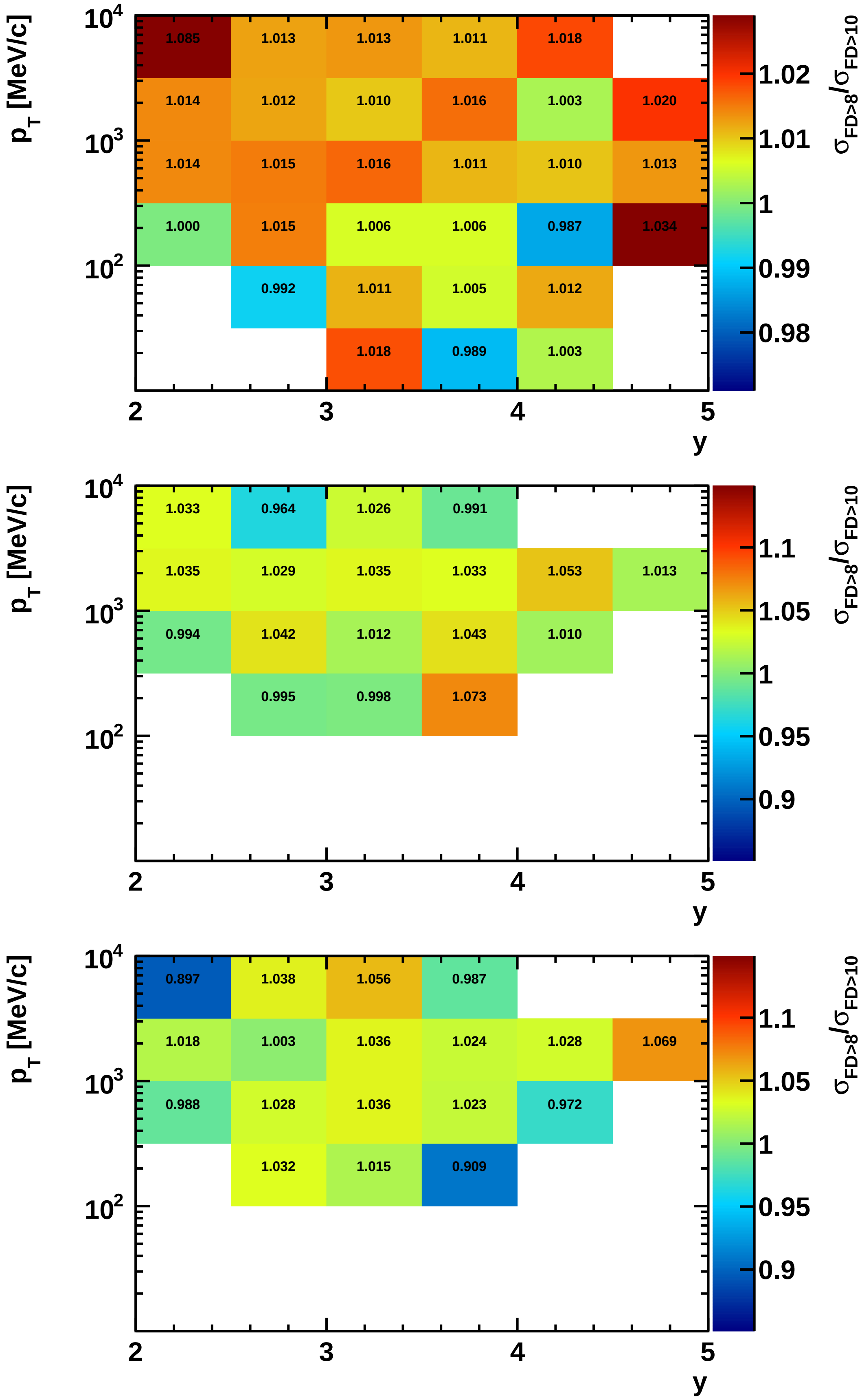

Figure 5.62: Ratios between the cross-sections obtained from MD samples with FD > 8 and FD > 10 for K_S^0 (top), Λ^0 (middle) and $\overline{\Lambda^0}$ (bottom).

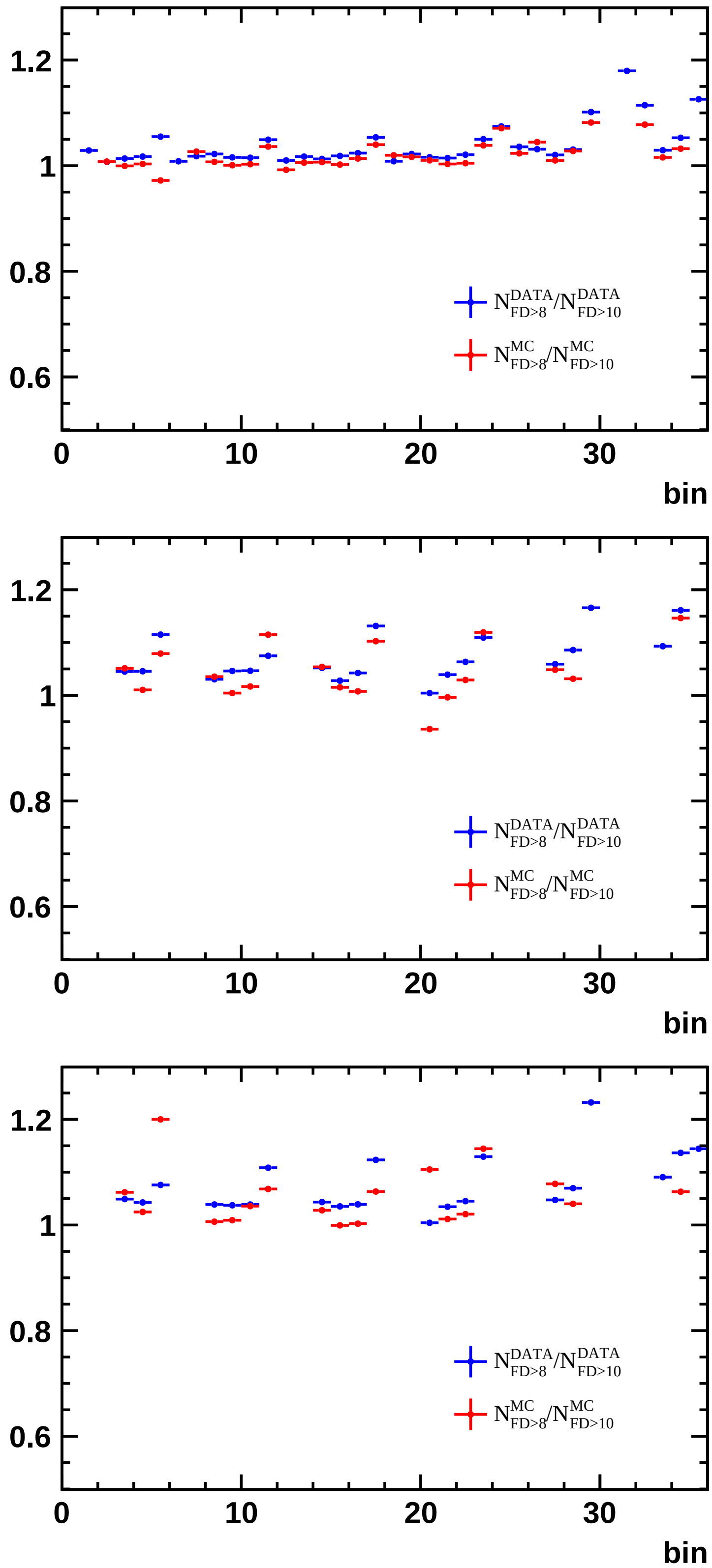

Figure 5.63: Data and MC ratios of yields from samples with FD > 8 and FD > 10 for K^0_S (top), Λ^0 (middle) and $\overline{\Lambda^0}$ (bottom). The $n \times m$, where $n = m = 6$, bin matrix is converted into a single row vector through looping over n and m, where n and m correspond to the y and $\log(p_T[\mathrm{MeV/c}])$ bins, respectively. The bin numbers correspond to $6(n-1)+m$.

Due to the method of estimating the uncertainties, they will be fully correlated between the different V^0 hadrons. The correlation factors are either positive or negative with a strong preference for the former. The uncertainties on the ratios are shown in Figure 5.64. Most of the values are below 4.0%, but there are several bins towards the edges of the phase space with uncertainties as high as around 17.0%.

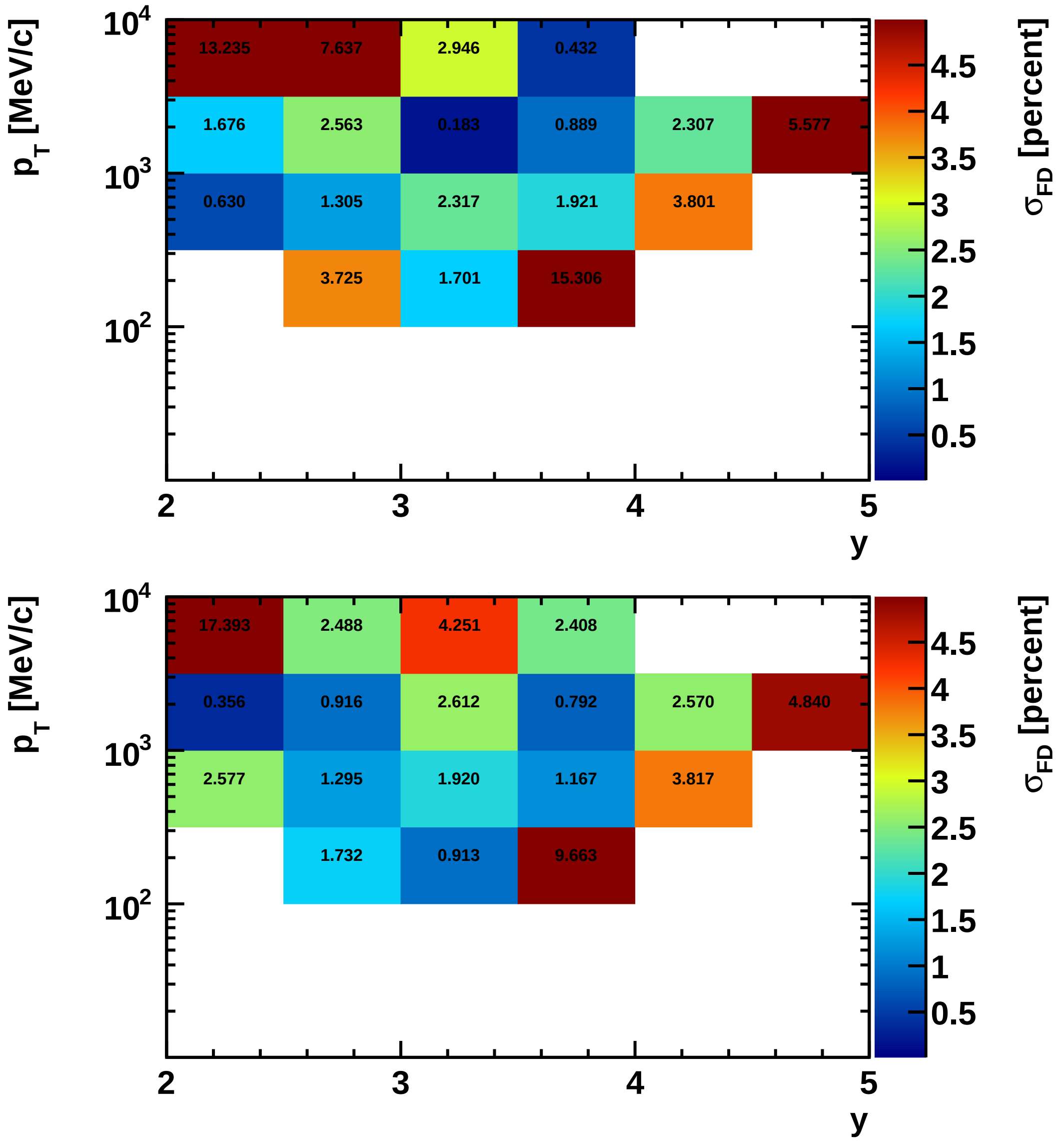

Figure 5.64: Relative systematic uncertainties from the Fisher discriminant cut for the $\overline{\Lambda^0}/\Lambda^0$ (top) and $\overline{\Lambda^0}/K^0_S$ (bottom) ratios.

5.22.7 Non-prompt fraction uncertainty

Based on the findings from Sections 5.11.2 and 5.20, the non-prompt fraction in data, f_n^{Data}, is set to the value from MC, f_n^{MC}, and a conservative 50% uncertainty is assigned to it, which is propagated to the cross-sections and ratios using standard error propagation [188]. The uncertainties are assumed to be fully correlated between baryons and antibaryons and uncorrelated between mesons and antibaryons.

The relative values for the cross-sections and ratios are shown in Figures 5.65 and 5.66, respectively. In the case of K_S^0, the uncertainties are mostly below 1.0% in the $p_T < 1.0$ GeV/c region and they increase with p_T to a maximum of around 3.5%. For the baryons and antibaryons, the values are lower than 1.5%, with a few exceptions at around 2.0-2.5%. The uncertainties on the antibaryon-meson ratios are mostly at the per mille level, with a few values larger than 1% at the edges of the phase space. Values of around 2.0% and 3.0-4.0% are observed in the lowest and highest p_T regions, respectively, covered by the antibaryon-baryon ratios. In the intermediate p_T regions, the uncertainties are between 1.0% and 2.0%.

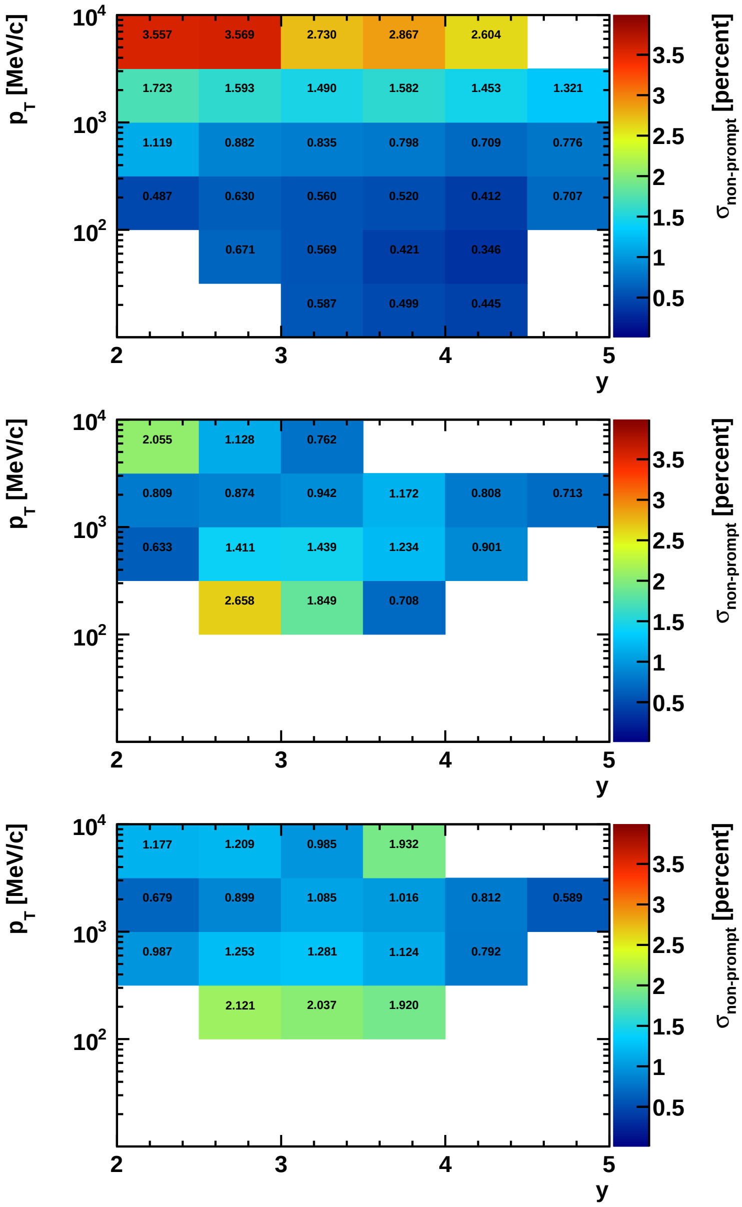

Figure 5.65: Relative systematic uncertainties from non-prompt fractions for K_S^0 (top), Λ^0 (middle) and $\overline{\Lambda^0}$ (bottom).

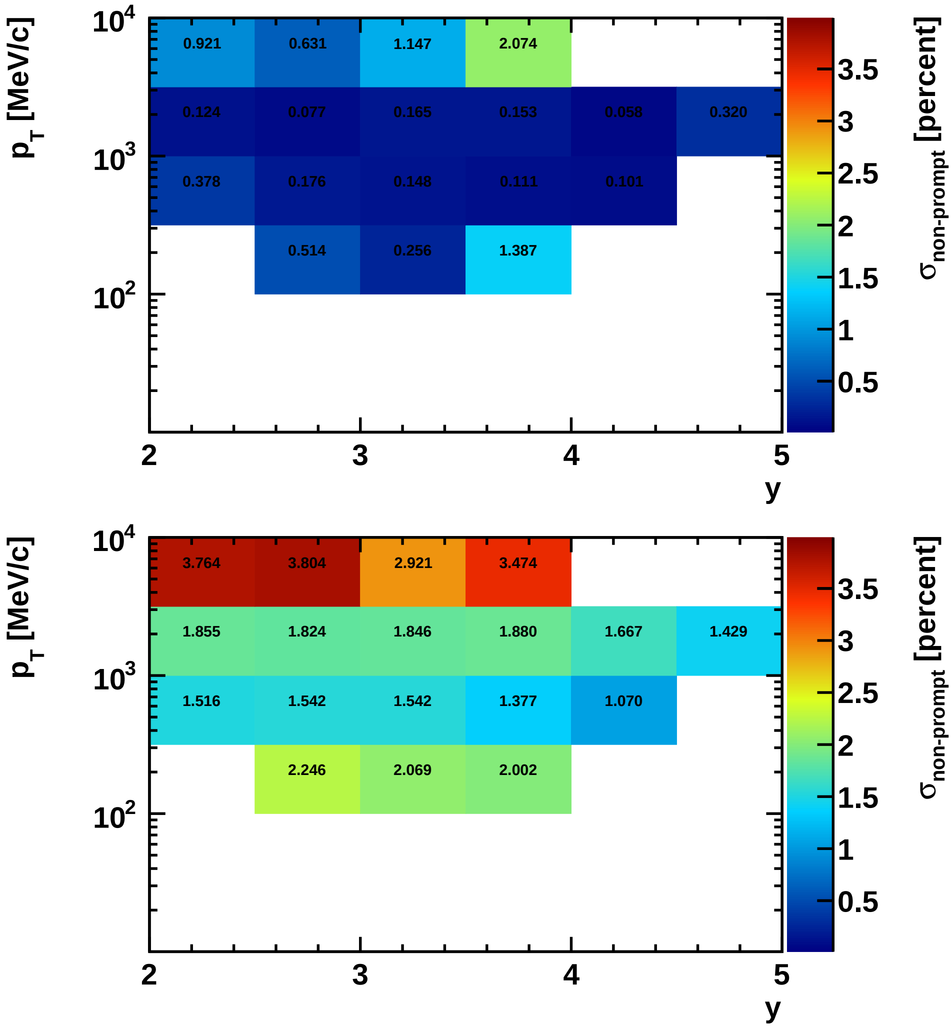

Figure 5.66: Relative systematic uncertainties from non-prompt fractions for the $\overline{\Lambda^0}/\Lambda^0$ (top) and $\overline{\Lambda^0}/K^0_S$ (bottom) ratios.

5.22.8 Branching fractions

The relative uncertainty on the branching fraction of $K^0_S \to \pi^+\pi^-$ is negligible, while the one on $\Lambda^0 \to p\pi^-$ is around 0.8%, as can be seen in Table 5.16. This is propagated as a systematic uncertainty to the $\Lambda^0/\overline{\Lambda^0}$ cross-sections and antibaryon-meson ratios. As the uncertainties are fully correlated between Λ^0 and $\overline{\Lambda^0}$, they cancel out in the case of the antibaryon-baryon ratios.

Table 5.16: Branching fractions of the decays used in this analysis. The values are taken from [24].

Decay	$\mathcal{B}$
$K^0_S \to \pi^+\pi^-$	69.20% ± 0.05%
$\Lambda^0 \to p\pi^-$	63.90% ± 0.50%

5.23 Total uncertainties

The total relative uncertainties for the cross-section and ratios are given in Figures 5.67 and 5.68, respectively. The values for the cross-sections are around 7.0-8.0% in the central phase space bins and rise to values of between 10.0% and 20.0% at the edges, with generally lower uncertainties for K_S^0. The uncertainties on the ratios are lower and higher in the central and peripheral bins, respectively, due to the interplay of correlated and uncorrelated uncertainties on the cross-sections.

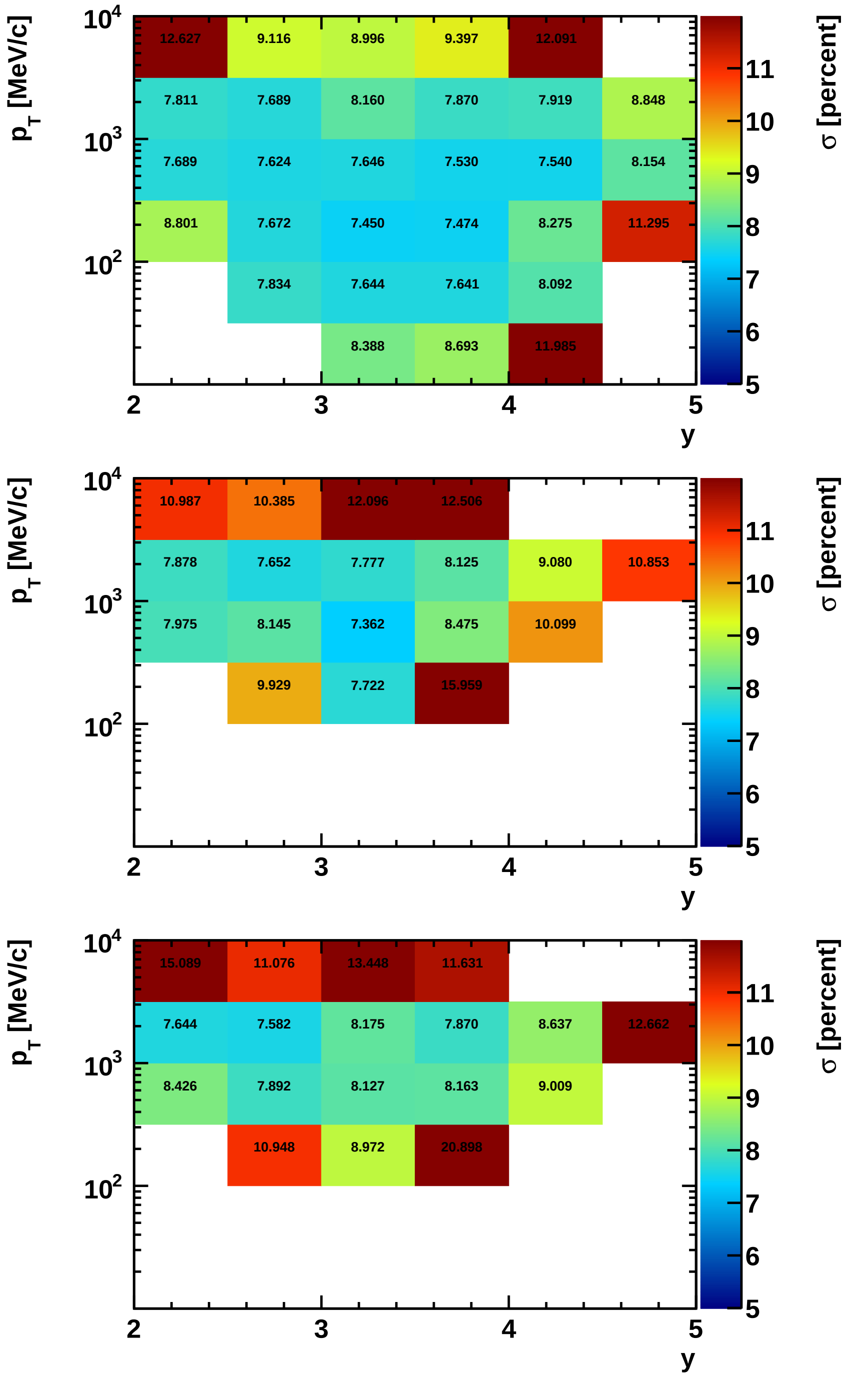

Figure 5.67: Relative total uncertainties for K_S^0 (top), Λ^0 (middle) and $\overline{\Lambda^0}$ (bottom).

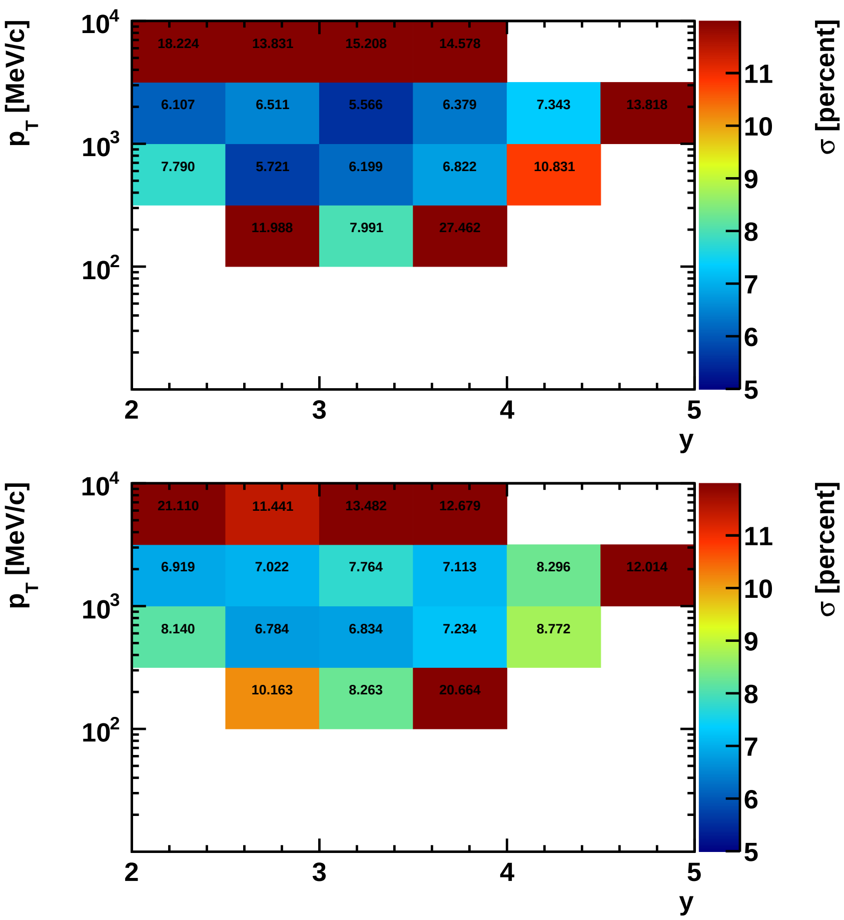

Figure 5.68: Relative total uncertainties for the $\overline{\Lambda^0}/\Lambda^0$ (top) and $\overline{\Lambda^0}/K^0_S$ (bottom) ratios.

5.24 Conclusions

The V^0 cross-sections and ratios have been measured and their respective uncertainties have been estimated. The values of the cross-sections in the full analysis phase space are $\sigma_{K^0_S} = 64\,501.5 \pm 4\,787.3$ µb, $\sigma_{\Lambda^0} = 22\,106.3 \pm 1\,656.3$ µb and $\sigma_{\overline{\Lambda^0}} = 21\,013.7 \pm 1\,654.3$ µb, and the ones for the $\overline{\Lambda^0}/\Lambda^0$ and $\overline{\Lambda^0}/K^0_S$ ratios are 0.960 ± 0.052 and 0.329 ± 0.023, respectively. The uncertainties given represent the quadratic sum of the statistical and systematic uncertainties. The statistical component is negligible. The large uncertainties on the efficiencies motivate the development of tag-and-probe methods using V^0 daughters in order to obtain more accurate and, at the same time, more precise values. The total uncertainties are foreseen to drop by a few percent after the improved efficiency correction. The predictions of PYTHIA 8.219 do not describe the measured values well, more so in the case of $\Lambda^0/\overline{\Lambda^0}$.

General conclusions

As discussed in Chapter 2, perturbative QCD calculations are no longer applicable at momentum transfer scales of ~ 1 GeV/c^2 (the hadronization scale) and below. The treatment of hadronic collisions at high energies is further complicated by the emergence of MPI. Monte Carlo hadronic collisions generators employing various phenomenological models which treat hadronization and MPI have been developed.

Unprecedented collision energies of up to $\sqrt{s} = 13$ TeV have been reached at the LHC and the experiments it hosts operate at high luminosities. Among the four major experiments, namely ATLAS, ALICE, CMS, and LHCb, only the latter covers the "forward" pseudorapidity region. The high performance tracking system of LHCb, together with the high integrated luminosities of stored minimum bias data, allow for precise measurements of observables relating to light flavour hadron production like cross-sections and production ratios. These in turn may be used for the tuning of the hadronization and MPI parameters.

Two topics were considered for this thesis, namely a study of the predictions of LHC tuned generators for observables measured in the "forward" region at the LHCb and TOTEM experiments, and the analysis of V^0 cross-sections and ratios measured at LHCb in pp collisions at $\sqrt{s} = 13$ TeV.

The general conclusion of the former is that, although the tuning with "central" region measurements improves the predictions in the "forward" region to some degree, better descriptions are to be obtained via the constraining of the parameters with "forward" measurements, i.e. from LHCb and TOTEM. The charged energy flow is best described by SIBYLL 2.3, while the LHC tunes of PYTHIA and EPOS have the best predictions for the charged hadron multiplicities and densities. The baryon number transport and the strangeness suppression are best described by EPOS LHC and QGSJETII-04, respectively [16].

The V^0 cross-sections and ratios were measured in a two-dimensional phase space defined by $2 \leq y < 5$ and $1 \leq \log(p_T[\mathrm{MeV/c}]) < 4$ divided into a 6×6 array of symmetric bins. The full analysis phase space values were measured to be:

- $\sigma_{K_S^0} = 64\,501.5 \pm 4\,787.3$ µb;
- $\sigma_{\Lambda^0} = 22\,106.3 \pm 1\,656.3$ µb;
- $\sigma_{\overline{\Lambda^0}} = 21\,013.7 \pm 1\,654.3$ µb;
- $\overline{\Lambda^0}/\Lambda^0 = 0.960 \pm 0.052$;
- $\overline{\Lambda^0}/K_S^0 = 0.329 \pm 0.023$;

where the given uncertainties represent the statistical and systematic uncertainties added in quadrature. The statistical uncertainties are negligible in comparison to the systematic ones.

Studies regarding several aspects have been conducted, i.e. background sources, efficiency of selecting signal using the "truth" information, effects of selection cuts, MC/Data comparison, bin migration, non-prompt contamination, generator predictions, hadronic interactions in the detector etc.

Besides the $\sim$4.0% systematic uncertainty coming from the luminosity measurements, the largest systematic uncertainties are due to the efficiency determination. These are driven by several aspects, i.e. the lack of coverage of the low momentum and high rapidity regions by the TrackCalib efficiency ratios, the use of muons in computing the former, which leads to uncertainties due to hadronic interactions in the detector, and low MC statistics at the edges of the analysis phase-space. Tag-and-probe methods using V^0 daughters will be employed in a future study in order to obtain more accurate cross-section measurements and at the same time, significantly reduce the systematic uncertainties from the efficiency determination. The other identified sources of systematic uncertainties are the selection of the fit model, the Fisher discriminant selection cut, the non-prompt contaminant fractions, and the branching fractions.

An LHCb Analysis Note will be built upon these preliminary results, which have been presented during an LHCb QEE (QCD, Electroweak, and Exotica) working group meeting, receiving positive feedback.

Bibliography

[1] T. Sjöstrand, S. Mrenna, P. Skands, "PYTHIA 6.4 Physics and Manual", JHEP 0605:026,2006. DOI: 10.1088/1126-6708/2006/05/026.

[2] T. Pierog *et al.*, "EPOS LHC : test of collective hadronization with LHC data", Phys. Rev. C 92, 034906 (2015). DOI: 10.1103/PhysRevC.92.034906.

[3] S. Ostapchenko, "Monte Carlo treatment of hadronic interactions in enhanced Pomeron scheme: I. QGSJET-II model", Phys.Rev.D83:014018,2011. DOI: 10.1103/PhysRevD.83.014018.

[4] F. Riehn, R. Engel *et al.*, "A new version of the event generator Sibyll", 34th International Cosmic Ray Conference (ICRC 2015), The Hague, Netherlands, C15-07-30, PoS ICRC2015 (2016) 558, arXiv:1510.00568.

[5] G. Aad *et al.* (ATLAS Collaboration), "The ATLAS Experiment at the CERN Large Hadron Collider", JINST 3 (2008) S08003. DOI: 10.1088/1748-0221/3/08/S08003.

[6] K. Aamodt *et al.* (ALICE Collaboration), "The ALICE experiment at the CERN LHC", JINST 3 (2008) S08002. DOI: 10.1088/1748-0221/3/08/S08002.

[7] S. Chatrchyan *et al.* (CMS Collaboration), "The CMS Experiment at the CERN LHC", JINST 3 (2008) S08004. DOI: 10.1088/1748-0221/3/08/S08004.

[8] A. Augusto Alves, Jr. *et al.* (LHCb Collaboration), "The LHCb Detector at the LHC", JINST 3 (2008) S08005. DOI: 10.1088/1748-0221/3/08/S08005.

[9] G. Anelli *et al.* (TOTEM Collaboration), "The TOTEM experiment at the CERN Large Hadron Collider", JINST 3 (2008) S08007. DOI: 10.1088/1748-0221/3/08/S08007.

[10] R. Aaij *et al.* (LHCb Collaboration), "Measurement of the forward energy flow in pp collisions at $\sqrt{s} = 7$ TeV", Eur. Phys. J. C (2013) 73:2421. DOI: 10.1140/epjc/s10052-013-2421-y. HepData DOI: 10.17182/hepdata.61691. Rivet analysis: LHCB_2013_I1208105.

[11] R. Aaij *et al.* (LHCb Collaboration), "Measurement of charged-particle multiplicities and densities in pp collisions at $\sqrt{s} = 7$ TeV in the forward region", Eur. Phys. J. C (2014) 74:2888. DOI: 10.1140/epjc/s10052-014-2888-1. HepData DOI: 10.17182/hepdata.63498. Rivet analysis: LHCB_2014_I1281685.

[12] R. Aaij *et al.* (LHCb Collaboration), "Measurement of charged-particle multiplicities in pp collisions at $\sqrt{s} = 7$ TeV in the forward region", Eur. Phys. J. C (2012) 72: 1947. DOI: 10.1140/epjc/s10052-012-1947-8. HepData DOI: 10.17182/hepdata.65435.

[13] G. Antchev *et al.* (TOTEM Collaboration), "Measurement of the forward charged particle pseudorapidity density in pp collisions at $\sqrt{s} = 7$ TeV with the TOTEM experiment", Europhys.Lett. 98 (2012) 31002. DOI: 10.1209/0295-5075/98/31002. HepData DOI: 10.17182/hepdata.59403.

[14] R. Aaij *et al.* (LHCb Collaboration), "Measurement of prompt hadron production ratios in pp collisions at $\sqrt{s} = 0.9$ and 7 TeV", Eur. Phys. J. C 72 (2012) 2168. DOI: 10.1140/epjc/s10052-012-2168-x. Rivet analysis: LHCB_2012_I1119400.

[15] R. Aaij *et al.* (LHCb Collaboration), "Measurement of V^0 production ratios in pp collisions at $\sqrt{s} = 0.9$ and 7 TeV", J. High Energ. Phys. (2011) 2011: 34. DOI: 10.1007/JHEP08(2011)034. Rivet analysis: LHCB_2011_I917009.

[16] A.C. Ene, A. Jipa, L.E. Giubega, "Study of Monte Carlo event generators for proton-proton collisions at LHC energies in the forward region", Chinese Physics C Vol. 43, No. 8 (2019) 083001. DOI: 10.1088/1674-1137/43/8/083001.

[17] R. Aaij *et al.* (LHCb Collaboration), "LHCb detector performance", Int.J.Mod.Phys. A30 (2015) no.07, 1530022. DOI: 10.1142/S0217751X15300227.

[18] C.G. Blanks, "V^0 production ratios at LHCb and the alignment of its RICH detectors", PhD Thesis, Imperial College London, 2011. Link: http://hdl.handle.net/10044/1/9209 (Last visited on 06.03.2020).

[19] R. Aaij *et al.* (LHCb Collaboration), "Prompt K_S^0 production in pp collisions at $\sqrt{s} = 0.9$ TeV", Physics Letters B 693 (2010) 69-80. DOI: 10.1016/j.physletb.2010.08.055.

[20] G. Aad *et al.* (ATLAS Collaboration), "K_S^0 and Λ production in pp interactions at $\sqrt{s} = 0.9$ and 7 TeV measured with the ATLAS detector at the LHC", Phys. Rev. D 85, 012001, 2012. DOI: 10.1103/PhysRevD.85.012001.

[21] K. Aamodt *et al.* (ALICE Collaboration), "Strange particle production in proton-proton collisions at $\sqrt{s} = 0.9$ TeV with ALICE at the LHC", Eur. Phys. J. C 71, 1594 (2011). DOI: 10.1140/epjc/s10052-011-1594-5.

[22] E. Abbas *et al.* (ALICE Collaboration), "Mid-rapidity antibaryon to baryon ratios in pp collisions at $\sqrt{s} = 0.9$, 2.76 and 7 TeV measured by ALICE", Eur. Phys. J. C 73, 2496 (2013). DOI: 10.1140/epjc/s10052-013-2496-5.

[23] V. Khachatryan *et al.* (CMS Collaboration), "Strange particle production in pp collisions at $\sqrt{s} = 0.9$ and 7 TeV", J. High Energ. Phys. 2011, 64 (2011). DOI: 10.1007/JHEP05(2011)064.

[24] M. Tanabashi *et al.* (Particle Data Group), "2018 Review of particle physics", Phys. Rev. D 98, 030001, 2018. DOI: 10.1103/PhysRevD.98.030001.

[25] Y. Nagashima, "Elementary Particle Physics, Volume 1: Quantum Field Theory and Particles", Wiley-VCH, 2010, ISBN: 978-3-527-40962-4.

[26] Y. Nagashima, "Elementary Particle Physics, Volume 2: Foundations of the Standard Model", Wiley-VCH, 2013, ISBN: 978-3-527-40966-2.

[27] N. Serra, "Kern- und Teilchenphysik IILecture 1: QCD", Physik-Institut, Universität Zürich. Link: `https://www.uzh.ch/cmsssl/physik/dam/jcr:3b17820b-b3b2-494e-922b-2bd19cd05cb6/Lecture1.pdf` (Last visited on 01.04.2020).

[28] S. Jowzaee, "SU(3) symmetry and Baryon wave functions", PhD seminar, FZ Juelich, Feb 2013. Link: `http://www.ips.if.uj.edu.pl/files/7bfde3a8c14adfe40f950dbdad96f13c/PhD%20talk-Jowzaee.pdf` (Last visited on 01.04.2020).

[29] F. Halzen, A.D. Martin, "Quarks and leptons. An Introductory Course in Modern Particle Physics", John Wiley & Sons, 1984, ISBN: 0-471-88741-2.

[30] Image from Wikimedia Commons. Original version: MissMJ (author), own work by uploader, PBS NOVA, Fermilab, Office of Science, United States Department of Energy, Particle Data Group. published under CC BY 3.0: https://creativecommons.org/licenses/by/3.0/legalcode. This version: Cush (author). Link: https://commons.wikimedia.org/wiki/File:Standard_Model_of_Elementary_Particles.svg (Last visited on 26.03.2020).

[31] B.R. Martin, G. Shaw, "Particle physics", 3rd edition, John Wiley & Sons, 2008, ISBN 978-0-470-03294-7.

[32] R.K. Ellis, W.J. Stirling, B.R. Webber, "QCD and Collider Physics", Cambridge University Press, 1996, ISBN 0-521-58189-3.

[33] M. Botje, "Lecture notes Particle Physics II, Quantum Chromo Dynamics: 5. Colour factors", Nikhef, Science Park, Amsterdam, 2013. Link: https://www.nikhef.nl/~h24/qcdcourse/section-5.pdf (Last visited on 01.04.2020).

[34] Jen-Chieh Peng, "Building Hadrons from Quarks", lecture notes. Link: https://courses.engr.illinois.edu/phys570/fa2017/chapter3.pdf (Last visited on 09.04.2020).

[35] M. Botje, "Lecture notes Particle Physics II, Quantum Chromo Dynamics: 6. Asymptotic Freedom", Nikhef, Science Park, Amsterdam, 2013. Link: https://www.nikhef.nl/~h24/qcdcourse/section-6.pdf (Last visited on 01.04.2020).

[36] Image from Wikimedia Commons. Authors: E2m, Stannered. Link: https://commons.wikimedia.org/wiki/File:Meson_nonet_-_spin_0.svg (Last visited on 31.03.2020).

[37] Image from Wikimedia Commons. Authors: E2m, Stannered. Link: https://commons.wikimedia.org/wiki/File:Meson_nonet_-_spin_1.svg (Last visited on 31.03.2020).

[38] R. Bijker, "Symmetries in Nuclear and Particle Physics", ICN-UNAM. Link: https://escuelafisicanuclear.uniandes.edu.co/images/images/notes/Bogota2012d.pdf (Last visited on 01.04.2020).

[39] Image from Wikimedia Commons. Own work by Trassiorf. Link: https://commons.wikimedia.org/wiki/File:Baryon-octet-small.svg (Last visited on 31.03.2020).

[40] Image from Wikimedia Commons. Own work by Trassiorf. Link: https://commons.wikimedia.org/wiki/File:Baryon-decuplet-small.svg (Last visited on 31.03.2020).

[41] G. D'Ambrosio, G. Isidori, "CP Violation in Kaon Decays", Int.J.Mod.Phys.A 13 (1998) 1-94. DOI: 10.1142/S0217751X98000020.

[42] M. Botje, "Lecture notes Particle Physics II, Quantum Chromo Dynamics: 8. The Structure of the Proton", Nikhef, Science Park, Amsterdam, 2013. Link: https://www.nikhef.nl/~h24/qcdcourse/section-8.pdf (Last visited on 14.04.2020).

[43] F.D. Aaron *et al.* (H1 and ZEUS Collaborations), "Combined measurement and QCD analysis of the inclusive $e^{\pm}p$ scattering cross sections at HERA", J. High Energ. Phys. 2010, 109 (2010). DOI: 10.1007/JHEP01(2010)109.

[44] E. Levin, "Everything about reggeons. Part I: Reggeons in "soft" interaction", TAUP 2465-97, DESY 97-213. arXiv: hep-ph/9710546.

[45] E. Levin, "The Pomeron: Yesterday, today and tomorrow", CBPF-NF-010/95. arXiv: hep-ph/9503399.

[46] C. Ewerz, "The Odderon in Quantum Chromodynamics", HD-THEP-02-35. arXiv: hep-ph/0306137.

[47] E. Levin, "An introduction to Pomerons", DESY 98-120, TAUP 2522/98. arXiv: hep-ph/9808486.

[48] V. Schatz, "High energy scattering in the Regge limit", PhD. Thesis, HD-THEP-03-21. arXiv: hep-ph/0307326.

[49] A.D. Martin *et al.*, "Diffractive Physics", Plenary talk at 6$^{\text{th}}$ International Conference on Quarks and Nuclear Physics, Ecole Polytechnique, Palaiseau, Paris, April 2012, IPPP/12/39, DCPT/12/78. arXiv: 1206.2124.

[50] R. Field, "The Underlying Event in Hadronic Collisions", Annu. Rev. Nucl. Part. Sci. 2012. 62:453–83. DOI: 10.1146/annurev-nucl-102711-095030.

[51] V.A. Khoze *et al.*, "Elastic Scattering and Diffractive dissociation in the light of LHC data", contribution to the special issue of the International Journal of Modern Physics A on "Elastic and diffractive scattering" coordinated by Christophe Royon, IPPP/14/14, DCPT/14/28. arXiv: 1402.2778.

[52] S. Navin, "Diffraction in PYTHIA", LUTP-09-23, MCnet/10/09, arXiv:1005.3894.

[53] S.K. Prasad *et al.*, ""Soft" and "hard" interactions in proton-proton collisions at LHC energies", contribution to International Conference on Matter at Extreme Conditions: Then & Now (ICMEC 2014), Kolkata, India, January 2014, Proc.Indian Natl.Sci.Acad. 81 (2015) 1, 213-216. DOI: 10.16943/ptinsa/2015/v81i1/48071.

[54] V. Tudorache, M. Cuciuc, "Initial and Final State Radiation studies for top quark mass reconstruction in dileptonic channel for $\sqrt{s} = 7$ TeV collisions", Romanian Reports in Physics, Vol. 64, No. 4, P. 945–956, 2012. Link: `http://www.rrp.infim.ro/2012_64_4/art04Tudorache-bunfinal.pdf` (Last visited on 28.04.2020).

[55] T. Sjöstrand, "Particle Physics Phenomenology: 3. Evolution equations and final-state showers", Lecture notes, Lund, Sweden, February 2015. Link: `http://home.thep.lu.se/~torbjorn/ppp2015/lec3.pdf` (Last visited on 04.05.2020).

[56] T. Sjöstrand, "Particle Physics Phenomenology: 3. Evolution equations and final-state showers", Lecture notes, Lund, Sweden, January 2018. Link: `http://home.thep.lu.se/~torbjorn/ppp2018/lec3.pdf` (Last visited on 04.05.2020).

[57] P. Bartalini *et al.*, "Multi-Parton Interactions at the LHC", ANL-HEP-PR-11-65, CMS-CR-2011-048, DESY 11-185, LTH929, KA-TP-32-2011, TTK-11-52. arXiv: 1111.0469.

[58] T. Sjöstrand *et al.*, "An Introduction to PYTHIA 8.2", LU TP 14-36, MCNET-14-22, CERN-PH-TH-2014-190, FERMILAB-PUB-14-316-CD, DESY 14-178, SLAC-PUB-16122. arXiv: 1410.3012.

[59] B. Andersson *et al.*, "Parton fragmentation and string dynamics", Phys.Rept. 97 (1983) 31-145. DOI: 10.1016/0370-1573(83)90080-7.

[60] T. Sjöstrand *et al.*, "Introduction to Event Generators 4", Lecture notes, CTEQ/MCnet School, DESY, July 2016. Link: `http://home.thep.lu.se/~torbjorn/talks/desy16d.pdf` (Last visited on 05.05.2020).

[61] P. Skands *et al.*, "Tuning PYTHIA 8.1: the Monash 2013 Tune", J. Eur. Phys. J. C (2014) 74: 3024. DOI: 10.1140/epjc/s10052-014-3024-y.

[62] PYTHIA Collaboration, "PYTHIA 8.2 Online User Manual". Link: `http://home.thep.lu.se/~torbjorn/pythia82html/Welcome.html` (Last visited on 05.05.2020).

[63] B.R. Webber, “A QCD model for jet fragmentation including soft gluon interference”, Nucl. Phys. B 238 (1984) 492-528. DOI 10.1016/0550-3213(84)90333-X.

[64] The CRMC project homepage: https://web.ikp.kit.edu/rulrich/crmc.html (Last visited: Sept 29, 2017).

[65] T. Sjöstrand, “Particle Physics Phenomenology - 5. Matching and Merging”, Lecture notes, Lund University, Lund, Sweden, 24 February 2015, http://home.thep.lu.se/~torbjorn/ppp2015/lec5.pdf.

[66] T. Sjöstrand, “PDFs in an event generator”, LHC and the Standard Model: Physics and Tools, CERN, 16 June 2017, http://home.thep.lu.se/~torbjorn/talks/cern17pdf.pdf.

[67] S. Argyropoulos, T. Sjöstrand, “Effects of color reconnection on $t\bar{t}$ final states at the LHC”, J. High Energ. Phys. 2014, 43 (2014). DOI: 10.1007/JHEP11(2014)043.

[68] J.R. Christiansen, P.Z. Skands, “String formation beyond leading colour”, J. High Energ. Phys. 2015, 3 (2015). DOI: 10.1007/JHEP08(2015)003.

[69] T. Sjöstrand *et al.*, “A Brief Introduction to PYTHIA 8.1”, Computer Physics Communications Volume 178, Issue 11, 1 June 2008, Pages 852-867. DOI: 10.1016/j.cpc.2008.01.036.

[70] R. Corke, T. Sjöstrand, “Interleaved parton showers and tuning prospects”, J. High Energ. Phys. (2011) 2011: 32. DOI: 10.1007/JHEP03(2011)032.

[71] H.J. Drescher *et al.*, “Parton-Based Gribov-Regge Theory”, Physics Reports Volume 350, Issues 2-4, September 2001, Pages 93-289. DOI: 10.1016/S0370-1573(00)00122-8.

[72] T. Pierog, K. Werner, “EPOS Model and Ultra High Energy Cosmic Rays”, Nuclear Physics B - Proceedings Supplements Volume 196, December 2009, Pages 102-105. DOI: 10.1016/j.nuclphysbps.2009.09.017.

[73] S. Porteboeuf, T. Pierog, K. Werner, “Producing Hard Processes Regarding the Complete Event: The EPOS Event Generator”, Proceedings of the XLVth Rencontres de Moriond (La Thuile, Italy, 2010) Pages 135-140, http://moriond.in2p3.fr/QCD/2010/Proceedings10/Porteboeuf.pdf.

[74] K. Werner *et al.*, “Parton ladder splitting and the rapidity dependence of transverse momentum spectra in deuteron-gold collisions at RHIC”, Phys.Rev.C 74 (2006) 044902. DOI: 10.1103/PhysRevC.74.044902.

[75] S. Ostapchenko, D. Heck, “Hadronic Interactions in QGSJET-II: Physics and Results”, 29th International Cosmic Ray Conference Pune (2005) 7, 135-138.

[76] S. Ostapchenko, “QGSJET-II: towards reliable description of very high energy hadronic interactions”, Nuclear Physics B - Proceedings Supplements Volume 151, Issue 1, January 2006, Pages 143-146. DOI: 10.1016/j.nuclphysbps.2005.07.026.

[77] S. Ostapchenko, “Status of QGSJET”, AIP Conf.Proc. 928 (2007) 118-125. DOI: 10.1063/1.2775904.

[78] S. Ostapchenko, “QGSJET-II: physics, recent improvements, and results for air showers”, EPJ Web Conf. 52 (2013) 02001, C12-08-10.1, DOI: 10.1051/epjconf/20135202001

[79] K. Werner *et al.*, “Core-Corona Separation in Ultrarelativistic Heavy Ion Collisions”, Phys.Rev.Lett.98:152301, 2007. DOI: 10.1103/PhysRevLett.98.152301.

[80] G.I. Lykasov, M.N. Sergeenko, “Semihard Hadron Processes and Quark-gluon String Model”, Z.Phys. C70 (1996) 455-462. DOI: 10.1007/s002880050123.

[81] S. Ostapchenko, "Studies of Very High Energy Cosmic Rays: Status, Puzzles, and the Impact of LHC Data", Progress of Theoretical Physics Supplement, Volume 193, 1 March 2012, Pages 204–211. DOI: 10.1143/PTPS.193.204

[82] E. Ahn *et al.*, "Cosmic ray event generator Sibyll 2.1", Phys. Rev. D 80 : 094003, 2009. DOI: 10.1103/PhysRevD.80.094003.

[83] R. Engel *et al.*, "The hadronic interaction model Sibyll - past, present and future", ISVHECRI 2016 - XIX International Symposium on Very High Energy Cosmic Ray Interactions, EPJ Web of Conferences 145, 08001 (2017). DOI: 0.1051/epjconf/201714508001.

[84] F. Riehn, "Hadronic multiparticle production in SIBYLL - from LHC to air showers", LIP-Seminar, May 2016. Link: https://indico.lip.pt/event/221/attachments/372/452/Felix_Riehn_lip_seminar.pdf (Last visited on 20.05.2020).

[85] A. Fedynitch *et al.*, "Hadronic interaction model SIBYLL 2.3c and inclusive lepton fluxes", Phys. Rev. D 100, 103018, 2019. DOI: 10.1103/PhysRevD.100.103018.

[86] F. Riehn *et al.*, "The hadronic interaction model SIBYLL 2.3c and Feynman scaling", PoS ICRC2017 (2017) 301, arXiv:1709.07227.

[87] F. Riehn *et al.*, "Charm production in SIBYLL", EPJ Web of Conferences 99, 12001 (2015). DOI: https://doi.org/10.1051/epjconf/20159912001.

[88] CERN official website. Link: https://home.cern (Last visited on 19.09.2019).

[89] Xabier Cid Vidal, Ramon Cid, Outreach website about LHC. Link: http://lhc-closer.es/taking_a_closer_look_at_lhc/1.physics_at_lhc (Last visited on 15.02.2020).

[90] S. Baird, "Accelerators for pedestrians", AB-Note-2007-014 OP.

[91] E. Todesco and J. Wenninger, "Large Hadron Collider momentum calibration and accuracy", Phys. Rev. Accel. Beams 20, 081003, 2017. DOI: 10.1103/PhysRevAccelBeams.20.081003.

[92] B.J. Holzer, "Introduction to Longitudinal Beam Dynamics", CERN, Geneva, Switzerland. arXiv: 1404.0927.

[93] F. Tecker, "Longitudinal Beam Dynamics", CERN, Geneva, Switzerland. arXiv: 1601.04901.

[94] M. Migliorati, "Longitudinal beam dynamics". Link: https://agenda.infn.it/event/11951/attachments/8432/9474/07_longitudinal_dynamics.pdf (Last visited on 04.10.2019).

[95] H. Wiedemann, "Particle Accelerator Physics", Springer, Berlin, 2007.

[96] Shyh-Yuan Lee, "Accelerator physics", World Scientific, 1999.

[97] W. Herr and Bruno Muratori, "Concept of luminosity", CERN, Geneva, Switzerland.

[98] Paul Avery, "Cross section, Flux, Luminosity, Scattering Rates", lecture notes. Link: http://www.phys.ufl.edu/~avery/course/4390/f2015/lectures/cross_section_flux.pdf (Last visited on 10.10.2019).

[99] R. Aaij *et al.* (LHCb Collaboration), "Precision luminosity measurements at LHCb", JINST 9 (2014) no.12, P12005. DOI: 10.1088/1748-0221/9/12/P12005.

[100] P. Hopchev, "Beam-Gas Imaging Results", CERN-Proceedings-2011-001, pp. 64-68.

[101] M.A. Furman, "The Møller Luminosity Factor", Center for Beam Physics, Lawrence Berkeley National Laboratory, LBNL-53553, CBP Note-543, 2003.

[102] S. White, "Determination of the absolute luminosity at the LHC", High Energy Physics - Experiment [hep-ex]. Université Paris Sud - Paris XI, 2010. English. tel-00537325. Link: https://tel.archives-ouvertes.fr/tel-00537325 (Last visited on 10.10.2019).

[103] L. Rossi and O. Brüning, "Introduction to the HL-LHC Project", CERN, Accelerator and Technology Sector, Genève 23, CH-1211, Switzerland.

[104] S.N. Webb, "Factorisation of beams in van der Meer scans and measurements of the ϕ^*_η distribution of $Z \to e^+e^-$ events in pp collisions at $\sqrt{s} = 8$ TeV with the ATLAS detector", PhD. Thesis, University of Manchester, Faculty of Engineering and Physical Sciences, School of Physics and Astronomy, 2015, CERN-THESIS-2015-054.

[105] S.M. White *et al.*, "First luminosity scans in the LHC", MOPEC014, Proceedings of IPAC'10, Kyoto, Japan.

[106] S.M. White *et al.*, "Luminosity optimisation and calibration in the LHC", WE6PFP015, Proceedings of PAC09, Vancouver, BC, Canada.

[107] S. van der Meer, "Calibration of the effective beam height in the ISR", ISR-PO/68-31, KEK68-64.

[108] G. Aad *et al.* (ATLAS Collaboration), "Improved luminosity determination in *pp* collisions at $\sqrt{s} = 7$ TeV using the ATLAS detector at the LHC", Eur. Phys. J. C (2013) 73: 2518. DOI: 10.1140/epjc/s10052-013-2518-3.

[109] R. Aaij *et al.* (LHCb Collaboration), "Absolute luminosity measurements with the LHCb detector at the LHC", JINST 7 (2012) P01010. DOI: 10.1088/1748-0221/7/01/P01010.

[110] C. Barschel *et al.*, "Preliminary luminosity calibration at $\sqrt{s} = 13$ TeV (p-p)", LHCb Analysis Note, LHCb-ANA-2015-036, 2016.

[111] LHCb Operations Plots Webpage. Private communication.

[112] The LHCb Collaboration, "Definition of the coordinate system", Engineering/Techinal Note LHCB-C-EN-0001 version 1.0.

[113] J. van Tilburg, M. Needham, Website with an overview of the simulation, digitization and reconstruction software for the LHCb Silicon Tracker (ST) project. Link: https://lhcb.physik.uzh.ch/ST/software/minutes/stereo.pdf (Last visited on 08.11.2019).

[114] W. Herr *et al.*, "How do we have to operate the LHCb spectrometer magnet?", LHC Project Note 419, 2009.

[115] O. Brüning *et al.* (Editorial Board, CERN), "LHC Design Report Vol.1: The LHC Main Ring", CERN-2004-003-V-1, CERN, Geneva, 2004.

[116] B.J. Holzer, "Spectrometer operation in IR2 & IR8", CERN, Geneva, Switzerland. Link: http://inspirehep.net/record/1650696/files/1639581_33-40.pdf (Last visited on 12.11.2019).

[117] R. Aaij *et al.* (LHCb Collaboration), "Performance of the LHCb Vertex Locator", JINST 9 P09007.

[118] T. Szumlak *et al.*, "Reconstruction of Cluster Positions in the LHCb VELO", LHCb Note, LHCb-2007-151, 2007.

[119] E. Nappi and J. Seguinot, "Ring Imaging Cherenkov Detectors: The state of the art and perspectives", La Rivista del Nuovo Cimento 28(8):1-130, 2005. DOI: 10.1393/ncr/i2006-10004-6.

[120] R. Forty and Olivier Schneider, "RICH pattern recognition", LHCb Note, LHCb-98-040, 1998.

[121] R. Mureşan, "Cherenkov Ring Reconstruction Methods", LHCb Note, LHCb-2007-121, 2007.

[122] J. van Tilburg, "Track simulation and reconstruction in LHCb", PhD. Thesis, Vrije Universiteit Amsterdam, 2005, CERN-THESIS-2005-040.

[123] R.M. van der Eijk, "Track reconstruction in the LHCb experiment", PhD. Thesis, University of Amsterdam, 2002, CERN-THESIS-2002-032.

[124] LHCb "Standard set of performance numbers" webpage. Link: http://lhcb.web.cern.ch/lhcb/speakersbureau/html/PerformanceNumbers.html (Last visited on 19.11.2019).

[125] F. Archilli *et al.*, "Performance of the Muon Identification at LHCb", JINST 8 (2013) P10020. DOI: 10.1088/1748-0221/8/10/P10020.

[126] F. Dordei, on behalf of the LHCb Collaboration, "LHCb detector and trigger performance in Run II", EPJ Web of Conferences 164, 01016 (2017). DOI: 10.1051/epjconf/201716401016.

[127] R. Aaij *et al.* (LHCb Collaboration), "Design and performance of the LHCb trigger and full real-time reconstruction in Run 2 of the LHC", JINST 14 (2019) no.04, P04013. DOI: 10.1088/1748-0221/14/04/P04013.

[128] R. Aaij *et al.* (LHCb Collaboration), "Measurement of the track reconstruction efficiency at LHCb", JINST 10 (2015) no.02, P02007. DOI: 10.1088/1748-0221/10/02/P02007.

[129] E. Rodrigues, "Tracking definitions", LHCb Internal Note, LHCb-2007-006, 2007.

[130] M. De Cian *et al.*, "Fast neural-net based fake track rejection in the LHCb reconstruction", LHCb-PUB-2017-011.

[131] E. Rodrigues, "Dealing with clones in the tracking", LHCb Note, LHCb-2006-057, 2006.

[132] M. Kucharczyk *et al.*, "Primary Vertex Reconstruction at LHCb", LHCb Public Note, LHCb-PUB-2014-044, 2014.

[133] A. Dzierda *et al.*, "Primary Vertex reconstruction for Run II of data taking", LHCb Internal Note, LHCb-INT-2016-034, 2016.

[134] A. Jaeger *et al.*, "Measurement of the track finding efficiency", LHCb Public Note, LHCb-PUB-2011-025, 2012.

[135] M. De Cian, "Track Reconstruction Efficiency and Analysis of $B^0 \to K^* \mu^+ \mu^-$ at the LHCb Experiment", PhD Thesis, CERN-THESIS-2013-145, University of Zürich, 2013. URL: https://cds.cern.ch/record/1605179/files/CERN-THESIS-2013-145.pdf.

[136] LHCb TrackCalib TWiki. Link: https://twiki.cern.ch/twiki/bin/view/LHCb/TrackCalib (Last visited on 15.02.2020).

[137] M. Kolpin *et al.*, "TrackCalib tutorial", 86^{th} LHCb Week, December 5^{th} 2017.

[138] LHCb Tracking Efficiencies TWiki, 2015, EM Data Reco15em/Turbo01em vs MC 2015, Sim09b (Reco15em/Turbo01em) results. Private communication.

[139] R. Aaij *et al.* (LHCb Collaboration), "Precision measurement of the $B_S^0 - \overline{B_S^0}$ oscillation frequency with the decay $B_S^0 \to D_S^- \pi^+$", New J. Phys. 15 053021, 2013. DOI: 10.1088/1367-2630/15/5/053021/pdf.

[140] R. Aaij *et al.* (LHCb Collaboration), "Updated measurement of time-dependent *CP*-violating observables in $B_S^0 \to J/\psi K^+ K^-$ decays", Eur.Phys.J. C79 (2019) no.8, 706. DOI: 10.1140/epjc/s10052-019-7159-8.

[141] R. Aaij *et al.* (LHCb Collaboration), “Updated measurement of time-dependent CP-violating phase ϕ_S from $B_S^0 \to J/\psi\pi^+\pi^-$ decays in 13 TeV pp collisions”, Phys. Lett. B797 (2019). arXiv: 1903.05530.

[142] K. Govorkova (on behalf of the LHCb Collaboration), “Mixing and time-dependent CP violation in beauty at LHCb”, Moriond EW 2019. Link: http://moriond.in2p3.fr/2019/EW/slides/5_Thursday/1_morning/2_cpv_govorkova_moriondEW_2019.pdf (Last visited on 06.03.2020).

[143] The LHCb Collaboration, “LHCb Computing Techinal Design Report”, CERN-LHCC-2005-019, LHCb-TDR-11, CERN, Geneva, 2005.

[144] G. Corti *et al.*, “Software for the LHCb Experiment”, IEEE Trans. Nucl. Sci. 53 (2006) 1323-1328.

[145] G. Barrand *et al.*, “GAUDI - A software architecture and framework for building HEP data processing applications”, Comput. Phys. Commun. 140 (2001) 45-55.

[146] M. Clemencic *et al.* on behalf of the LHCb Collaboration, “The LHCb Simulation Application, Gauss: Design, Evolution and Experience”, International Conference on Computing in High Energy and Nuclear Physics (CHEP 2010), J. Phys.: Conf. Ser.331 032023. DOI: 10.1088/1742-6596/331/3/032023/pdf.

[147] D. Müller on behalf of the LHCb Collaboration, “Adopting new technologies in the LHCb Gauss simulation framework”, 23$^{\mathrm{rd}}$ International Conference on Computing in High Energy and Nuclear Physics (CHEP 2018), EPJ Web of Conferences 214, 02004 (2019). DOI: 10.1051/epjconf/201921402004.

[148] I. Belyaev *et al.* on behalf of the LHCb Collaboration, “Handling of the generation of primary events in Gauss, the LHCb simulation framework”, International Conference on Computing in High Energy and Nuclear Physics (CHEP 2010), Journal of Physics: Conference Series 331 (2011) 032047. DOI: 10.1088/1742-6596/331/3/032047/pdf.

[149] A. Ryd *et al.*, “EvtGen: A Monte Carlo Generator for B-Physics”, EvtGen V00-11-06.

[150] T. Gleisberg *et al.*, “Event generation with SHERPA 1.1”, FERMILAB-PUB-08-477-T, SLAC-PUB-13420, ZU-TH-17-08, DCPT-08-138, IPPP-08-69, EDINBURGH-2008-30, MCNET-08-14, JHEP 0902 (2009) 007. DOI: 10.1088/1126-6708/2009/02/007.

[151] P. Golonka, Z. Was, “PHOTOS Monte Carlo: a precision tool for QED corrections in Z and W decays”, Eur. Phys. J. C (2006) 45: 97. DOI: 10.1140/epjc/s2005-02396-4.

[152] The GEANT4 official website. Link: https://geant4.web.cern.ch/ (Last visited on 15.02.2020).

[153] D. Volyanskyy, M. Schmelling, “Measurement of the forward energy flow in pp collisions at $\sqrt{s} = 7$ TeV with the LHCb experiment”, LHCb Analysis Note, LHCb-ANA-2012-086, 2012.

[154] K. Dreimanis, “Measurement of particle multiplicity and energy flow in pp collisions at 13 TeV with the LHCb detector”, PhD. Thesis, University of Liverpool, 2017, CERN-THESIS-2017-310.

[155] M. Schmelling *et al.*, “Measurement of the inelastic pp cross-section at a center-of-mass energy of $\sqrt{s} = 13$ TeV”, LHCb Analysis Note, LHCb-ANA-2016-077, Version 3.5, 2018.

[156] M. Schmelling, “Luminosity calibration for the leading bunch nobias-triggered data from the 2015 early measurement runs”, LHCb Internal Note, LHCb-INT-2017-015, 2017.

[157] LHCb NuMuPileUp Twiki. Link: https://twiki.cern.ch/twiki/bin/view/LHCb/NuMuPileUp (Last visited on 15.02.2020).

[158] M. Knecht *et al.*, "Measurement of V^0-particle production at LHCb with 2009 data", LHCb Analysis Note LHCb-INT-2010-022, 2010.

[159] T. Blake *et al.*, "Production ratios of prompt V^0 particles at LHCb from pp collisions at $\sqrt{s} = 0.9$ TeV and 7 TeV", LHCb Analysis Note LHCb-ANA-2011-026, 2011.

[160] Private communication from Alexandru T. Grecu. LHCb Database.

[161] C. Burr *et al.*, "Measurements of prompt charm production cross-sections in pp collisions at $\sqrt{s} = 5$ TeV", LHCb Analysis Note, LHCb-ANA-2016-019, 2016.

[162] C. Burr *et al.*, "Measurements of prompt charm production cross-sections in pp collisions at $\sqrt{s} = 13$ TeV in 2015 data", LHCb Analysis Note, LHCb-ANA-2015-023, 2015.

[163] F. Dettori, "Measurement of strange hadron production ratios and perspectives for the search of $D^0 \to \mu^+\mu^-$ decay at LHCb", PhD Thesis, Universita degli Studi di Cagliari, 2010, CERN-THESIS-2011-022.

[164] R. Aaij *et al.* (LHCb Collaboration), "Prompt K^0_S production in pp collisions at $\sqrt{s} = 0.9$ TeV", Phys. Lett. B693 (2010) 69-80. DOI: 10.1016/j.physletb.2010.08.055.

[165] R. Sahoo, "Relativistic Kinematics", Lecture delivered in IX SERC School on Experimental High Energy Physics, IIT Madras, India, 12-14 Dec. 2013. arXiv: 1604.02651.

[166] E. Daw, "Lecture 7 - Rapidity and Pseudorapidity", 2012. Link: http://www.hep.shef.ac.uk/edaw/PHY206/Site/2012_course_files/phy206rlec7.pdf (Last visited on 06.03.2020).

[167] T. Brambach *et al.*, "Measurement of the inclusive ϕ cross-section in pp collisions at $\sqrt{s} = 7$ TeV", LHCb Analysis Note, LHCb-ANA-2011-034, 2011.

[168] S. Weglarczyk, "Kernel density estimation and its application", ITM Web of Conferences 23, 00037 (2018). DOI: 10.1051/itmconf/20182300037.

[169] R. Aaij *et al.* (LHCb Collaboration), "Erratum to: Measurements of prompt charmproduction cross-sections in pp collisions at $\sqrt{s} = 13$ TeV", J. High Energ. Phys. 2017, 74 (2017). DOI: 10.1007/JHEP05(2017)074. HepData DOI: 10.17182/hepdata.73066.v2.

[170] C. Amsler *et al.* (Particle Data Group), "2008 Review of particle physics", Physics Letters B667, 1 (2008). Link: http://pdg.lbl.gov/2009/download/rpp-2008-plB667.pdf (Last visited on 03.03.2020).

[171] LHCb Tracking Efficiencies TWiki, Information on the absorption of hadrons. Link: https://twiki.cern.ch/twiki/bin/view/LHCb/TrackingEffAbsLength (Last visited on 06.03.2020).

[172] Silvia Masciocchi, "Hadronic Calorimeters", SS2017, Heidelberg, July 2017. Link: https://www.physi.uni-heidelberg.de/~sma/teaching/ParticleDetectors2/sma_HadronicCalorimeters.pdf (Last visited on 06.03.2020).

[173] R.K. Bock, "Collision Length" webpage. https://pe2bz.philpem.me.uk/Comm01/--Ion-Photon-RF/--Scintillation/Site-004/node30.html (Last visited on 06.03.2020).

[174] Particle Data Group (PDG), "Atomic and nuclear properties of materials" webpage. Link: http://pdg.lbl.gov/2011/AtomicNuclearProperties/HTML_PAGES/013.html (Last visited on 06.03.2020).

[175] S. Miglioranzi, "Material interactions studies", CERN, 2010. Link: https://indico.cern.ch/event/82520/contributions/2099155/attachments/1067656/1522643/mat_miglioranzi.pdf (Last visited on 06.03.2020).

[176] S. Miglioranzi, G. Corti, "Material interaction cross section studies", LHCb Internal Note LHCb-INT-2011-002, 2011.

[177] RooFit online manual. Link: https://root.cern/manual/roofit/ (Last visited on 31.07.2020).

[178] ROOT website. Link: https://root.cern.ch/ (Last visited on 07.03.2020).

[179] F. James and M. Winkler, "Minuit User's Guide", CERN, Geneva, 2004. Link: http://inspirehep.net/record/1258345/files/mnusersguide.pdf (Last visited on 07.03.2020).

[180] RooFit documentation. Link: https://web.pa.msu.edu/people/brock/file_sharing/ATLAS/root/roofit/doc/v524/ (Last visited on 07.03.2020).

[181] F. James, "Statistical Methods in Experimental Physics", 2nd Edition, 2006. DOI: 10.1142/6096.

[182] P. Avery, "Combining Measurements with Correlated Errors", CBX 95-55, 1996. Link: http://citeseerx.ist.psu.edu/viewdoc/download?doi=10.1.1.55.7731&rep=rep1&type=pdf&fbclid=IwAR1R65nNFbUsW0r9-9DerRJd4u1vX2rcFH0_67BTypnbW1vHn0eDPFoZ3HU (Last visited on 07.03.2020).

[183] M. Schmelling, "Soft-QCD very early measurements", LHCb Early measurements 2021 Meeting, 11.11.2019.

[184] Liupan An *et al.*, "J/ψ pair production in pp collisions at $\sqrt{s} = 13$ TeV", LHCb Analysis Note LHCb-ANA-2016-057, 2017.

[185] M. Aaboud *et al.* (ATLAS Collaboration), "Search for resonances in diphoton events at $\sqrt{s} = 13$ TeV with the ATLAS detector", J. High Energ. Phys. (2016) 2016: 1. DOI: 10.1007/JHEP09(2016)001.

[186] S. Das, "A simple alternative to the Crystal Ball function". arXiv: arXiv:1603.08591.

[187] Kai-Fend Chen, "Computational methods in experimental particle physics, Lecture 11: Extract Information from Data", National Taiwan University, 2015. Link: https://hep1.phys.ntu.edu.tw/~kfjack/lecture/hepcomp/2015/11/lecture-11.pdf (Last visited on 07.03.2020).

[188] K.O. Arras, "An Introduction To Error Propagation: Derivation, Meaning and Examples of Equation $C_Y = F_X C_X F_X^T$", Technical Report No. EPFL-ASL-TR-98-01 R3, September 1998.

Author's activity

A. A.C. Ene, "Particle production in pp collisions at LHC energies" (RO: "Producerea de particule în ciocniri pp la energii LHC"), master's thesis, Faculty of Physics of the University of Bucharest, 2016. Link to text (in Romanian): http://www.nipne.ro/dpp/Collab/LHCb/docs/theses2016/ENE_lucrare_disertatie.pdf.

B. A.C. Ene, "Experiments for the study of neutrino oscillations", (RO: "Experimente pentru studierea oscilaţiilor neutrinilor"), bachelor's thesis, Faculty of Physics of the University of Bucharest, 2014.

The author's activity consisting of publications, conferences etc. during the PhD. school as of July 2020 are given in the following. AIS is the Absolute Influece Score of the journal. The values of AIS quoted below are the most recent readily available at the time of the writing of this thesis and are taken from the AIS JCR 2019 (June 2020 edition) table found at https://uefiscdi.gov.ro/scientometrie-baze-de-date.

8.1 Publications (cumulative AIS = 167.975)

1. **A.C. Ene**, A. Jipa, L.E. Giubega, "Study of Monte Carlo event generators for proton-proton collisions at LHC energies in the forward region", Chinese Phys. C 43 083001 (2019). https://doi.org/10.1088/1674-1137/43/8/083001. AIS = 0.763.

2. L.E. Giubega, A. Jipa, **A.C. Ene**, "Study of Λ resonances in the $\Lambda_b \to \Lambda^*(\to p^+K^-)\gamma$ decay using helicity formalism", Rom.J.Phys. 62 (2017) 401. http://www.nipne.ro/rjp/2017_62_1-2/RomJPhys.62.401.pdf. AIS = 0.170.

8.1.1 LHCb publications

1. R. Aaij, **A.C. Ene** *et al.* (LHCb Collaboration), "Measurement of the inelastic pp cross-section at a centre-of-mass energy of 13 TeV", J. High Energ. Phys. 2018, 100 (2018). https://doi.org/10.1007/JHEP06(2018)100. AIS = 1.027.

2. R. Aaij, **A.C. Ene** *et al.* (LHCb Collaboration), "Measurement of the CP asymmetry in $B^- \to D_s^- D^0$ and $B^- \to D^- D^0$ decays", J. High Energ. Phys. 2018, 160 (2018). https://doi.org/10.1007/JHEP05(2018)160. AIS = 1.027.

3. R. Aaij, **A.C. Ene** *et al.* (LHCb Collaboration), "Measurement of CP violation in $B^0 \to D^\mp\pi^\pm$". J. High Energ. Phys. 2018, 84 (2018). https://doi.org/10.1007/JHEP06(2018)084. AIS = 1.027.

4. R. Aaij, **A.C. Ene** *et al.* (LHCb Collaboration), "Evidence for the decay $B_S^0 \to \overline{K}^{*0}\mu^+\mu^-$", J. High Energ. Phys. 2018, 20 (2018). https://doi.org/10.1007/JHEP07(2018)020. AIS = 1.027.

5. R. Aaij, **A.C. Ene** *et al.* (LHCb Collaboration), "Measurement of Υ production in pp collisions at $\sqrt{s}$ = 13 TeV", J. High Energ. Phys. 2018, 134 (2018). https://doi.org/10.1007/JHEP07(2018)134. AIS = 1.027.

6. R. Aaij, **A.C. Ene** *et al.* (LHCb Collaboration), "Observation of the decay $\Lambda_b^0 \to \Lambda_c^+ p\overline{p}\pi^-$", Phys. Lett. B 784 (2018) 101-111. https://doi.org/10.1016/j.physletb.2018.07.033. AIS = 1.112.

7. R. Aaij, **A.C. Ene** *et al.* (LHCb Collaboration), "Measurement of forward top pair production in the dilepton channel in pp collisions at $\sqrt{s} = 13$ TeV", J. High Energ. Phys. 2018, 174 (2018). https://doi.org/10.1007/JHEP08(2018)174. AIS = 1.027.

8. R. Aaij, **A.C. Ene** *et al.* (LHCb Collaboration), "Search for CP violation using triple product asymmetries in $\Lambda_b^0 \to pK^-\pi^+\pi^-$, $\Lambda_b^0 \to pK^-K^+K^-$ and $\Xi_b^0 \to pK^-K^-\pi^+$ decays", J. High Energ. Phys. 2018, 39 (2018). https://doi.org/10.1007/JHEP08(2018)039. AIS = 1.027.

9. R. Aaij, **A.C. Ene** *et al.* (LHCb Collaboration), "Measurement of CP asymmetries in two-body $B^0_{(s)}$-meson decays to charged pions and kaons", Phys. Rev. D 98, 032004 (2018). https://doi.org/10.1103/PhysRevD.98.032004. AIS = 0.954.

10. R. Aaij, **A.C. Ene** *et al.* (LHCb Collaboration), "Observation of a New Ξ_b^- Resonance", Phys. Rev. Lett. 121, 072002 (2018). https://doi.org/10.1103/PhysRevLett.121.072002. AIS = 3.153.

11. R. Aaij, **A.C. Ene** *et al.* (LHCb Collaboration), "Search for a dimuon resonance in the Υ mass region", J. High Energ. Phys. 2018, 147 (2018). https://doi.org/10.1007/JHEP09(2018)147. AIS = 1.027.

12. R. Aaij, **A.C. Ene** *et al.* (LHCb Collaboration), "Measurement of $D_s^\pm$ production asymmetry in pp collisions at $\sqrt{s} = 7$ and 8 TeV", J. High Energ. Phys. 2018, 8 (2018). https://doi.org/10.1007/JHEP08(2018)008. AIS = 1.027.

13. R. Aaij, **A.C. Ene** *et al.* (LHCb Collaboration), "Measurement of the CKM angle γ using $B^\pm \to DK^\pm$ with $D \to K_S^0\pi^+\pi^-$, $K_S^0K^+K^-$ decays", J. High Energ. Phys. 2018, 176 (2018). https://doi.org/10.1007/JHEP08(2018)176. AIS = 1.027.

14. R. Aaij, **A.C. Ene** *et al.* (LHCb Collaboration), "Measurement of the Lifetime of the Doubly Charmed Baryon Ξ_{cc}^{++}", Phys. Rev. Lett. 121, 052002 (2018). https://doi.org/10.1103/PhysRevLett.121.052002. AIS = 3.153.

15. R. Aaij, **A.C. Ene** *et al.* (LHCb Collaboration), "Central exclusive production of J/ψ and $\psi(2S)$ mesons in pp collisions at $\sqrt{s} = 13$ TeV", J. High Energ. Phys. 2018, 167 (2018). https://doi.org/10.1007/JHEP10(2018)167. AIS = 1.027.

16. R. Aaij, **A.C. Ene** *et al.* (LHCb Collaboration), "Measurement of $Z \to \tau^+\tau^-$ production in proton-proton collisions at $\sqrt{s} = 8$ TeV", J. High Energ. Phys. 2018, 159 (2018). https://doi.org/10.1007/JHEP09(2018)159. AIS = 1.027.

17. R. Aaij, **A.C. Ene** *et al.* (LHCb Collaboration), "Observation of the decay $\Lambda_b^0 \to \psi(2S)2\pi^-$", J. High Energ. Phys. 2018, 131 (2018). https://doi.org/10.1007/JHEP08(2018)131. AIS = 1.027.

18. R. Aaij, **A.C. Ene** *et al.* (LHCb Collaboration), "Observation of the decay $\overline{B}_s^0 \to \chi_{c2}K^+k^-$ in the ϕ mass region", J. High Energ. Phys. 2018, 191 (2018). https://doi.org/10.1007/JHEP08(2018)191. AIS = 1.027.

19. R. Aaij, **A.C. Ene** *et al.* (LHCb Collaboration), "Measurement of Angular and CP Asymmetries in $D^0 \to \pi^+\pi^-\mu^+\mu^-$ and $D^0 \to K^+K^-\mu^+\mu^-$ Decays", Phys. Rev. Lett. 121, 091801 (2018). https://doi.org/10.1103/PhysRevLett.121.091801. AIS = 3.153.

20. R. Aaij, **A.C. Ene** *et al.* (LHCb Collaboration), "Search for beautiful tetraquarks in the $\Upsilon(1S)\mu^+\mu^-$ invariant-mass spectrum", J. High Energ. Phys. 2018, 86 (2018). https://doi.org/10.1007/JHEP10(2018)086. AIS = 1.027.

21. R. Aaij, **A.C. Ene** *et al.* (LHCb Collaboration), "Observation of $B_s^0 \to \overline{D}^{*0}\phi$ and search for $B^0 \to \overline{D}^0\phi$ decays", Phys. Rev. D 98, 071103(R) (2018). https://doi.org/10.1103/PhysRevD.98.071103. AIS = 0.954.

22. R. Aaij, **A.C. Ene** *et al.* (LHCb Collaboration), "First Observation of the Doubly Charmed Baryon Decay $\Xi_{cc}^{++} \to \Xi_c^{+}\pi^{+}$", Phys. Rev. Lett. 121, 162002 (2018). https://doi.org/10.1103/PhysRevLett.121.162002. AIS = 3.153.

23. R. Aaij, **A.C. Ene** *et al.* (LHCb Collaboration), "Measurement of the Ω_c^0 Baryon Lifetime", Phys. Rev. Lett. 121, 092003 (2018). https://doi.org/10.1103/PhysRevLett.121.092003. AIS = 3.153.

24. R. Aaij, **A.C. Ene** *et al.* (LHCb Collaboration), "Angular moments of the decay $\Lambda_b^0 \to \Lambda\mu^+\mu^-$ at low hadronic recoil", J. High Energ. Phys. 2018, 146 (2018). https://doi.org/10.1007/JHEP09(2018)146. AIS = 1.027.

25. R. Aaij, **A.C. Ene** *et al.* (LHCb Collaboration), "Search for CP violation in $\Lambda_b^0 \to pK^-$ and $\Lambda_b^0 \to pK^-$ decays", Phys. Lett. B 787 (2018) 124-133. https://doi.org/10.1016/j.physletb.2018.10.039. AIS = 1.112.

26. R. Aaij, **A.C. Ene** *et al.* (LHCb Collaboration), "Observation of the decay $B_s^0 \to \overline{D}^0 K^+K^-$", Phys. Rev. D 98, 072006 (2018). https://doi.org/10.1103/PhysRevD.98.072006. AIS = 0.954.

27. R. Aaij, **A.C. Ene** *et al.* (LHCb Collaboration), "Measurement of the time-integrated CP asymmetry in $D^0 \to K_S^0 K_S^0$ decays", J. High Energ. Phys. 2018, 48 (2018). https://doi.org/10.1007/JHEP11(2018)048. AIS = 1.027.

28. R. Aaij, **A.C. Ene** *et al.* (LHCb Collaboration), "Measurement of the CKM angle γ using $B^\pm \to DK^\pm$ with $D \to K_S^0\pi^+\pi^-$, $K_S^0K^+K^-$ decays", J. High Energ. Phys. 2018, 176 (2018). https://doi.org/10.1007/JHEP08(2018)176. AIS = 1.027.

29. R. Aaij, **A.C. Ene** *et al.* (LHCb Collaboration), "Measurement of the relative $B^- \to D^0/D^{*0}/D^{**0}\mu^-\overline{\nu}_\mu$ branching fractions using B^- mesons from $\overline{B}_{s2}^{*0}$ decays", Phys. Rev. D 99, 092009 (2019). https://doi.org/10.1103/PhysRevD.99.092009. AIS = 0.954.

30. R. Aaij, **A.C. Ene** *et al.* (LHCb Collaboration), "Measurement of Antiproton Production in p-He Collisions at $\sqrt{s_{NN}} = 110$" GeV", Phys. Rev. Lett. 121, 222001 (2018). https://doi.org/10.1103/PhysRevLett.121.222001. AIS = 3.153.

31. R. Aaij, **A.C. Ene** *et al.* (LHCb Collaboration), "Search for lepton-flavour-violating decays of Higgs-like bosons", Eur. Phys. J. C 78, 1008 (2018). https://doi.org/10.1140/epjc/s10052-018-6386-8. AIS = 1.152.

32. R. Aaij, **A.C. Ene** *et al.* (LHCb Collaboration), "Prompt Λ_c^+ production in pPb collisions at $\sqrt{s_{NN}} = 5.02$ TeV", J. High Energ. Phys. 2019, 102 (2019). https://doi.org/10.1007/JHEP02(2019)102. AIS = 1.027.

33. R. Aaij, **A.C. Ene** *et al.* (LHCb Collaboration), "Evidence for an $\eta_c(1S)\pi^-$ resonance in $B^0 \to \eta_c(1S)K^+\pi^-$ decays", Eur. Phys. J. C 78, 1019 (2018). https://doi.org/10.1140/epjc/s10052-018-6447-z. AIS = 1.152.

34. R. Aaij, **A.C. Ene** *et al.* (LHCb Collaboration), "Observation of Two Resonances in the $\Lambda_b^0\pi^\pm$ Systems and Precise Measurement of $\Sigma_b^\pm$ and $\Sigma_b^{*\pm}$ Properties", Phys. Rev. Lett. 122, 012001 (2019). https://doi.org/10.1103/PhysRevLett.122.012001. AIS = 3.153.

35. R. Aaij, **A.C. Ene** *et al.* (LHCb Collaboration), "Measurement of the branching fractions of the decays $D^+ \to K^-K^+K^+$, $D^+ \to \pi^-\pi^+K^+$ and $D_s^+ \to \pi^-K^+K^+$", J. High Energ. Phys. 2019, 176 (2019). https://doi.org/10.1007/JHEP03(2019)176. AIS = 1.027.

36. R. Aaij, **A.C. Ene** *et al.* (LHCb Collaboration), "Measurement of the Charm-Mixing Parameter y_{CP}", Phys. Rev. Lett. 122, 011802 (2019). https://doi.org/10.1103/PhysRevLett.122.011802. AIS = 3.153.

37. R. Aaij, **A.C. Ene** *et al.* (LHCb Collaboration), "Study of Υ production in pPb collisions at $\sqrt{s_{NN}} = 8.16$ TeV", J. High Energ. Phys. 2018, 194 (2018). https://doi.org/10.1007/JHEP11(2018)194. AIS = 1.027.

38. R. Aaij, **A.C. Ene** *et al.* (LHCb Collaboration), "First Measurement of Charm Production in its Fixed-Target Configuration at the LHC", Phys. Rev. Lett. 122, 132002 (2019). https://doi.org/10.1103/PhysRevLett.122.132002. AIS = 3.153.

39. R. Aaij, **A.C. Ene** *et al.* (LHCb Collaboration), "Search for CP violation through an amplitude analysis of $D^0 \to K^+K^-\pi^+\pi^-$ decays", J. High Energ. Phys. 2019, 126 (2019). https://doi.org/10.1007/JHEP02(2019)126. AIS = 1.027.

40. R. Aaij, **A.C. Ene** *et al.* (LHCb Collaboration), "Search for the rare decay $B^+ \to \mu^+\mu^-\mu^+\nu_\mu$", Eur. Phys. J. C 79, 675 (2019). https://doi.org/10.1140/epjc/s10052-019-7112-x. AIS = 1.152.

41. R. Aaij, **A.C. Ene** *et al.* (LHCb Collaboration), "Study of the $B^0 \to \rho(770)^0K^*(892)^0$ decay with an amplitude analysis of $B^0 \to (\pi^+\pi^-)(K^+\pi^-)$ decays", J. High Energ. Phys. 2019, 26 (2019). https://doi.org/10.1007/JHEP05(2019)026. AIS = 1.027.

42. R. Aaij, **A.C. Ene** *et al.* (LHCb Collaboration), "Measurement of the branching fraction and CP asymmetry in $B^+ \to J/\psi\rho^0$ decays", Eur. Phys. J. C 79, 537 (2019). https://doi.org/10.1140/epjc/s10052-019-6698-3. AIS = 1.152.

43. R. Aaij, **A.C. Ene** *et al.* (LHCb Collaboration), "Model-Independent Observation of Exotic Contributions to $B^0 \to J/\psi K^+\pi^-$ Decays", Phys. Rev. Lett. 122, 152002 (2019). https://doi.org/10.1103/PhysRevLett.122.152002. AIS = 3.153.

44. R. Aaij, **A.C. Ene** *et al.* (LHCb Collaboration), "Observation of the doubly Cabibbo-suppressed decay $\Xi_c^+ \to p\phi$", J. High Energ. Phys. 2019, 84 (2019). https://doi.org/10.1007/JHEP04(2019)084. AIS = 1.027.

45. R. Aaij, **A.C. Ene** *et al.* (LHCb Collaboration), "Measurement of the mass and production rate of Ξ_b^- baryons", Phys. Rev. D 99, 052006 (2019). https://doi.org/10.1103/PhysRevD.99.052006. AIS = 0.954.

46. R. Aaij, **A.C. Ene** *et al.* (LHCb Collaboration), "Measurement of the branching fractions of the decays $\Lambda_b^0 \to \psi(2S)\Lambda$ and $\Lambda_b^0 \to J/\psi\Lambda$", J. High Energ. Phys. 2019, 126 (2019). https://doi.org/10.1007/JHEP03(2019)126. AIS = 1.027.

47. R. Aaij, **A.C. Ene** *et al.* (LHCb Collaboration), "Observation of $B^0_{(s)} \to J/\psi p\bar{p}$ Decays and Precision Measurements of the $B^0_{(s)}$ Masses", Phys. Rev. Lett. 122, 191804 (2019). https://doi.org/10.1103/PhysRevLett.122.191804. AIS = 3.153.

48. R. Aaij, **A.C. Ene** *et al.* (LHCb Collaboration), "Measurement of B^+, B^0 and Λ_b^0 production in pPb collisions at $\sqrt{s_{NN}} = 8.16$ TeV", Phys. Rev. D 99, 052011 (2019). https://doi.org/10.1103/PhysRevD.99.052011. AIS = 0.954.

49. R. Aaij, **A.C. Ene** *et al.* (LHCb Collaboration), "Dalitz plot analysis of the $D^+ \to K^-K^+K^+$ decay", J. High Energ. Phys. 2019, 63 (2019). https://doi.org/10.1007/JHEP04(2019)063. AIS = 1.027.

50. R. Aaij, **A.C. Ene** *et al.* (LHCb Collaboration), "Measurement of b hadron fractions in 13 TeV pp collisions", Phys. Rev. D 100, 031102(R) (2019). https://doi.org/10.1103/PhysRevD.100.031102. AIS = 0.954.

51. R. Aaij, **A.C. Ene** *et al.* (LHCb Collaboration), "Amplitude analysis of $B_s^0 \to K_S^0K^\pm\pi^\mp$ decays", J. High Energ. Phys. 2019, 114 (2019). https://doi.org/10.1007/JHEP06(2019)114. AIS = 1.027.

52. R. Aaij, **A.C. Ene** *et al.* (LHCb Collaboration), "Search for CP Violation in $D_s^+ \to K_S^0\pi^+$, $D^+ \to K_S^0K^+$, and $D^+ \to \phi\pi^+$ Decays", Phys. Rev. Lett. 122, 191803 (2019). https://doi.org/10.1103/PhysRevLett.122.191803. AIS = 3.153.

53. R. Aaij, **A.C. Ene** *et al.* (LHCb Collaboration), "Measurement of the Mass Difference Between Neutral Charm-Meson Eigenstates", Phys. Rev. Lett. 122, 231802 (2019). https://doi.org/10.1103/PhysRevLett.122.231802. AIS = 3.153.

54. R. Aaij, **A.C. Ene** *et al.* (LHCb Collaboration), "Measurement of the CP-violating phase ϕ_s from $B_s^0 \to J/\psi\pi^+\pi^-$ decays in 13 TeV pp collisions", Phys. Lett. B 797 (2019) 134789. https://doi.org/10.1016/j.physletb.2019.07.036. AIS = 1.112.

55. R. Aaij, **A.C. Ene** *et al.* (LHCb Collaboration), "Measurements of CP asymmetries in charmless four-body Λ_b^0 and Ξ_b^0 decays", Eur. Phys. J. C 79, 745 (2019). https://doi.org/10.1140/epjc/s10052-019-7218-1. AIS = 1.027.

56. R. Aaij, **A.C. Ene** *et al.* (LHCb Collaboration), "Observation of CP Violation in Charm Decays", Phys. Rev. Lett. 122, 211803 (2019). https://doi.org/10.1103/PhysRevLett.122.211803. AIS = 3.153.

57. R. Aaij, **A.C. Ene** *et al.* (LHCb Collaboration), "Search for Lepton-Universality Violation in $B^+ \to K^+l^+l^-$ Decays", Phys. Rev. Lett. 122, 191801 (2019). https://doi.org/10.1103/PhysRevLett.122.191801. AIS = 3.153.

58. R. Aaij, **A.C. Ene** *et al.* (LHCb Collaboration), "Near-threshold D$\overline{\text{D}}$ spectroscopy and observation of a new charmonium state", J. High Energ. Phys. 2019, 35 (2019). https://doi.org/10.1007/JHEP07(2019)035. AIS = 1.027.

59. R. Aaij, **A.C. Ene** *et al.* (LHCb Collaboration), "Observation of an Excited B_c^+ State", Phys. Rev. Lett. 122, 232001 (2019). https://doi.org/10.1103/PhysRevLett.122.232001. AIS = 3.153.

60. R. Aaij, **A.C. Ene** *et al.* (LHCb Collaboration), "Observation of a Narrow Pentaquark State, $P_c(4312)^+$, and of the Two-Peak Structure of the $P_c(4450)^+$", Phys. Rev. Lett. 122, 222001 (2019). https://doi.org/10.1103/PhysRevLett.122.222001. AIS = 3.153.

61. R. Aaij, **A.C. Ene** *et al.* (LHCb Collaboration), "First Observation of the Radiative Decay $\Lambda_b^0 \to \Lambda\gamma$", Phys. Rev. Lett. 123, 031801 (2019). https://doi.org/10.1103/PhysRevLett.123.031801. AIS = 3.153.

62. R. Aaij, **A.C. Ene** *et al.* (LHCb Collaboration), "Measurement of Charged Hadron Production in Z-Tagged Jets in Proton-Proton Collisions at $\sqrt{s} = 8$ TeV", Phys. Rev. Lett. 123, 232001 (2019). https://doi.org/10.1103/PhysRevLett.123.232001. AIS = 3.153.

63. R. Aaij, **A.C. Ene** *et al.* (LHCb Collaboration), "A search for $\Xi_{cc}^{++} \to D^+pK^-\pi^+$ decays", J. High Energ. Phys. 2019, 124 (2019). https://doi.org/10.1007/JHEP10(2019)124. AIS = 1.027.

64. R. Aaij, **A.C. Ene** *et al.* (LHCb Collaboration), "Measurement of CP-Violating and Mixing-Induced Observables in $B_s^0 \to \phi\gamma$ Decays", Phys. Rev. Lett. 123, 081802 (2019). https://doi.org/10.1103/PhysRevLett.123.081802. AIS = 3.153.

65. R. Aaij, **A.C. Ene** *et al.* (LHCb Collaboration), "Search for the Lepton-Flavor-Violating Decays $B_s^0 \to \tau^\pm\mu^\mp$ and $B^0 \to \tau^\pm\mu^\mp$", Phys. Rev. Lett. 123, 211801 (2019). https://doi.org.10.1103/PhysRevLett.123.211801. AIS = 3.153.

66. R. Aaij, **A.C. Ene** *et al.* (LHCb Collaboration), "Amplitude analysis of the $B^0_{(s)} \to K^{*0}\overline{K}^{*0}$ decays and measurement of the branching fraction of the $B^0 \to K^{*0}\overline{K}^{*0}$ decay", J. High Energ. Phys. 2019, 32 (2019). https://doi.org/10.1007/JHEP07(2019)032. AIS = 1.027.

67. R. Aaij, **A.C. Ene** *et al.* (LHCb Collaboration), "Amplitude Analysis of $B^\pm \to \pi^\pm K^+K^-$ Decays", Phys. Rev. Lett. 123, 231802 (2019). AIS = 3.153.

68. R. Aaij, **A.C. Ene** *et al.* (LHCb Collaboration), "Measurement of CP observables in the process $B^0 \to DK^{*0}$ with two- and four-body D decays", J. High Energ. Phys. 2019, 41 (2019). https://doi.org/10.1007/JHEP08(2019)041. AIS = 1.027.

69. R. Aaij, **A.C. Ene** *et al.* (LHCb Collaboration), "Precision measurement of the Λ_c^+, Ξ_c^+, and Ξ_c^0 baryon lifetimes", Phys. Rev. D 100, 032001. https://doi.org/10.1103/PhysRevD.100.032001. AIS = 0.954.

70. R. Aaij, **A.C. Ene** *et al.* (LHCb Collaboration), "Updated measurement of time-dependent CP-violating observables in $B_S^0 \to J/\psi K^+K^-$ decays", Eur. Phys. J. C 79, 706 (2019). https://doi.org/10.1140/epjc/s10052-019-7159-8. AIS = 1.152.

71. R. Aaij, **A.C. Ene** *et al.* (LHCb Collaboration), "Observation of the $\Lambda_b^0 \to \chi_{c1}(3872)pK^-$ decay", J. High Energ. Phys. 2019, 28 (2019). https://doi.org/10.1007/JHEP09(2019)028. AIS = 1.027.

72. R. Aaij, **A.C. Ene** *et al.* (LHCb Collaboration), "Measurement of CP violation in the $B_s^0 \to \phi\phi$ decay and search for the $B^0 \to \phi\phi$ decay", J. High Energ. Phys. 2019, 155 (2019). https://doi.org/10.1007/JHEP12(2019)155. AIS = 1.027.

73. R. Aaij, **A.C. Ene** *et al.* (LHCb Collaboration), "Observation of New Resonances in the $\Lambda_b^0\pi^+\pi^-$ System", Phys. Rev. Lett. 123, 152001 (2019). https://doi.org/10.1103/PhysRevLett.123.152001. AIS = 3.153.

74. R. Aaij, **A.C. Ene** *et al.* (LHCb Collaboration), "Measurement of $\psi(2S)$ production cross-sections in proton-proton collisions at $\sqrt{s} = 7$ and 13 TeV", Eur. Phys. J. C 80, 185 (2020). https://doi.org/10.1140/epjc/s10052-020-7638-y. AIS = 1.152.

75. R. Aaij, **A.C. Ene** *et al.* (LHCb Collaboration), "Search for Lepton-Flavor Violating Decays $B^+ \to K^+\mu^\pm e^\mp$", Phys. Rev. Lett. 123, 241802 (2019). https://doi.org/10.1103/PhysRevLett.123.241802. AIS = 3.153.

76. R. Aaij, **A.C. Ene** *et al.* (LHCb Collaboration), "Observation of Several Sources of CP Violation in $B^+ \to \pi^+\pi^+\pi^-$ Decays", Phys. Rev. Lett. 124, 031801 (2020). https://doi.org/10.1103/PhysRevLett.124.031801. AIS = 3.153.

77. R. Aaij, **A.C. Ene** *et al.* (LHCb Collaboration), "Amplitude analysis of the $B^+ \to \pi^+\pi^+\pi^-$ decay", Phys. Rev. D 101, 012006 (2020). https://doi.org/PhysRevD.101.012006. AIS = 0.954.

78. R. Aaij, **A.C. Ene** *et al.* (LHCb Collaboration), "Search for the doubly charmed baryon Ξ_{cc}^+", Sci. China Phys. Mech. Astron. 63, 221062 (2020). https://doi.org/10.1007/s11433-019-1471-8. AIS = 0.501.

79. R. Aaij, **A.C. Ene** *et al.* (LHCb Collaboration), "Search for $A' \to \mu^+\mu^-$ Decays", Phys. Rev. Lett. 124, 041801 (2020). https://doi.org/10.1103/PhysRevLett.124.041801. AIS = 3.153.

80. R. Aaij, **A.C. Ene** *et al.* (LHCb Collaboration), "Measurement of f_s/f_u Variation with Proton-Proton Collision Energy and B-Meson Kinematics", Phys. Rev. Lett. 124, 122002 (2020). https://doi.org/10.1103/PhysRevLett.124.122002. AIS = 3.153.

81. R. Aaij, **A.C. Ene** *et al.* (LHCb Collaboration), "Measurement of Ξ_{cc}^{++} production in pp collisions at $\sqrt{s} = 13$ TeV", Chinese Phys. C 44 022001 (2020). https://doi.org/10.1088/1674-1137/44/2/022001. AIS = 0.763.

82. R. Aaij, **A.C. Ene** *et al.* (LHCb Collaboration), "Measurement of the B_c^- meson production fraction and asymmetry in 7 and 13 TeV pp collisions", Phys. Rev. D 100, 112006 (2019). https://doi.org/10.1103/PhysRevD.100.112006. AIS = 0.954.

83. R. Aaij, **A.C. Ene** *et al.* (LHCb Collaboration), "Updated measurement of decay-time-dependent CP asymmetries in $D^0 \to K^+K^-$ and $D^0 \to \pi^+\pi^-$ decays", Phys. Rev. D 101, 012005 (2020). https://doi.org/10.1103/PhysRevD.101.012005. AIS = 0.954.

84. R. Aaij, **A.C. Ene** *et al.* (LHCb Collaboration), "Measurement of the $\eta_c(1S)$ production cross-section in pp collisions at $\sqrt{s} = 13$ TeV", Eur. Phys. J. C 80, 191 (2020). https://doi.org/10.1140/epjc/s10052-020-7733-0. AIS = 1.152.

85. R. Aaij, **A.C. Ene** *et al.* (LHCb Collaboration), "Determination of quantum numbers for several excited charmed mesons observed in $B^- \to D^{*+}\pi^+\pi^-$ decays", Phys. Rev. D 101, 032005 (2020). https://doi.org/10.1103/PhysRevD.101.032005. AIS = 0.954.

86. R. Aaij, **A.C. Ene** *et al.* (LHCb Collaboration), "Observation of the semileptonic decay $B^+ \to p\bar{p}\mu^+\nu_\mu$", J. High Energ. Phys. 2020, 146 (2020). https://doi.org/10.1007/JHEP03(2020)146. AIS = 1.027.

87. R. Aaij, **A.C. Ene** *et al.* (LHCb Collaboration), "Precision measurement of the Ξ_{cc}^{++} mass", J. High Energ. Phys. 2020, 49 (2020). https://doi.org/10.1007/JHEP02(2020)049. AIS = 1.027.

88. R. Aaij, **A.C. Ene** *et al.* (LHCb Collaboration), "Isospin Amplitudes in $\Lambda_b^0 \to J/\psi\Lambda(\Sigma^0)$ and $\Xi_b^0 \to J/\psi\Xi^0(\Lambda)$ Decays", Phys. Rev. Lett. 124, 111802 (2020). https://doi.org/10.1103/PhysRevLett.124.111802. AIS = 3.153.

89. R. Aaij, **A.C. Ene** *et al.* (LHCb Collaboration), "Measurement of CP violation in $B^0 \to D^{*\pm}D^{\mp}$ decays", J. High Energ. Phys. 2020, 147 (2020). https://doi.org/10.1007/JHEP03(2020)147. AIS = 1.027.

90. R. Aaij, **A.C. Ene** *et al.* (LHCb Collaboration), "Test of lepton universality with $\Lambda_b^0 \to pK^-l^+l^-$ decays", J. High Energ. Phys. 2020, 40 (2020). https://doi.org/10.1007/JHEP05(2020)040. AIS = 1.027.

91. R. Aaij, **A.C. Ene** *et al.* (LHCb Collaboration), "First Observation of Excited Ω_b^- *States*", Phys. Rev. Lett. 124, 082002 (2020). https://doi.org/10.1103/PhysRevLett.124.082002. AIS = 3.153.

92. R. Aaij, **A.C. Ene** *et al.* (LHCb Collaboration), "Measurement of $|V_{cb}|$ with $B_s^0 \to D_s^{(*)-}\mu^+\nu_\mu$ decays", Phys. Rev. D 101, 072004 (2020). https://doi.org/10.1103/PhysRevD.101.072004. AIS = 0.954.

93. R. Aaij, **A.C. Ene** *et al.* (LHCb Collaboration), "Search for the Rare Decays $B_s^0 \to e^+e^-$ and $B^0 \to e^+e^-$", Phys. Rev. Lett. 124, 211802 (2020). https://doi.org/10.1103/PhysRevLett.124.211802. AIS = 3.153.

94. R. Aaij, **A.C. Ene** *et al.* (LHCb Collaboration), "Observation of New Ξ_c^0 Baryons Decaying to $\Lambda_c^+K^-$", Phys. Rev. Lett. 124, 222001 (2020). https://doi.org/10.1103/PhysRevLett.124.222001. AIS = 3.153.

95. R. Aaij, **A.C. Ene** *et al.* (LHCb Collaboration), "Observation of a new baryon state in the $\Lambda_b^0\pi^+\pi^-$ mass spectrum", J. High Energ. Phys. 2020, 136 (2020). https://doi.org/10.1007/JHEP06(2020)136.

96. R. Aaij, **A.C. Ene** *et al.* (LHCb Collaboration), "Measurement of CP observables in $B^\pm \to DK^\pm$ and $B^\pm \to D\pi^\pm$ with $D \to K_S^0K^\pm\pi^\mp$ decays", J. High Energ. Phys. 2020, 58 (2020). https://doi.org/10.1007/JHEP06(2020)058.

97. R. Aaij, **A.C. Ene** *et al.* (LHCb Collaboration), "Measurement of CP-Averaged Observables in the $B^0 \to K^{*0}\mu^+\mu^-$ Decay", Phys. Rev. Lett. 125, 011802 (2020). https://doi.org/10.1103/PhysRevLett.125.011802.

8.2 Conferences

8.2.1 International conferences

1. **A.C. Ene**, "Study of strange and beauty particles production in pp interactions at $\sqrt{s} =$ 13 TeV using PYTHIA", The 17th International Balkan Workshop on Applied Physics, Constanţa, July 2017. http://ibwap.univ-ovidius.ro/2017/uploads/template/IBWAP_2017_program.pdf.

2. **A.C. Ene**, "Monte Carlo event generation for pp collisions, phenomenological models and tuning", WE-Heraeus Physics School: QCD – Old Challenges and New Opportunities, Bad Honnef, September 2017. https://indico.cern.ch/event/614845/contributions/.

3. **A.C. Ene**, "Proton-proton collision generators. Predictions at $\sqrt{s} = 7$ TeV and the forward physics at LHC", TIM 2018 Physics Conference, Timişoara, May 2018. https://timconference.uvt.ro/archive/tim18/Conference_Schedule_TIM18.pdf.

4. **A.C. Ene**, "Monte Carlo event generator predictions for forward physics in sqrt(s) = 7 TeV proton-proton collisions, 7th International Conference on New Frontiers in Physics" (ICNFP 2018), 04-12 July 2018, Kolymbari, Greece. https://indico.cern.ch/event/663474/attachments/1625006/2701476/Program_5_July.xlsx.
5. A. Jipa, O. Ristea, **A.C. Ene** *et al.*, "Simulation results on bulk properties and hydrodynamic behaviours of the high excited and dense nuclear matter in relativistic nuclear collisions at FAIR energies", 7th International Conference on New Frontiers in Physics" (ICNFP 2018), 04-12 July 2018, Kolymbari, Greece. https://indico.cern.ch/event/663474/attachments/1625006/2701476/Program_5_July.xlsx.
6. **A.C. Ene**, "LHC minimum bias measurements in the forward region from proton-proton collisions and predictions of Monte Carlo event generators", The 19th International Balkan Workshop on Applied Physics and Materials Science, Constanţa, July 2019. http://ibwap.ro/wp-content/uploads/2019/07/IBWAP-book-of-abstracts-2019.pdf.

8.2.2 National/local conferences

1. **A.C. Ene**, "Comparison of cosmic ray collisions generators and PYTHIA", Workshop on sensors and High Energy Physics (21-22 October 2016), Ştefan cel Mare University of Suceava, Suceava, October 2016.
2. **A.C. Ene**, "Comparison of cosmic ray models with PYTHIA", Young Researchers Scientific Meeting @ IFIN-HH, Bucharest-Măgurele, December 2016.
3. **A.C. Ene**, A. Jipa, "Comparison of cosmic ray collisions generators and PYTHIA predictions for proton-proton interactions at LHC energies", Bucharest University Faculty of Physics 2017 Meeting, June 2017.
4. A. Jipa, C. Besliu, **A.C. Ene** *et al.*, "Possible new insights on the dynamics or relativistic nuclear collisions from CBM Experiment from FAIR-GSI", Bucharest University Faculty of Physics 2017 Meeting, June 2017.
5. **A.C. Ene**, "Monte Carlo event generation for pp collisions, phenomenological models and tuning", ISAB: Young Scientists Forum, Bucharest-Măgurele, October 2017.
6. **A.C. Ene**, "Study of Monte Carlo event generators taking as reference LHCb data", Young Researchers Scientific Meeting @ IFIN-HH, Bucharest-Măgurele, December 2017.
7. **A.C. Ene**, A. Jipa, "Global event observables in forward physics at LHCb. Predictions of Monte Carlo event generators for proton-proton collisions at $\sqrt{s} = 7$ TeV", Bucharest University Faculty of Physics 2018 Meeting, June 2018.
8. C. Besliu, A. Jipa, **A.C. Ene** *et al.*, "On the evolution of the relativistic and ultrarelativistic nuclear collisions studies. Old and new results and their continuity", Bucharest University Faculty of Physics 2018 Meeting, June 2018.
9. **A.C. Ene**, "Prompt V^0 production cross-sections and ratios in pp collisions at $\sqrt{s} = 13$ TeV measured at the LHCb experiment", Young Researchers Scientific Meeting @ IFIN-HH, Bucharest-Magurele, December 2018.
10. **A.C. Ene**, "Prompt V^0 production cross-sections and ratios in pp collisions at $\sqrt{s} = 13$ TeV at the LHCb experiment", ISAB: Young Scientists Forum, Bucharest-Măgurele, December 2019.
11. **A.C. Ene**, "Analysis of prompt V^0 production cross-sections and ratios in pp collisions at $\sqrt{s} = 13$ TeV measured at the LHCb experiment", Young Researchers Scientific Meeting @ IFIN-HH, Bucharest-Magurele, December 2019.

8.2.3 Internal LHCb collaboration talks

1. **A.C. Ene**, "Prompt V^0 production cross-sections and ratios in pp collisions at $\sqrt{s} = 13$ TeV", QEE (QCD, Electroweak and Exotica) Meeting, 23.09.2019.

8.3 Schools, workshops etc.

1. Frontiers in particle physics: Flavor Physics, 7-11 November 2016, Niels Bohr Institute, Copenhagen, Denmark.
2. Geant4 school at IFIN-HH, 14-18 November 2016, IFIN-HH, Bucharest-Măgurele, Romania.
3. 84$^{\text{th}}$ LHCb Week 12 - 16 June 2017, CERN, Meyrin, Switzerland.
4. Workshop on the Standard Model and Beyond - 17th Hellenic School and Workshops on Elementary Particle Physics and Gravity, 2-10 September 2017, Corfu, Greece. **Financial support granted.**
5. Workshop on Particle Physics and Cosmology Tools - 17th Hellenic School and Workshops on Elementary Particle Physics and Gravity, 9-14 September 2017, Corfu, Greece.
6. WE-Heraeus Physics School – QCD - Old Challenges and New Opportunities, 24-30 September 2017, Bad Honnef, Germany. **Financial support granted.**
7. LHCb Implications Workshop, 8-10 November 2017, CERN, Meyrin, Switzerland.
8. 94$^{\text{th}}$ LHCb Week 02 - 06 December 2019, CERN, Meyrin, Switzerland.

8.4 Outreach

1. Organizer of LHCb MasterClass 2017 at Universitatea "Ştefan cel Mare", Suceava, Romania.
2. Organizer of parallel session of LHCb MasterClass 2018 at Colegiul Naţional "Constantin Carabella", Târgovişte, Romania.
3. Organizer of LHCb MasterClass 2019 at Colegiul Naţional "Ienăchiţă Văcărescu", Târgovişte, Romania.

8.5 Courses

1. "Introduction to Nuclear and Particle Physics",18.09.2018-13.11.2018, at Centrul de Pregătire şi Specializare în Domeniul Nuclear (CPSDN).

8.6 Academic

2016 - Present: Laboratory classes held for the "Phenomenology of Nuclear and Elementary Particle Physics at high energies" and "Experimental Relativistic Nuclear Physics" courses of professor A. Jipa for the Physics of the Atom, Nucleus, Elementary Particles, Astrophysics and Applications Master's program of the Faculty of Physics, University of Bucharest.